NASA Technical Paper 1877

Behavior of Aircraft Antiskid Braking Systems on Dry and Wet Runway Surfaces

Hydromechanically Controlled System

John A. Tanner, Sandy M. Stubbs,
and Eunice G. Smith

AUGUST 1981

NASA

NASA Technical Paper 1877

Behavior of Aircraft Antiskid Braking Systems on Dry and Wet Runway Surfaces

Hydromechanically Controlled System

John A. Tanner, Sandy M. Stubbs,
and Eunice G. Smith
Langley Research Center
Hampton, Virginia

NASA
National Aeronautics
and Space Administration

**Scientific and Technical
Information Branch**

1981

CONTENTS

SUMMARY

An experimental investigation was conducted at the Langley Aircraft Landing Loads and Traction Facility to study the braking and cornering response of a hydromechanically controlled aircraft antiskid braking system. The investigation, conducted on dry and wet runway surfaces, utilized one main gear wheel, brake, and tire assembly of a McDonnell Douglas DC-9 series 10 airplane. The landing-gear strut was replaced by a dynamometer.

During maximum braking, average braking behavior indexes based upon brake pressure, brake torque, and drag-force friction coefficient developed by the antiskid system were generally higher on the dry runway surfaces than on the wet surfaces. On the wet surfaces, these indexes were reduced at higher carriage speeds and when new treads were replaced by worn treads. The three braking behavior indexes gave similar results but the agreement was not sufficient to allow them to be used interchangeably as a measure of the braking behavior for this antiskid system. Furthermore, these braking behavior indexes are based upon maximum values of pressure, torque, and drag-force friction coefficient, which may vary from system to system, and any comparisons between different antiskid systems based solely upon these indexes may be technically misleading. The average cornering behavior index based upon the side-force friction coefficient developed by the tire under antiskid control was decreased on wet runway surfaces, with yaw angles greater than 1°, and when tires with new treads were replaced by those with worn treads. The interaction between braking and cornering forces indicated that, during antiskid cycling, the side-force friction coefficient was significantly reduced during portions of the braking cycles. During the transition from a dry to a flooded surface under heavy braking, the wheel entered into a deep skid, but the antiskid system reacted quickly by reducing brake pressure and performed normally during the remainder of the run on the flooded surface. The brake-pressure recovery following transition from a flooded to a dry surface was shown to be a function of the antiskid modulating orifice.

INTRODUCTION

Over the years, the number and variety of airplanes using antiskid braking systems have steadily increased until most current commercial and military jet airplanes are now equipped with various skid control devices. The earliest antiskid systems were generally designed to prevent wheel lockups and excessive tire wear on dry pavements. Modern skid control devices, however, are more sophisticated and are designed to provide maximum braking effort while maintaining full antiskid protection under all weather conditions. Operating statistics of modern jet airplanes indicate that these antiskid systems are both effective and dependable; the several million landings that are made each year in routine fashion with no serious operating problems attest to this fact.

However, it has been well established, both from flight tests and from field experience, that the performance of these systems is subject to degradation on slippery runways; consequently, dangerously long roll-out distances and reduced steering capability can result during some airplane landing operations (refs. 1 to 5). There is a need to study different types of antiskid braking systems in order to find reasons for the degraded braking performance that occurs under adverse runway conditions; there is also a need to obtain data for the development of more advanced systems that will insure safe ground handling operations under all weather conditions.

In an effort to meet these needs, an experimental research program has been undertaken to study the single-wheel behavior of several different airplane antiskid braking systems under the controlled conditions afforded by the Langley Aircraft Landing Loads and Traction Facility (formerly called the Langley Landing Loads Track). The types of skid control devices undergoing study in this program include a velocity-rate-controlled system (ref. 6); a slip-ratio-controlled system with ground speed reference from an unbraked nose wheel (ref. 7); a slip-velocity-controlled system (ref. 8); and described in this paper, a hydromechanically controlled system. The investigation of all these systems is being conducted with a single main wheel, brake, and tire assembly of a McDonnell Douglas DC-9 series 10 airplane.

The purpose of this paper is to present the results from a study of the behavior of a hydromechanically controlled aircraft antiskid braking system under maximum braking effort. The parameters varied in the study included carriage speed, tire loading, yaw angle, tire tread condition, and runway wetness conditions. A discussion of the effects of each of these parameters on the behavior of the skid control system is presented. In addition, comparisons are made between data obtained with the skid control system and data obtained from single-cycle braking tests without antiskid protection.

Dunlop Limited provided the antiskid-system hardware for this investigation, and the Federal Aviation Administration (FAA) provided the wheels, brakes, and tires.

SYMBOLS

Values are given in both SI and U.S. Customary Units. The measurements and calculations were made in U.S. Customary Units. Factors relating the two systems are given in reference 9.

d	position of footprint center of pressure
F_V	tire vertical force
F_X	drag force parallel to plane of wheel
F_Y	side force perpendicular to plane of wheel
h	axle height

I	moment of inertia
P	power
p	pressure
r	tire rolling radius
S	wheel slip ratio
T	torque
t	time
V	carriage speed
α	angular acceleration
β	behavior index
μ	friction coefficient
ψ	yaw angle
ω	test wheel angular velocity

Subscripts:

b	braking
c	cornering
d	drag
F	friction
f	final value
g	gross
max	maximum value
o	initial value
p	pressure
r	free rolling
s	side

T torque

t tire

A bar over a symbol denotes an average value.

APPARATUS AND TEST PROCEDURE

Test Tires

The tires used in this investigation were 40 × 14, type VII, bias-ply aircraft tires of 22 ply rating with a rated maximum speed of 200 knots (1 knot = 0.5144 m/sec). The tires were stock retreads with a six-groove tread pattern, and the study included both new and worn tread configurations. A photograph of the two test tires having new and worn treads is presented in figure 1. The new tread had a groove depth of 0.71 cm (0.28 in.) and was considered new until the groove depth decreased to 0.36 cm (0.14 in.). To generate worn tires, a commercially available tire grinding machine was employed to remove tread rubber uniformly from the retreaded tire until a groove depth of 0.05 cm (0.02 in.) remained. This simulated worn tire was probably in a worse wear condition than is normally experienced in airplane operations. Throughout this investigation, the tire inflation pressure was maintained at the normal airline operational pressure of 0.97 MPa (140 psi).

Test Facility

The investigation was performed by using a 4800-kg (106 000-lbm) test carriage at the Langley Aircraft Landing Loads and Traction Facility described in reference 10. Figure 2 is a photograph of the carriage with the test wheel assembly installed; figure 3 is a closeup view of the wheel and other components. An instrumented dynamometer was used instead of a landing-gear strut to support the wheel and brake assembly because it provided an accurate measurement of the tire-ground forces.

For the tests described in this paper, approximately 274 m (900 ft) of the available 366 m (1200 ft) of flat concrete test runway was used to provide braking and cornering data on a dry surface, on an artificially damp surface, on an artificially flooded surface, and on a natural rain wet surface. With the exception of transient runway friction tests, the entire runway had a uniform surface wetness condition, and antiskid cycling occurred for the entire 274 m (900 ft). The 61 m (200 ft) of runway preceding the test section was used for the initial wheel spin-up and brake actuation, and the 30.5 m (100 ft) beyond the test section was retained for brake release. To obtain a damp condition, the test surface was lightly wetted with no standing water. For the flooded runway condition, the surface was surrounded by a flexible dam and flooded to a depth of approximately 1.0 cm (0.4 in.). For the natural rain surface condition no measurement of water depth was made.

The concrete surface in the test area had a light broom finish in a transverse direction, and the surface texture was not completely uniform, as shown by the texture depth measurements in the following sketch:

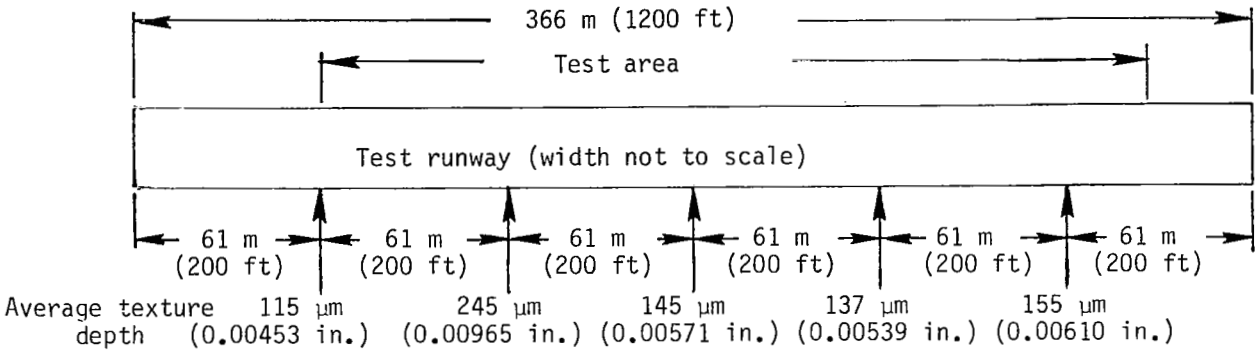

Details of the texture depth measurement technique are presented in reference 11. The average texture depth of the test runway was 159 μm (0.00626 in.), which is slightly less than that of a typical operational runway. (See ref. 12, for example.) The test runway was quite level compared with airport runways and had no crown. During the course of testing on the dry surface, particularly with a yawed tire, rubber was deposited on the runway and it was necessary to clean the surface periodically.

Skid Control System

A hydromechanically controlled skid control unit was used in this investigation and adapted to an existing braking system that had the correct hydraulic components for a single wheel of a DC-9 series 10 airplane. Since the control unit was not designed for this particular airplane, certain installation modifications were necessary to make the two systems compatible. The control unit itself, rather than being installed in a hollow axle as designed, was mounted on an auxiliary axle as shown in figure 3. The auxiliary axle was driven by the test wheel through a steel-reinforced, cogged, rubber timing belt operating over one-to-one drive ratio notched pulleys. This drive system had been used previously in a number of investigations and was found to have no slippage or other undesirable dynamic effects (refs. 6 to 8). The tests were conducted with the skid control unit in the "as received" condition without optimization adjustments. Figure 4 is a photograph of the major hydraulic components of the simulated braking system, upstream from the antiskid hardware, installed on the test carriage; figure 5 is a schematic of the system. The brake system is activated by opening the pilot metering valve (fig. 5), which allows brake fluid to flow from a high-pressure accumulator and brake selector valve through the hydraulic fuse and antiskid control valve to the brake. The sole function of the brake selector valve and hydraulic fuse was to duplicate the DC-9 hydraulic

system. A pneumatic piston shown in figure 4 was used to open the pilot metering valve to its full stroke; thus, maximum braking effort for all tests was provided.

The antiskid control unit is a hydraulic valve mechanically connected to the braked wheel. The opening and closing of the valve is controlled by the energy stored in a small flywheel. The flywheel and aircraft wheel spin up together through an overrunning clutch mechanism. During a brake cycle, the flywheel is used as a spin-up speed reference. During braking without skidding, the torque given up by the flywheel is balanced by a spring. At the onset of a skid, when the angular deceleration of the braked wheel exceeds a certain preselected threshold value, the flywheel overruns and expands the spring. The relative motion thus produced operates the mechanism to release the brake pressure. When the wheel recovers from the skid and the angular deceleration again drops below the threshold value, the spring is recompressed; thus, brake reapplication is permitted. The rate at which pressure is applied to the brake is controlled by an orifice which is sized for a specific airplane application. Brake release is restrained only by line size and component resistances.

Typical time histories of wheel speed, wheel acceleration, brake pressure, and the resulting drag-force friction coefficient μ_d are presented in figure 6 to help describe the system operation. The points labeled Ⓐ to Ⓝ are used to highlight events which occur during antiskid cycling. In the figure, the brake pressure is initially applied (Ⓐ to Ⓑ) and results in a slight decrease in wheel speed (Ⓒ); the early braking effort does not cause the tire to enter a skid and the brake pressure is held constant at the maximum system pressure (Ⓑ to Ⓓ). Eventually the braking effort causes the tire to enter a deep skid (Ⓔ) and, consequently, an increase in the wheel deceleration (Ⓕ) beyond the threshold value (dashed line in fig. 6) causes a pressure release (Ⓓ to Ⓖ). The high spin-up acceleration of the wheel (Ⓗ) and the subsequent spring-back response of the tire (Ⓘ) causes a momentary fluctuation in the brake pressure (Ⓙ) before the brake pressure is reapplied (Ⓚ to Ⓛ) with a corresponding increase in the friction level (Ⓜ to Ⓝ). Beyond 10 sec, the wheel deceleration again moves beyond the apparent threshold value, and the brake release cycle is repeated.

Instrumentation

The tire friction forces were measured with the dynamometer shown in figure 3 and illustrated schematically in figure 7. Strain gages were mounted on the five dynamometer support beams; two of the beams were used for measuring vertical forces, two were used for measuring drag forces parallel to the wheel plane, and a single beam was used for measuring side force perpendicular to the wheel plane. Four accelerometers on the test wheel axle provided information for inertia corrections to the force data. The brake torque was measured with torque links which were independent of the drag-force beams. Transducers were installed in the hydraulic system (fig. 4) to measure pressures at the pilot metering valve, at the antiskid inlet, at the brake, and in the return line between the brake and the hydraulic reservoir. A pressure relief valve in the return line maintained a back pressure of 448 kPa (65 psi) in the hydraulic lines, and all the pressure transducers were calibrated to read zero at this

pressure. A steel-reinforced, cogged, rubber timing belt was driven by the test wheel to run an auxiliary axle which drove the pulse (ac) alternator which was used to obtain a measure of the test wheel angular velocity and acceleration. As previously mentioned, the auxiliary axle also drove the antiskid control unit. A lightweight trailing wheel was mounted on the side of the test carriage (as shown in fig. 8), and the output from a dc generator mounted on its axle recorded the carriage speed and was combined with the output from the test wheel pulse alternator to compute instantaneous slip velocity and slip ratio. All data outputs were fed into signal conditioning equipment and then into two frequency-modulated tape recorders. A time code was recorded on both recorders to provide synchronization of the two sets of data.

Test Procedure

The technique for the braking tests with and without antiskid protection consisted of rotating and locking the yoke holding the dynamometer and tire assembly to the chosen yaw angle, propelling the test carriage to the desired speed, applying a preselected vertical load on the tire, and recording the outputs from the onboard instrumentation. For antiskid tests, the brake was actuated by a pneumatic piston at the pilot metering valve, which gave full pedal deflection or maximum braking, and the antiskid system modulated the braking effort. The runway surface condition was essentially uniform over the entire length; the brake was applied the full distance and was released prior to carriage arrestment.

In addition to antiskid braking tests, single-cycle braking tests were made without antiskid protection. These single brake cycles consisted of applying sufficient brake pressure to bring the tire from a free-rolling condition to a locked-wheel skid and then releasing the brake to allow full tire spin-up prior to the next cycle. For single-cycle braking, the runway surface was divided into three sections (dry, damp, and flooded), and brake pressure was applied by triggering devices at each section along the test track.

The nominal carriage speeds for both types of tests ranged from 36 to 102 knots and were measured approximately midway along the runway where, after initial acceleration, the carriage was coasting through the test section with some speed decay due to carriage wheel friction, air drag, and the braking of the test tire. Tire vertical loading was maintained hydraulically and ranged from approximately 58 kN (13 000 lbf) to 111 kN (25 000 lbf), which represented a nominal landing weight and a refused take-off weight, respectively, for a single main wheel of the DC-9. Tests were run on tire yaw angles from 0^{o} to 9^{o}. The nominal brake-system pressure was maintained near 14 MPa (2000 psi).

Data Reduction

All data were recorded on analog magnetic tape filtered to 1000 Hz. All analog data were then filtered through a low-pass filter (cutoff frequencies of 5 Hz for carriage speed and 60 Hz for all other data) and digitized at 250 samples/sec. Time histories used in the data analysis and those in the appendix are plotted at 50 samples/sec. From these digitized data, direct mea-

surements were obtained of the carriage speed, the braked-wheel angular velocity and acceleration, the brake pressure and torque, the drag force F_x (sum of two beams), the side force F_y, the vertical force applied to the tire F_v (sum of two beams), and the accelerations of the dynamometer. The instantaneous vertical-, drag-, and side-force data were corrected for inertia effects and were combined to compute both the instantaneous drag-force friction coefficient μ_d parallel to the direction of motion and the side-force friction coefficient μ_s perpendicular to the direction of motion. The load transfer between the two drag-force beams (fig. 7) provided a measure of the alining torque about the vertical or steering axis of the wheel. The braked-wheel angular velocity was combined with the carriage speed to yield wheel slip velocity and slip ratio. Pertinent data obtained from all the antiskid braking tests are presented in table I, together with parameters which describe each test condition.

Time histories of some of the measured parameters for a typical antiskid braking test are presented in figure 9(a). These plots start just prior to wheel spin-up and end approximately 1 sec after the release of brake pressure. As previously mentioned, the vertical and drag forces are each the summation of two data channels with corrections made for acceleration effects. The time histories of figure 9(b) are the parameters calculated from the data of figure 9(a). Although brake pressure is a measured parameter, it is included in figure 9(b) to serve as a reference.

DEFINITIONS

An assessment of the behavior of an antiskid braking system subjected to a wide variety of operational conditions requires careful consideration of many variables. Four methods are used in this paper to analyze the behavior of this antiskid braking system; these methods are based upon the following parameters: brake pressure, brake torque, tire friction coefficient, and the stopping and cornering power generated by the antiskid system. The development of the parameters used to describe the antiskid-system behavior is discussed in the following paragraphs.

Brake Pressure

One method of determining antiskid-system behavior is to compare the average brake pressure $\bar{p}$ to the maximum brake pressure $\bar{p}_{max}$ developed by the system. This method is defined in references 13, 14, and 15 as a comparison of the area under the brake-pressure time history with the area beneath a pressure profile obtained from the envelope defined by the peaks in the brake-pressure time history. It is noted in reference 13 that an examination of the wheel-speed time history must show sufficient variations in both magnitude and frequency to demonstrate that the brake is not torque-limited. According to reference 14, this method of study may be open to objection, especially for rate threshold systems, because the threshold rate may be lower than the maximum attainable deceleration, or the pressure may continue to increase while the wheel is spinning down. Furthermore, mechanical lags in the brake may not allow the brake-pressure time history to coincide with the drag-force-friction-coefficient time history. However, in the absence of other data, this process can be applied

to the analysis of airplane test data and may prove helpful for comparison purposes (ref. 14).

Typical examples of the relatively smooth brake-pressure trace are shown in figure 10. The average pressure $\bar{p}$ developed by the antiskid system during a given test is defined by the expression

$$\bar{p} = \frac{1}{t_f - t_o} \int_{t_o}^{t_f} p \, dt \tag{1}$$

where t_o and t_f, identified in figure 10, enclosed the time interval over which $\bar{p}$ is measured. The time t_o represents the point at which the brake pressure is first applied. The time t_f is taken just prior to brake release at the end of the test section. The average pressure is computed for each braking test by numerical integration techniques. The maximum pressure $\bar{p}_{max}$ is derived in much the same way as $\bar{p}$, except that the dashed curves in figure 10 that are formed by joining the straight line segments between the pressure peaks are used.

The slope of the least-squares line through the origin, which fairs the data when $\bar{p}$ is plotted as a function of $\bar{p}_{max}$, is defined as the pressure braking behavior index $\bar{\beta}_{b,p}$.

Brake Torque

A second indication of antiskid-system behavior is the ratio of the average brake torque $\bar{T}$ to the maximum torque $\bar{T}_{max}$ developed during a test (refs. 13 and 15). In many test programs, it is difficult to measure the brake torque; hence, torque is not commonly used to study antiskid-system behavior. Fortunately, the instrumented dynamometer used in this investigation gives a direct and independent measure of brake torque. According to reference 16, the relationship between brake torque and friction force is more easily defined than the relationship between brake pressure and friction force. This relationship, described fully in reference 2, is

$$\text{Torque} = F_x h + F_v d - I\alpha \tag{2}$$

and indicates that brake torque is defined by a linear combination of moments and thus cannot be uniquely defined by the product of drag force F_x and its moment arm h. When the tire operates at a fixed slip velocity such that α becomes negligible and d is relatively small, then the torque may more closely reflect the drag-force friction coefficient. In most cases, however, antiskid cycling results in rapid wheel speed changes and significant shifts d in the fore-and-aft position of the footprint center of pressure. Thus, peaks in the

brake-torque time histories may not coincide with the peaks in the μ_d time histories; however, the brake-torque time histories for this antiskid system are relatively smooth (fig. 10), and the torque ratios are presented as an independent method to study antiskid behavior.

The average brake torque $\bar{T}$ developed by the antiskid system during a given test is defined by an expression similar to that for $\bar{p}$. This expression

$$\bar{T} = \frac{1}{t_f - t_o} \int_{t_o}^{t_f} T \, dt \tag{3}$$

was also computed from measured torque time histories by numerical integration techniques. The maximum torque $\bar{T}_{max}$ was derived in the same way as the average torque except that the dashed curves in figure 10 that were formed by joining straight line segments between the torque peaks were used.

The slope of the least-squares line through the origin, which fairs the data when $\bar{T}$ is plotted as a function of $\bar{T}_{max}$, is defined as the torque braking behavior index $\bar{\beta}_{b,T}$.

Friction Coefficients

Drag-force friction coefficients.- Many references acknowledge the existence of a peak or maximum value of drag-force friction coefficient. (See refs. 16 to 26 for examples.) Most antiskid systems actively seek this peak friction coefficient or are designed to operate within a relatively narrow range of slip velocities or slip ratios in which this peak is assumed to occur; thus, maximum airplane deceleration is provided (ref. 27). Accordingly, reference 13 defines the brake-pressure and torque ratios as indirect indicators of antiskid-system behavior and regards the ratio of average developed to maximum achieved ground reaction forces due to braking effort as a direct indication of the antiskid-system braking behavior. However, friction data can be more difficult to analyze.

During this investigation, the antiskid system exhibited two distinct response modes. Response mode A is defined as antiskid cycling with well-defined incipient skid points as shown in figure 10(a). Response mode B is defined as antiskid cycling without well-defined incipient skid points as shown in figure 10(b). Mode A response has been reported frequently in the literature. (See refs. 1, 2, 6, and 8 for examples.) In this study, response mode A is generally associated with new tires at yaw angles of 0^o, 1^o, and 3^o and represent more than three-quarters of the data. When response mode A was observed, values of $\mu_{d,max}$, denoted by the circles in figure 10(a), were measured near the incipient skid points. Using incipient skid points for obtaining $\mu_{d,max}$ is a well-established and accepted method. (See refs. 1, 13, 15, 22, and 25 for examples.)

Mode B response was reported previously in references 7 and 8. In the present investigation, response mode B is associated with the worn tire and with the higher yaw angles. This type response is probably the result of the interaction between the antiskid cycling frequency and the tire mechanical properties. The possible effect that this interaction may have on the shape of the curve for μ plotted against slip and hence the $\mu_{d,max}$ incipient skid relationship is shown in references 1, 6, 7, and 8 and is discussed in some detail in reference 28. Since response mode B generally precluded determinations of $\mu_{d,max}$ from incipient skid points, an alternate approach was employed based upon fixed time increments. For this method, the μ_d time history was divided into uniform time increments and the apparent $\mu_{d,max}$ value nearest each time line was measured (circled points in fig. 10(b)). These $\mu_{d,max}$ values were occasionally supplemented by data from well-defined incipient skids within the time history.

The distinction between response modes A and B is only made with respect to the friction-coefficient data. The pressure and torque data were always treated as mode A data.

The average drag-force friction coefficient $\bar{\mu}_d$ developed by the antiskid system during a given test is defined by the expression

$$\bar{\mu}_d = \frac{1}{t_f - t_o} \int_{t_o}^{t_f} \mu_d \, dt \tag{4}$$

and was computed for each braking test with the use of numerical integration techniques. (See refs. 13, 15, and 29.) The average maximum drag-force friction coefficient $\bar{\mu}_{d,max}$ was derived in the same way as $\bar{\mu}_d$ except that a friction-coefficient profile formed by joining the straight-line segments between the friction coefficient peaks was used. Values of $\bar{\mu}_{d,max}$ are not available for torque-limited braking tests because the maximum friction level could not be confirmed. (Torque-limited in this investigation refers to the situation where, for a given supply pressure, the brake torque is insufficient to cause a spin-down of the tire.) It is apparent that no antiskid cycling occurs when the brake is torque-limited.

The drag-force friction coefficient that is observed when there is no braking results from the tire rolling resistance and is assumed to remain constant throughout a test run; this average friction coefficient is labeled $\bar{\mu}_r$ in figure 10. For those tests on flooded surfaces, $\bar{\mu}_r$ also includes the resistance attributed to fluid drag (ref. 2). When the ratio of the average developed $\bar{\mu}_d$ to the maximum achieved drag-force friction coefficient $\bar{\mu}_{d,max}$ is computed, $\bar{\mu}_r$ is subtracted from both the numerator and denominator to isolate the friction coefficient attributed to the braking effort.

The slope of the least-squares line through the origin, which fairs the data when $\bar{\mu}_d - \bar{\mu}_r$ is plotted as a function of $\bar{\mu}_{d,max} - \bar{\mu}_r$, is defined as the braking-friction behavior index $\bar{\beta}_{b,F}$.

Side-force friction coefficients.- The maximum side-force friction coefficient $\bar{\mu}_{s,max}$ for a yawed-wheel braking test was usually obtained when the yawed wheel was freely rolling prior to brake application but after spin-up transients as shown in figure 10(a). (See refs. 23 and 30 for examples.) Occasionally, however, the variability of μ_s during a run was so great that an alternate method, illustrated in figure 10(b), was used. For this method, a number of $\mu_{s,max}$ values were obtained during the braking portion of the run near points of full wheel-speed recovery, which indicated a momentary relaxation of the braking effort (three circled points in figure 10(b)). The $\mu_{s,max}$ profile formed by joining the straight-line segments between the μ_s peaks was numerically integrated to establish $\bar{\mu}_{s,max}$

$$\bar{\mu}_{s,max} = \frac{1}{t_f - t_o} \int_{t_o}^{t_f} \mu_{s,max} \, dt \tag{5}$$

The average side-force friction coefficient $\bar{\mu}_s$ was derived in the same way for each yawed-wheel braking test except that μ_s time histories were used.

The slope of the least-squares line through the origin, which fairs the data when $\bar{\mu}_s$ is plotted as a function of $\bar{\mu}_{s,max}$, is defined as the cornering-friction behavior index $\bar{\beta}_{c,F}$.

Power Terms

As noted in reference 6, the behavior of an antiskid system can also be expressed in terms of the gross stopping power developed by the braking system and by the stopping and cornering power dissipated by the tire. These various power terms are defined in reference 6 in terms of the carriage speed V, the total drag force F_x parallel to the wheel plane, the side force F_y perpendicular to the wheel plane, the yaw angle ψ, and the slip ratio S. Time histories of some of these variables during a typical antiskid braking test are presented in figure 11. Slip ratio is the instantaneous ratio of the slip velocity of the braked wheel $V - r\omega$ to the carriage speed V and is given by the following equation:

$$S = \frac{V - r\omega}{V} \tag{6}$$

where r is the effective rolling radius for the test tire which was computed from the unbraked rolling distance and wheel-revolution count for each run. The value of r varied from 0.439 to 0.474 m (1.44 to 1.55 ft), depending on the various combinations of tire vertical load and speed. The following expressions are defined over the interval between t_o and t_f in figure 11.

Gross stopping power.- The gross stopping power $P_{d,g}$ developed by the antiskid system during a braking test is derived from forces opposing the direction of motion and is a measure of the overall braking effort. The expression for that power is

$$P_{d,g} = \frac{1}{t_f - t_o} \int_{t_o}^{t_f} (F_x \cos \psi + F_y \sin \psi) V \, dt \tag{7}$$

where $F_x \cos \psi + F_y \sin \psi$ converts the measured drag and side forces noted in figure 11 to a single drag force opposing carriage motion. The product of velocity and time yields the distance through which the force acts and completes the work equation. Dividing the work by the duration provides a measure of the power being generated.

Tire stopping power.- A measure of the stopping power dissipated by the tire $P_{d,t}$ is given by

$$P_{d,t} = \frac{1}{t_f - t_o} \int_{t_o}^{t_f} [(F_x \cos \psi + F_y \sin \psi) VS + F_y \sin \psi (1 - S) V] \, dt \tag{8}$$

where the carriage speed is multiplied by the slip ratio to obtain the slip velocity (relative speed between tire and pavement). The last term in equation (8), $\int_{t_o}^{t_f} F_y \sin \psi (1 - S) V \, dt$, is an estimate of the work dissipated by the rolling resistance, which is attributed to a yawed rolling tire. The value of $P_{d,t}$ is thus an indicator of the tread wear associated with the braking effort.

Tire cornering power.- The cornering power dissipated by the tire $P_{c,t}$ can be closely approximated by the expression

$$P_{c,t} = \frac{1}{t_f - t_o} \int_{t_o}^{t_f} (F_y \cos \psi - F_x \sin \psi)(1 - S)V \sin \psi \, dt \qquad (9)$$

where $F_y \cos \psi - F_x \sin \psi$ converts the measured side and drag forces to a single side force perpendicular to the direction of motion and where $(1 - S)V$ is the braked wheel speed which, when multiplied by $\sin \psi$, yields the tire lateral velocity. The value of $P_{c,t}$ is an indicator of the tread wear associated with the cornering effort.

RESULTS AND DISCUSSION

As mentioned previously, pertinent data obtained from all the antiskid braking tests are presented in table I, together with parameters which describe each test condition. In addition, time histories of key parameters from all the tests are presented in the appendix. The tabular data and the time histories in the appendix are given for the convenience of the user in plotting the data in ways other than those presented in this report. The following sections describe the braking-system behavior, the tire frictional behavior under skid control, and the antiskid-system behavior under a variety of operating conditions.

Braking-System Behavior

In order to study the behavior of the antiskid system, it is first necessary to establish the response characteristics of the braking system and its components. The following paragraphs describe the braking-system hydraulic response, the brake pressure-torque response, and the antiskid-system response to transient friction conditions.

Hydraulic response.- Time histories from run 32 are presented in figure 12 to illustrate the hydraulic response characteristics of the antiskid braking system. The hydraulic lags associated with brake application can be determined by examining the antiskid inlet pressure and the brake pressure. At brake application, the antiskid inlet pressure quickly rises to the system pressure of approximately 13 MPa (1900 psi) and remains steady for the remainder of the test. There is a lag of 10 msec before the pressure impulse is seen at the brake, and this lag is attributed to flow restrictions through approximately 4 m (13 ft) of hydraulic line (inside diameter of 0.81 cm (0.32 in.)) which separate the two pressure transducers. About 1.7 sec are required for the brake pressure to reach a maximum value, and the rate of this pressure application and all subsequent pressure reapplications is controlled by the antiskid-system modulation orifice.

The initial brake-pressure ramp may weigh more heavily in the determination of the antiskid-system braking behavior during these track tests than during an actual airplane braking stop. During the track tests, several runs are necessary to cover a representative speed range and the initial brake-pressure ramp is repeated for each run; however, during an airplane braking stop, this initial brake-pressure ramp might appear only once.

The hydraulic lags associated with brake release under antiskid control can be determined by examining the brake-system behavior following the deep skid approximately 7 sec into the run described by figure 12. The antiskid system senses the skid when the wheel deceleration increases beyond the threshold level identified by the dashed line. There is a lag of 20 msec following detection of the skid before the brake pressure begins to reduce and an additional 120 msec is required to complete the pressure dump. The brake torque release lags the pressure dump by another 60 msec. Thus, hydraulic lags totaling approximately 200 msec are associated with this antiskid brake release cycle. This duration is greater than the 80 msec required for the tire to lock up following a transition from a dry to a damp section of the runway. A portion of these lags may be attributed to the hydraulic line lengths necessary to install the antiskid system on the test carriage.

Pressure-torque response.- The relationship between brake pressure and brake torque is shown in figure 13 where arrowheads are used to indicate increasing pressure for the initial braking cycle and decreasing pressure during the brake release at the end of the run. The figure clearly shows that the hysteretic nature of the pressure-torque relationship for this friction condition results in substantial variations in the brake torque for a given brake pressure. This characteristic is most notable during the first brake cycle when the temperature of the brake is essentially the ambient temperature and would suggest that the temperature of the brake has a significant influence on its ability to develop torque. According to reference 31, the pressure-torque response during the initial brake cycle may also be affected by gradual equilization of force through the stack of stators and rotors as keyway friction is overcome. For the test shown, most of the cycling occurred at brake pressures between 4 and 11 MPa (600 and 1500 psi).

The large hysteresis loop associated with the initial brake cycle may weigh more heavily in the determination of the antiskid-system braking behavior during these track tests than during an actual airplane braking stop and for the same reason as noted previously for the initial brake-pressure ramp.

Response to runway friction transition.- The adaptive characteristics of the antiskid system are illustrated by time histories of the wheel speed, wheel angular acceleration, brake pressure, and drag-force friction coefficient as presented in figure 14 for two transient runway friction conditions. The response of the braking system to a single transition from a dry to a flooded runway is presented in figures 14(a) and 14(b) for nominal carriage speeds of 41 knots and 97 knots, respectively. At both test speeds, the brake pressure reached a nominal system operating pressure of 13 MPa (1950 psi) and was not modulated by the antiskid system on the dry surface. Upon entering the flooded section, the wheel in both tests rapidly decelerated to a deep skid, as noted by the immediate reduction in wheel speed. At a carriage speed of 41 knots, the antiskid

system reacted quickly to permit the wheel to recover from the skid, and the remainder of the braking test was conducted with proper antiskid protection. As shown in figure 14(b), at a carriage speed of 97 knots, the wheel did not recover immediately after all brake pressure was released. Instead, the wheel recovered from the skid when the carriage speed was reduced to 92 knots. The predicted spin-up hydroplaning speed for the tire, based upon a tire inflation pressure of 0.97 MPa (140 psi), was 91 knots (ref. 5), which is equivalent to a wheel speed of approximately 15.6 rps; thus, once the tire had spun down, insufficient torque was being developed between the tire and the pavement to spin up the tire until the carriage speed was reduced.

Time histories of test runs that were selected to illustrate the response of the braking system during the transition from a flooded to a dry runway surface are presented in figures 14(c) and 14(d), for nominal carriage speeds of 67 knots and 98 knots, respectively. In both tests, the wheel was spun up to carriage speed on a dry surface prior to entering the flooded test section, and the brakes were applied at or near the start of the flooded section. Figure 14(c) shows that, at 67 knots, the antiskid system modulates the brake pressure on the flooded portion of the runway. Upon reaching the dry section, at about 5 sec, the brake pressure increased at a rate controlled by the modulating orifice. No further pressure modulation was observed for the remainder of the run.

For the test run at a nominal carriage speed of 98 knots (fig. 14(d)), the wheel commenced to spin down on the flooded section before brakes were applied due to dynamic tire hydroplaning. The calculated spin-down hydroplaning speed was 106 knots, which is equivalent to a wheel speed of approximately 18.2 rps (ref. 5). The antiskid system acted as designed and prevented the application of pressure to the brake. Upon reaching the dry section, the wheel rapidly spun up to the carriage speed, and approximately 1.5 sec later, the brake pressure began to increase at a rate controlled again by the modulating orifice.

Tire Frictional Behavior Under Skid Control

The runway/tire maximum drag- and side-force friction values are discussed here to provide a quantitative measure of the surface condition and for use in updating tire friction models with data from realistic antiskid operating conditions.

Effect of test parameters on maximum drag-force friction coefficient.- The average maximum drag-force friction coefficient $\bar{\mu}_{d,max}$ as developed by the unyawed tire under dry, damp, and flooded conditions is presented as a function of carriage speed in figure 15. The fairings in the figure are linear least-squares curve fits of the data. As expected, values of $\bar{\mu}_{d,max}$ for the wet runways are substantially lower than those for the dry runway, and the difference is greater for the flooded surface than for the damp surface, particularly at the higher speeds. An extrapolation of the linear curve fit of $\bar{\mu}_{d,max}$ for the flooded condition would be seen to approach negligible values near the predicted tire spin-down hydroplaning speed of 106 knots (ref. 5). Also noted in the figure is the maximum value of the drag-force friction coefficient, 0.78, which was predicted from the empirical expression developed in reference 32 for

the test tire operating at very low speeds. It is apparent that the dry data for $\bar{\mu}_{d,max}$ is in good agreement with this prediction.

The friction data of figure 15 were obtained at a yaw angle of 0°. The fairings of these data are reconstructed in figure 16, together with corresponding data obtained at yaw angles of 1°, 3°, and 6°, to show the effect of yaw angle on $\bar{\mu}_{d,max}$. The figure shows that the effect of yaw angle is dependent upon the surface condition and carriage speed. With the introduction of yaw, $\bar{\mu}_{d,max}$ is reduced on the damp surface and is relatively unaffected when the surface is flooded. On the dry surface, $\bar{\mu}_{d,max}$ is shown to decrease only when the yaw angle was increased to 6°.

The effect of tire tread wear on $\bar{\mu}_{d,max}$ is presented in figure 17, in which values of $\bar{\mu}_{d,max}$ for tires having new and worn treads are plotted as a function of carriage speed for three test surface conditions. The new tread data were again obtained from the faired curves of figure 15. The data indicate that when the new tread is replaced by a worn tread, there is little degradation in $\bar{\mu}_{d,max}$ on the dry surface, but there is a pronounced reduction on the damp and flooded runway surfaces. These trends are in good agreement with similar trends noted in references 2, 6, 7, and 8.

Effect of test parameters on maximum side-force friction coefficient.- The maximum side-force friction coefficients developed by the yawed rolling tire under dry, damp, and flooded conditions are plotted as a function of carriage speed in figure 18. The fairings in the figure are linear least-squares curve fits of the data. As discussed previously, these coefficients were generally measured during the unbraked portion of the run and, for the wet runway surface, are generally lower than those for the dry runway, with the difference becoming greater with increasing yaw angle, water depth, and speed. As expected, the values of $\bar{\mu}_{s,max}$ increase with increasing yaw angle for the range of yaw angles tested. On the flooded surface, $\bar{\mu}_{s,max}$ is shown to approach zero as the speed approaches the predicted tire spin-down hydroplaning speed of 106 knots.

The effect of tread wear on $\bar{\mu}_{s,max}$ is shown in figure 19 where the values of $\bar{\mu}_{s,max}$ at a yaw angle of 6° on dry, damp, and flooded runway surfaces are plotted as a function of carriage speed. The new tread data were obtained from the faired curves in figure 18 for a yaw angle of 6°. On the dry and damp surfaces the values of $\bar{\mu}_{s,max}$ were reduced when the new tread was replaced by a worn tread. On the flooded surface only one datum point is available from the worn tire tests and it is in close agreement with the data from the new tire tests.

Interaction between braking and cornering.- The interaction between braking and cornering is illustrated by the typical yawed-tire friction response to antiskid braking on dry runway surface shown in figure 20. The drag- and side-force friction coefficients μ_d and μ_s are plotted as a function of slip ratio for the tire yawed to 6° and operating at a nominal carriage speed of 56 knots. The data presented in the figure illustrate the irregular nature of the friction coefficient to which the antiskid braking system must respond. The apparently random perturbations may result from a combination of such factors as small fluctuations in the tire vertical load due to runway unevenness, flexibility in the wheel support which could be reflected in the measured drag and side forces,

variations in the runway surface texture, tire and brake temperatures, and the spring coupling provided by the tire between the wheel and the pavement. Reference 28 discusses some of these factors in more detail. The figure also demonstrates the deterioration in tire cornering capability with increased braking effort (higher slip ratio). The value of μ_s is reduced approximately 70 percent at a slip ratio of 0.4. This cornering reduction during the braking cycles is consistent with similar cornering reductions noted during previous antiskid braking tests (refs. 1, 6, 7, and 8) and further illustrates the cornering/braking dilemma faced by antiskid designers.

Effect of cyclic braking on maximum drag-force friction coefficients.- So far, the friction data presented herein were derived from cyclic brake operations. However, there is in the literature a large body of tire friction data available which were obtained under single-cycle conditions, and a discussion of the two data sets is appropriate. A comparison of values of $\mu_{d,max}$ measured during single-cycle braking tests made without antiskid protection and the average of corresponding values measured under the same test conditions with the antiskid system operational is presented in figure 21. The single-cycle data were obtained approximately 5 yr prior to the present antiskid braking tests and were previously reported in references 6 to 8. In figure 21, data are presented separately for dry, damp, and flooded test conditions and for all the test conditions combined. These data include coefficients for tests at similar speeds, yaw angles, vertical loads, and for worn as well as new tread configurations. The data for each test condition are faired by a least-squares straight line through the plot origins. The data indicate that the maximum drag-force friction coefficients obtained from the single-cycle braking tests tend to be lower than the average maximum coefficient developed by antiskid system on the dry and damp test surfaces. On the flooded surface, the two sets of data are in close agreement. When the data from all three surface wetness conditions are compared simultaneously, the least-squares curve fit indicates that the single-cycle data are approximately 10 percent lower than the maximum drag-force friction coefficient developed by the antiskid system. The agreement between the two sets of data is quite good considering the time span between acquisition of the $\mu_{d,max}$ values. However, the implication is quite clear that caution should be exercised in any estimate of antiskid-system braking behavior that is based solely upon $\mu_{d,max}$ values obtained from single-cycle tests.

Antiskid-System Behavior Analysis

Braking behavior.- In this section, four terms are used to describe the extent of the braking effort and to examine the antiskid behavior: (1) the pressure braking behavior index $\bar{\beta}_{b,p}$, which assesses the ability of the system to control brake pressure; (2) the torque braking behavior index $\bar{\beta}_{b,T}$, which assesses the system torque control; (3) the friction-braking behavior index $\bar{\beta}_{b,F}$, which measures the ability of the antiskid system to use the apparent maximum friction coefficient at the tire/runway interface; and (4) the total stopping power $\bar{P}_{d,g}$ that is developed by the antiskid system.

Presented in figure 22 are plots of $\bar{p}$ as a function of $\bar{p}_{max}$, $\bar{T}$ as a function of $\bar{T}_{max}$, and $\bar{\mu}_d - \bar{\mu}_r$ as a function of $\bar{\mu}_{d,max} - \bar{\mu}_r$. Data are plotted for all braking tests except those which were torque-limited throughout the

entire run, those involving tire hydroplaning, and those performed to examine the effects of a runway friction transition. In each case, the dry data and the wet data are plotted separately. The different surface wetness conditions are denoted by different symbols, but no distinction is made for the various test parameters such as carriage speeds, yaw angles, and tire vertical forces. The solid line in each plot represents the line of perfect agreement between the average developed and maximum achieved behavior parameter; it has a unit slope and is denoted as the line of ideal behavior. The dashed line in each plot is the least-squares fit passing through the plot origin. The slope of each dashed line represents the average braking behavior index for each data set. (See fig. 16 of ref. 26.)

On the dry runway surfaces, the average braking behavior indexes $\bar{\beta}_b$ determined from the pressure, torque, and friction ratios vary between 0.74 and 0.81, a difference of approximately 9 percent. On the wet runway surfaces, the variation in $\bar{\beta}_b$ is between 0.69 and 0.78, a difference of approximately 13 percent. A comparison of the $\bar{\beta}_b$ values for the wet runway surfaces with the $\bar{\beta}_b$ values for the dry runway surfaces indicates a reduction of 12 percent and 7 percent in the pressure and friction braking behavior indexes, respectively, and an increase of 3 percent in the torque braking behavior index. Thus, figure 22 generally shows that the antiskid braking system suffers a degraded braking-index level on the wet runway surfaces, in addition to the obvious reduction in friction coefficient. Although the antiskid braking behavior indexes derived from the three parameters give similar results, sufficient differences still exist to suggest that the three indexes should not be used interchangeably as a measure of the braking behavior. It should also be emphasized that the braking behavior indexes are based upon maximum achieved values of pressure, torque, and friction which may vary from one antiskid system to another, and any comparisons between different antiskid systems based solely upon these indexes may be technically misleading since there is no common base for comparison.

To isolate the effect that various test parameters have on the pressure, torque, and friction indexes, data from figure 22 are plotted in figures 23 to 27. Each figure is divided into three parts: (a) pressure indexes, (b) torque indexes, and (c) friction indexes. Each plot includes the line of ideal behavior and the least-squares fit passing through the origin, from which the average braking behavior index $\bar{\beta}_b$ is determined. The trends observed for some test conditions may be influenced by a small sample size.

The effect of carriage speed on braking behavior indexes is shown in figure 23. The data indicate that in general the effect of increasing speed is to reduce the pressure, torque, and friction indexes and this trend is observed for all three surface wetness conditions. No data are available at 100 knots on the flooded runway surface due to tire hydroplaning.

Figure 24 presents the effect of yaw angle on the braking behavior indexes. The data indicate that these indexes are generally higher for the yawed braking tests than for the unyawed braking tests under all surface wetness conditions.

The effect of variations in the vertical force on the braking behavior indexes is shown in figure 25. No data are available for vertical forces

greater than 89 kN (20 000 lbf) on the dry runway surfaces and no consistent trends were observed for the remaining test conditions.

Shown in figure 26 is the effect of tread wear on the braking behavior indexes. On the dry runway surfaces, the indexes are insensitive to tire tread wear. Under damp conditions the indexes are lower when the new tread is replaced with a worn tread. On the flooded runway the opposite trend is observed, but this is probably due to the small sample size.

Presented in figure 27 is the effect of system response mode on the braking behavior indexes. Insufficient data are available to discuss the effect of response mode on the dry runway surfaces and these data are not plotted. On the wet runway surfaces, however, the data indicate that mode B system response produces significant increases in the braking behavior indexes over those obtained from mode A operation; this was observed for all three indexes.

In summary, the data presented in figures 23 to 27 imply that the braking behavior of the antiskid system would not be adversely affected by cross-wind operations (yaw-angle effects) or fluctuations in the tire vertical loading but might be degraded by excessive tread wear on damp runway surfaces. These results also indicate that the antiskid system will be more effective as the aircraft speed is reduced during the landing rollout. Finally, the data indicate that higher antiskid-system braking behavior indexes are achieved when the antiskid system operates in response mode B.

The gross stopping power $P_{d,g}$ (eq. (7)) developed by the antiskid system, which is a measure of the overall antiskid braking effort, is listed in table I for each test condition. Figure 28 presents bar charts of these data in terms of $\bar{P}_{d,g}$, a numerical average of all the data for a given test condition. For example, the dry, 50-knot bar graph is the average of all dry runs at 50 knots, including the various yaw angles, vertical forces, and tread configurations. Data from torque-limited tests and from tests involving tire hydroplaning are included in the figure, but no data are included from tests performed under transient runway friction conditions. As expected, because of higher available friction coefficients, the gross stopping power on the dry surface is much higher than that on the wet runway surfaces. On the dry surface, $\bar{P}_{d,g}$ increases with carriage speed and to a lesser extent with increasing vertical force and with a new tread configuration; the wheel yaw angle appears to have no consistent effect. On the wet surfaces, $\bar{P}_{d,g}$ increases with carriage speed and decreases with yaw angle; the value of $\bar{P}_{d,g}$ is higher for the heavy weight condition (vertical force greater than 89 kN (20 000 lbf)) and for the new tread configuration.

The stopping power dissipated by the tire alone $P_{d,t}$ (eq. (8)) is only a small fraction of the gross stopping power, but it does provide an indication of the tread wear associated with the braking effort; thus, the ideal antiskid system would maximize $P_{d,g}$ and minimize $P_{d,t}$. Values of $P_{d,t}$ are listed in table I for each test condition; the data are averaged and plotted as bar graphs in figure 29 to show the effects attributed to test parameter variations. Data from all tests except those performed to study the effect of a runway friction transition are included in the figure. The figure shows that for corresponding conditions, $\bar{P}_{d,t}$ is higher on the dry surface than on the wet surface except for the heavy vertical force tests. On the dry surface, $\bar{P}_{d,t}$ generally

increases with carriage speed and yaw angle (for yaw angles greater than 1°). The value of $\bar{P}_{d,t}$ is reduced for the heavy vertical force (greater than 89 kN (20 000 lbf)) and when the new tread is replaced with a worn tread. On the wet runway surfaces, $\bar{P}_{d,t}$ is higher at a carriage speed of 100 knots than for the other test speeds and increases with vertical force. The value of $\bar{P}_{d,t}$ decreases when the yaw angle is increased beyond 1° and when the new tread is replaced with a worn tread. The data presented in figure 29 indicate that the most severe tread wear occurs during combined braking and cornering operations on a dry surface.

The ratio of tire stopping power to gross stopping power for each test is plotted as a function of $\bar{\mu}_{d,max}$ in figure 30. Data are not included for torque-limited tests, for tests performed under transient runway friction conditions, or for tests involving tire hydroplaning. The linear curve which fairs the data represents a least-squares fit and indicates that the ratio increases slightly with the friction level. This would suggest an increase in tread wear (as is also suggested by the amount of rubber deposited on the runway) during braking tests on the dry surface). The ratio of $P_{d,t}$ to $P_{d,g}$ appears to be insensitive to variations in the yaw angle for this antiskid braking system.

Cornering behavior.- Antiskid systems are not designed to maximize cornering performance since good cornering is not compatible with heavy braking but cornering is important for directional control, especially when cross winds are present.

Presented in figures 31 to 33 are plots of $\bar{\mu}_s$ as a function of $\bar{\mu}_{s,max}$ to show the effect several test parameters have on the cornering behavior indexes $\bar{\beta}_{c,F}$. The test parameter levels and surface wetness conditions are plotted separately. Each plot includes the line of ideal behavior and the least-squares fit passing through the plot origin from which the average cornering behavior index is obtained. It should again be emphasized that trends observed for some test conditions may be influenced by a small sample size.

The effect of yaw angle on the cornering behavior indexes is shown in figure 31. Data are presented for all three wetness conditions at 1°, 3°, and 6°. The test run at 9° was on a damp runway surface. These indexes are somewhat higher on the dry runway surfaces than on the wet runway surfaces. The data also indicate that these indexes are generally higher for the 1° yaw angle than for the higher yaw angles.

Figure 32 shows the effect of carriage speed on the cornering behavior indexes. Only the 6° yaw angle data are presented in the figure. On the dry surfaces, the cornering indexes decrease with speed, whereas on the damp runway surfaces these indexes are relatively insensitive to variations in carriage speed. At 100 knots on the flooded runway surfaces, hydroplaning effects have completely eliminated the tire cornering capability.

Presented in figure 33 is the effect of tread wear on the cornering behavior indexes. Again only the 6° yaw angle data are presented. All three surface wetness conditions show a decrease in the indexes when a new tire is replaced by a worn tire, and this decrease is much more pronounced on the wet runway surfaces.

The cornering power dissipated by the tire $P_{C,t}$ (eq. (9)) not only is indicative of the overall cornering capability of the tire during the antiskid controlled braking but also provides an indication of the increased tread wear associated with the steering effort. The effects of test parameter variations on $\bar{P}_{C,t}$ are presented in figure 34 as bar graphs. The data indicate that $\bar{P}_{C,t}$ values are, as expected, generally higher on the dry surfaces than on the wet surfaces for similar test parameter conditions. The one exception to this trend occurs at a carriage speed of 100 knots. The value of $\bar{P}_{C,t}$ also increases when the yaw angle is increased and, surprisingly, when the new tread is replaced with a worn tread. Although $\bar{\beta}_{C,F}$ is reduced for yaw angles greater than 1° (fig. 31) the values of $\bar{P}_{C,t}$ increased substantially when the yaw angle was increased (fig. 34); thus, both power terms and behavior-index terms are needed when studying the characteristics of antiskid systems.

SUMMARY OF RESULTS

An experimental investigation was conducted at the Langley Aircraft Landing Loads and Traction Facility to study the braking and cornering response of a hydromechanically controlled aircraft antiskid braking system. The investigation, conducted on dry and wet runway surfaces, utilized one main gear wheel, brake, and tire assembly of a McDonnell Douglas DC-9 series 10 airplane.

The experimental investigation indicates the following results:

1. During maximum braking, average braking behavior indexes based upon brake pressure, torque, and drag-force friction coefficient developed by the antiskid system were generally higher on the dry surfaces than on the wet surfaces.

2. On the wet surfaces, these indexes were reduced at higher carriage speeds and when new treads were replaced by worn treads.

3. The three braking behavior indexes gave similar results but the agreement was not sufficient to allow them to be used interchangeably as a measure of the braking behavior for this antiskid system.

4. These braking behavior indexes are based upon maximum values of pressure, torque, and drag-force friction coefficient which may vary from system to system, and any comparisons between different antiskid systems based solely upon these indexes may be technically misleading.

5. The average gross stopping power generated by the brake system was considerably higher on the dry surfaces than on the wet surfaces.

6. That portion of the stopping power which was dissipated by the tire and which provided an indication of the tire wear was observed to be greatest during combined braking and cornering on a dry surface.

7. The average cornering behavior index based upon the side-force friction coefficient developed by the tire under antiskid control was decreased on wet surfaces, with yaw angles larger than 1°, and when tires with treads were replaced by those with worn treads.

8. The interaction between braking and cornering forces indicated that during antiskid cycling, the side-force friction coefficient was significantly reduced during portions of the braking cycles.

9. During the transition from a dry to a flooded surface under heavy braking, the wheel entered into a deep skid but the antiskid system reacted properly by quickly reducing brake pressure and performed normally during the remainder of the run on the flooded surface.

10. The brake-pressure recovery following transition from a flooded to a dry surface was shown to be a function of the antiskid modulating orifice.

Langley Research Center
National Aeronautics and Space Administration
Hampton, VA 23665
May 20, 1981

REFERENCES

1. Tanner, John A.: Performance of an Aircraft Tire Under Cyclic Braking and of a Currently Operational Antiskid Braking System. NASA TN D-6755, 1972.

2. Horne, Walter B.; and Leland, Trafford J. W.: Influence of Tire Tread Pattern and Runway Surface Condition on Braking Friction and Rolling Resistance of a Modern Aircraft Tire. NASA TN D-1376, 1962.

3. Tracy, William V., Jr.: Wet Runway Aircraft Control Project (F-4 Rain Tire Project). ASD-TR-74-37, U.S. Air Force, Oct. 1974. (Available from DTIC as AD A004 768.)

4. Danhof, Richard H.; and Gentry, Jerauld R.: RF-4C Wet Runway Performance Evaluation. FTC-TR-66-6, U.S. Air Force, May 1966. (Available from DTIC as AD 486 049.)

5. Horne, Walter B.; McCarty, John L.; and Tanner, John A.: Some Effects of Adverse Weather Conditions on Performance of Airplane Antiskid Braking Systems. NASA TN D-8202, 1976.

6. Stubbs, Sandy M.; and Tanner, John A.: Behavior of Aircraft Antiskid Braking Systems on Dry and Wet Runway Surfaces - A Velocity-Rate-Controlled, Pressure-Bias-Modulated System. NASA TN D-8332, 1976.

7. Tanner, John A.; and Stubbs, Sandy M.: Behavior of Aircraft Antiskid Braking Systems on Dry and Wet Runway Surfaces - A Slip-Ratio-Controlled System With Ground Speed Reference From Unbraked Nose Wheel. NASA TN D-8455, 1977.

8. Stubbs, Sandy M.; Tanner, John A.; and Smith, Eunice G.: Behavior of Aircraft Antiskid Braking Systems on Dry and Wet Runway Surfaces - A Slip-Velocity-Controlled, Pressure-Bias-Modulated System. NASA TP-1051, 1979.

9. Standard for Metric Practice. E 380-79, American Soc. Testing & Mater., c.1980.

10. Tanner, John A.: Fore-and-Aft Elastic Response Characteristics of 34 × 9.9, Type VII, 14 Ply-Rating Aircraft Tires of Bias-Ply, Bias-Belted, and Radial-Belted Design. NASA TN D-7449, 1974.

11. Leland, Trafford J. W.; Yager, Thomas J.; and Joyner, Upshur T.: Effects of Pavement Texture on Wet-Runway Braking Performance. NASA TN D-4323, 1968.

12. Yager, Thomas J.; Phillips, W. Pelham; Horne, Walter B.; and Sparks, Howard C. (appendix D by R. W. Sugg): A Comparison of Aircraft and Ground Vehicle Stopping Performance on Dry, Wet, Flooded, Slush-, Snow-, and Ice-Covered Runways. NASA TN D-6098, 1970.

13. Skid Control Performance Evaluation. ARP 862, Soc. Automot. Eng., Mar. 1, 1968.

14. Lester, W. G. S.: Some Factors Influencing the Performance of Aircraft Anti-Skid Systems. Tech. Memo. EP 550, British R.A.E., July 1973.

15. Brake Control Systems, Antiskid, Aircraft Wheels, General Specifications for. Mil. Specif. MIL-B-8075-D, Feb. 24, 1971.

16. Aircraft Stopping Systems. Aircr. Eng., vol. 47, no. 10, Oct. 1975, pp. 18-22.

17. Merritt, Leslie R.: Concorde Landing Requirement Evaluation Tests. Rep. No. FAA-FS-160-74-2, 1974.

18. Proceedings First International Skid Prevention Conference. Part I. Virginia Counc. Highway Invest. Res. (Charlottesville), Aug. 1959.

19. Flight Tests To Determine the Coefficient of Friction Between an Aircraft Tyre and Various Wet Runway Surfaces. Part 7: Trials on a Concrete Runway at Filton. S & T MEMO 3/62, British Minist. Aviat., May 1962.

20. Batterson, Sidney A.: Investigation of the Maximum Spin-up Coefficients of Friction Obtained During Tests of a Landing Gear Having a Static-Load Rating of 20,000 Pounds. NASA MEMO 12-20-58L, 1959.

21. Theisen, Jerome G.; and Edge, Philip M., Jr.: An Evaluation of an Accelerometer Method for Obtaining Landing-Gear Drag Loads. NACA TN 3247, 1954.

22. Sawyer, Richard H.; Batterson, Sidney A.; and Harrin, Eziaslav N.: Tire-to Surface Friction Especially Under Wet Conditions. NASA MEMO 2-23-59L, 1959.

23. Dreher, Robert C.; and Yager, Thomas J.: Friction Characteristics of 20 × 4.4, Type VII, Aircraft Tires Constructed With Different Tread Rubber Compounds. NASA TN D-8252, 1976.

24. Batterson, Sidney A.: Braking and Landing Tests on Some New Types of Airplane Landing Mats and Membranes. NASA TN D-154, 1959.

25. Zalovcik, John A.: Ground Deceleration and Stopping of Large Aircraft. Presented at Thirteenth Meeting of the Flight Test Panel of AGARD (Copenhagen, Denmark), Oct. 20-29, 1958.

26. Frictional and Retarding Forces on Aircraft Tyres. Part II: Estimation of Braking Force. Eng. Sci. Data Item No. 71026, R. Aeronaut. Soc., Oct. 1971.

27. Hirzel, E. A.: Antiskid and Modern Aircraft. [Preprint] 720868, Soc. Automot. Eng., Oct. 1972.

28. Batterson, Sidney A.: A Study of the Dynamics of Airplane Braking Systems as Affected by Tire Elasticity and Brake Response. NASA TN D-3081, 1965.

29. Frictional and Retarding Forces on Aircraft Tyres. Part I: Introduction. Eng. Sci. Data Item No. 71025 with Amendment A, R. Aeronaut. Soc., Aug. 1972.

30. Yager, Thomas J.; and McCarty, John L.: Friction Characteristics of Three 30 × 11.5-14.5, Type VIII, Aircraft Tires With Various Tread Groove Patterns and Rubber Compounds. NASA TP-1080, 1977.

31. Straub, H. H.; Yurczyk, R. F.; and Attri, N. S.: Development of a Pneumatic-Fluidic Antiskid System. AFFDL-TR-74-117, U.S. Air Force, Oct. 1974. (Available from DTIC as AD A009 170.)

32. Smiley, Robert F.; and Horne, Walter B.: Mechanical Properties of Pneumatic Tires With Special Reference to Modern Aircraft Tires. NASA TR R-64, 1960. (Supersedes NACA TN 4110.)

TABLE I.- SUMMARY OF TEST

Run	Response mode	Tire-tread condition	Brake supply pressure		Yaw angle, deg	Surface condition	Vertical load		Nominal speed, knots	$\bar{\mu}_d$	$\bar{\mu}_{d,max}$	$\bar{\mu}_r$	$\bar{p}$		$\bar{p}_{max}$	
			MPa	psi			kN	lbf × 1000					MPa	psi	MPa	psi
1	A	New	14	2000	0	Dry	59	13.3	39	0.59	0.78	0.03	10.2	1480	12.8	1862
2	A	New	13	1950	0	Dry	59	13.2	64	.58	.74	.03	7.9	1140	10.1	1471
3	A	New	13	1950	0	Dry	59	13.3	99	.47	.74	.03	8.4	1220	13.0	1881
4	A	New	14	2000	0	Dry	70	15.7	39	.55	.77	.04	9.3	1350	12.7	1837
5	A	New	13	1850	0	Dry	71	15.9	73	.44	.67	.02	10.8	1560	12.6	1827
6		New	13	1900	0	Dry	69	15.6	98	.43						
7	A	New	13	1900	0	Dry	71	15.9	97	.47	.64	.02	11.0	1590	12.8	1854
8		New	13	1850	0	Dry	93	20.9	61	.41						
9	A	New	13	1850	0	Damp	56	12.7	43	.47	.51	.04	5.6	808	7.4	1078
10	A	New	13	1950	0	Damp	57	12.8	69	.33	.47	.05	5.0	725	7.2	1049
11	A	New	13	1950	0	Damp	57	12.9	95	.28	.42	.05	4.1	589	5.1	736
12	A	New	13	1850	0	Damp	70	15.7	44	.30	.41	.04	4.0	576	5.8	840
13	A	New	14	2000	0	Damp	70	15.8	71	.26	.43	.04	4.3	624	7.0	1016
14	A	New	13	1950	0	Damp	70	15.7	98	.24	.40	.05	4.3	624	7.9	1139
15	A	New	13	1850	0	Damp	87	19.5	41	.37	.52	.04	7.9	1150	11.7	1690
16	A	New	13	1900	0	Damp	90	20.2	70	.26	.42	.04	4.8	689	7.2	1044
17	A	New	13	1950	0	Damp	90	20.3	96	.25	.36	.04	5.2	760	8.6	1243
18	A	New	13	1950	0	Damp	111	25.0	39	.34	.47	.03	9.0	1310	12.5	1816
19	A	New	13	1950	0	Damp	116	26.0	66	.28	.39	.04	6.4	927	9.1	1325
20	A	New	14	2000	0	Damp	115	25.9	96	.25	.34	.05	6.9	999	9.9	1443
21	A	New	13	1900	0	Flooded	56	12.7	46	.28	.42	.06	4.3	618	7.1	1031
22	A	New	13	1900	0	Flooded	56	12.7	72	.19	.24	.11	1.8	260	2.4	343
23	A	New	14	2000	0	Flooded	57	12.8	94	.11						
24	A	New	13	1850	0	Flooded	74	16.6	45	.27	.43	.04	5.3	772	9.2	1330
25	A	New	13	1900	0	Flooded	72	16.1	69	.23	.32	.11	3.0	442	4.3	620
26	A	New	13	1900	0	Flooded	71	15.9	96	.10						
27	A	New	13	1900	0	Flooded	89	20.1	45	.30	.46	.06	7.3	1060	11.4	1651
28	A	New	13	1900	0	Flooded	85	19.0	66	.23	.33	.08	4.3	625	6.7	968
29	A	New	14	2000	0	Flooded	113	25.3	37	.35	.46	.06	11.2	1620	12.6	1830
30	A	New	14	2000	0	Flooded	114	25.7	69	.25	.33	.11	6.2	896	8.9	1293
31	A	New	14	2000	0	Flooded	112	25.2	98	.07						
32	A	New	13	1900	0	(a)	68	15.3	41	.46	.62	.03	8.5	1230	11.9	1720
33	A	New	13	1950	0	(a)	68	15.2	65	.38	.60	.06	6.8	990	11.6	1682
34	A	New	13	1950	0	(a)	69	15.5	68	.25	.49	.03	4.3	625	9.2	1341
35	A	New	13	1950	0	(a)	70	15.7	97	.28	.42	.05	5.4	783	8.8	1282
36		New	13	1950	0	Dry/Flooded	69	15.6	41							
37		New	14	2000	0	Dry/Damp	69	15.6	70	.26						
38		New	13	1950	0	Dry/Flooded	69	15.4	97							
39		New	13	1950	0	Flooded/Dry	69	15.4	36							
40		New	13	1950	0	Flooded/Dry	68	15.3	67							
41		New	13	1850	0	Flooded/Dry	68	15.3	98							
42	A	New	13	1900	1	Dry	68	15.3	36	.65	.76	.04	12.1	1750	12.8	1855
43		New	13	1900	1	Dry	69	15.6	68	.54						
44		New	12	1800	1	Dry	70	15.8	99	.45						
45	A	New	13	1900	1	Damp	69	15.4	44	.38	.47	.04	6.5	940	8.9	1296
46	A	New	13	1950	1	Damp	69	15.6	66	.34	.45	.04	5.8	835	7.6	1099

[a]Alternating dry and damp at 30.5-m (100-ft) intervals.

CONDITIONS AND RESULTS

$\bar{T}$		$\bar{T}_{max}$		Torque limit, percent	$\bar{\mu}_s$	$\bar{\mu}_{s,max}$	Average slip ratio	Average slip velocity		Gross stopping power		Tire stopping power		Tire cornering power		Hydroplaning	Run
kN-m	ft-lbf	kN-m	ft-lbf					m/sec	ft/sec	kW	hp	kW	hp	kW	hp		
17.9	13 200	22.6	16 677	38			0.16	3.2	10.5	726	973	114	153			No	1
16.8	12 400	21.0	15 544				.15	4.9	16.2	1119	1500	179	240			No	2
14.6	10 800	21.9	16 162	54			.12	5.9	19.3	1417	1900	177	237			No	3
18.3	13 500	26.2	19 336	47			.21	4.2	13.7	798	1070	152	204			No	4
15.3	11 300	21.4	15 828	98			.10	3.8	12.6	1171	1570	126	169			No	5
				100			.08	4.0	13.0	1506	2020	125	168			No	6
15.4	11 400	19.7	14 564	98			.09	4.4	14.4	1641	2200	152	204			No	7
				100			.09	2.8	9.2	1208	1620	107	144			No	8
11.8	8 730	12.8	9 441				.14	3.0	9.8	528	708	72	96			No	9
8.9	6 570	11.3	8 342				.10	3.4	11.1	671	900	68	91			No	10
7.1	5 240						.08	3.9	12.7	813	1090	67	90			No	11
9.0	6 660	11.9	8 771				.14	3.3	10.9	490	657	74	99			No	12
8.4	6 240	12.4	9 150				.10	3.7	12.1	661	887	74	99			No	13
6.9	5 060	11.1	8 196				.10	4.9	16.2	835	1120	84	113			No	14
13.8	10 200	19.0	14 031	34			.14	2.9	9.5	688	922	89	119			No	15
10.5	7 777	14.3	10 553				.09	3.3	10.7	865	1160	86	115			No	16
9.7	7 170	13.3	9 857				.08	3.8	12.4	1119	1500	90	121			No	17
16.4	12 100	22.3	16 464	35			.15	3.1	10.1	776	1040	110	148			No	18
13.8	10 200	17.6	12 964				.11	3.9	12.7	1111	1490	130	175			No	19
11.8	8 710	15.6	11 528				.08	4.1	13.6	1417	1900	122	164			No	20
7.2	5 290	10.3	7 572				.15	3.8	12.4	379	508	59	79			No	21
2.9	2 140	3.5	2 575				.11	4.2	13.9	396	531	45	61			No	22
							.59	29.2	95.7	313	420	183	245			Yes	23
9.1	6 720	14.6	10 767				.20	4.7	15.4	471	632	91	122			No	24
5.9	4 370	7.4	5 460				.12	4.1	13.7	603	809	72	96			No	25
							.69	34.4	112.7	356	478	248	333			Yes	26
11.7	8 650	16.5	12 154				.18	4.2	13.8	638	856	113	151			No	27
8.1	5 990	10.7	7 870				.12	4.3	14.0	677	908	81	109			No	28
17.1	12 600	20.9	15 441	86			.13	2.5	8.3	783	1050	99	133			No	29
10.3	7 600	13.3	9 791				.12	4.3	14.2	1037	1390	130	175			No	30
							.80	40.9	134.3	417	559	322	432			Yes	31
15.0	11 100	20.3	15 001				.15	3.0	10.0	669	897	94	126			No	32
11.2	8 270	16.9	12 483				.10	3.5	11.4	858	1150	92	124			No	33
8.3	6 140	15.7	11 576				.11	3.8	12.6	623	836	72	96			No	34
8.5	6 250	12.2	8 982				.10	4.8	15.8	984	1320	95	127			No	35
				40			.16	3.3	10.7	590	791	79	106			No	36
				42			.15	5.2	17.2	673	903	78	105			No	37
				41			.55	26.6	87.4	629	843	158	212			No/Yes	38
				58			.13	2.5	8.2	673	903	84	112			No	39
				37			.10	3.4	11.2	932	1250	95	128			No	40
							.35	18.3	60.1	347	466	91	122			Yes/No	41
20.2	14 900	23.9	17 633	95	0.11	0.12	.13	2.4	8.0	835	1120	110	147	2	3	No	42
				100	.10		.10	3.4	11.0	1312	1760	123	165	4	5	No	43
				100	.11		.08	4.3	14.1	1596	2140	142	190	6	8	No	44
11.3	8 330	13.6	10 068		.08	.10	.14	3.2	10.5	608	816	85	114	2	3	No	45
10.4	7 710	12.0	8 830		.09	.10	.10	3.4	11.0	805	1080	83	111	4	5	No	46

TABLE I.-

Run	Response mode	Tire-tread condition	Brake supply pressure		Yaw angle, deg	Surface condition	Vertical load		Nominal speed, knots	$\bar{\mu}_d$	$\bar{\mu}_{d,max}$	$\bar{\mu}_r$	$\bar{p}$		$\bar{p}_{max}$	
			MPa	psi			kN	lbf × 1000					MPa	psi	MPa	psi
47	A	New	13	1850	1	Damp	70	15.7	95	0.27	0.35	0.04	4.0	575	4.9	708
48	A	New	13	1900	1	Flooded	69	15.5	45	.32	.43	.06	5.6	806	9.1	1321
49	B	New	13	1950	1	Flooded	68	15.3	67	.23	.27	.08	3.0	433	3.9	566
50		New	13	1950	1	Flooded	67	15.1	97	.08						
51	A	New	13	1850	1	Rain	69	15.5	99	.07	.13	.04	1.1	164	1.6	238
52	A	New	13	1950	3	Dry	70	15.7	47	.59	.76	.05	11.2	1630	12.7	1836
53	A	New	14	2000	3	Dry	69	15.5	79	.55	.74	.05	10.3	1490	12.9	1870
54	A	New	14	2000	3	Dry	71	15.9	98	.51	.69	.05	10.8	1560	12.7	1837
55	A	New	13	1850	3	Damp	69	15.6	42	.39	.46	.04	5.4	781	6.9	1001
56	A	New	13	1850	3	Damp	70	15.8	67	.33	.40	.06	3.9	563	4.9	705
57	A	New	13	1850	3	Damp	70	15.7	96	.22	.32	.05	3.2	459	3.9	564
58	A	New	13	1950	3	Flooded	69	15.6	45	.36	.46	.09	5.5	795	7.6	1100
59	A	New	13	1950	3	Flooded	70	15.7	45	.33	.42	.06	5.6	818	7.4	1080
60	B	New	13	1900	3	Flooded	69	15.5	69	.19	.23	.09	2.3	330	3.0	428
61		New	13	1850	3	Flooded	68	15.3	79	.14						
62	A	New	13	1900	6	Dry	71	15.9	56	.60	.71	.10	8.6	1250	10.4	1513
63	A	New	13	1950	6	Dry	71	15.9	78	.53	.63	.09	9.2	1330	11.3	1642
64	B	New	13	1850	6	Damp	69	15.5	42	.37	.41	.06	4.8	695	5.8	841
65	B	New	13	1850	6	Damp	69	15.6	70	.25	.29	.06	2.9	427	3.5	511
66	B	New	13	1950	6	Damp	69	15.5	96	.20	.27	.06	2.8	400	3.3	485
67	B	New	13	1950	6	Flooded	70	15.7	44	.36	.40	.09	4.9	707	6.0	877
68	A	New	13	1950	6	Flooded	69	15.5	70	.18	.23	.09	1.9	270	2.3	338
69		New	13	1950	6	Flooded	69	15.4	91	.07						
70	A	Worn	13	1950	0	Dry	69	15.6	50	.50	.69	.03	10.7	1550	12.9	1871
71	A	Worn	13	1950	0	Dry	69	15.5	72	.48	.70	.04	9.5	1380	12.1	1758
72		Worn	13	1900	0	Dry	70	15.7	98	.41						
73	A	Worn	13	1900	0	Damp	69	15.6	44	.27	.38	.04	5.0	725	7.5	1091
74	A	Worn	13	1900	0	Damp	70	15.7	72	.17	.28	.03	2.6	379	4.5	647
75	A	Worn	13	1950	0	Damp	70	15.7	98	.20	.32	.05	2.9	415	4.0	585
76	A	Worn	13	1900	0	Flooded	67	15.0	60	.15	.18	.09	1.7	251	2.2	322
77	B	Worn	13	1850	0	Flooded	68	15.2	72	.12	.13	.09	1.1	157	1.4	201
78	A	Worn	13	1950	0	(a)	69	15.6	52	.26	.48	.03	4.5	657	9.8	1415
79	A	Worn	13	1950	0	(a)	70	15.8	73	.19	.33	.03	2.9	427	5.5	800
80	A	Worn	13	1900	0	(a)	71	16.0	96	.17	.22	.02	3.3	485	4.6	674
81	A	Worn	14	2000	6	Dry	73	16.3	46	.51	.64	.05	9.8	1420	12.2	1763
82	A	Worn	13	1950	6	Dry	72	16.2	72	.45	.59	.05	8.3	1200	11.2	1619
83	A	Worn	13	1950	6	Dry	73	16.4	97	.40	.51	.04	7.9	1140	10.9	1574
84	B	Worn	13	1900	6	Damp	72	16.2	59	.11	.16	.02	2.1	308	2.8	408
85	B	Worn	13	1950	6	Damp	71	16.0	71	.11	.19	.04	1.6	239	2.2	316
86	B	Worn	13	1950	6	Damp	70	15.8	100	.08	.14	.03	1.7	244	2.1	311
87	B	Worn	13	1950	6	Flooded	69	15.5	61	.10	.11	.06	1.2	177	1.5	218
88		Worn	13	1950	6	Flooded	69	15.6	77	.10						
89		Worn	13	1950	6	Flooded	70	15.8	101	.03						
90	B	Worn	13	1950	9	Damp	69	15.6	50	.22	.28	.07	3.1	444	4.0	585
91	B	Worn	13	1950	9	Damp	72	16.1	102	.13	.20	.06	1.9	273	2.3	330

[a]Alternating dry and damp at 30.5-m (100-ft) intervals.

Concluded

$\bar{T}$		$\bar{T}_{max}$		Torque limit, percent	$\bar{\mu}_s$	$\bar{\mu}_{s,max}$	Average slip ratio	Average slip velocity		Gross stopping power		Tire stopping power		Tire cornering power		Hydroplaning	Run
kN-m	ft-lbf	kN-m	ft-lbf					m/sec	ft/sec	kW	hp	kW	hp	kW	hp		
8.5	6 260	9.6	7 126		0.09	0.10	0.09	4.4	14.4	940	1260	87	116	4	6	No	47
9.3	6 900	12.2	8 996		.06	.09	.18	4.0	13.2	521	699	86	115	1	2	No	48
5.3	3 910	5.8	4 284		.04	.07	.12	4.0	13.1	550	737	64	86	1	2	No	49
					.02		.89	44.8	147.1	269	361	239	320	0	0	Yes	50
2.6	1 910				.03	.05	.08	4.3	14.2	246	330	22	29	1	2	No	51
19.0	14 000	24.2	17 871	83	.23	.23	.14	3.2	10.6	999	1340	136	183	19	25	No	52
17.3	12 800	24.1	17 833	75	.22	.24	.14	5.5	17.9	1544	2070	208	279	30	40	No	53
16.8	12 400	19.9	14 708	80	.21	.24	.10	5.2	17.1	1805	2420	195	262	37	49	No	54
12.5	9 250	14.1	10 427		.15	.21	.16	3.6	11.7	588	789	98	131	10	14	No	55
10.0	7 410	11.1	8 234		.17	.21	.11	4.0	13.0	813	1090	95	128	20	27	No	56
6.8	5 030	7.9	5 811		.15	.19	.09	4.6	15.2	761	1020	74	99	25	34	No	57
10.5	7 730	12.5	9 215		.14	.20	.16	3.8	12.5	579	776	97	130	10	14	No	58
10.1	7 480	11.6	8 585		.12	.18	.17	4.1	13.5	536	719	92	124	9	12	No	59
3.8	2 770	4.4	3 217		.09	.12	.12	4.1	13.6	464	622	56	75	10	13	No	60
					.02		.41	17.3	56.7	396	531	151	203	3	4	Yes	61
17.7	13 100	20.7	15 283	32	.29	.40	.18	5.2	16.9	1245	1670	228	306	54	73	No	62
16.1	11 900	20.2	14 917	52	.34	.46	.15	5.9	19.4	1514	2030	236	317	90	121	No	63
10.7	7 880	11.5	8 475		.19	.28	.20	4.5	14.6	565	758	116	155	25	34	No	64
6.9	5 130	7.6	5 636		.21	.31	.14	4.9	16.1	640	858	89	120	48	65	No	65
5.1	3 770	5.8	4 317		.19	.30	.12	5.9	19.2	692	928	86	115	62	83	No	66
9.8	7 270	11.0	8 125		.17	.26	.18	4.1	13.5	563	755	105	141	24	32	No	67
3.1	2 280	3.5	2 611		.10	.16	.15	5.3	17.4	459	615	69	92	22	29	No	68
					-.01		.91	42.8	140.3	233	312	210	282	0	0	Yes	69
17.2	12 700	24.1	17 821	83			.11	2.6	8.6	865	1160	87	117			No	70
15.7	11 600	21.5	15 871	83			.10	3.6	11.8	1201	1610	116	156			No	71
				100			.06	2.9	9.6	1432	1920	91	122			No	72
8.8	6 520	11.9	8 803				.11	2.4	7.9	432	579	48	65			No	73
5.5	4 090	9.0	6 638				.08	2.9	9.6	435	584	37	50			No	74
5.6	4 110	7.6	5 596				.07	3.5	11.4	690	925	51	68			No	75
2.5	1 880	3.0	2 202				.09	2.9	9.4	309	414	29	39			No	76
1.1	804	1.3	930				.09	3.3	10.9	294	394	27	36			No	77
8.6	6 360	16.4	12 129				.11	3.0	10.0	483	648	51	68			No	78
5.7	4 220	9.9	7 340				.09	3.2	10.6	509	683	44	59			No	79
6.0	4 440	7.8	5 729				.07	3.3	10.9	600	804	44	59			No	80
17.6	13 000	22.7	16 795	39	.20	.20	.15	3.4	11.1	880	1180	131	176	34	46	No	81
15.3	11 300	20.2	14 939	41	.20	.30	.14	5.0	16.3	1208	1620	171	229	51	69	No	82
14.2	10 500	18.3	13 487		.18	.32	.12	6.1	19.9	1462	1960	195	261	65	87	No	83
3.8	2 840	5.2	3 860		.06	.17	.09	2.7	8.9	247	331	24	32	12	16	No	84
3.4	2 520	4.3	3 157		.04	.16	.08	3.0	9.9	276	370	26	35	10	14	No	85
2.6	1 910	3.4	2 490		.03	.14	.08	4.1	13.3	304	408	28	38	10	14	No	86
1.8	1 310	2.1	1 569		.01	.20	.12	3.7	12.0	213	286	25	34	1	2	No	87
					-.04		.45	18.5	60.6	262	352	116	155	-5	-7	Yes	88
					-.05		.91	47.0	154.2	93	125	79	106	-2	-3	Yes	89
6.4	4 720	7.9	5 815		.27	.42	.15	3.9	12.8	403	540	64	86	65	87	No	90
3.5	2 610	4.5	3 354		.24		.10	5.4	17.6	510	684	54	72	129	173	No	91

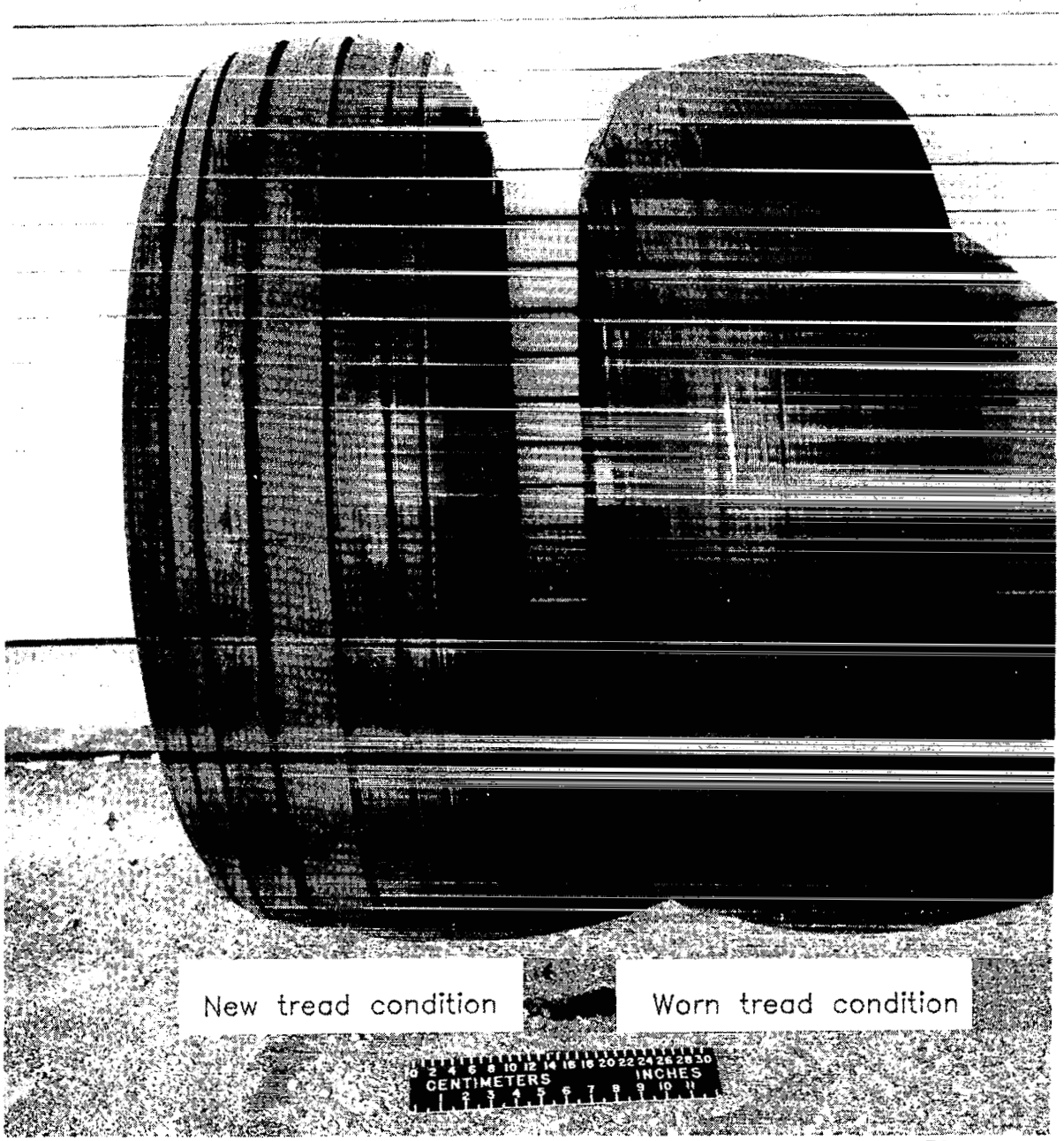

L-79-1976.1

Figure 1.- New and worn tread condition of six-groove, 40 × 14, type VII aircraft test tires.

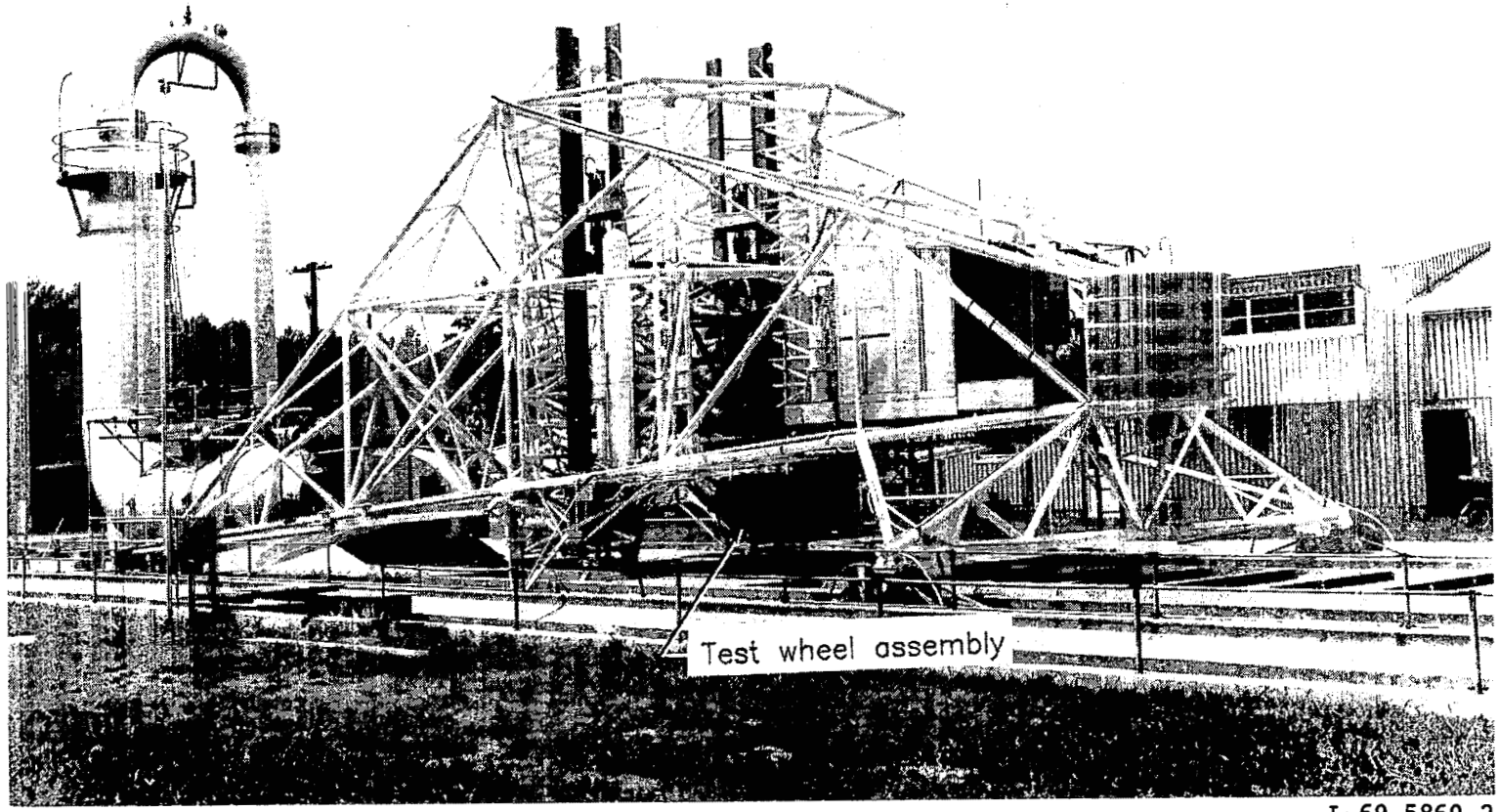

L-69-5860.2

Figure 2.- Test carriage.

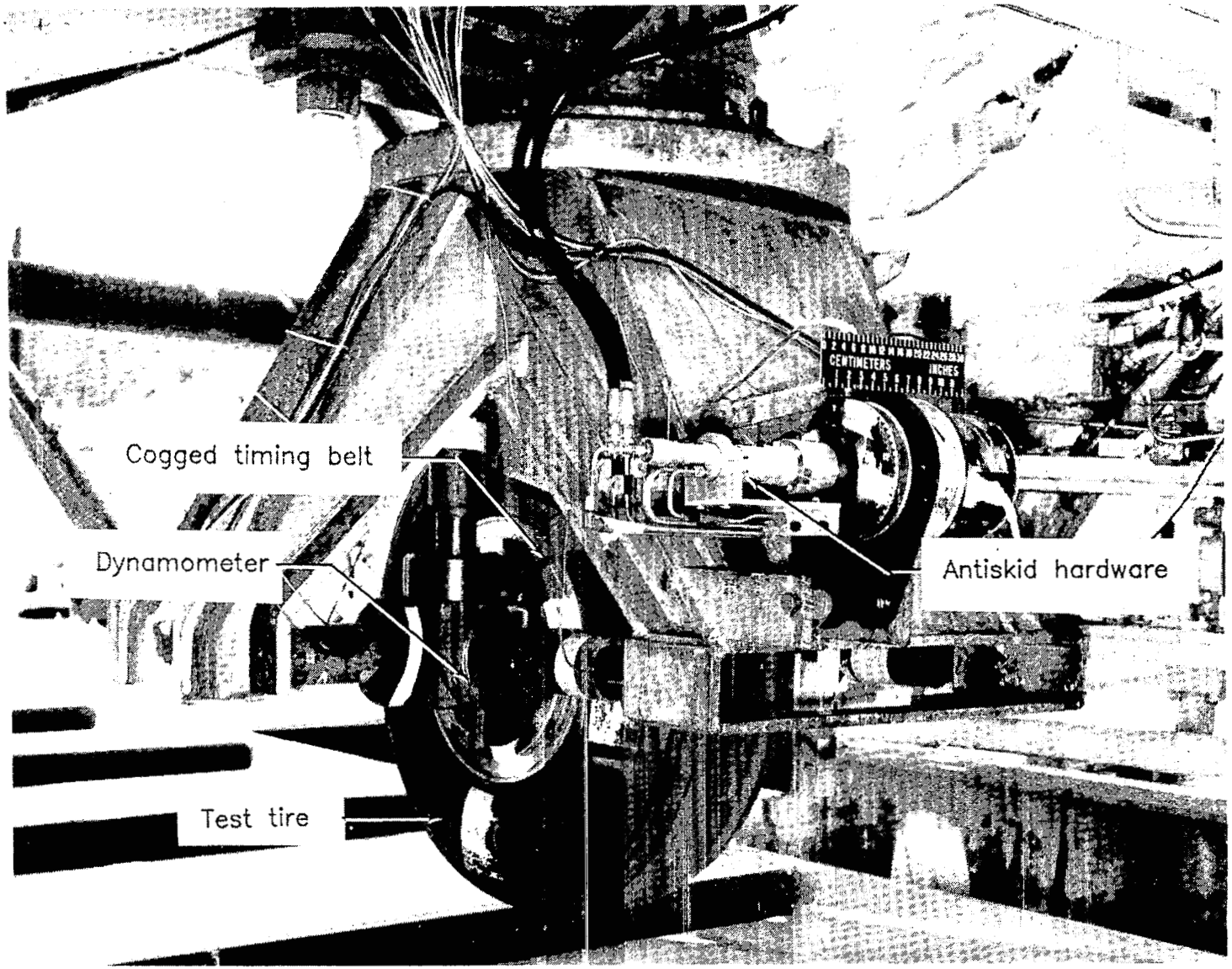

L-79-3532.1

Figure 3.- Test tire, instrumented dynamometer, and antiskid hardware.

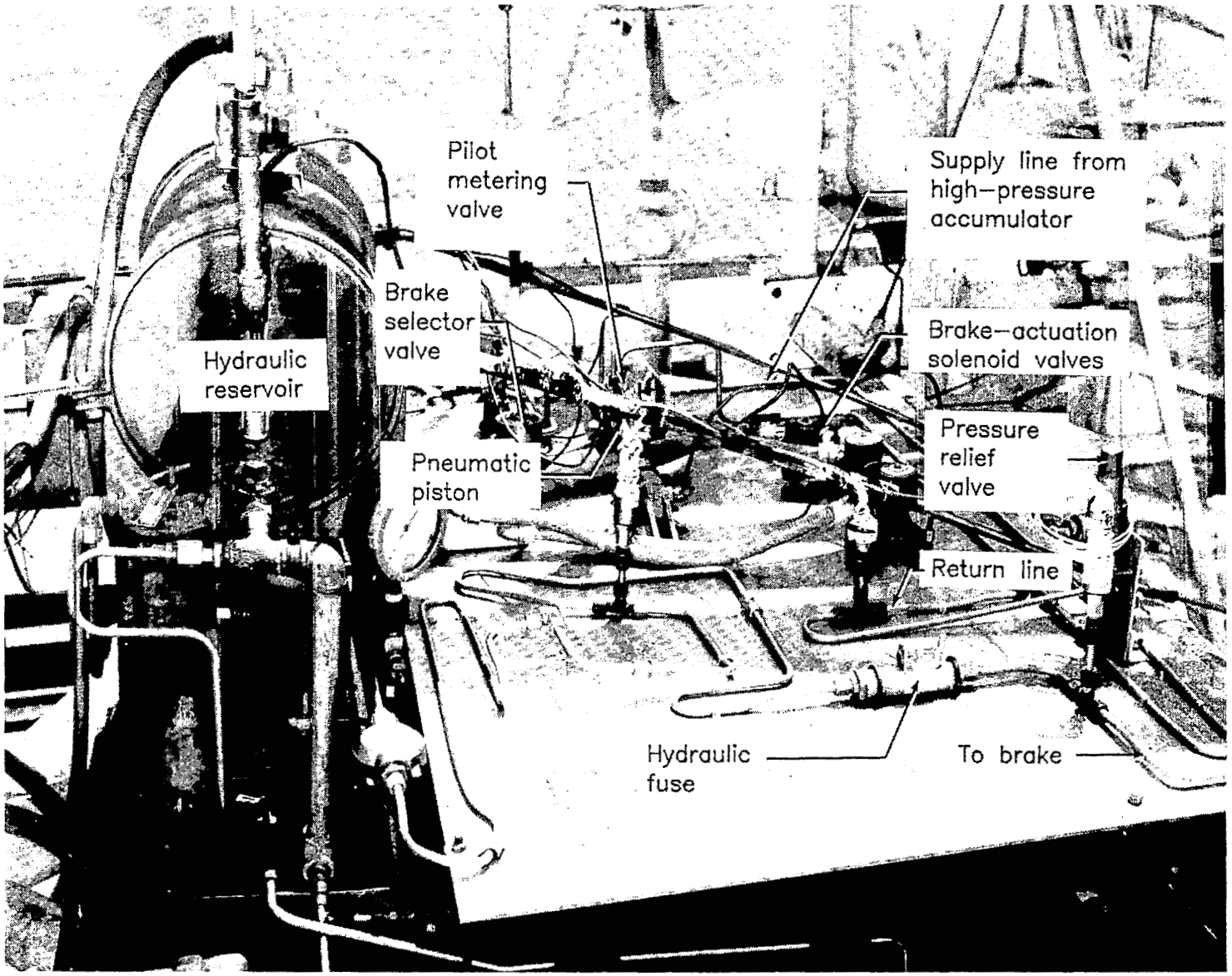

L-79-3533.1

Figure 4.- Layout of simulated braking system on test carriage.

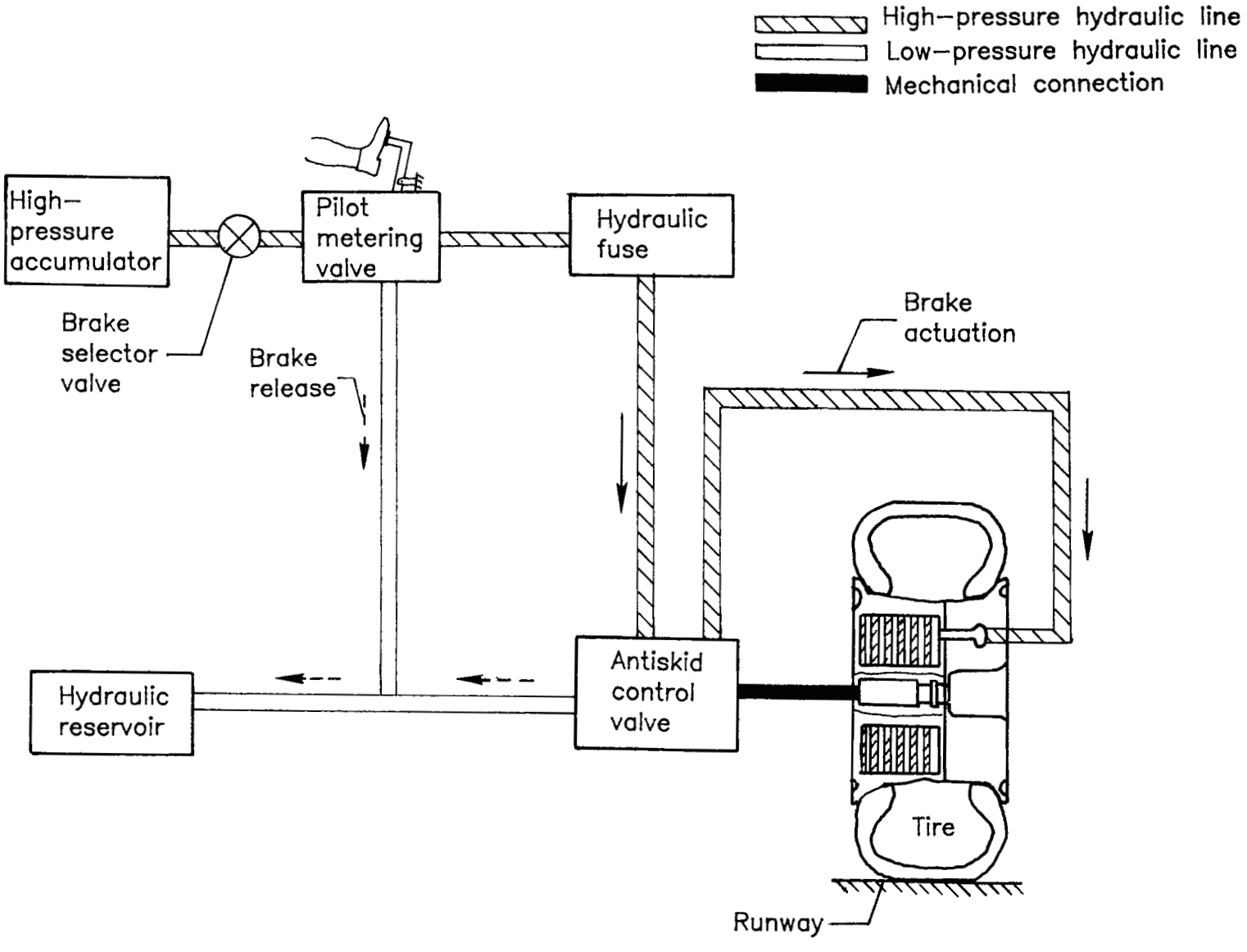

Figure 5.- Schematic of skid control system.

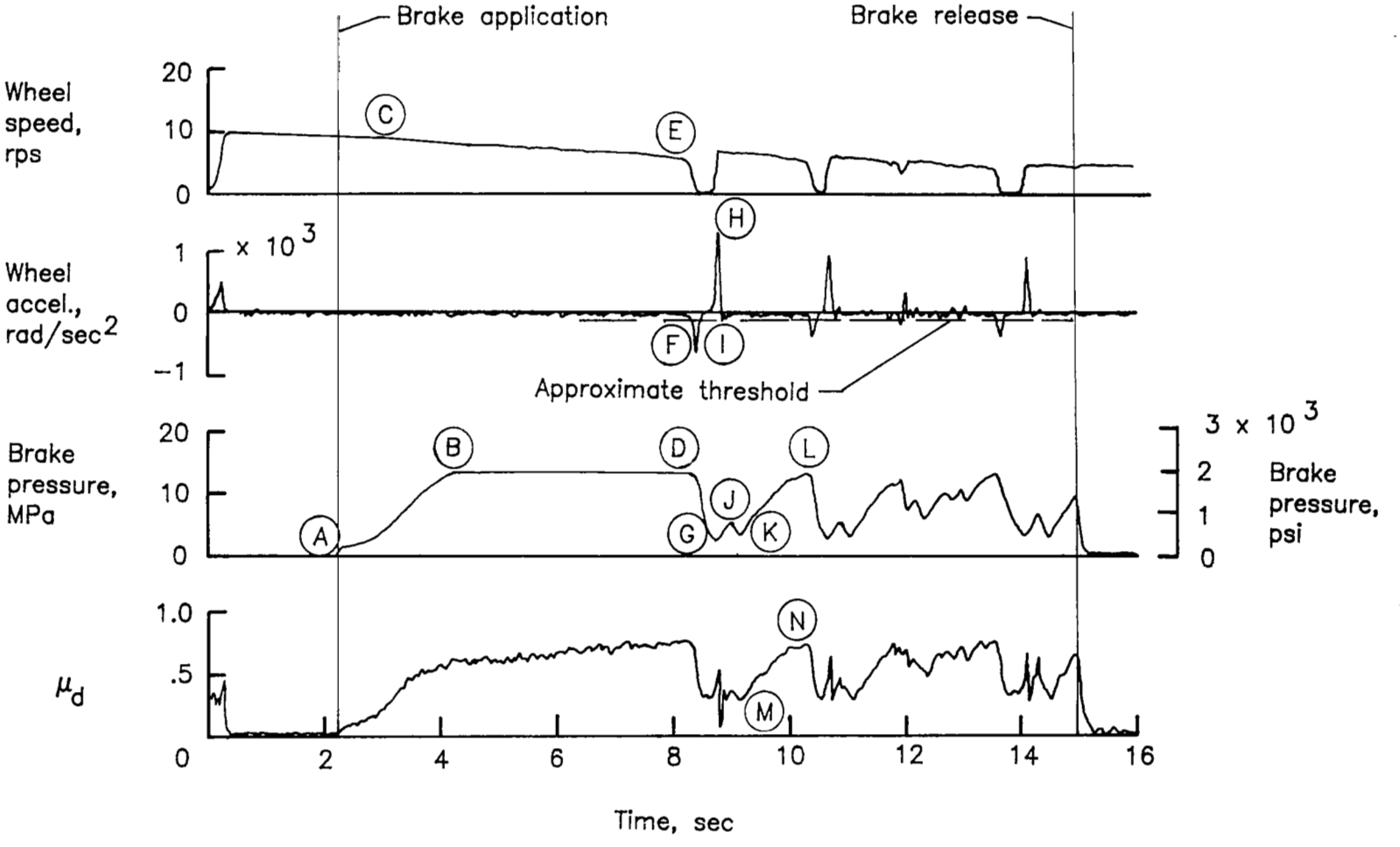

Figure 6.- Typical time histories of parameters to describe operation of antiskid system. Run 4 (table I); nominal carriage speed, 39 knots; vertical load, 70 kN (15 700 lbf); yaw angle, 0°; tire condition, new; surface condition, dry.

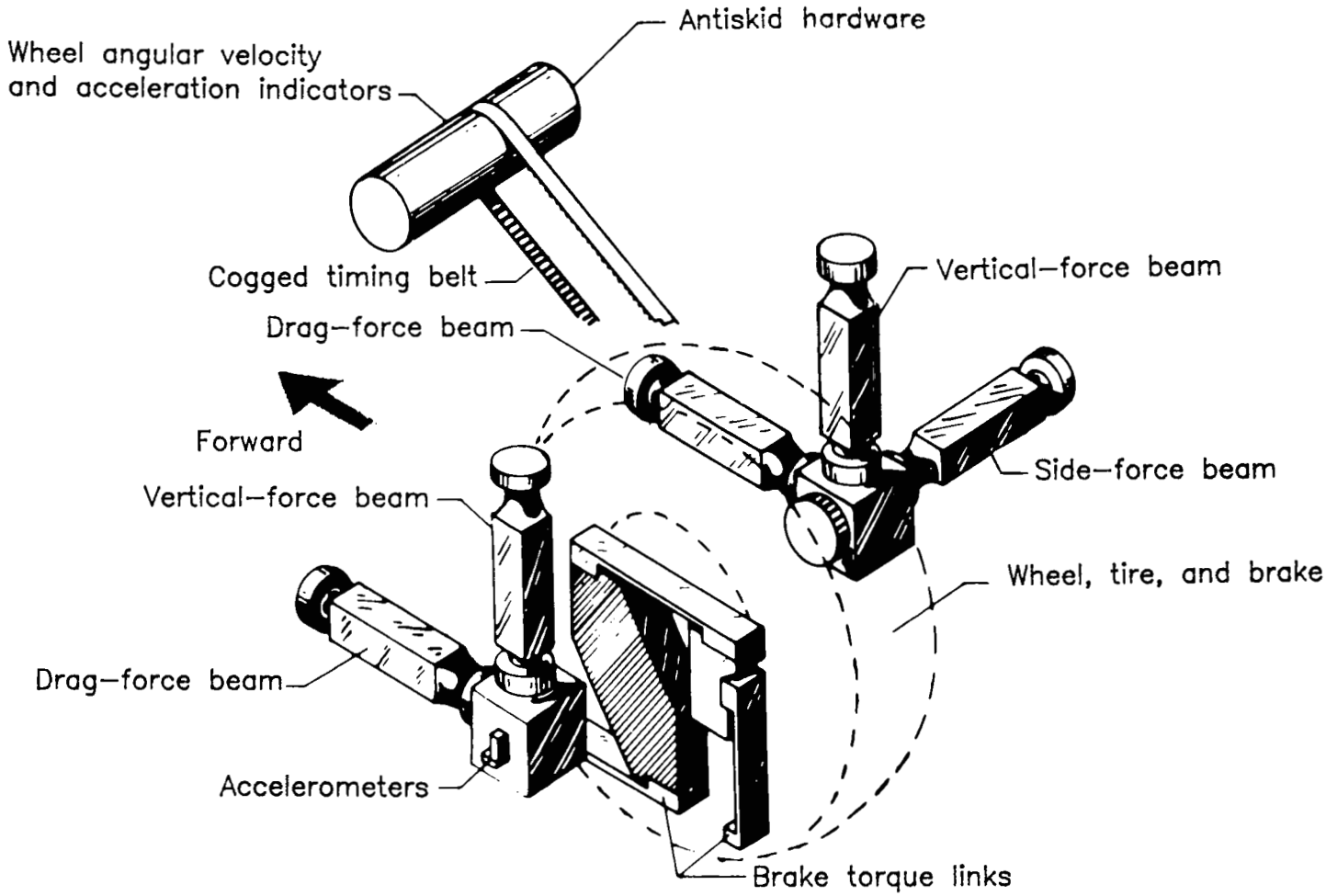

Figure 7.- Dynamometer details.

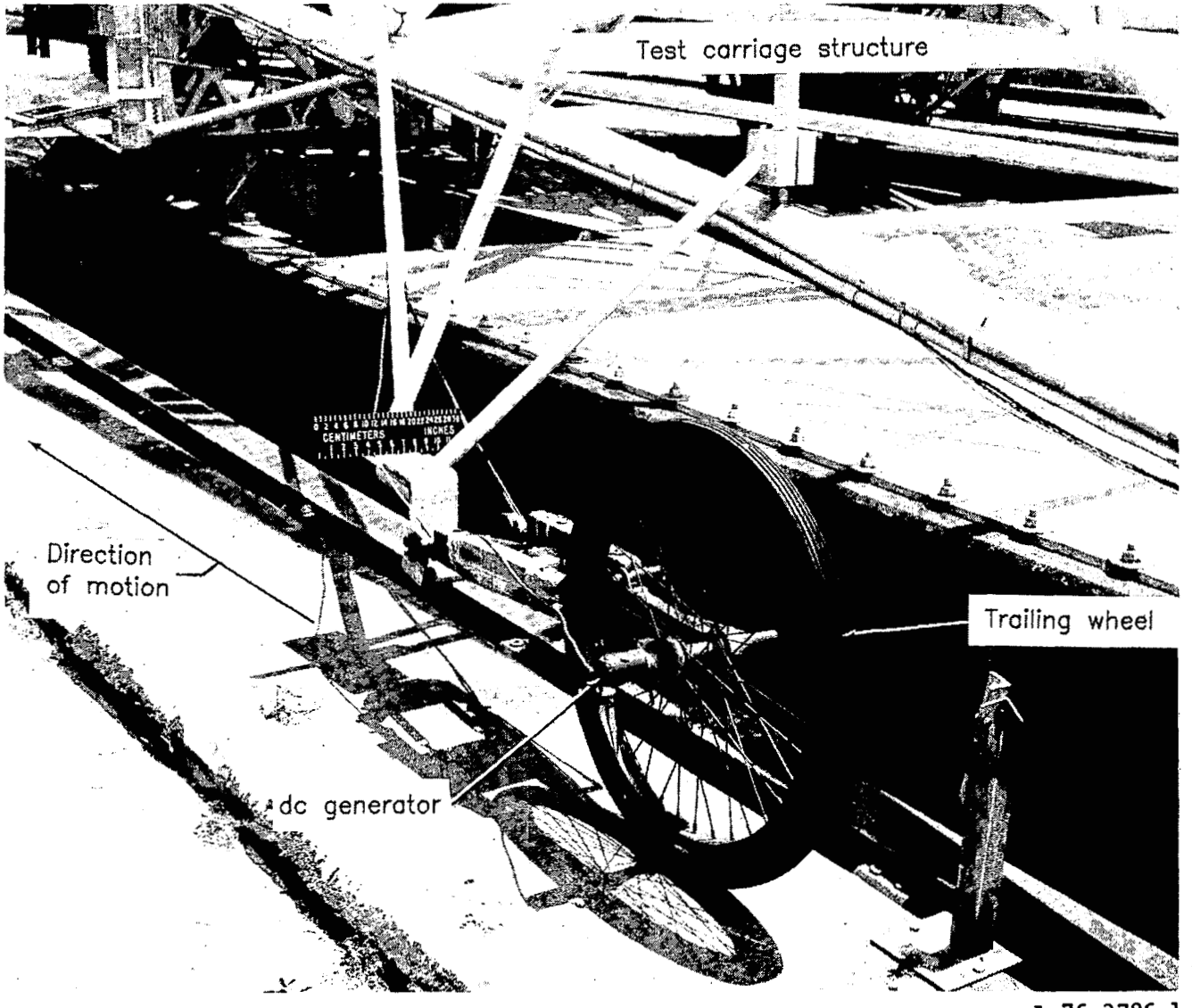

Figure 8.- Lightweight trailing wheel used to obtain carriage speed.

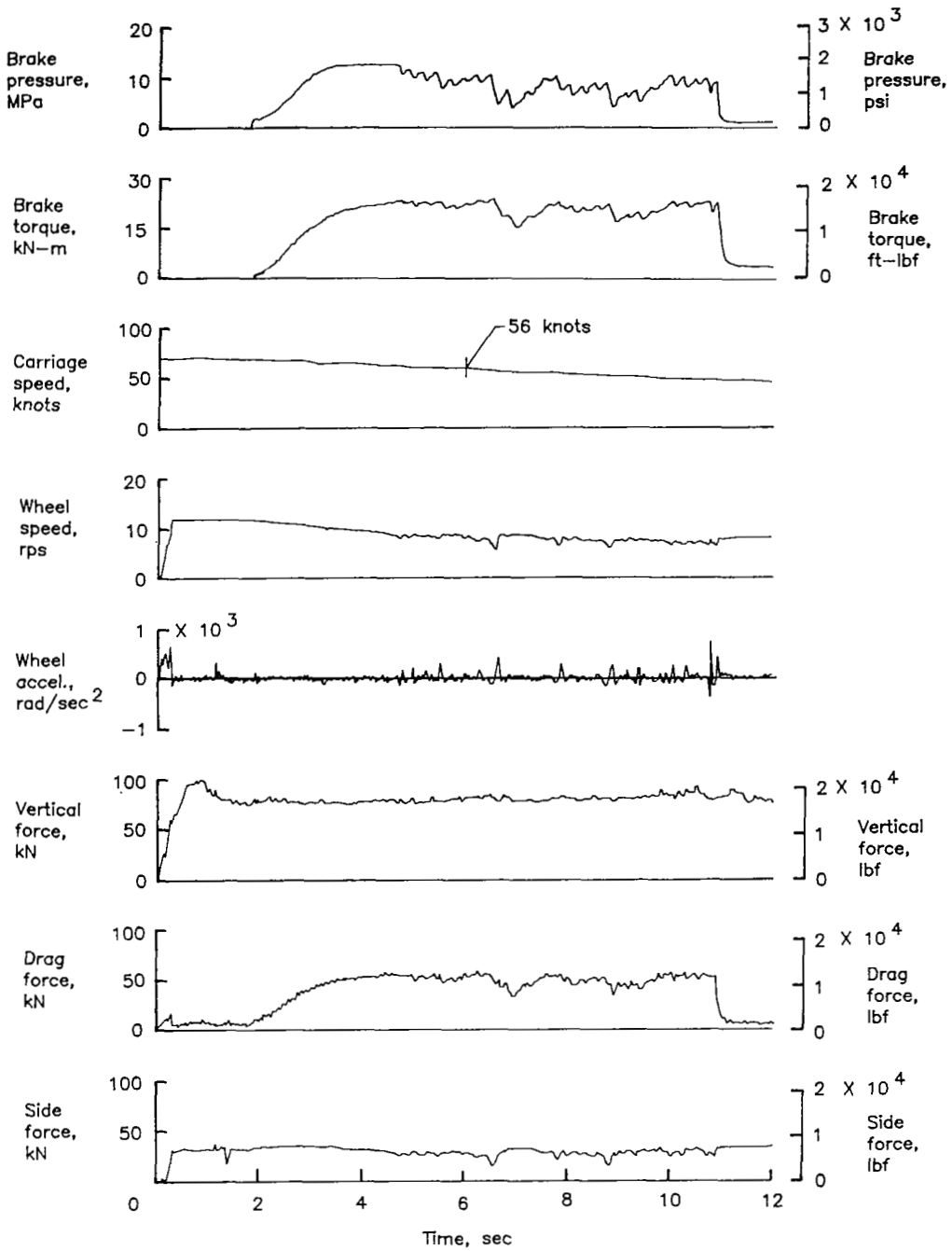

(a) Measured parameters.

Figure 9.- Typical time histories of measured and calculated parameters. Run 62; nominal carriage speed, 56 knots; vertical load, 71 kN (15 900 lbf); yaw angle, 6°; tire condition, new; surface condition, dry.

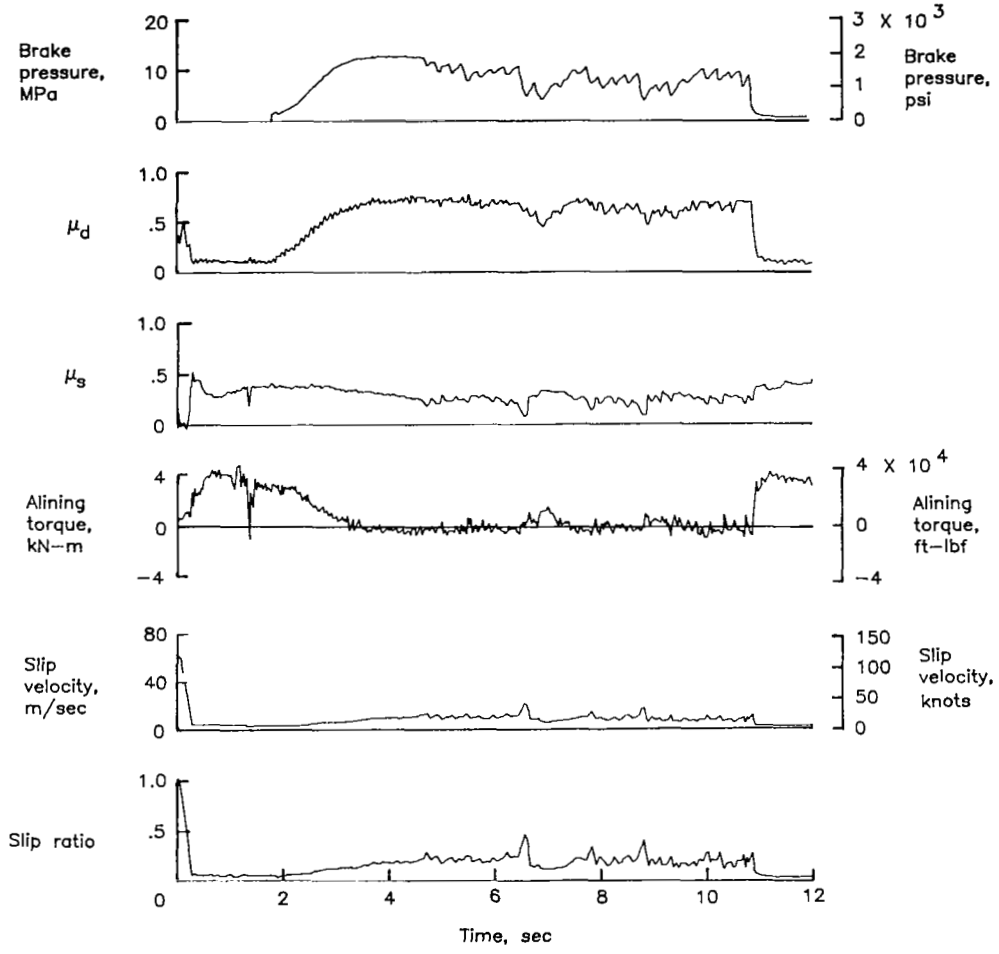

(b) Calculated parameters.

Figure 9.- Concluded.

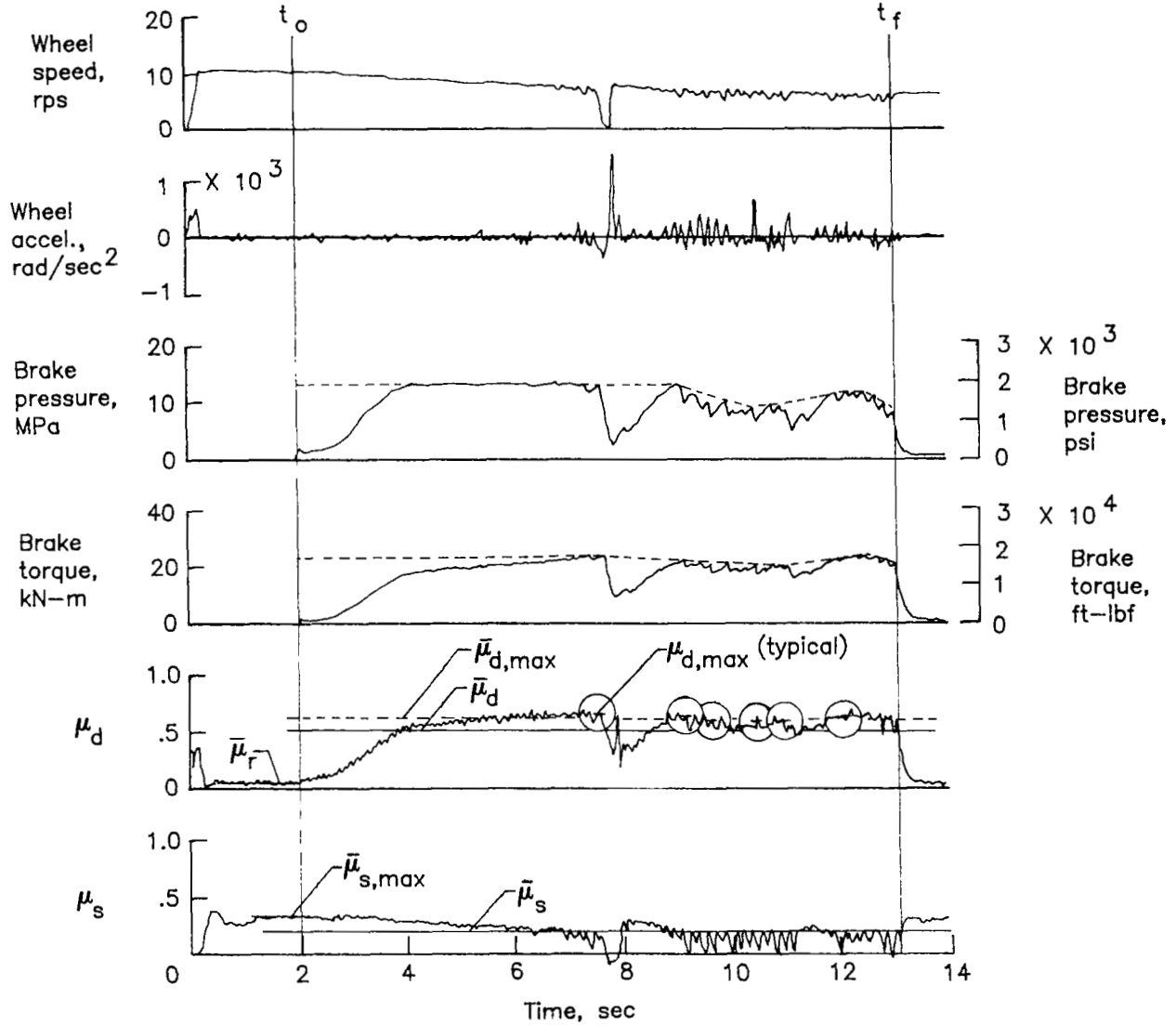

(a) Run 81; nominal carriage speed, 46 knots; vertical load, 73 kN (16 300 lbf); yaw angle, 6°; tire condition, worn; surface condition, dry.

Figure 10.- Definition of various friction terms.

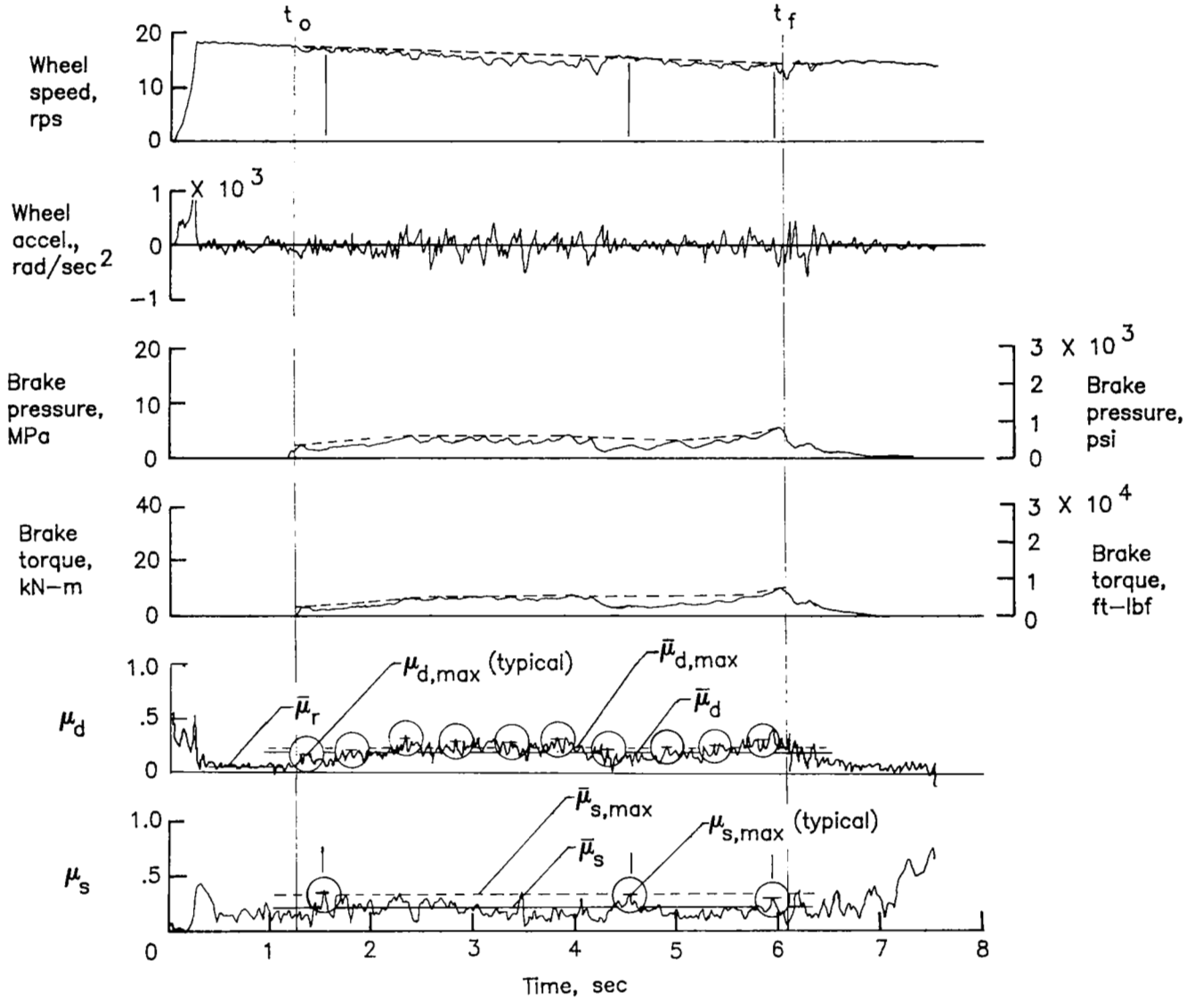

(b) Run 66; nominal carriage speed, 96 knots; vertical load, 69 kN (15 500 lbf); yaw angle, 6°; tire condition, new; surface condition, damp.

Figure 10.- Concluded.

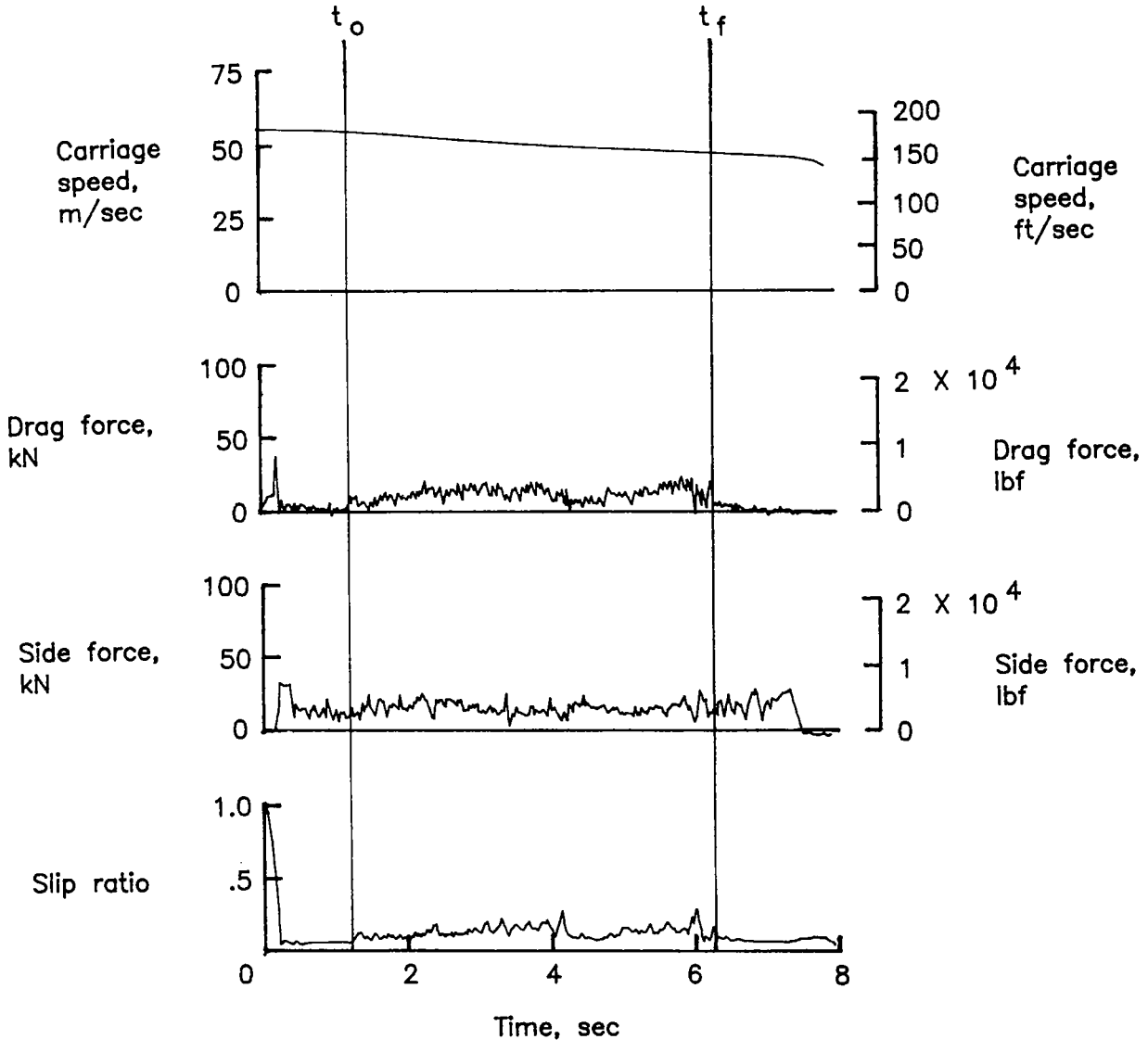

Figure 11.- Typical time histories of variables used to obtain power terms. Run 66; nominal carriage speed, 96 knots; vertical load, 69 kN (15 500 lbf); yaw angle, 6°; tire condition, new; surface condition, damp.

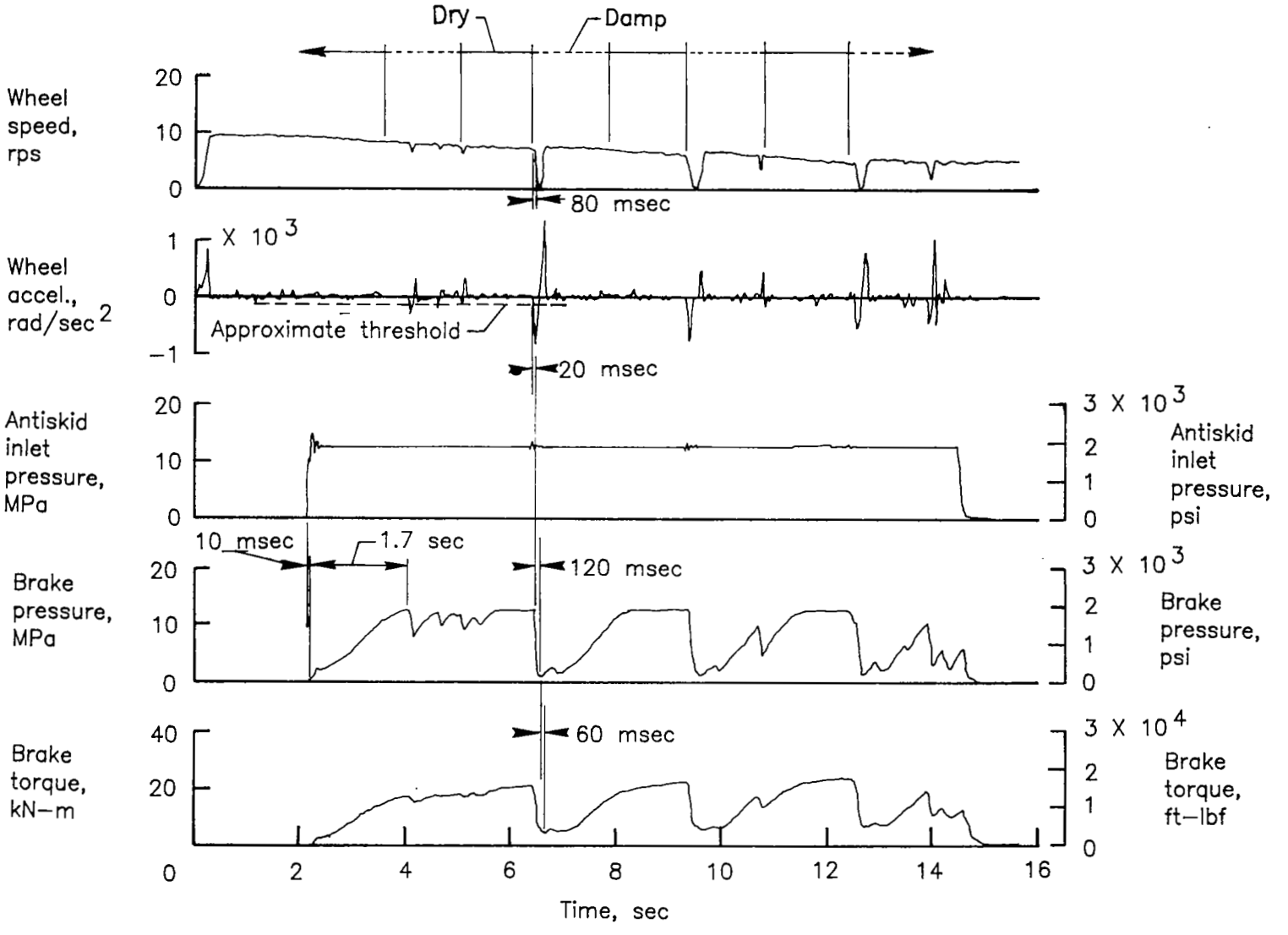

Figure 12.- Typical brake-system hydraulic response. Run 32; nominal carriage speed, 41 knots; vertical load, 68 kN (15 300 lbf); yaw angle, 0°; tire condition, new; surface condition, alternating dry and damp at 30.5-m (100-ft) intervals.

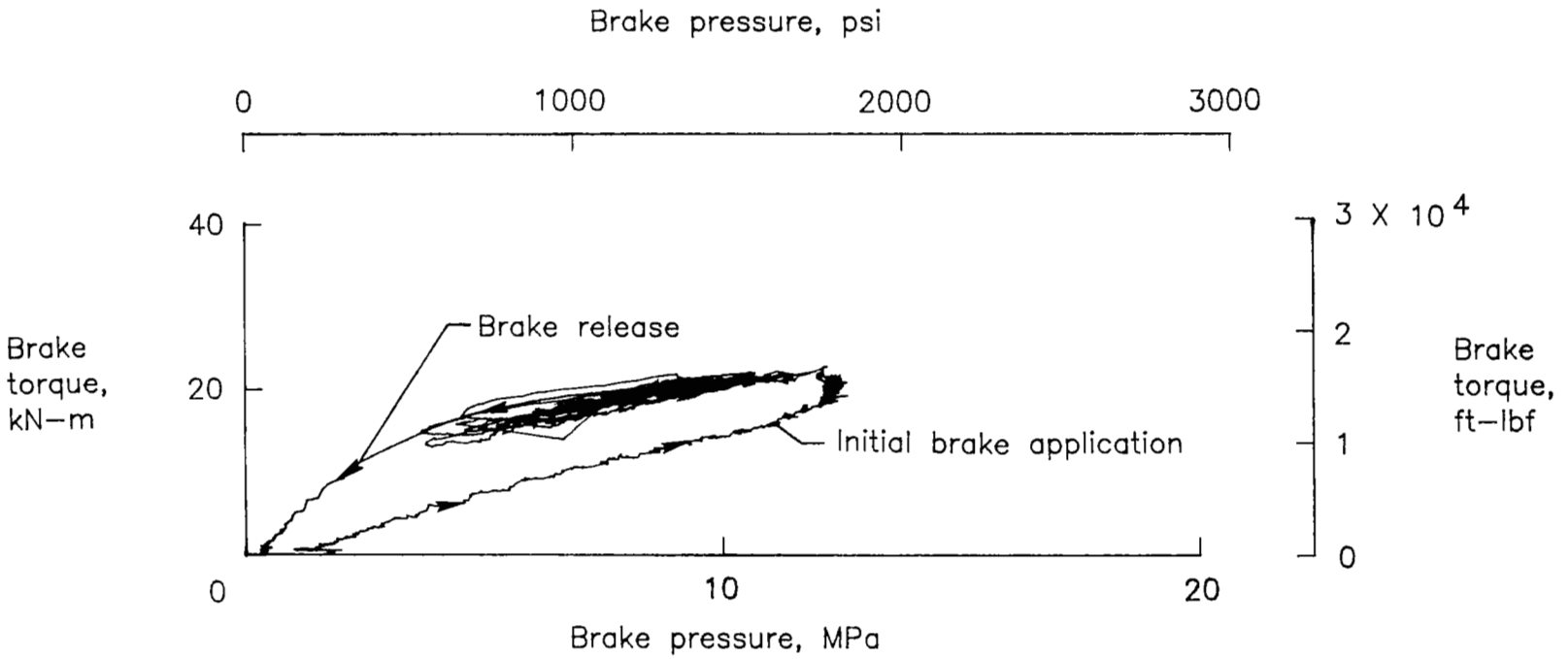

Figure 13.- Brake torque-pressure relationship. Run 62; nominal carriage speed, 56 knots; vertical load, 71 kN (15 900 lbf); yaw angle, 6°; tire condition, new; surface condition, dry.

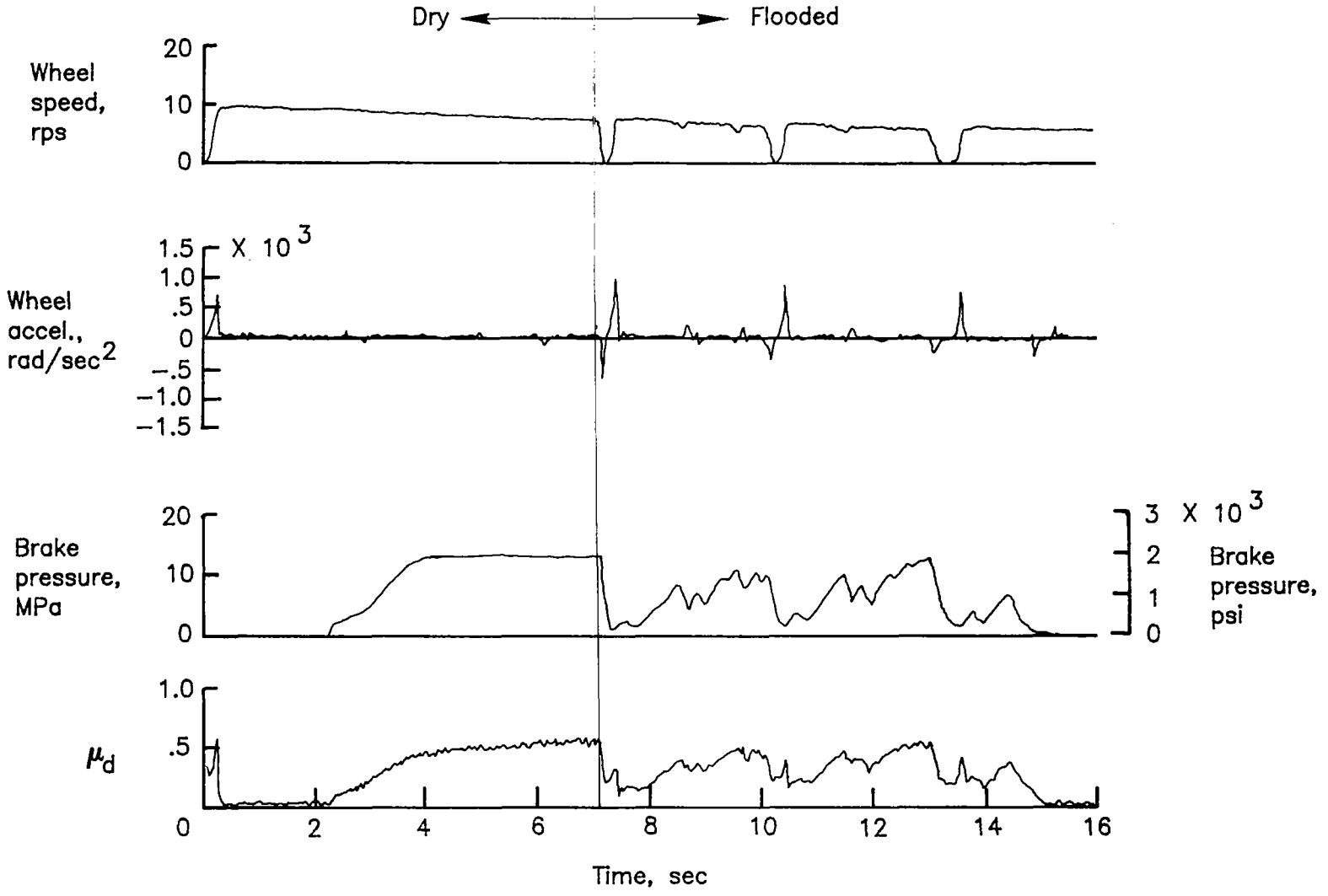

(a) Run 36; nominal carriage speed, 41 knots; vertical load, 69 kN (15 600 lbf); yaw angle, 0°; tire condition, new; surface condition, dry to flooded.

Figure 14.- Antiskid-system response to transient runway conditions.

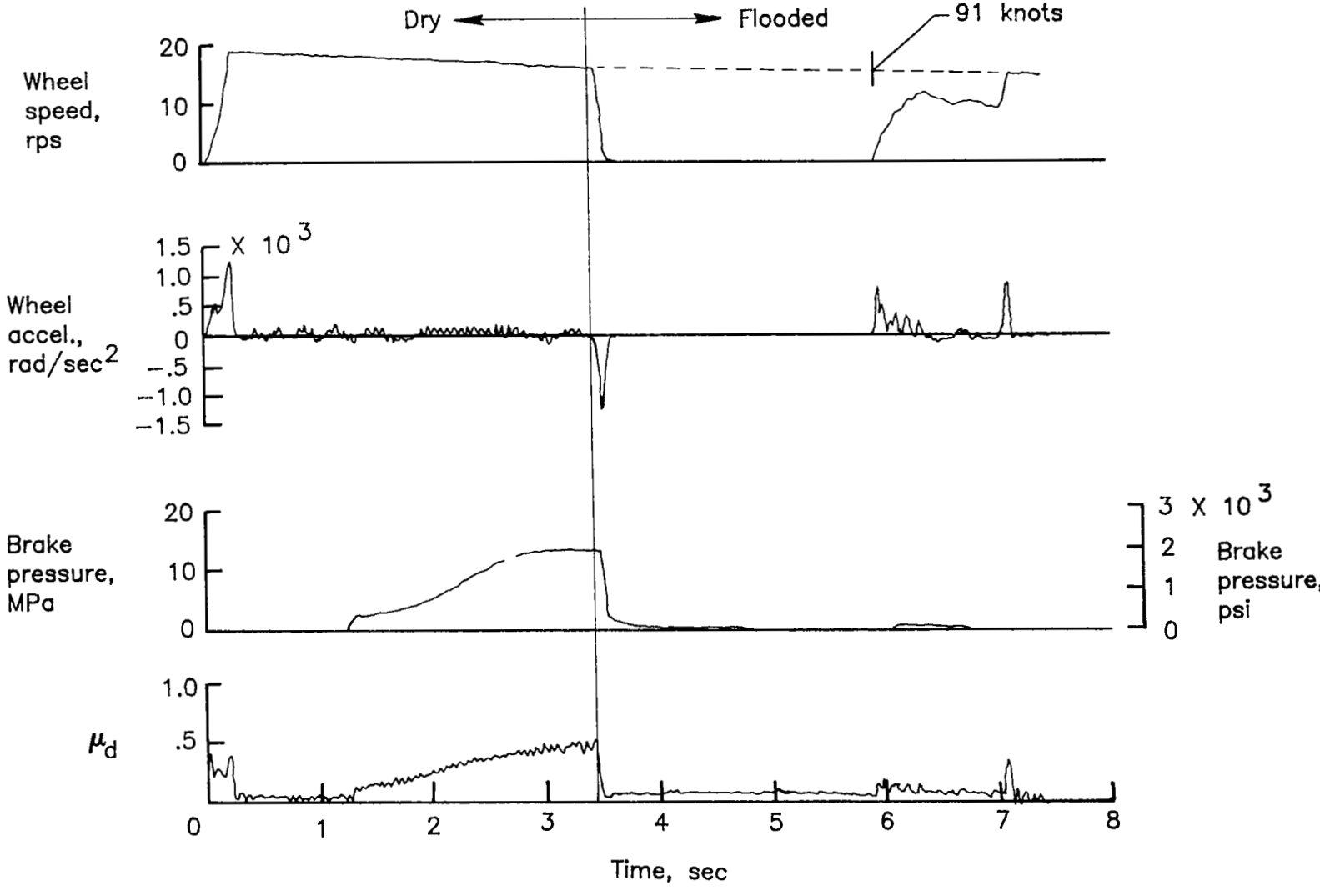

(b) Run 38; nominal carriage speed, 97 knots; vertical load, 69 kN (15 400 lbf); yaw angle, 0°; tire condition, new; surface condition, dry to flooded.

Figure 14.- Continued.

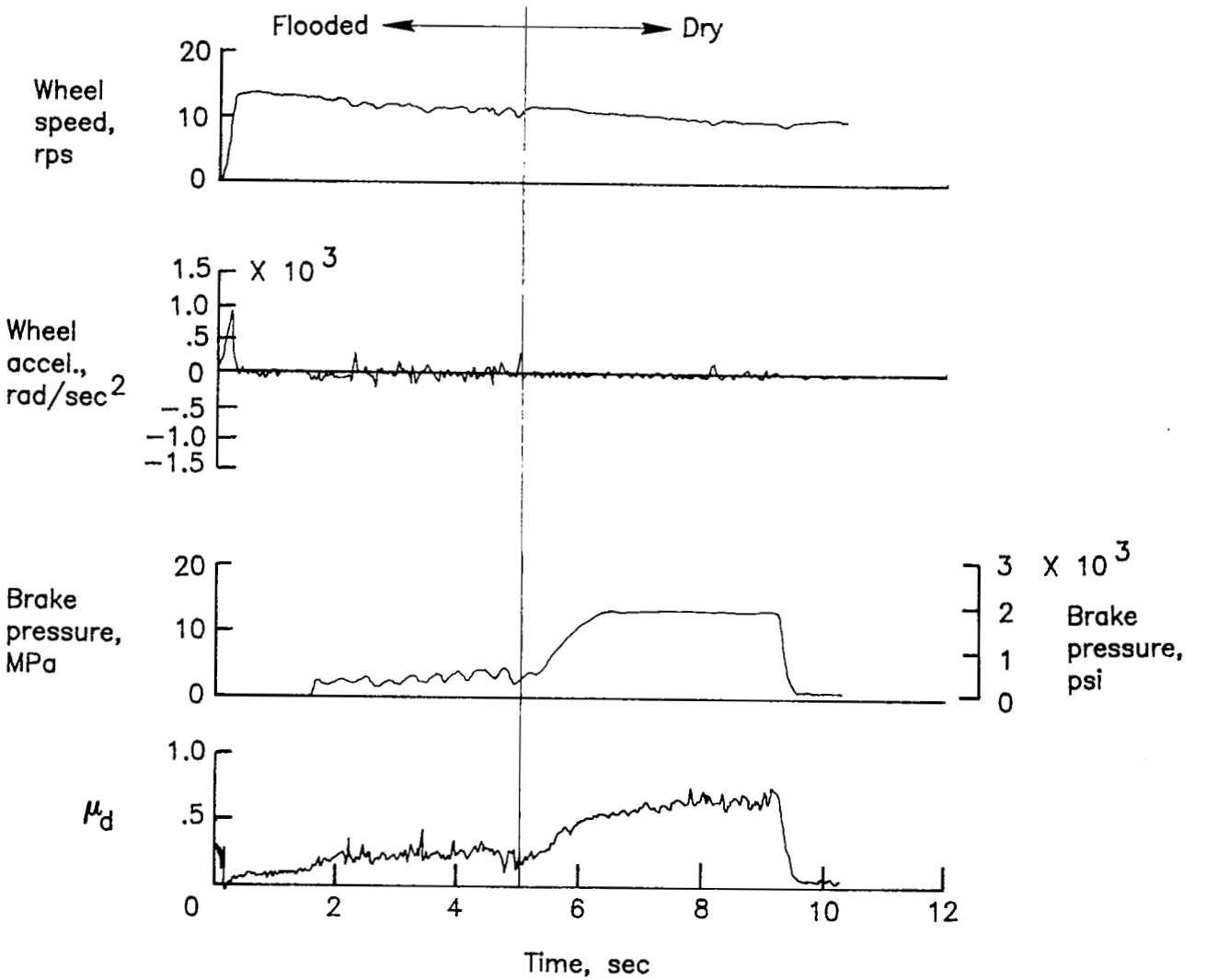

(c) Run 40; nominal carriage speed, 67 knots; vertical load, 68 kN (15 300 lbf); yaw angle, 0°; tire condition, new; surface condition, flooded to dry.

Figure 14.- Continued.

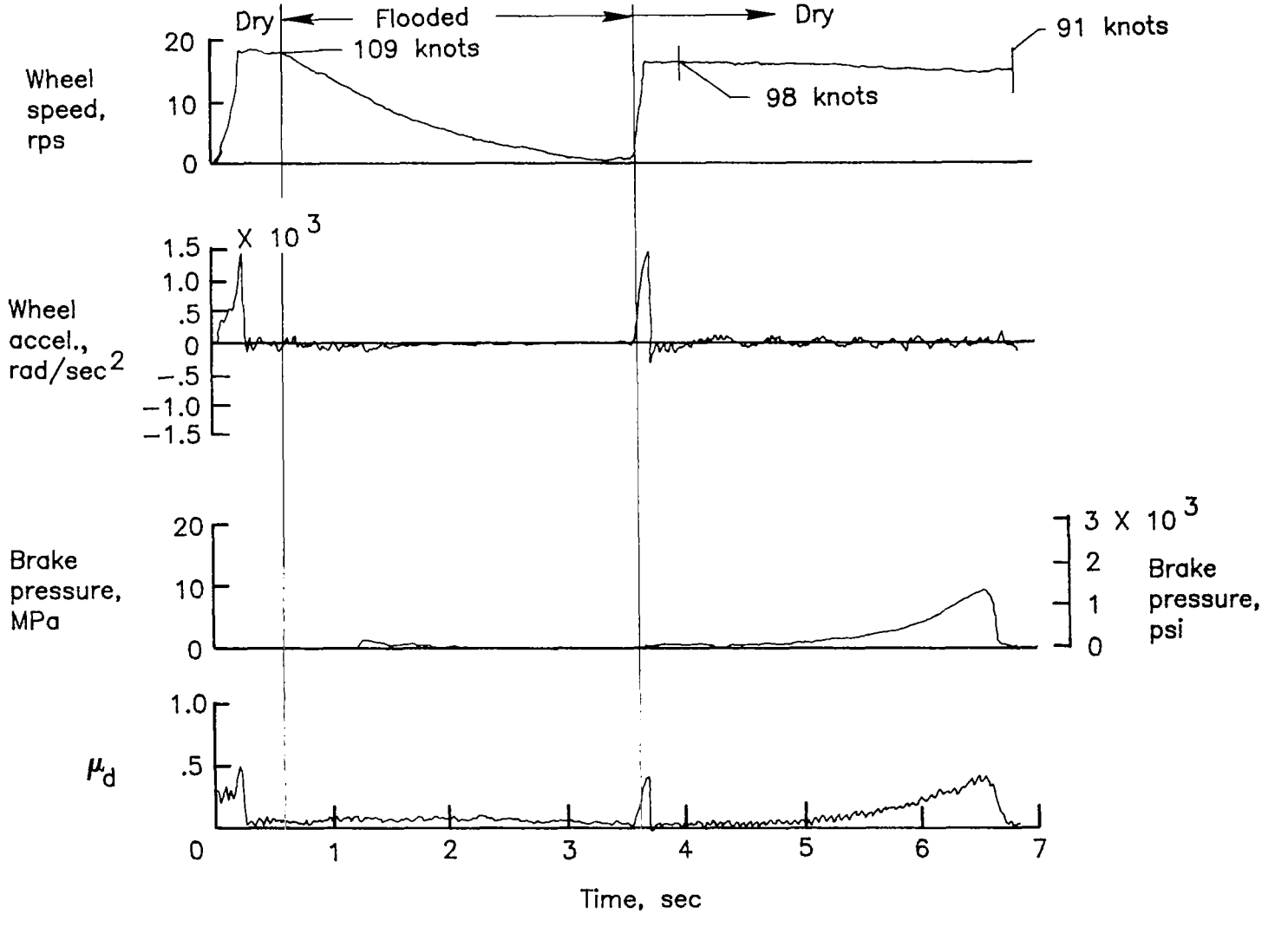

(d) Run 41; nominal carriage speed, 98 knots; vertical load, 68 kN (15 300 lbf); yaw angle, 0°; tire condition, new; surface condition, flooded to dry.

Figure 14.- Concluded.

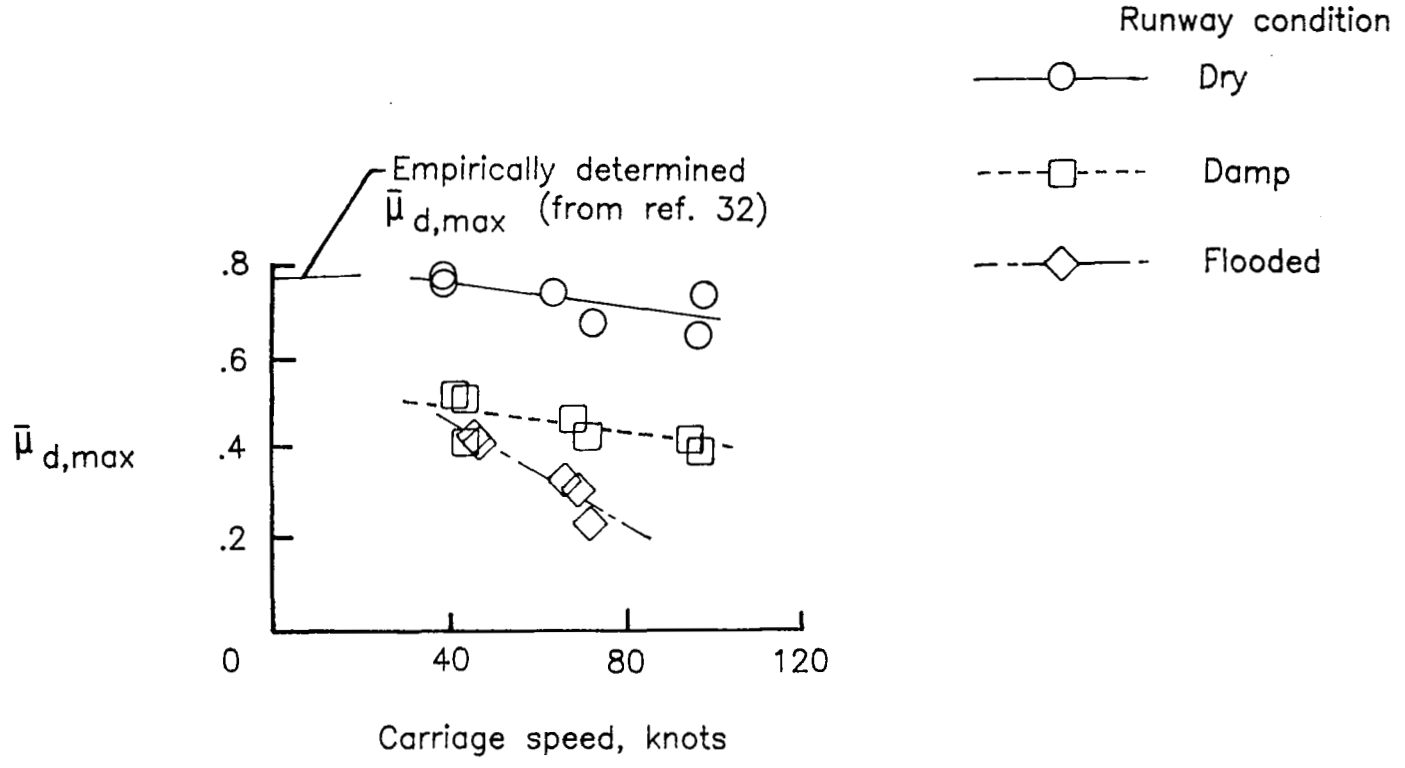

Figure 15.- Effect of carriage speed on maximum achieved drag-force friction coefficient. Vertical load, ≤89 kN (≤20 000 lbf); yaw angle, 0°; tire condition, new.

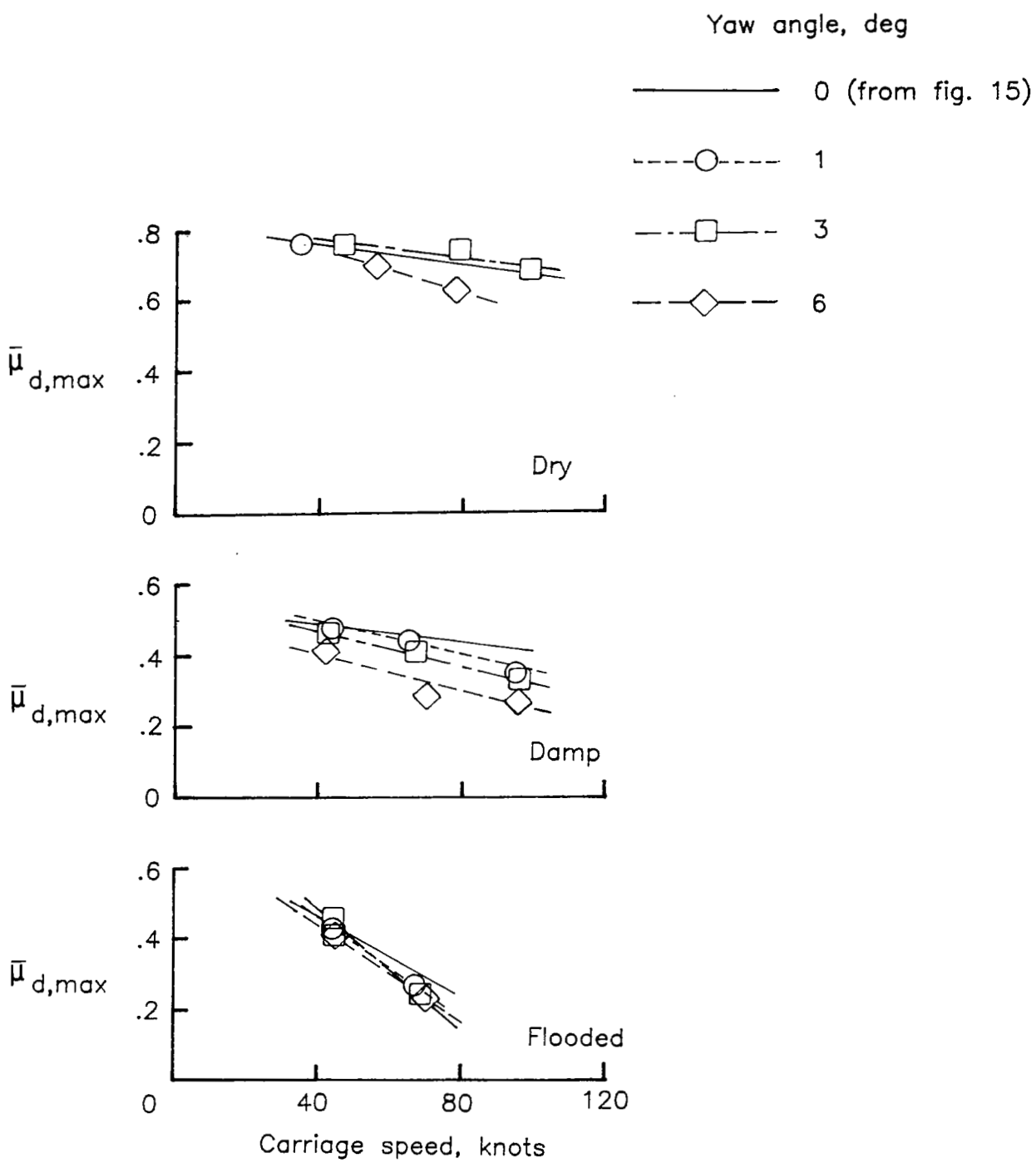

Figure 16.- Effect of yaw angle on maximum drag-force friction coefficient. Vertical load, ≦89 kN (≦20 000 lbf); tire condition, new.

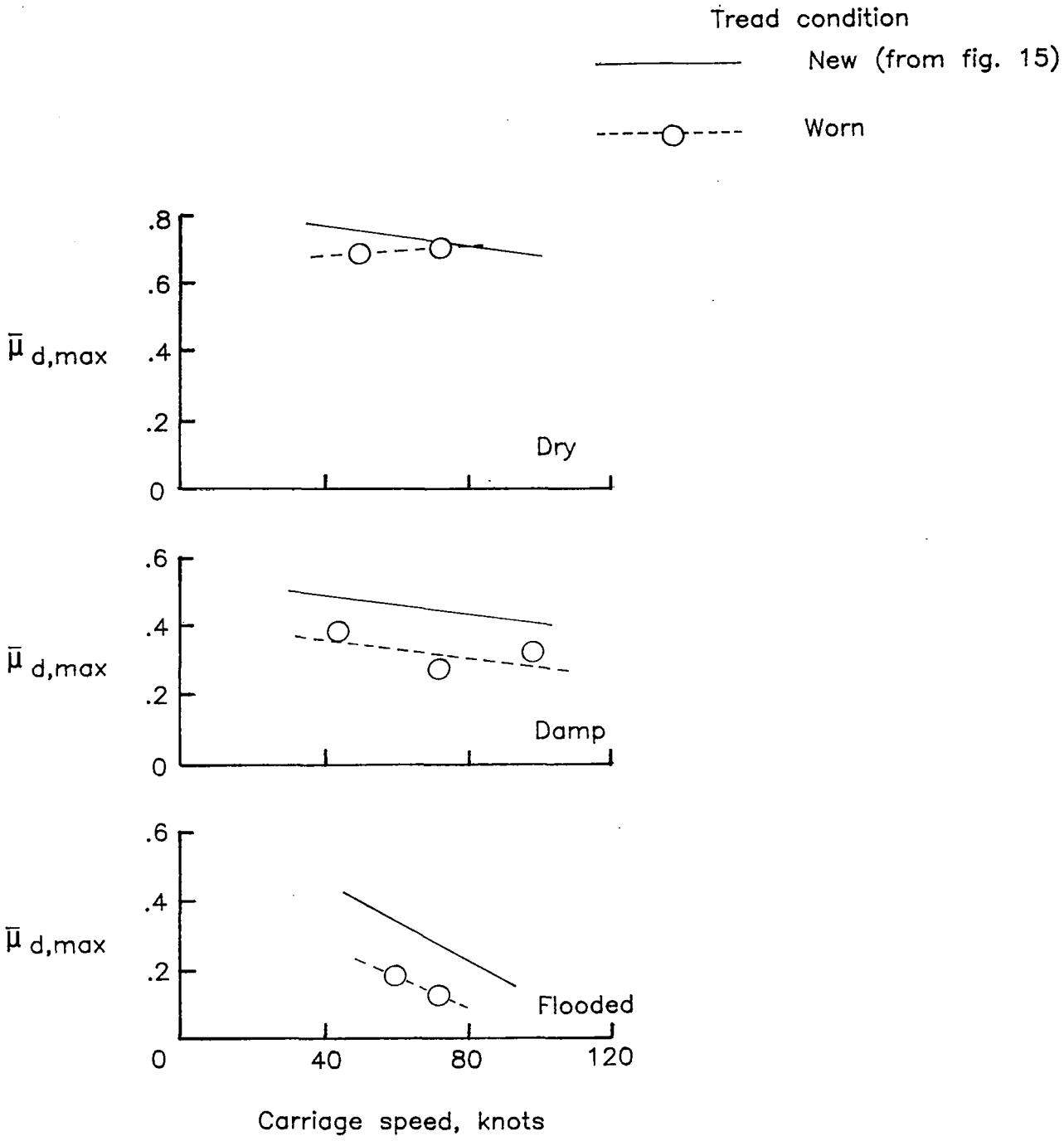

Figure 17.- Effect of tread wear on maximum drag-force friction coefficient. Vertical load, ≤89 kN (≤20 000 lbf); yaw angle, 0°.

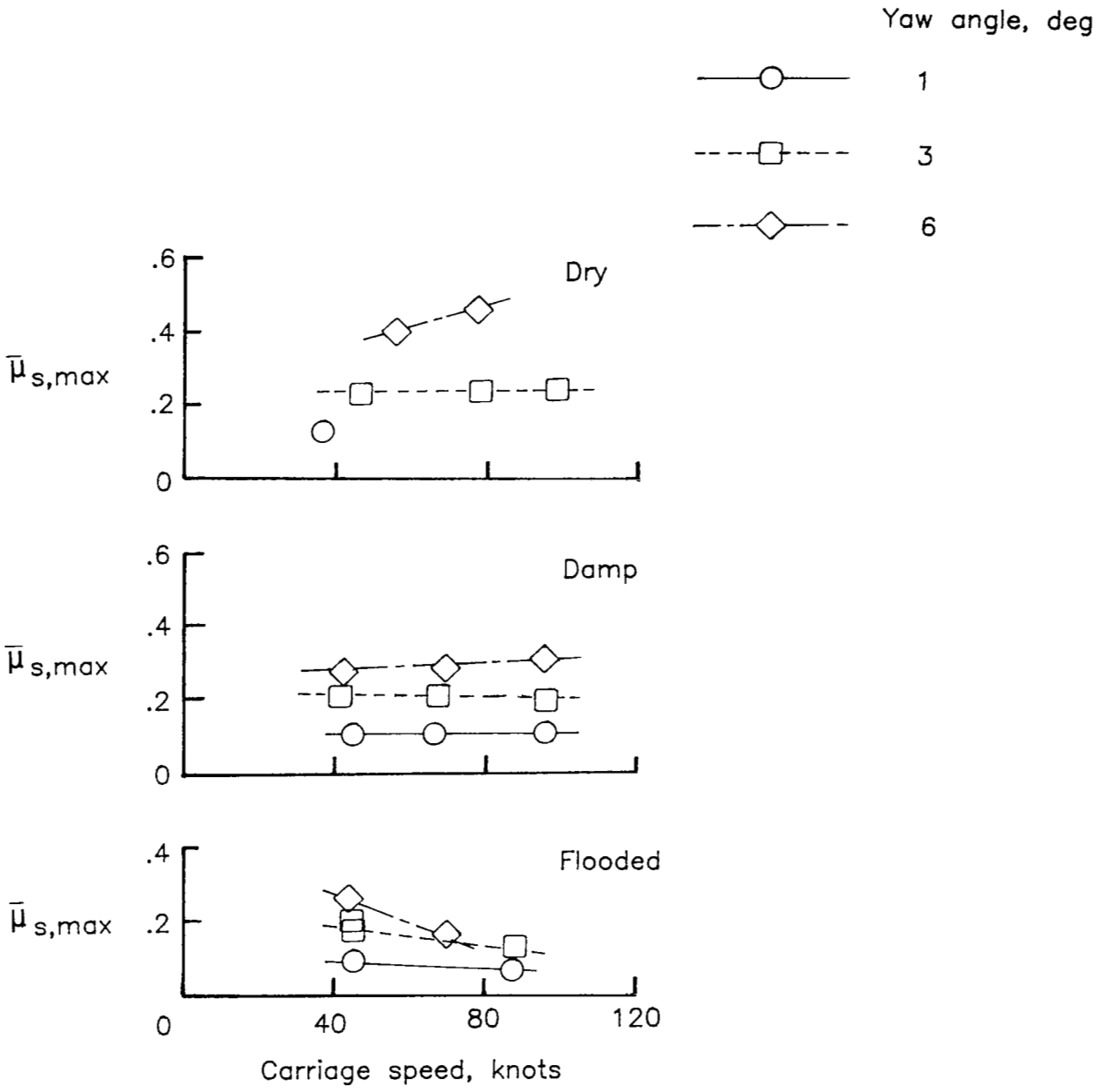

Figure 18.- Effect of carriage speed on maximum achieved side-force friction coefficient. Vertical load, ≦89 kN (≦20 000 lbf); free rolling (unbraked); tire condition, new.

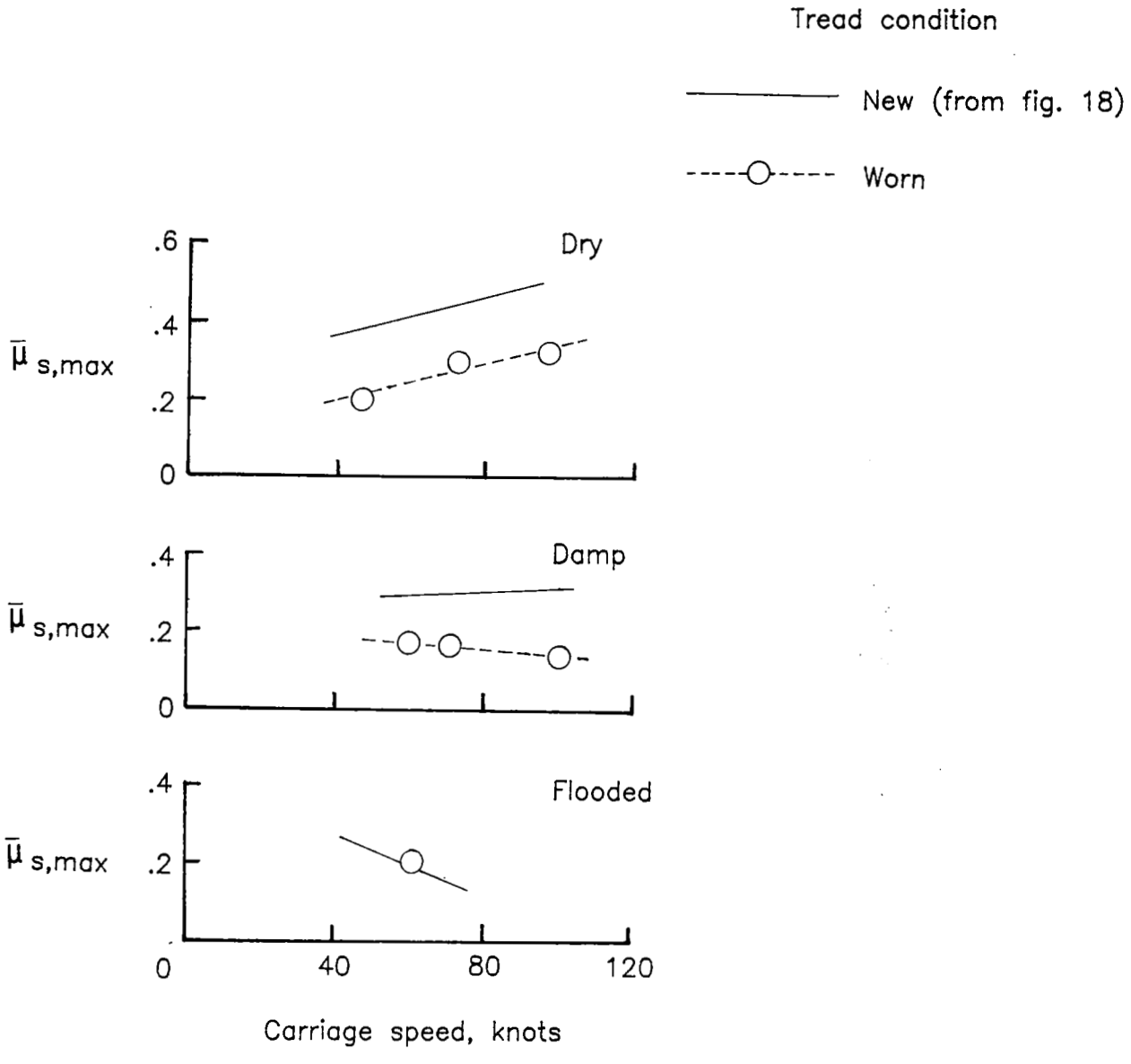

Figure 19.- Effect of tread wear on maximum achieved side-force friction coefficient. Vertical load, ≦89 kN (≦20 000 lbf); yaw angle, 6°; free rolling (unbraked).

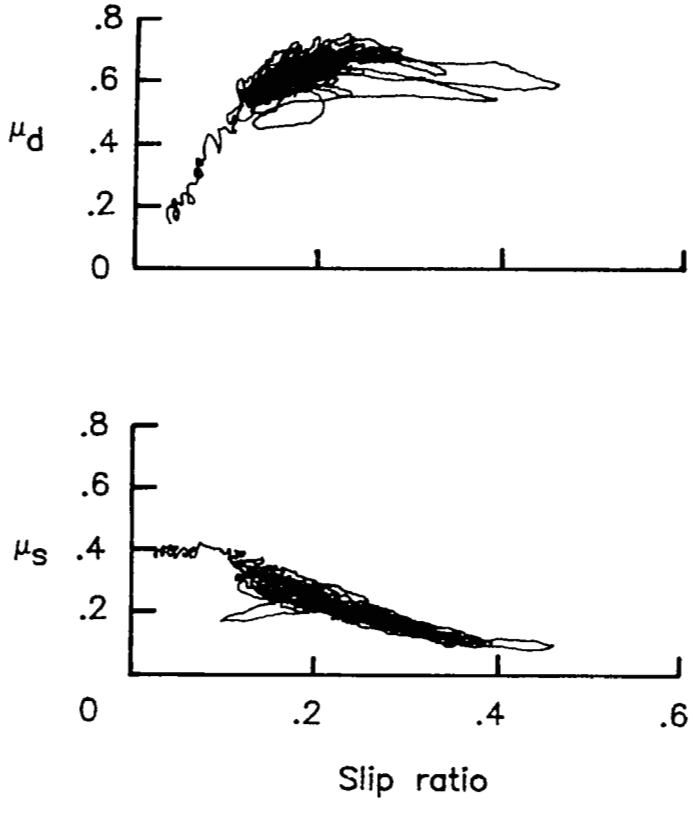

Figure 20.- Interaction between braking and cornering. Run 62; nominal carriage speed, 56 knots; vertical load, 71 kN (15 900 lbf); yaw angle, 6°; tire condition, new; surface condition, dry.

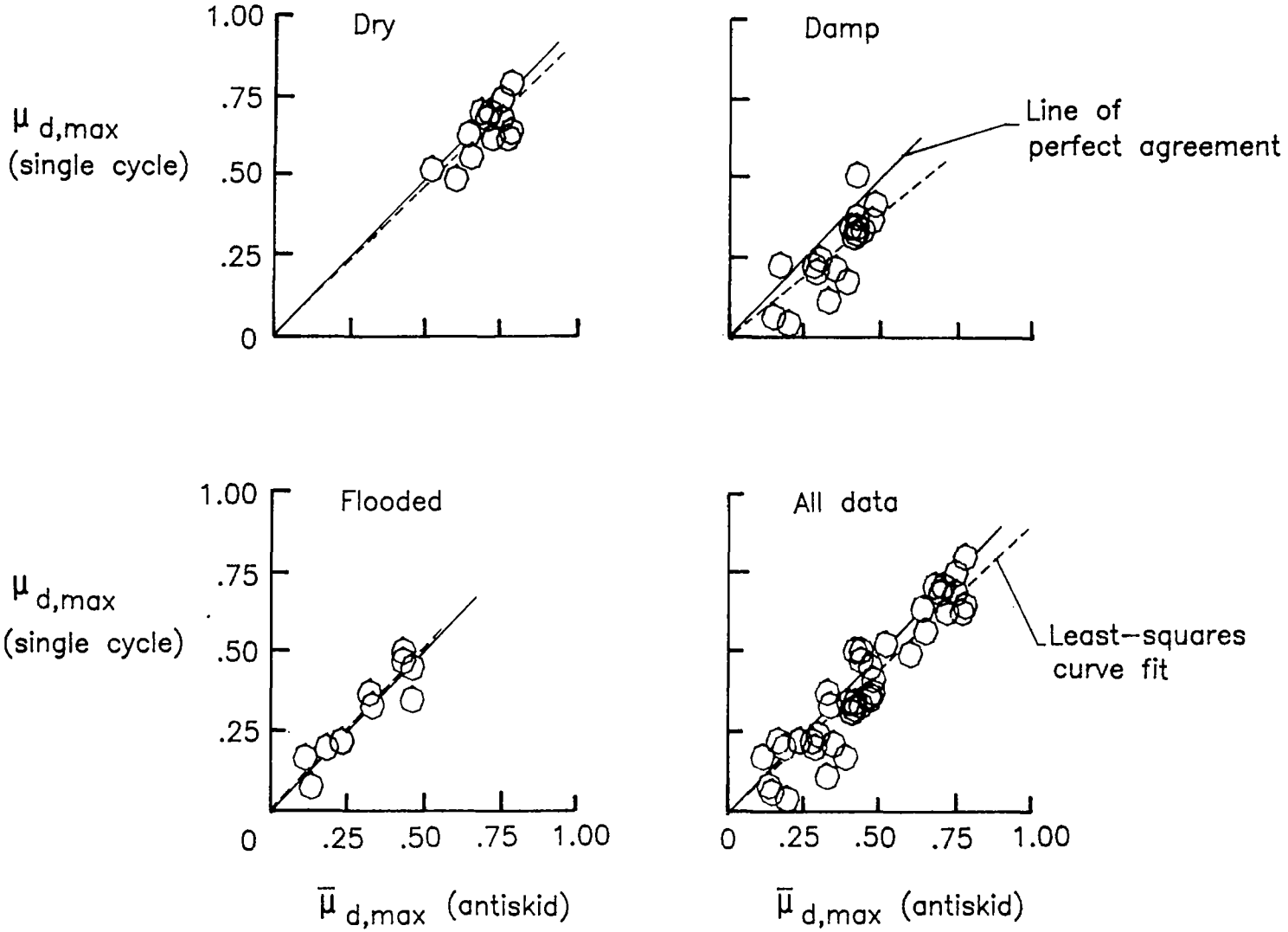

Figure 21.- Effect of cyclic braking on maximum achieved drag-force friction coefficient.

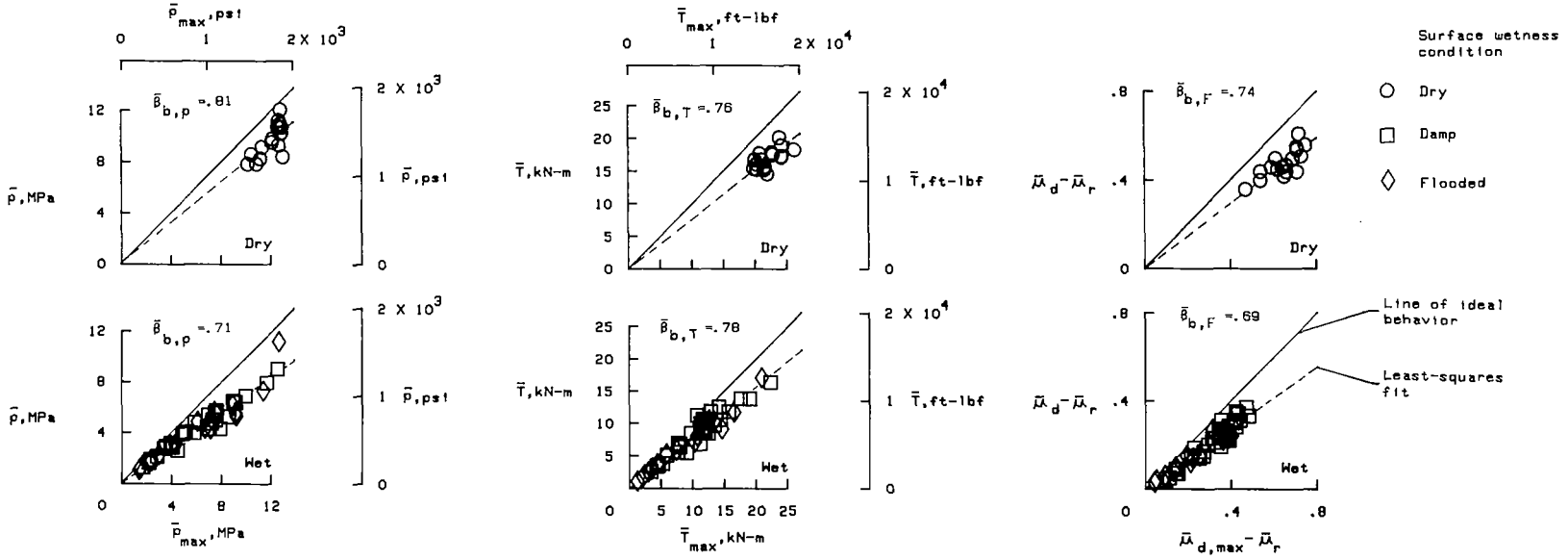

(a) Pressure ratios. (b) Torque ratios. (c) Friction ratios.

Figure 22.- Ratios of average developed to maximum achieved brake pressure, torque, and drag-force friction coefficient. Data include all runs except those which were torque-limited for entire run, those involving tire hydroplaning, and those performed to examine effects of runway friction transition.

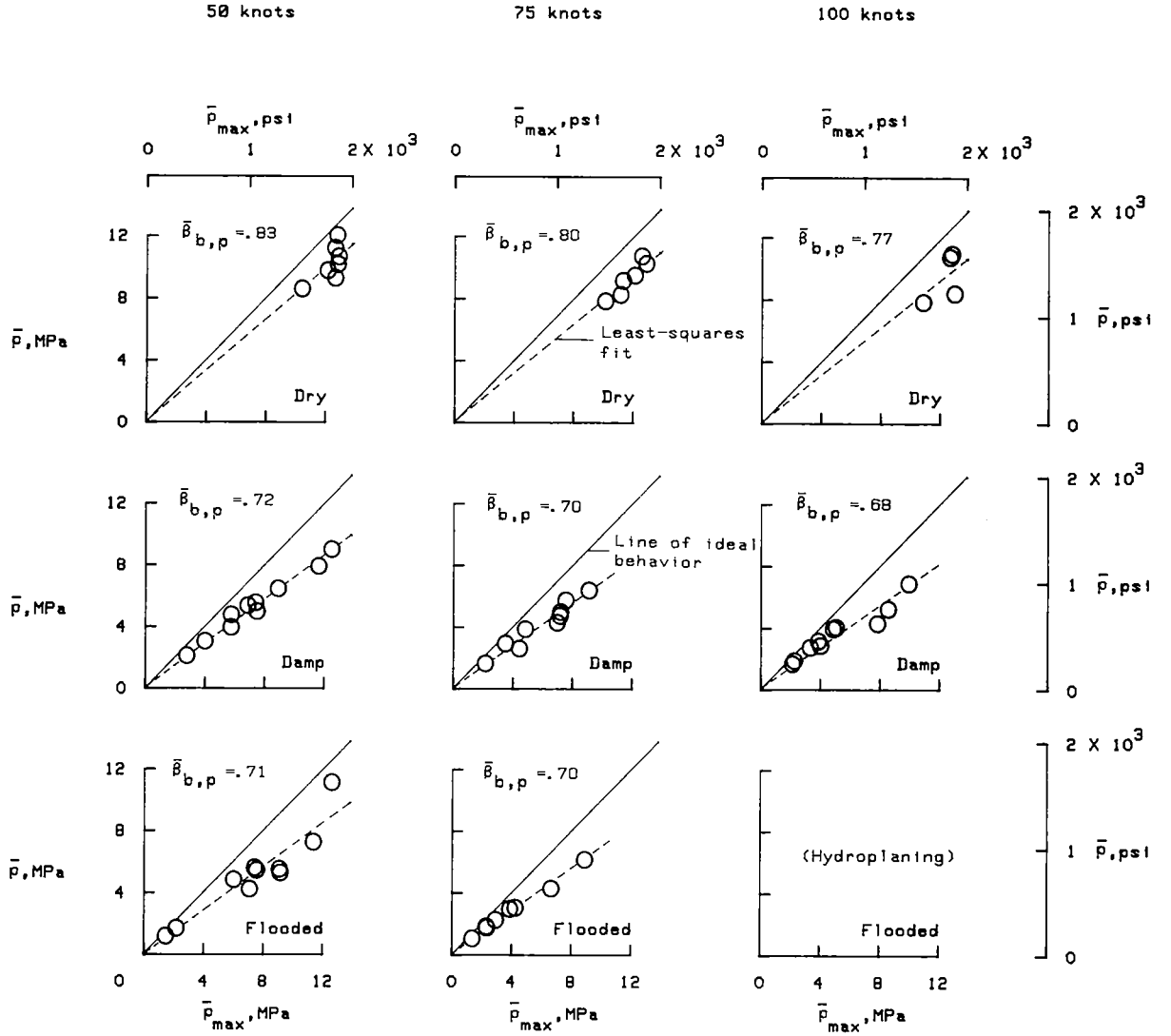

(a) Pressure ratios.

Figure 23.- Effect of carriage speed on brake pressure, torque, and friction ratios. Yaw angles, 0^o to 6^o.

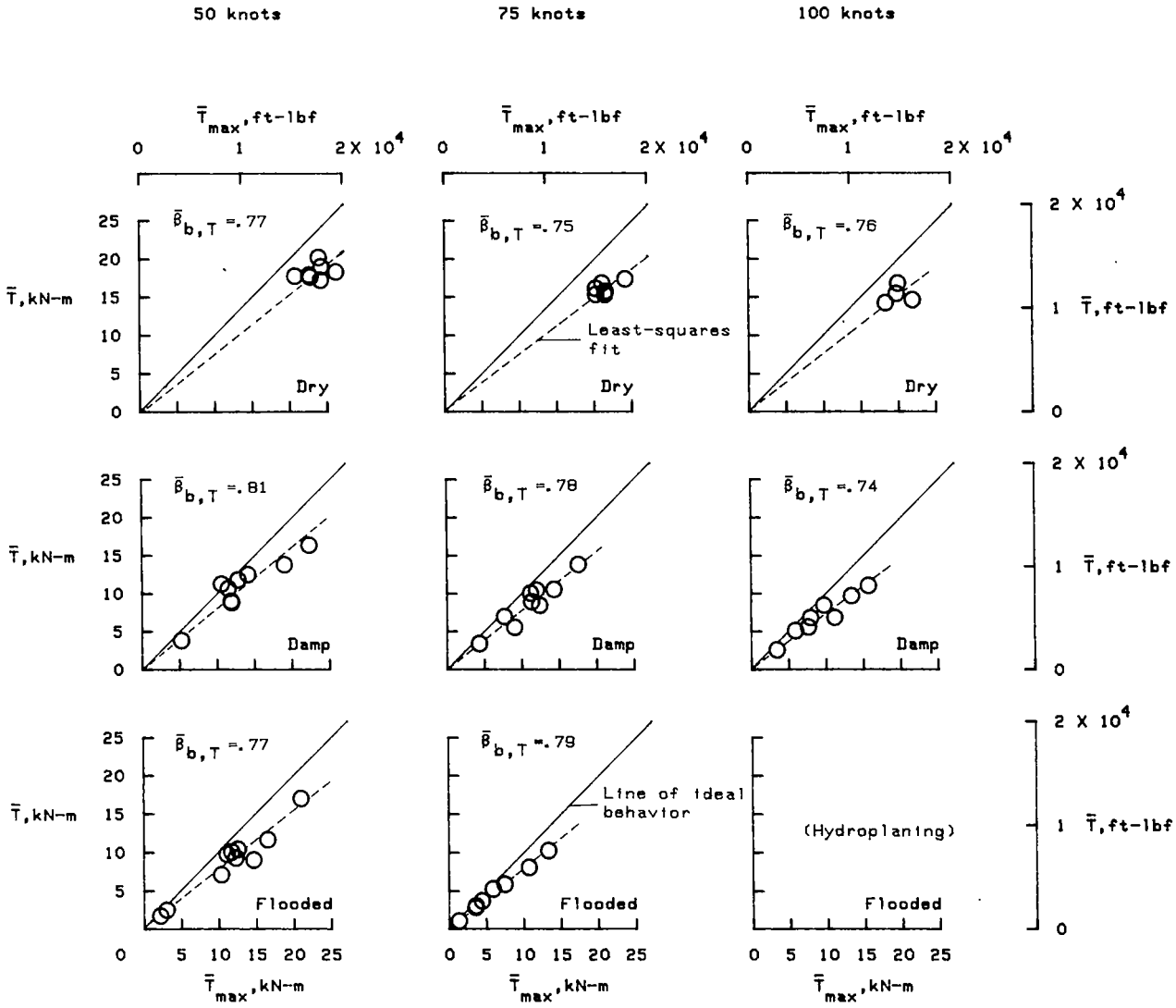

(b) Torque ratios.

Figure 23.- Continued.

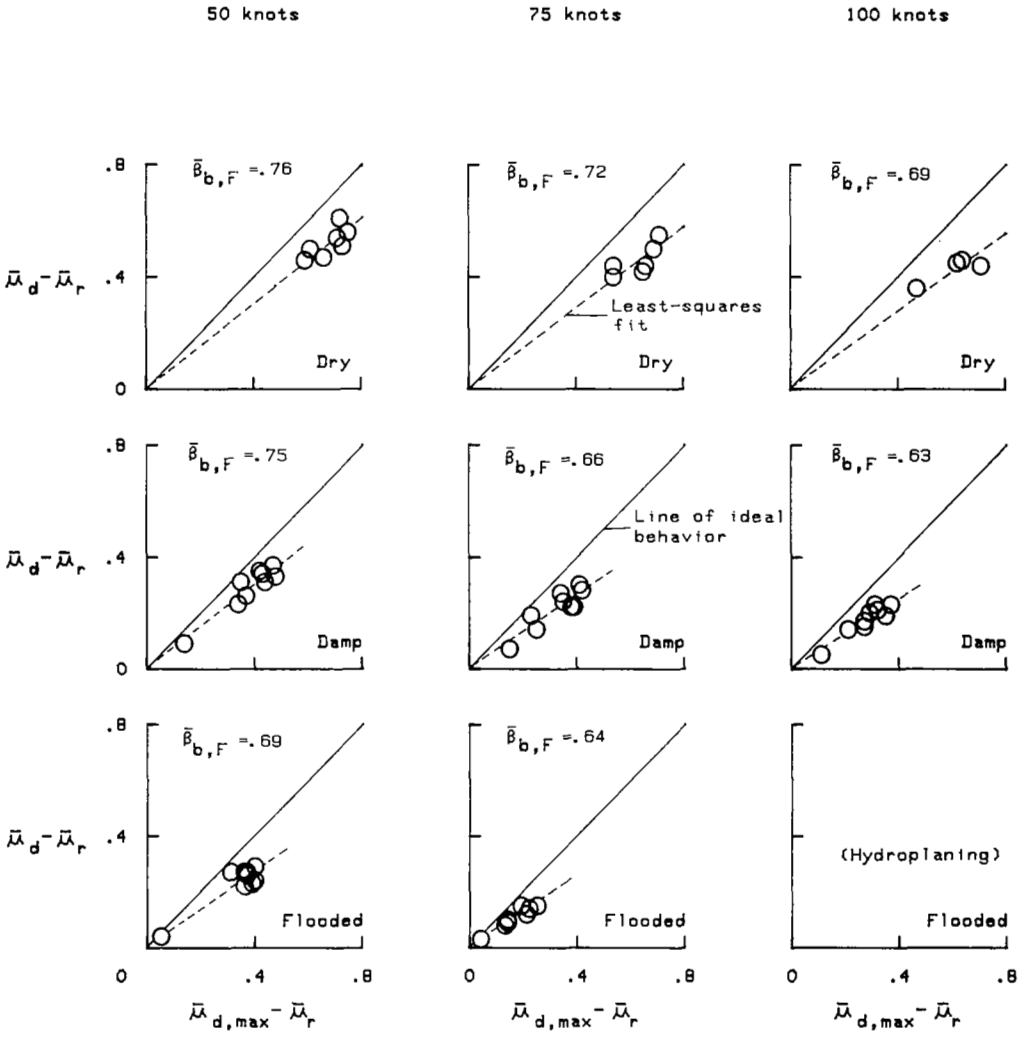

(c) Friction ratios.

Figure 23.- Concluded.

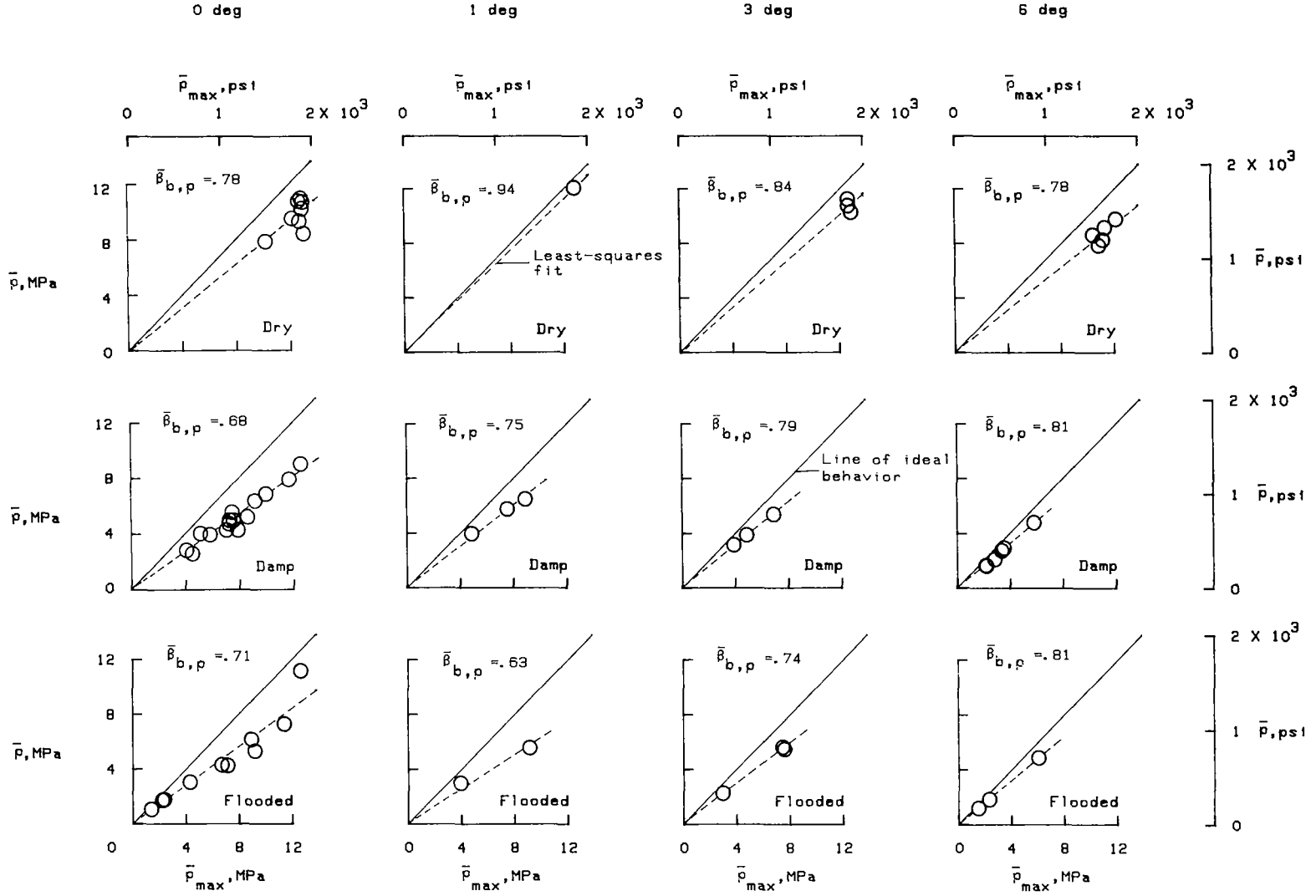

(a) Pressure ratios.

Figure 24.- Effect of yaw angle on brake pressure, torque, and friction ratios.

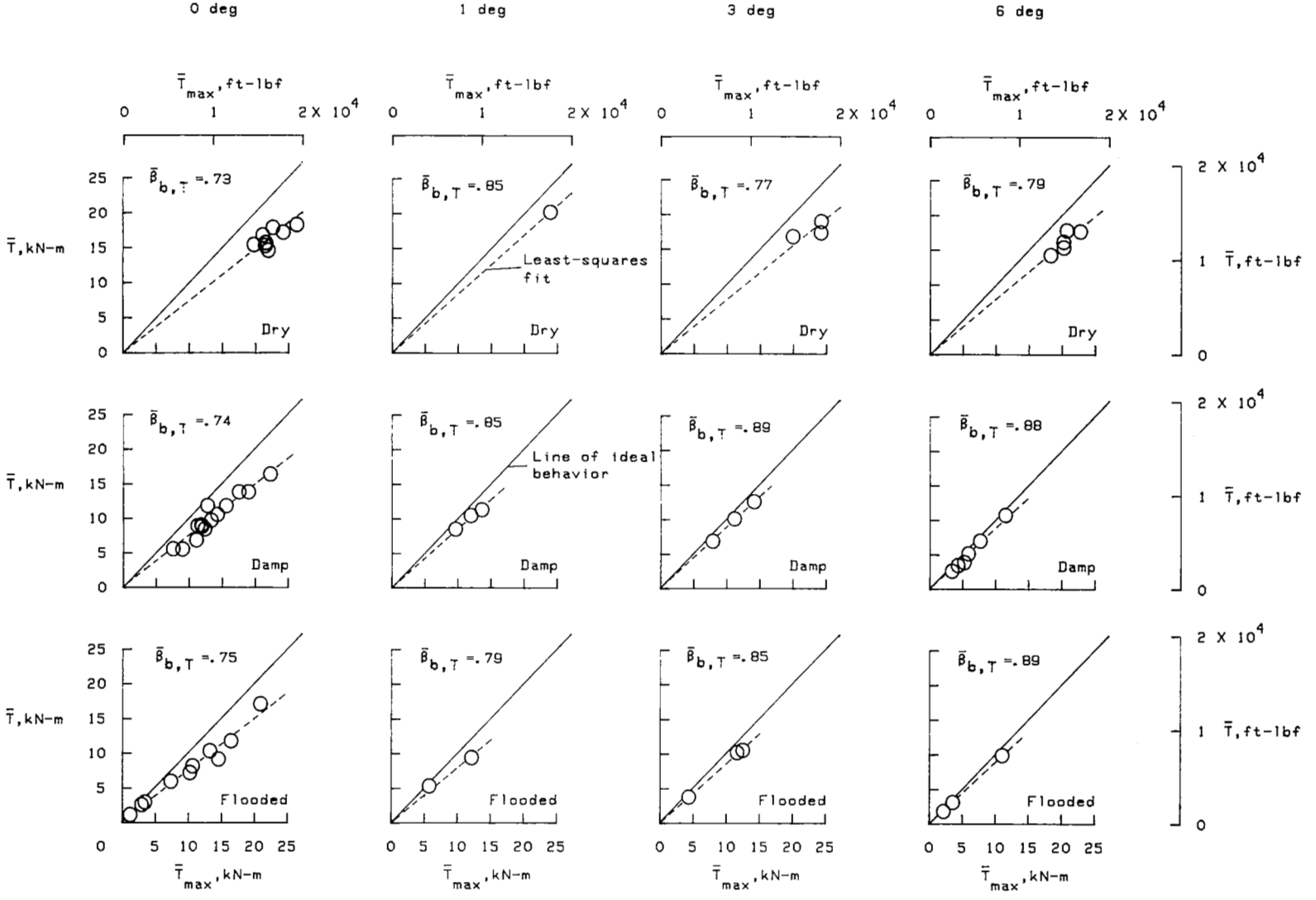

(b) Torque ratios.

Figure 24.- Continued.

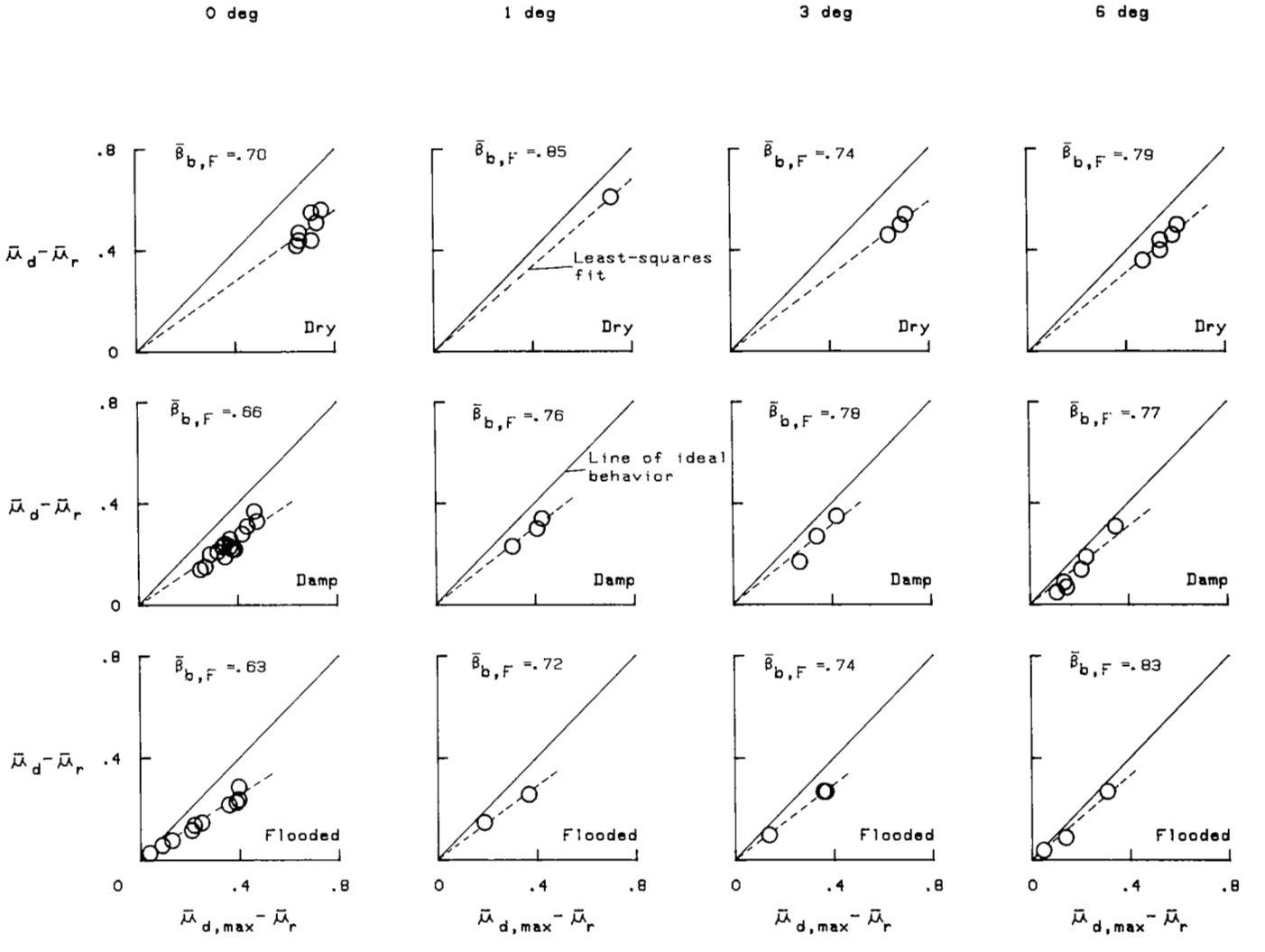

(c) Friction ratios.

Figure 24.- Concluded.

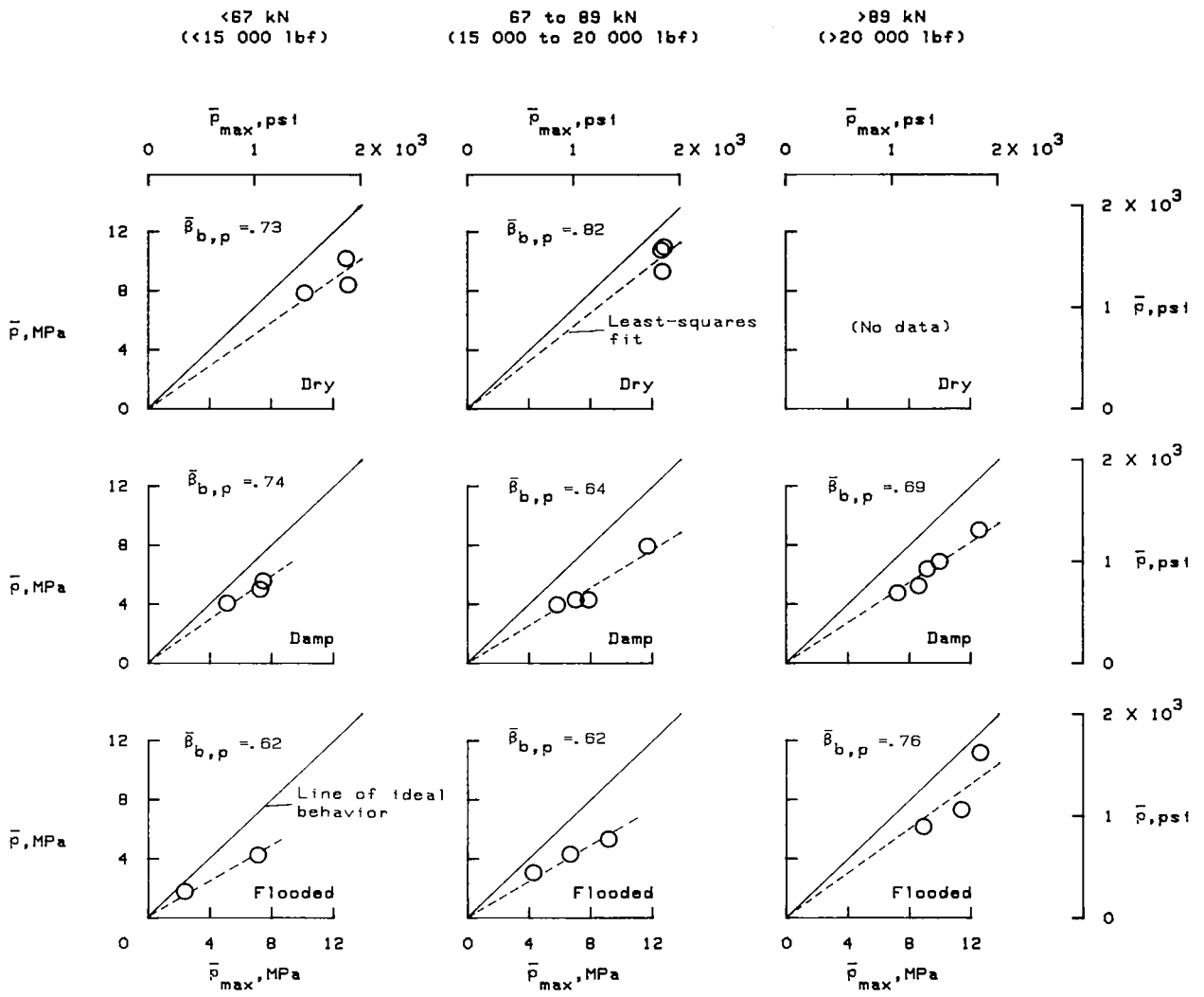

(a) Pressure ratios.

Figure 25.- Effect of vertical-force variations on brake pressure, torque, and friction ratios. Yaw angle, 0°; tire condition, new.

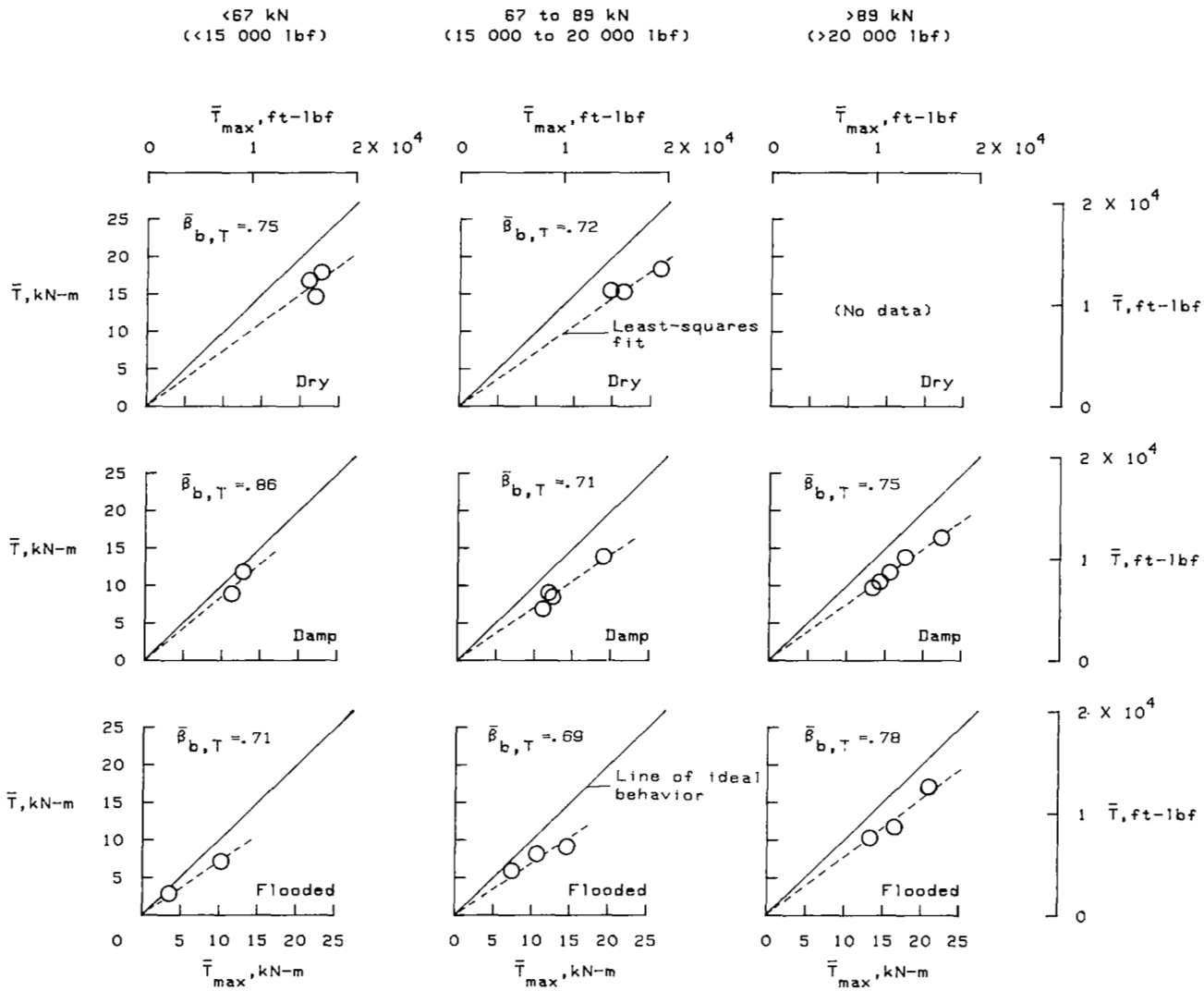

(b) Torque ratios.

Figure 25.- Continued.

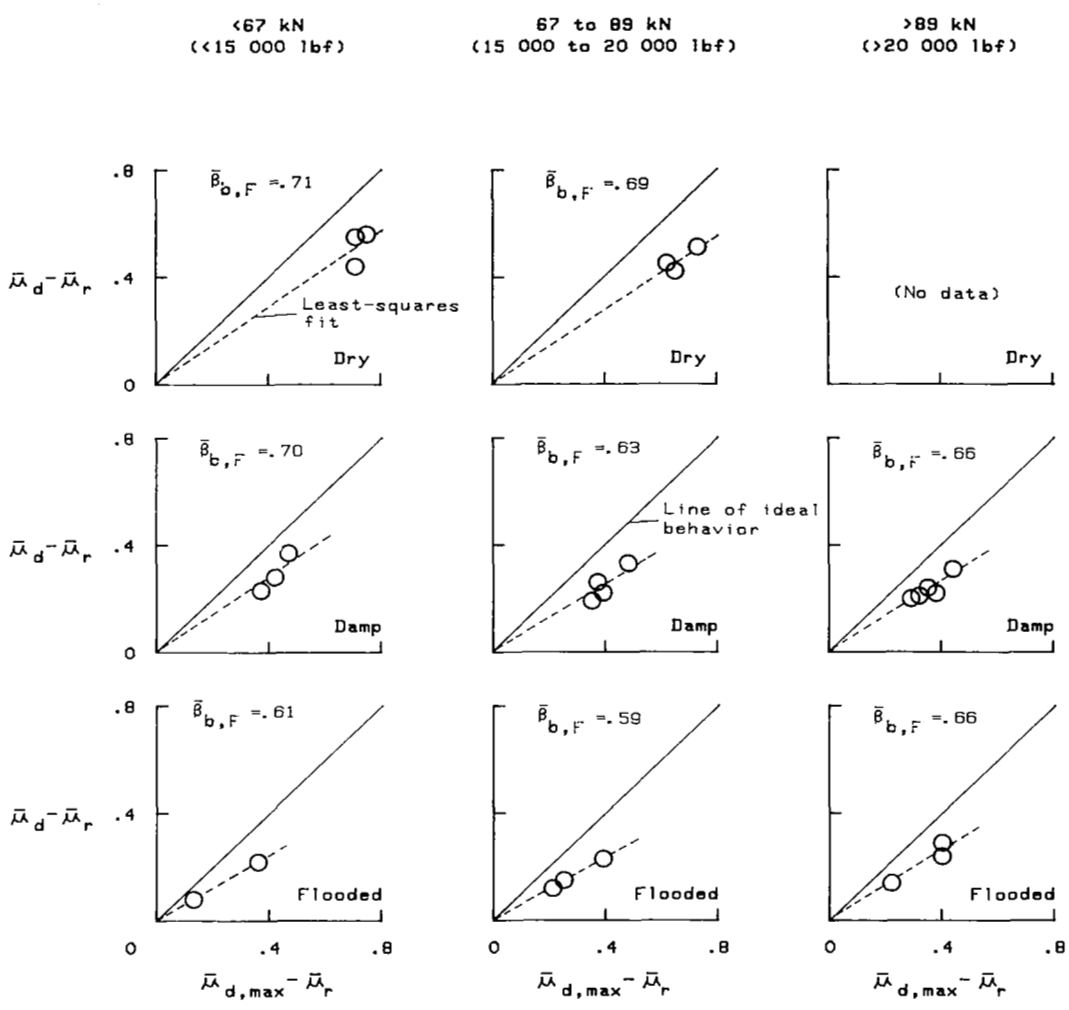

(c) Friction ratios.

Figure 25.- Concluded.

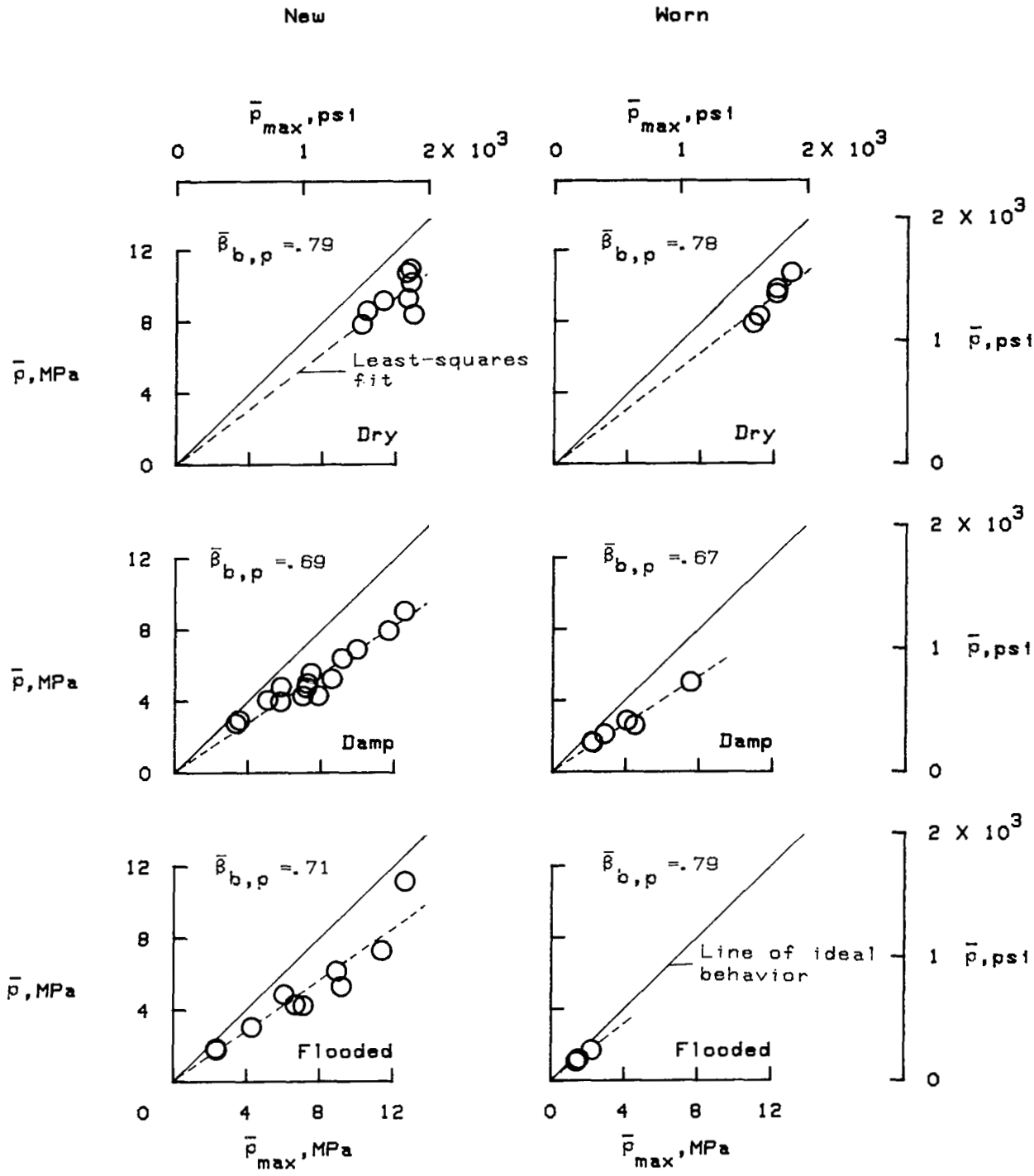

(a) Pressure ratios.

Figure 26.- Effect of tread wear on brake pressure, torque, and friction ratios.

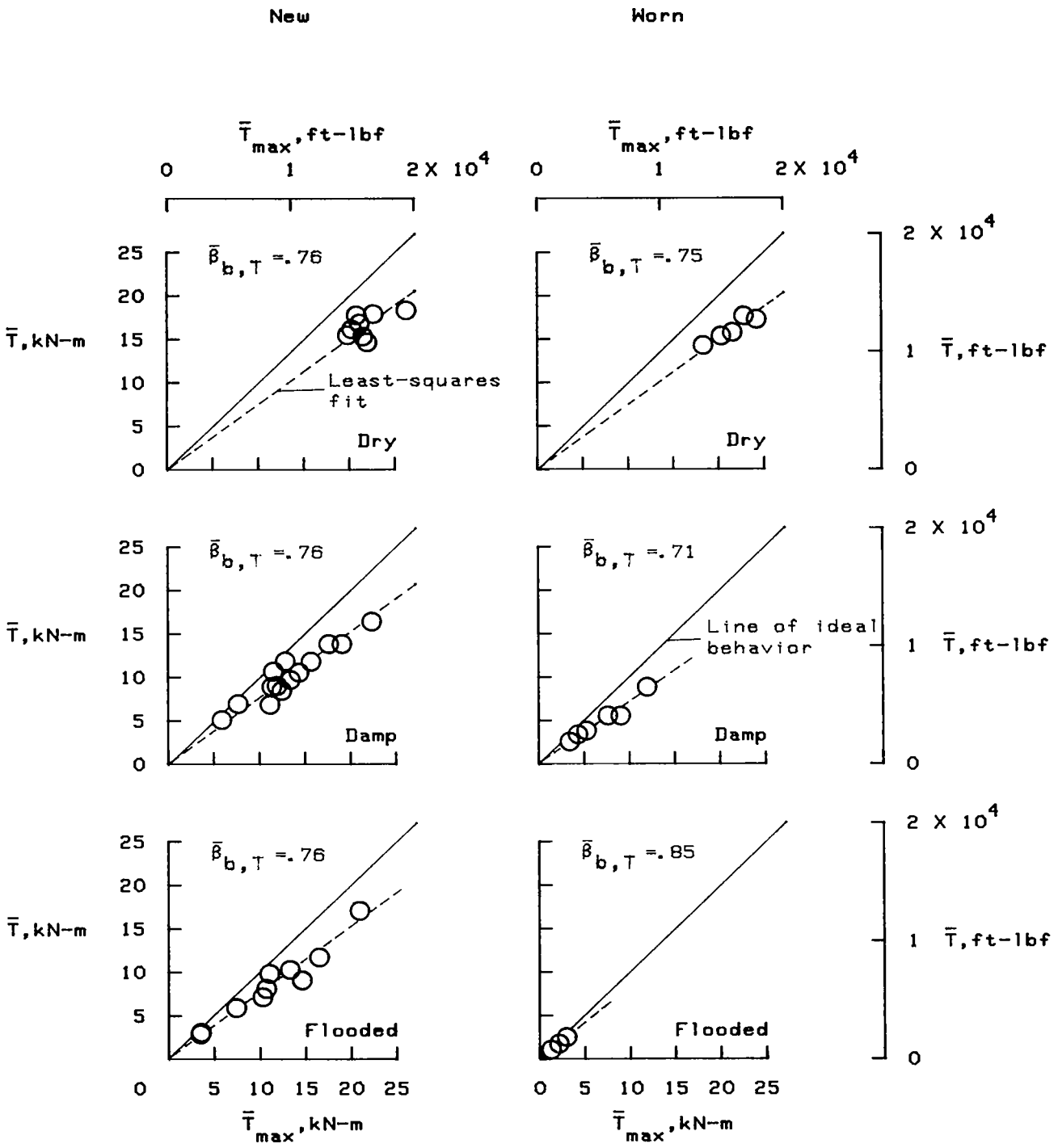

(b) Torque ratios.

Figure 26.- Continued.

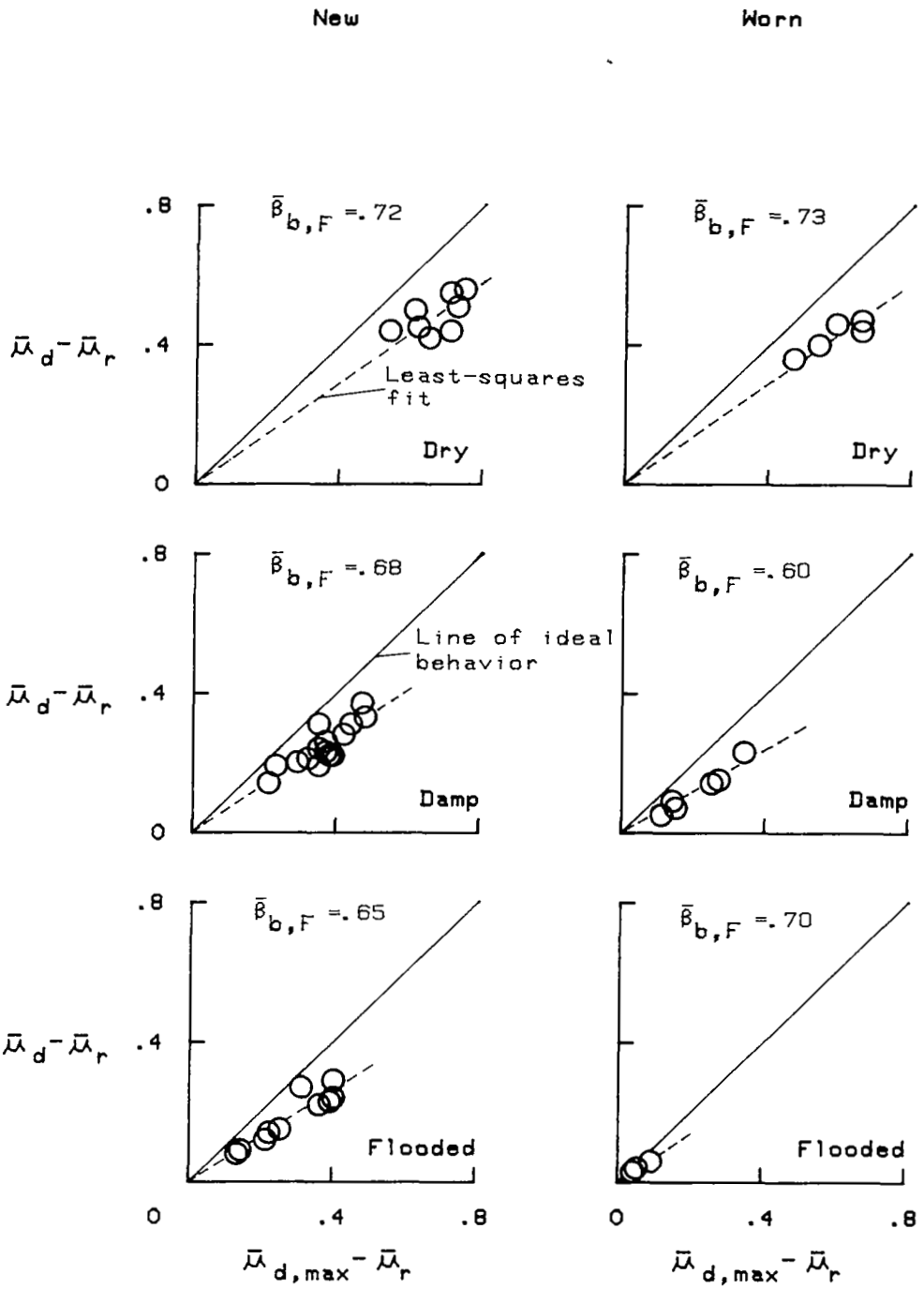

(c) Friction ratios.

Figure 26.- Concluded.

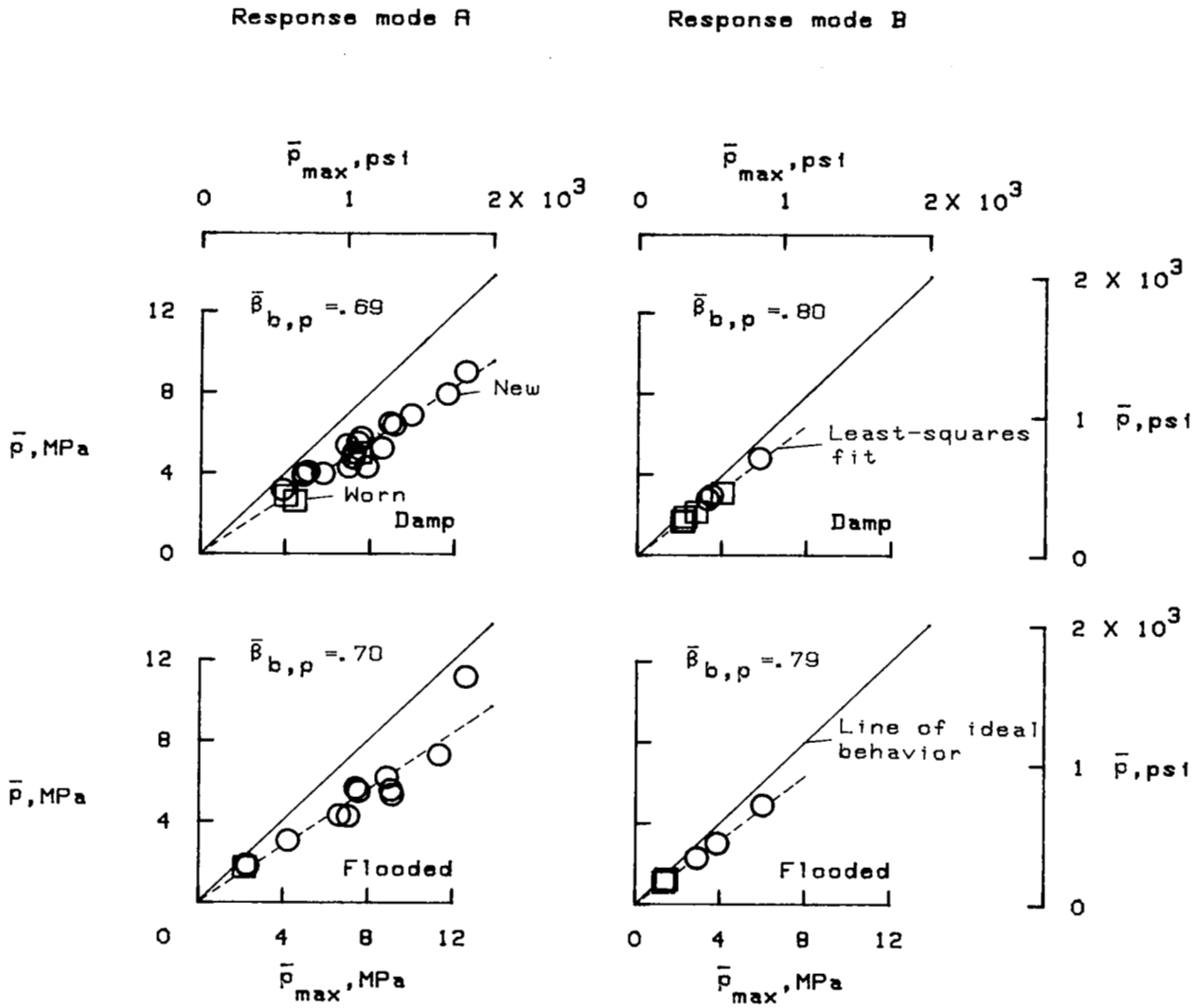

(a) Pressure ratios.

Figure 27.- Effect of system response mode on brake pressure, torque, and friction ratios. Yaw angle, 0^o.

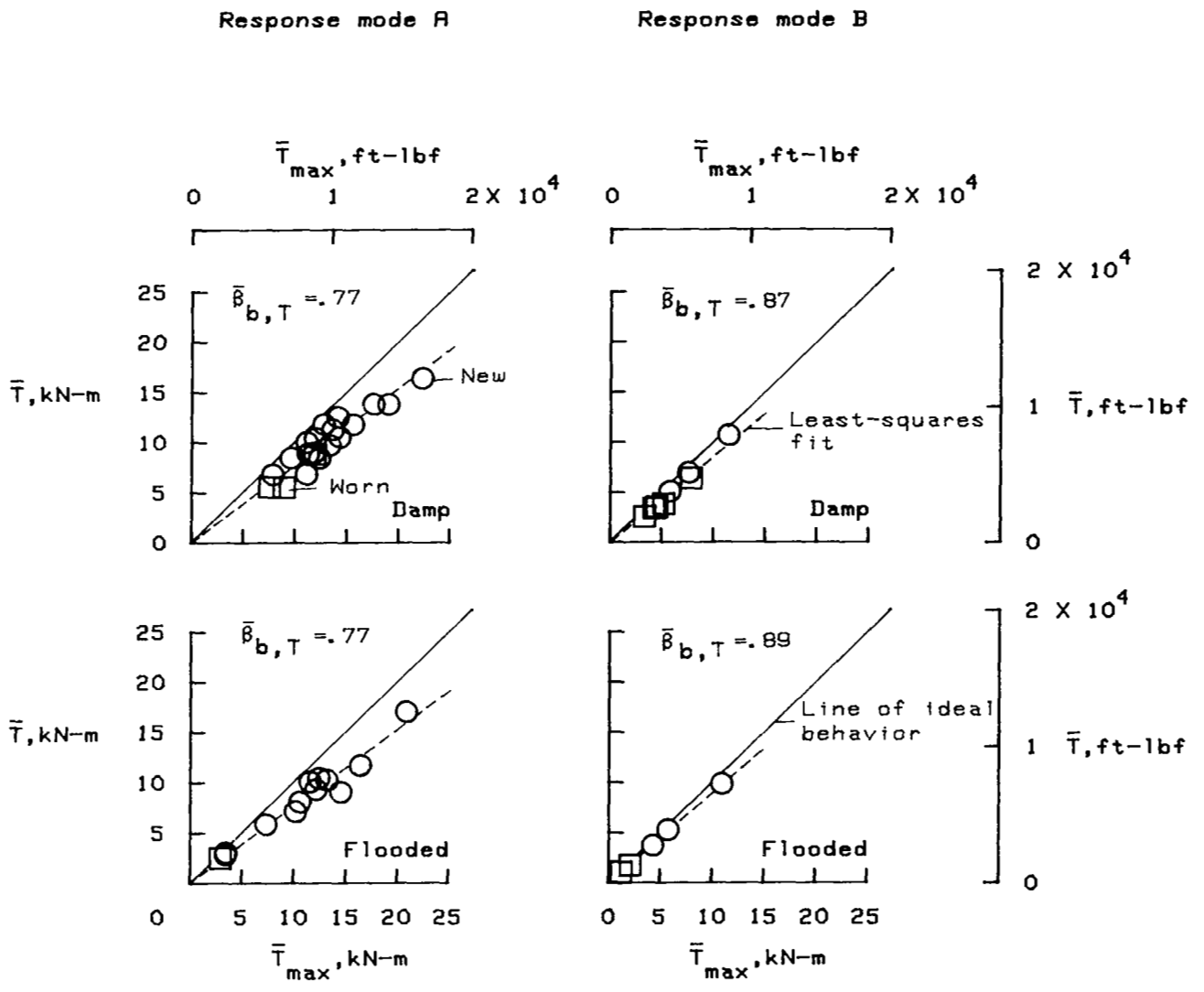

(b) Torque ratios.

Figure 27.- Continued.

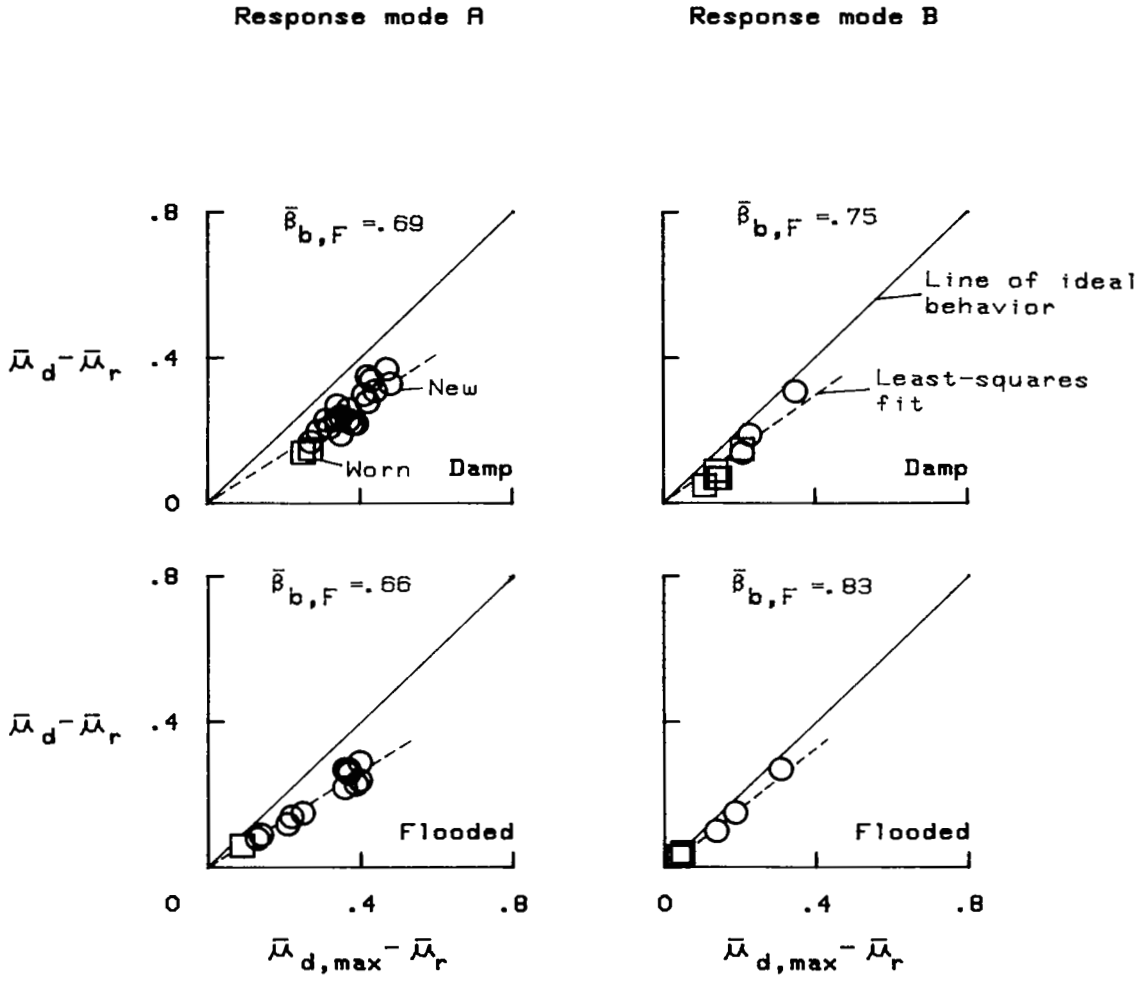

(c) Friction ratios.

Figure 27.- Concluded.

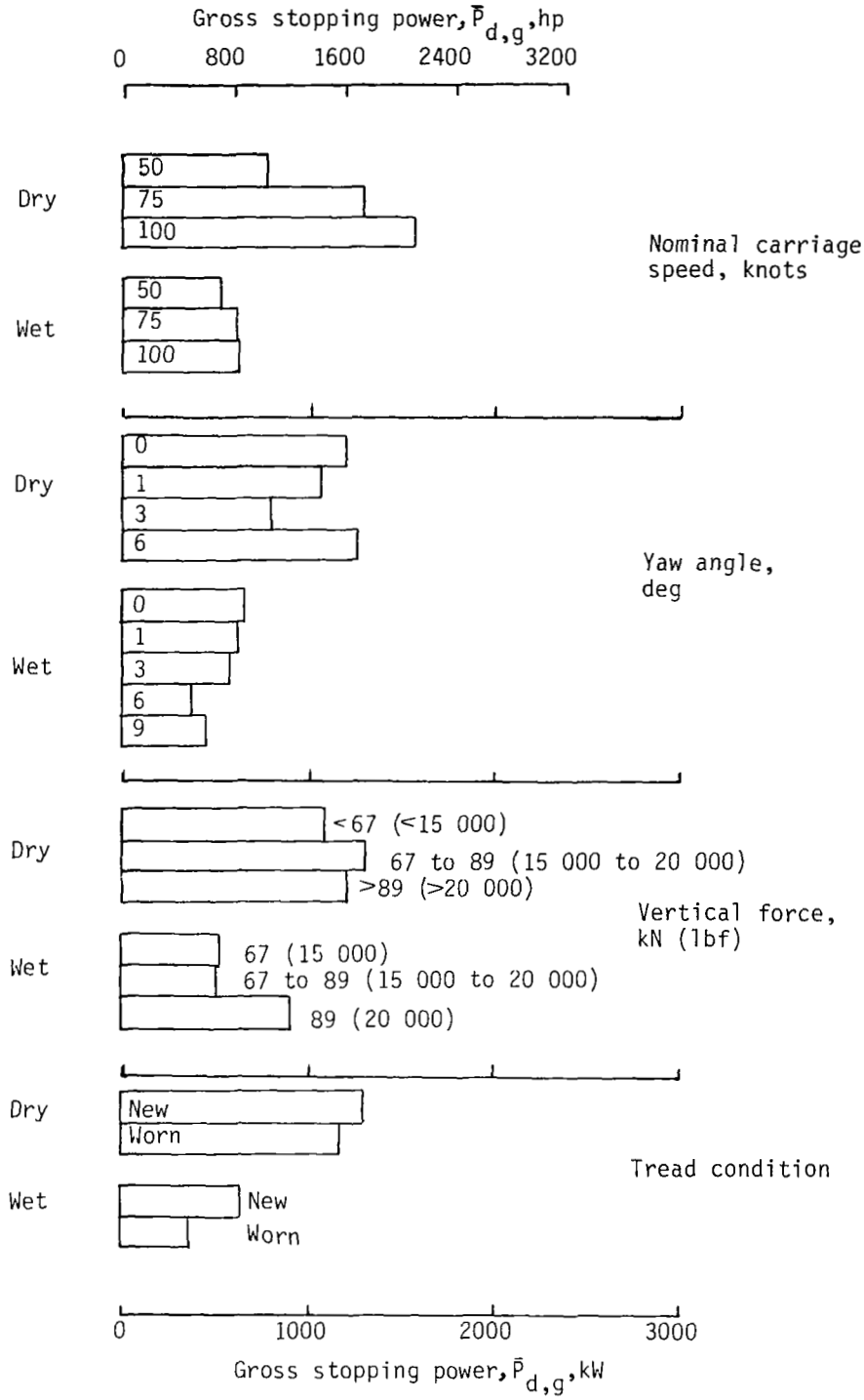

Figure 28.- Effect of test parameter variations on gross stopping power developed by antiskid braking system. Each bar graph represents average of several runs.

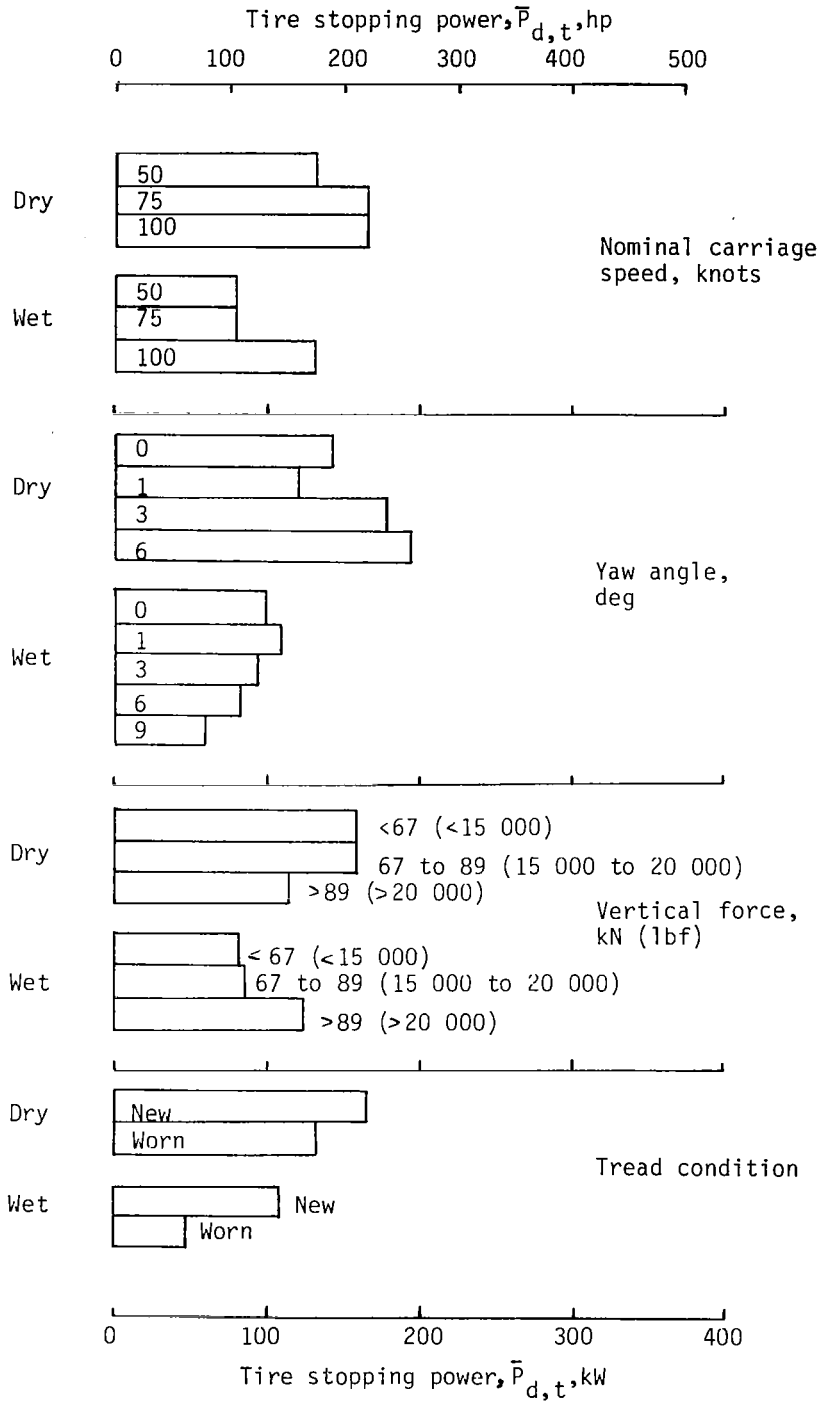

Figure 29.- Effect of test parameter variations on stopping power dissipated by tire.

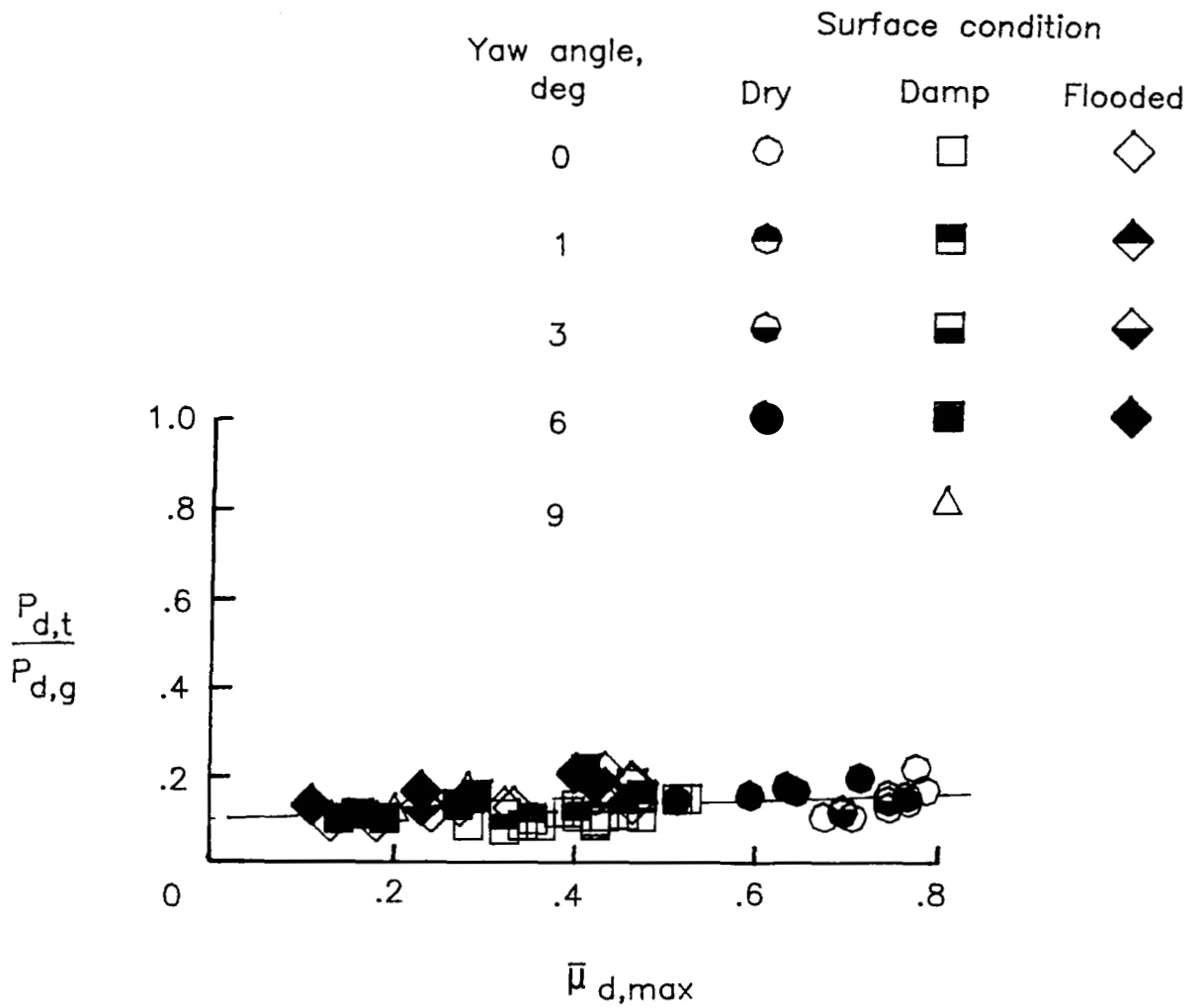

Figure 30.- Effect of maximum drag-force friction coefficient on ratio of tire stopping power to gross stopping power.

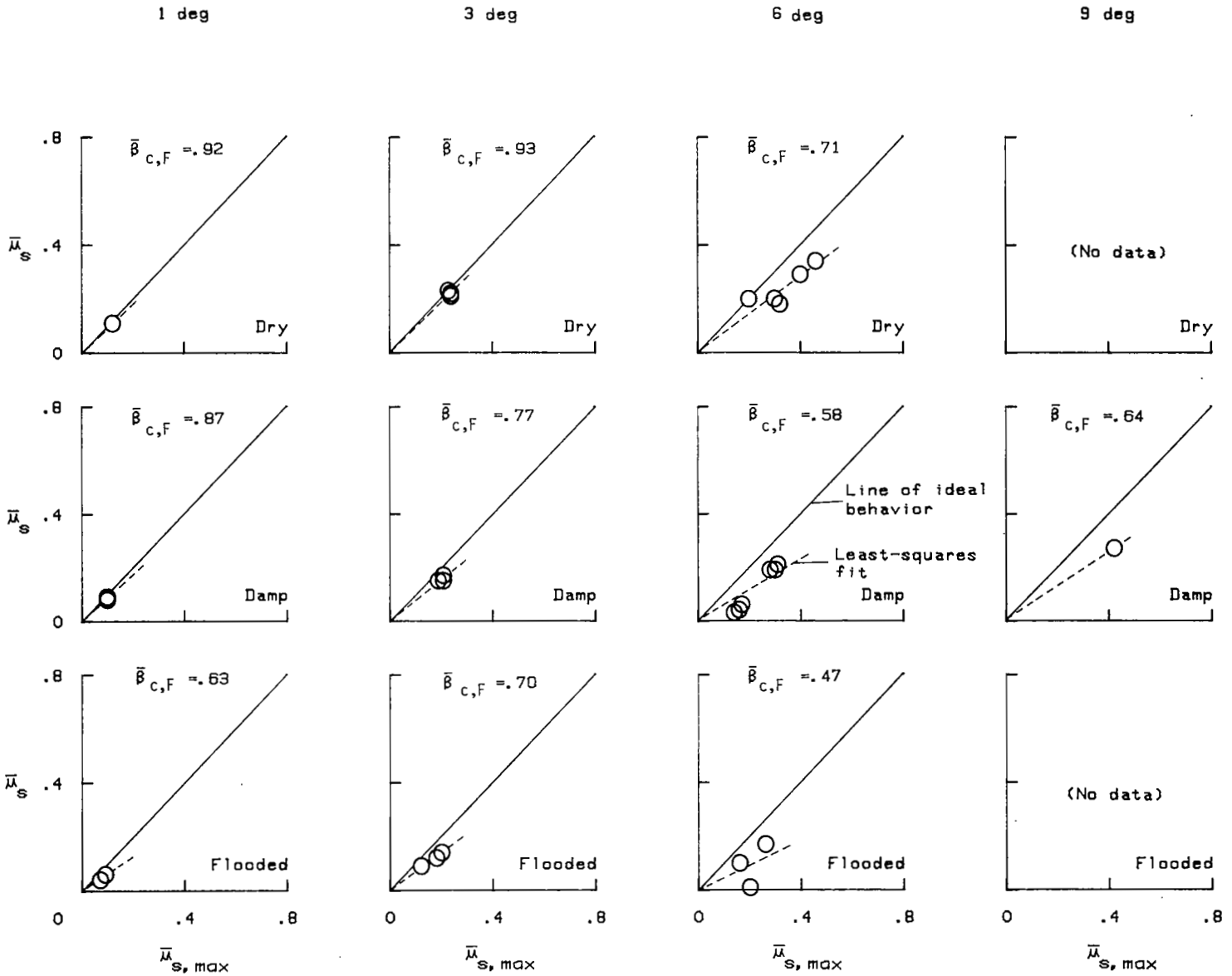

Figure 31.- Effect of yaw angle on cornering behavior index.

Error

An error occurred while processing this page. See the system log for more details.

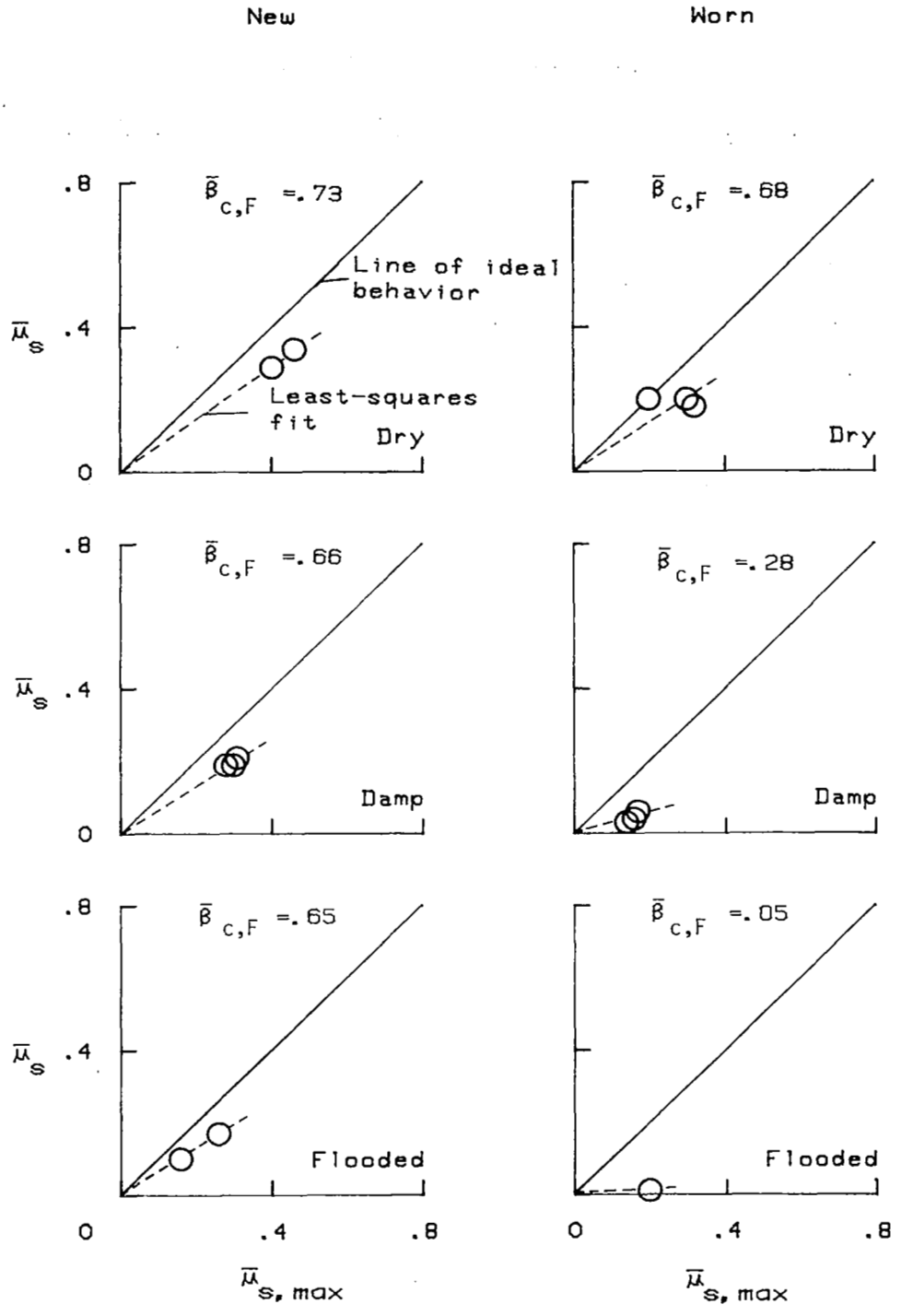

Figure 33.- Effect of tread wear on cornering behavior index. Yaw angle, 6°.

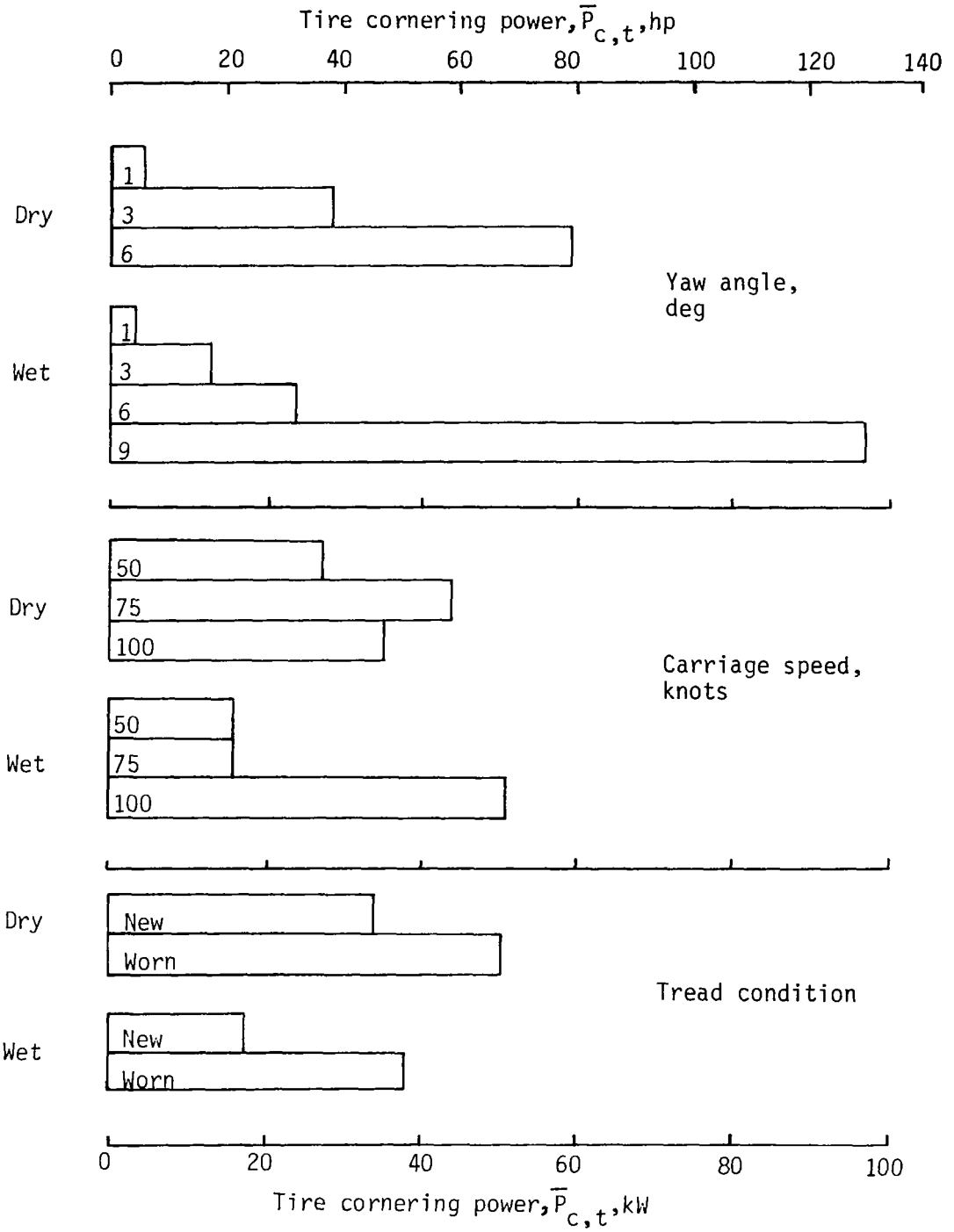

Figure 34.- Effect of test parameter variations on cornering power dissipated by tire.

APPENDIX

TIME HISTORIES

This appendix presents time histories in figures A1 to A91 of nine parameters which describe the behavior of the antiskid system during each test condition. These nine parameters, which are wheel speed, slip velocity, wheel acceleration, brake pressure, brake torque, drag-force friction coefficient, side-force friction coefficient, alining torque, and slip ratio, are given for the convenience of the user in studying detail characteristics of the antiskid system.

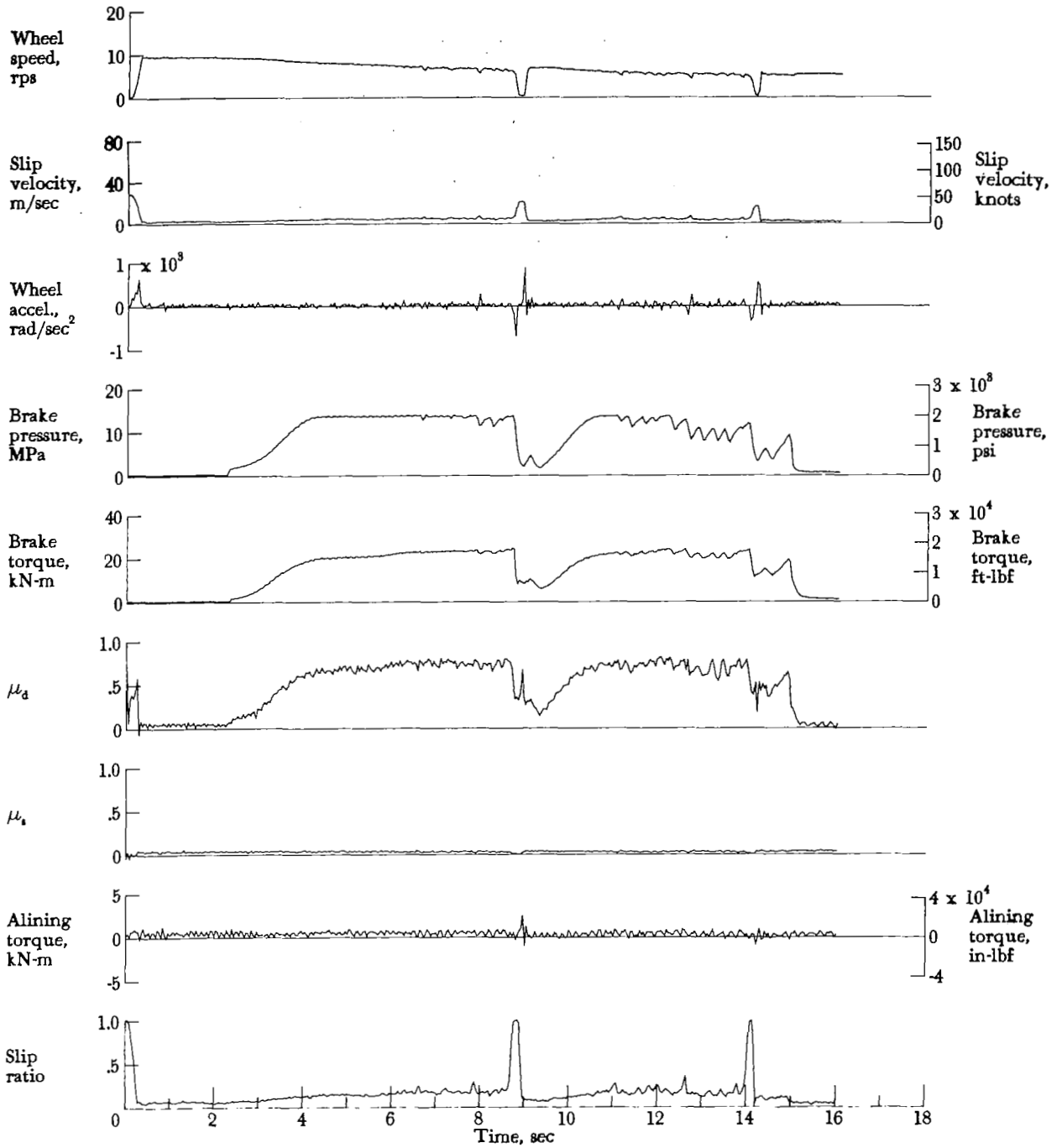

Figure A1.- Time histories for run 1. Nominal carriage speed, 39 knots; vertical load, 59.2 kN (13 300 lbf); yaw angle, 0°; brake pressure, 14 MPa (2000 psi); tire condition, new; surface condition, dry.

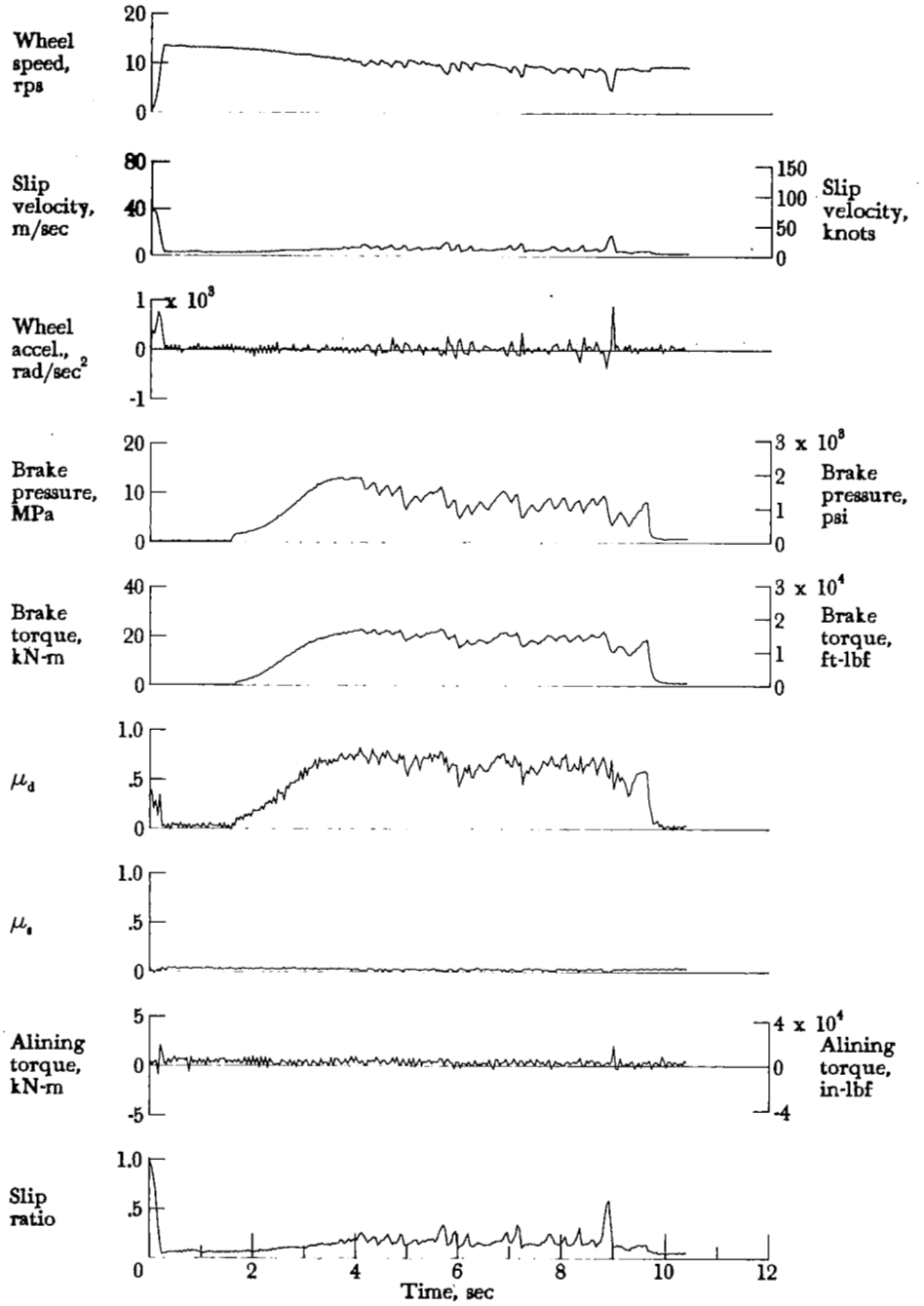

Figure A2.- Time histories for run 2. Nominal carriage speed, 64 knots; vertical load, 58.7 kN (13 200 lbf); yaw angle, 0°; brake pressure, 13 MPa (1950 psi); tire condition, new; surface condition, dry.

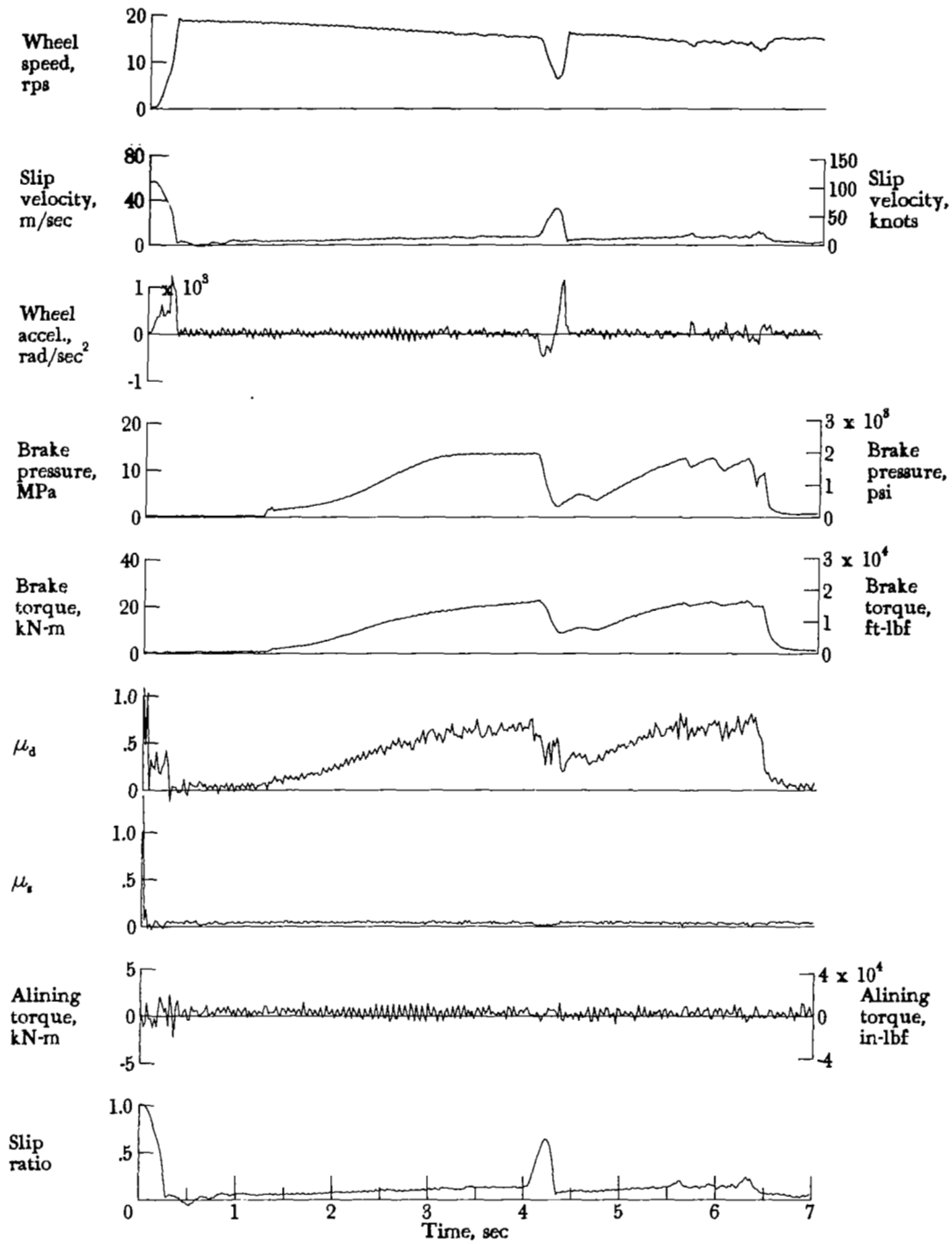

Figure A3.- Time histories for run 3. Nominal carriage speed, 99 knots; vertical load, 59.2 kN (13 300 lbf); yaw angle, 0°; brake pressure, 13 MPa (1950 psi); tire condition, new; surface condition, dry.

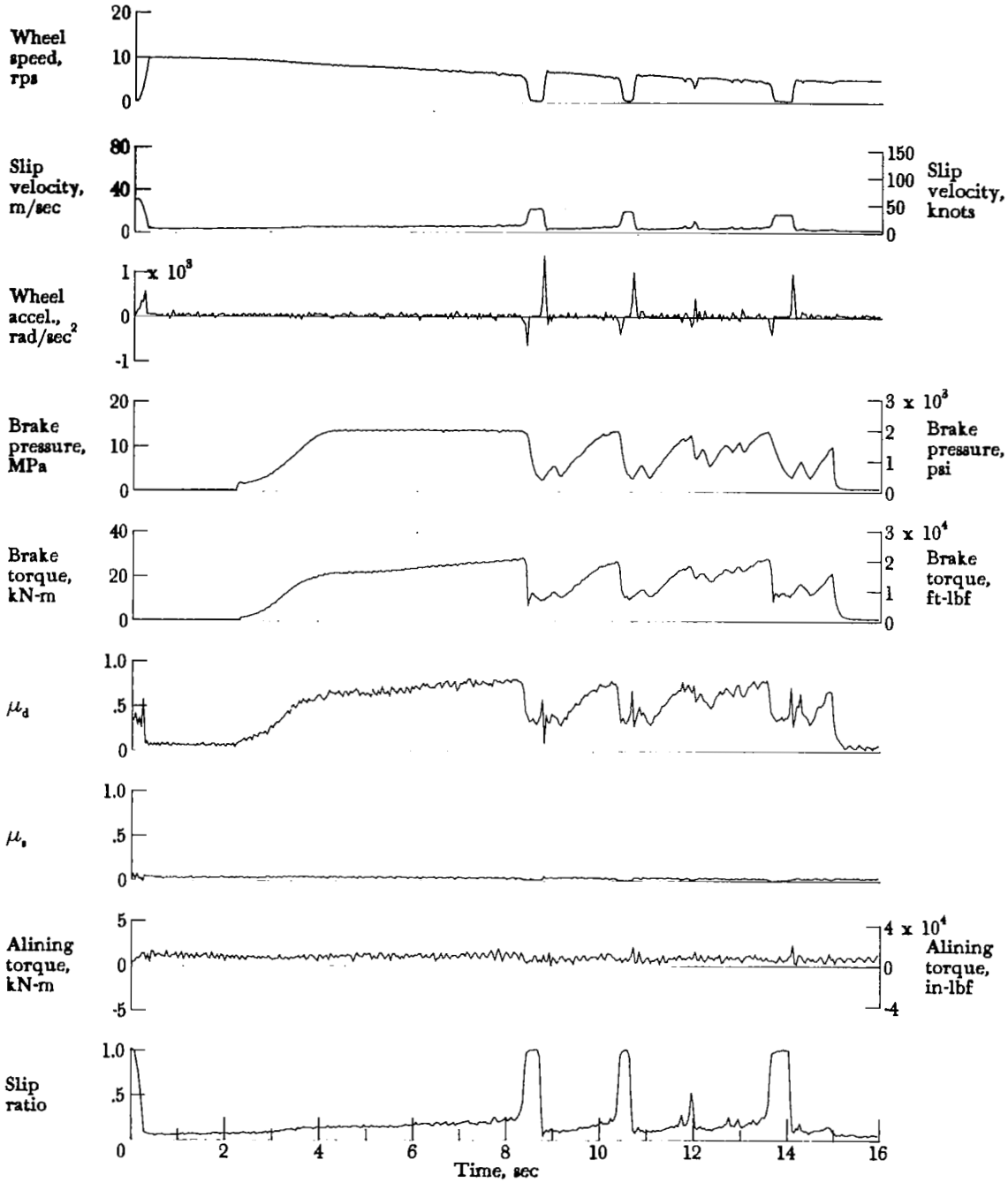

Figure A4.- Time histories for run 4. Nominal carriage speed, 39 knots; vertical load, 69.8 kN (15 700 lbf); yaw angle, 0°; brake pressure, 14 MPa (2000 psi); tire condition, new; surface condition, dry.

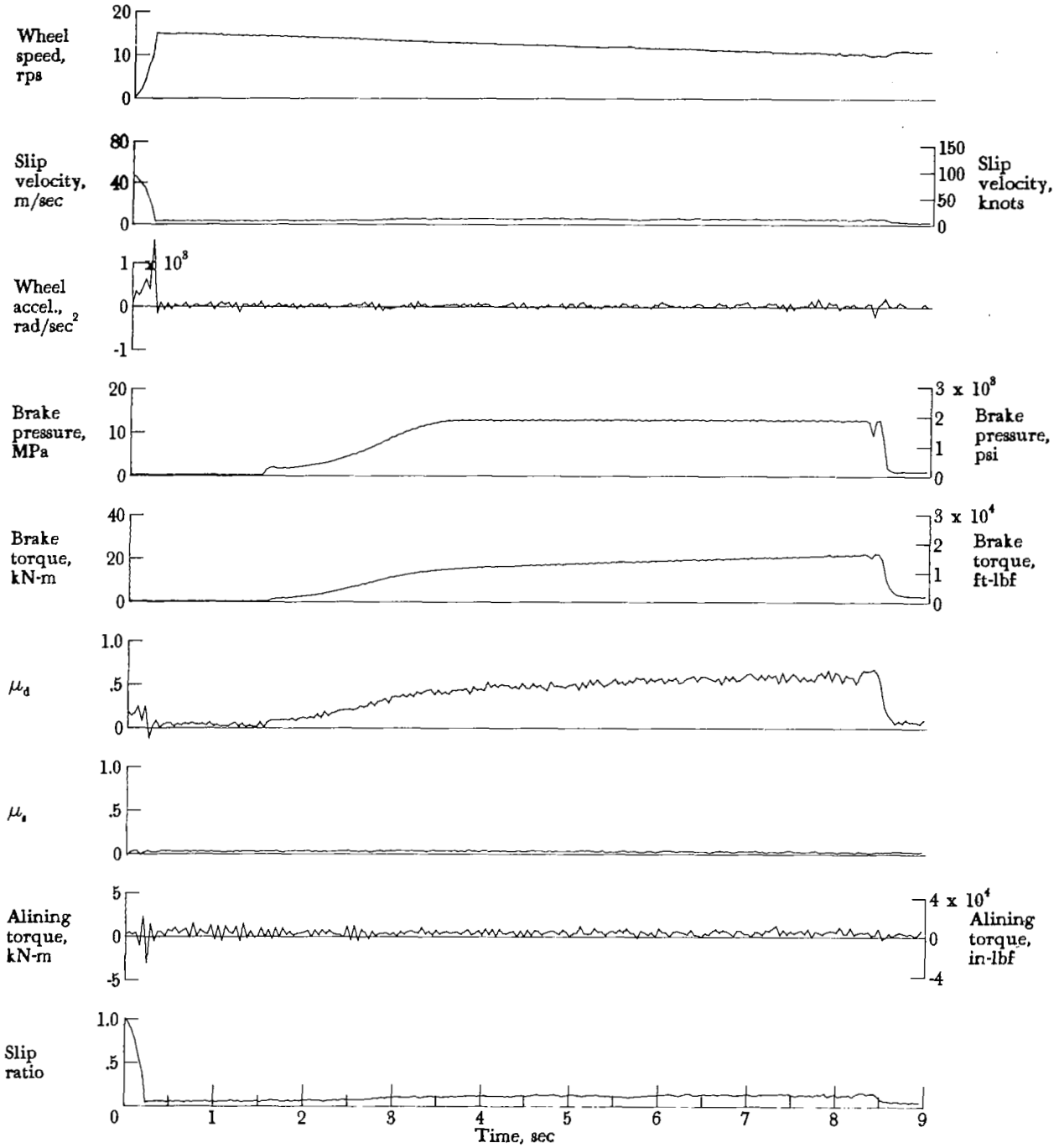

Figure A5.- Time histories for run 5. Nominal carriage speed, 73 knots; vertical load, 70.7 kN (15 900 lbf); yaw angle, 0°; brake pressure, 13 MPa (1850 psi); tire condition, new; surface condition, dry.

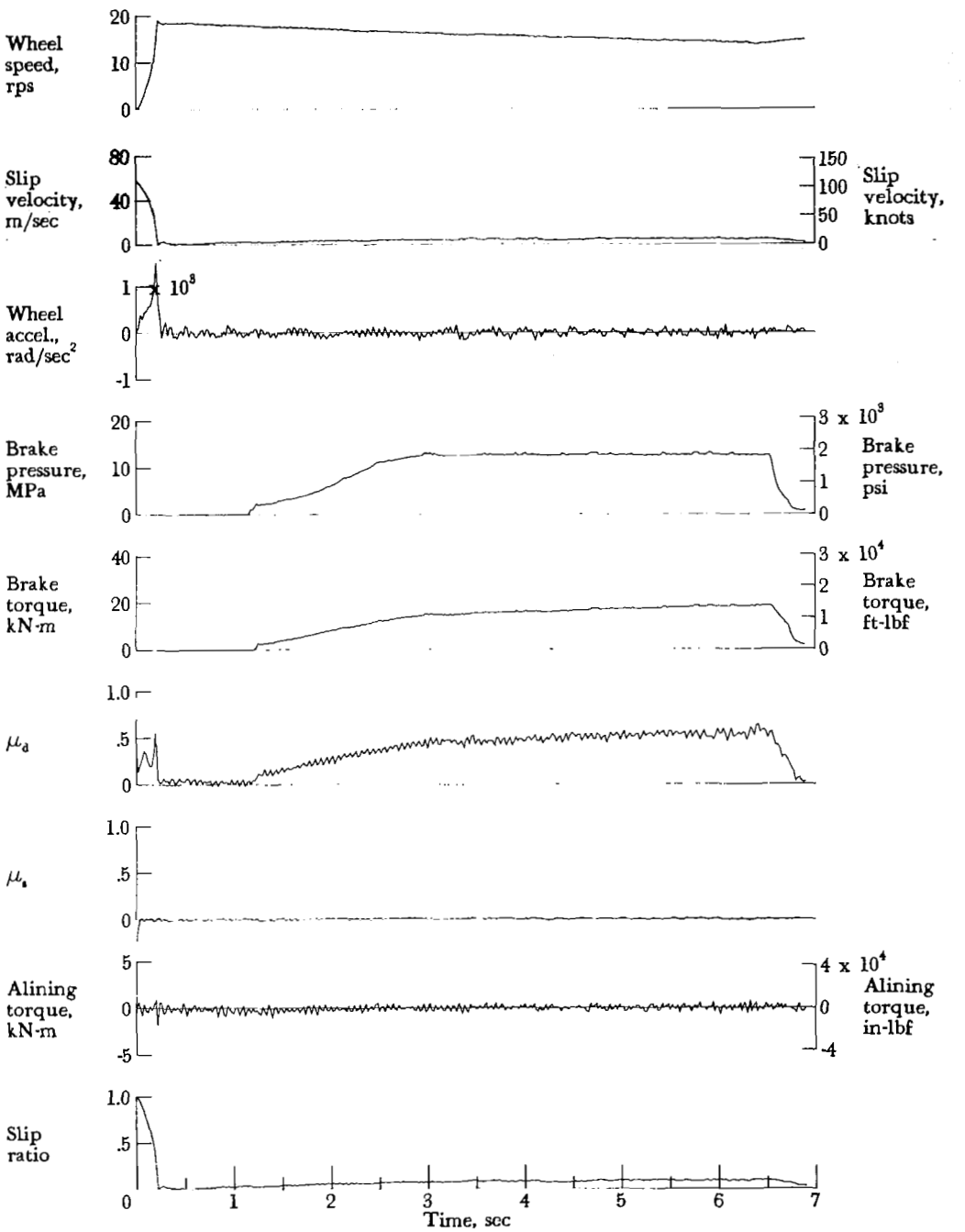

Figure A6.- Time histories for run 6. Nominal carriage speed, 98 knots; vertical load, 69.3 kN (15 600 lbf); yaw angle, 0°; brake pressure, 13 MPa (1900 psi); tire condition, new; surface condition, dry.

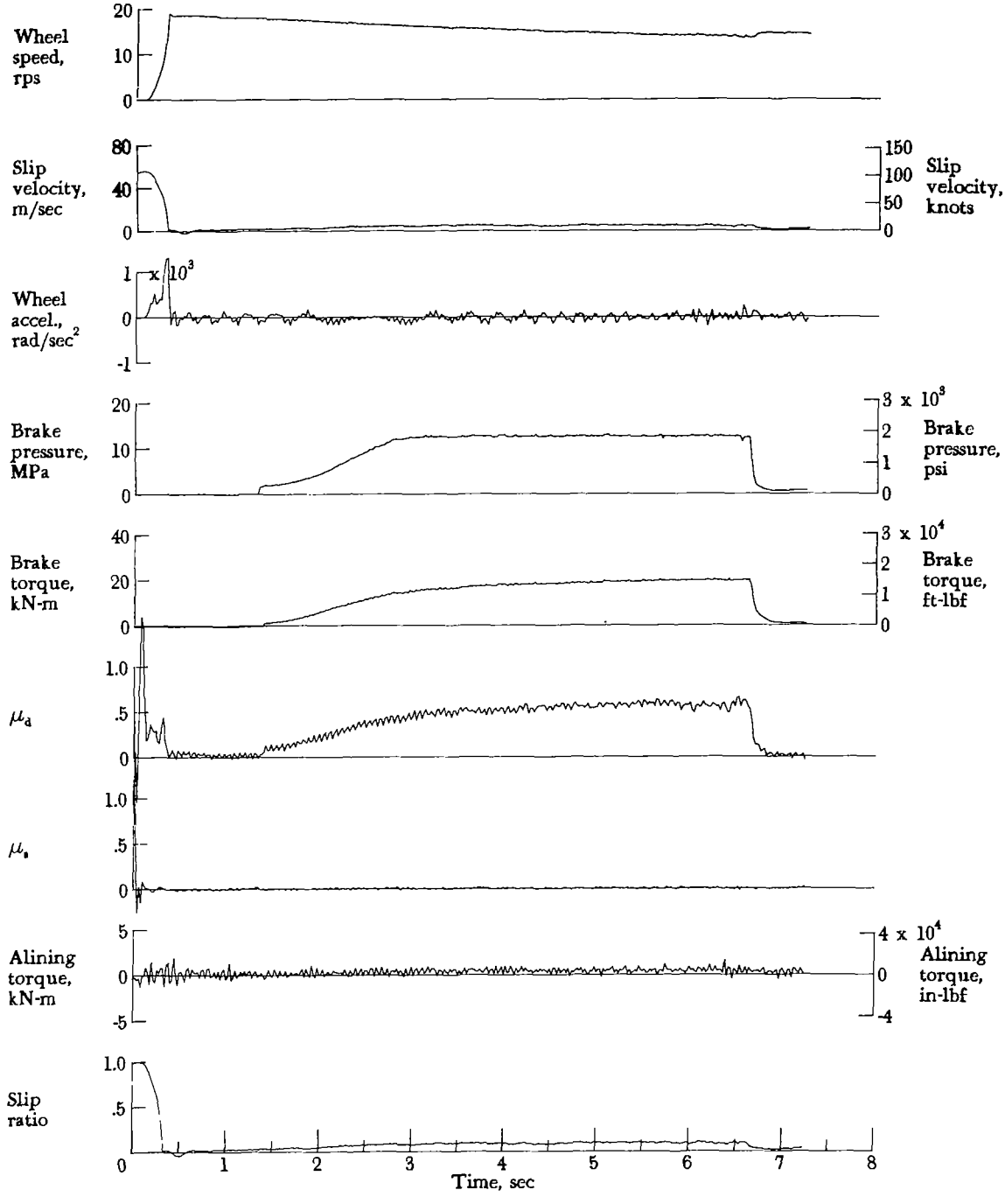

Figure A7.- Time histories for run 7. Nominal carriage speed, 97 knots; vertical load, 70.7 kN (15 900 lbf); yaw angle, 0°; brake pressure, 13 MPa (1900 psi); tire condition, new; surface condition, dry.

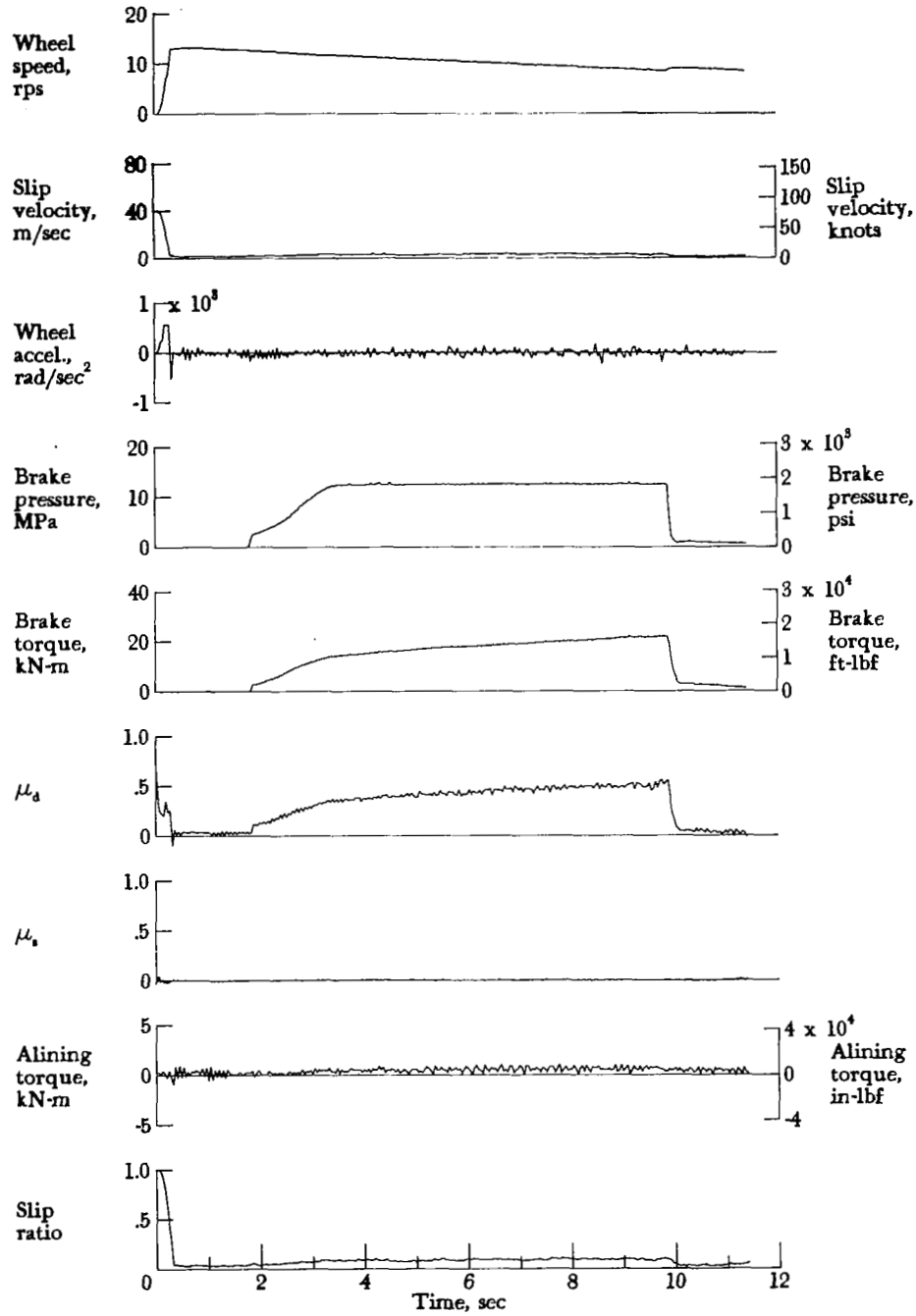

Figure A8.- Time histories for run 8. Nominal carriage speed, 61 knots; vertical load, 93.0 kN (20 900 lbf); yaw angle, 0°; brake pressure, 13 MPa (1850 psi); tire condition, new; surface condition, dry.

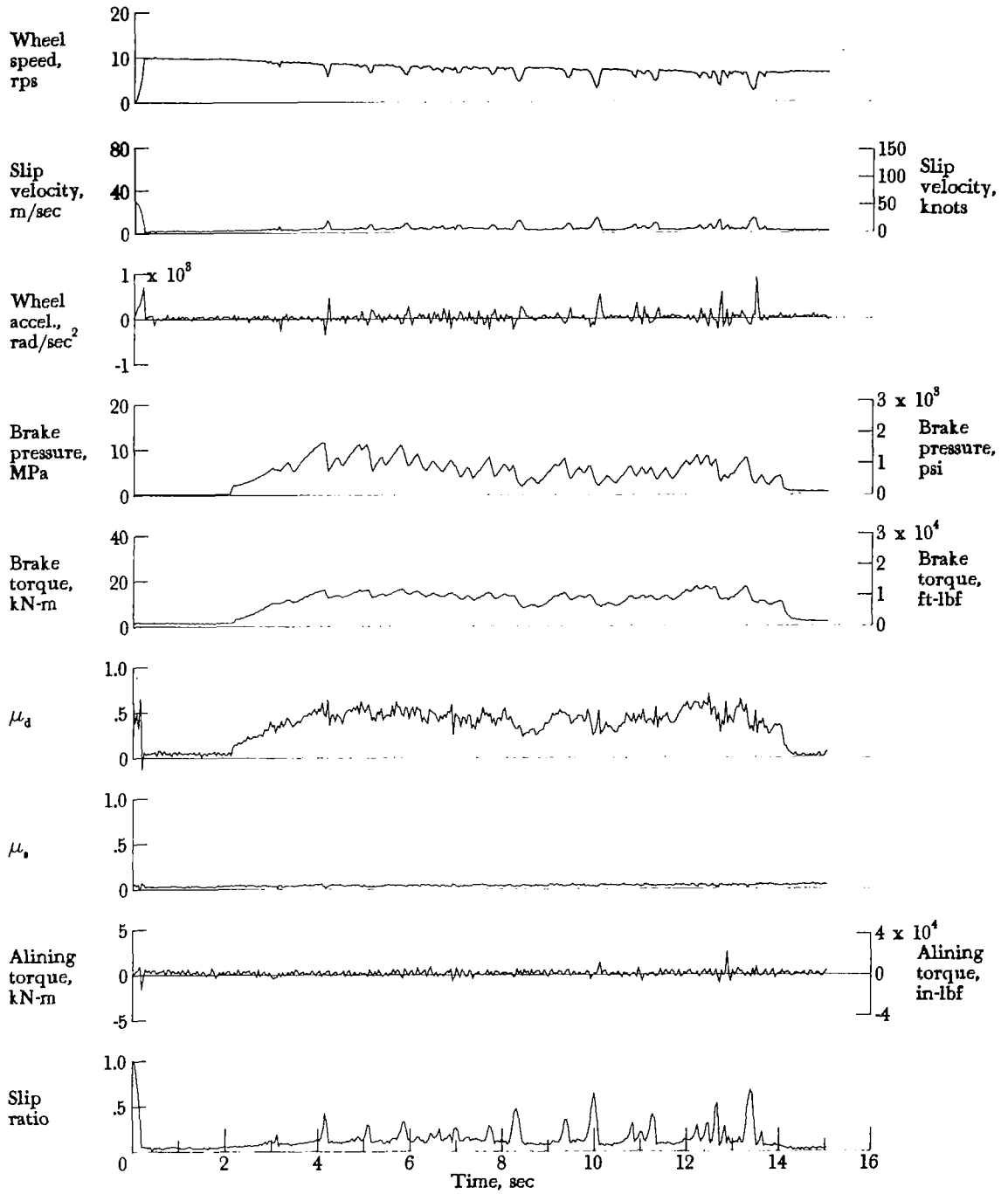

Figure A9.- Time histories for run 9. Nominal carriage speed, 43 knots; vertical load, 56.5 kN (12 700 lbf); yaw angle, 0°; brake pressure, 13 MPa (1850 psi); tire condition, new; surface condition, damp.

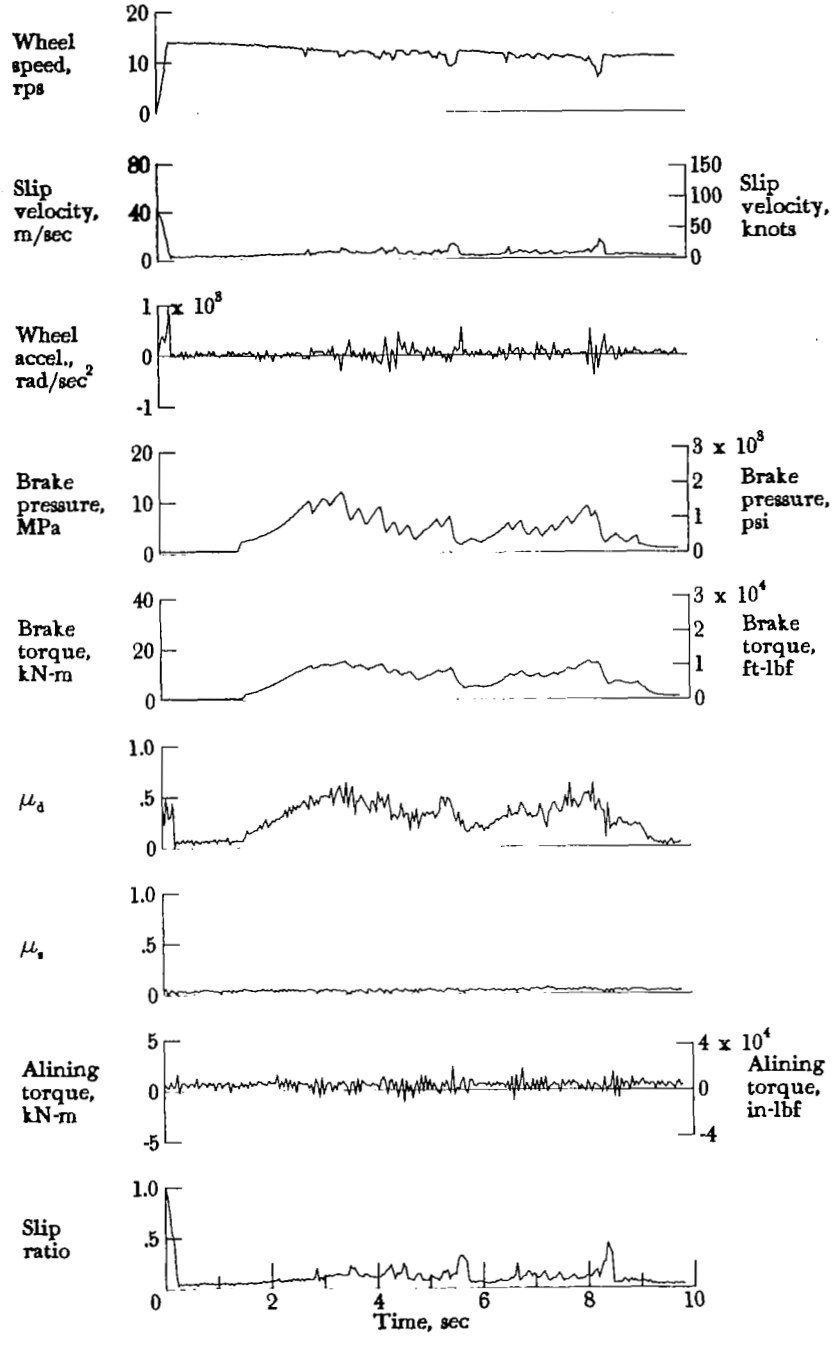

Figure A10.- Time histories for run 10. Nominal carriage speed, 69 knots; vertical load, 56.9 kN (12 800 lbf); yaw angle, 0°; brake pressure, 13 MPa (1950 psi); tire condition, new; surface condition, damp.

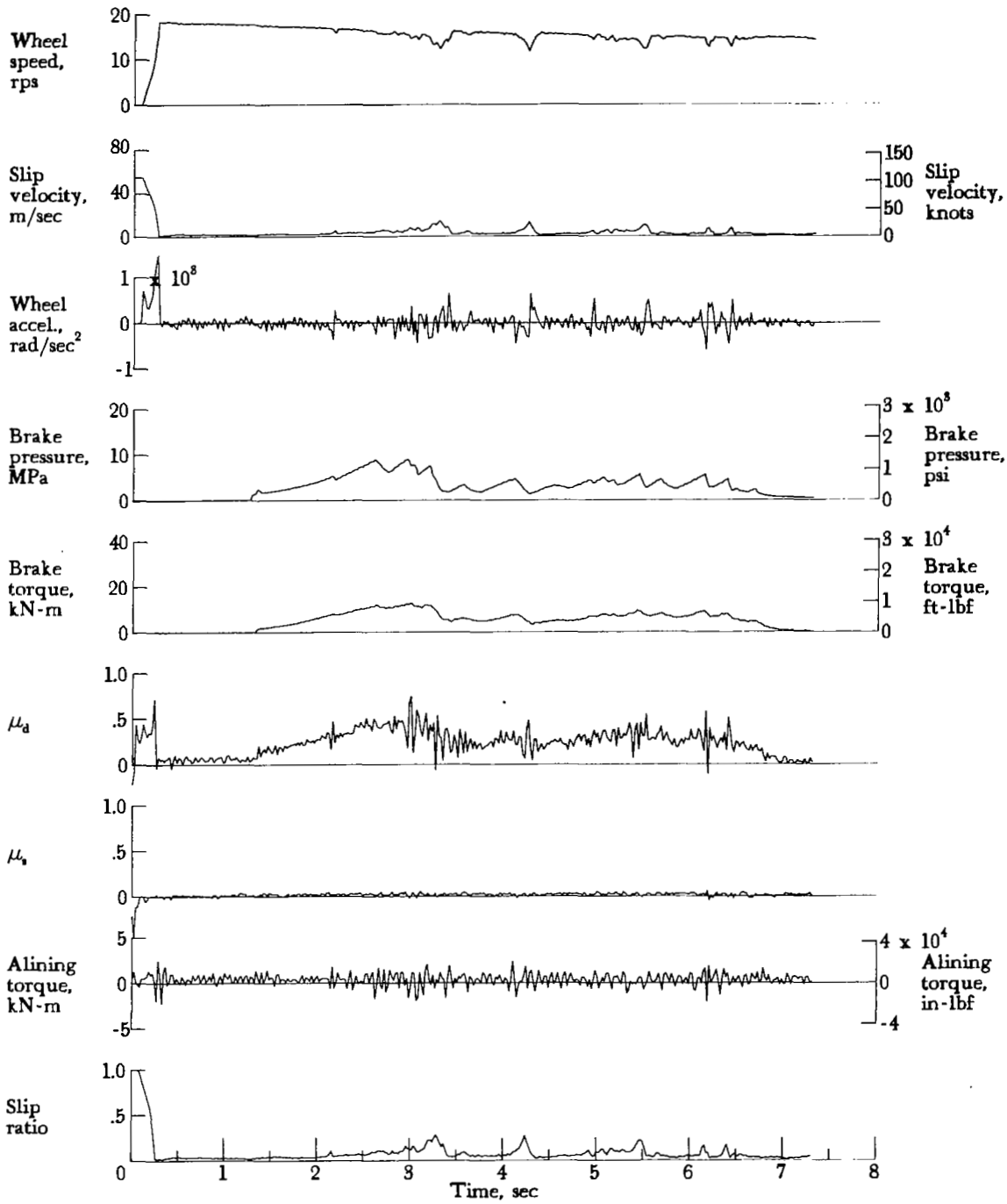

Figure A11.- Time histories for run 11. Nominal carriage speed, 95 knots; vertical load, 57.4 kN (12 900 lbf); yaw angle, 0°; brake pressure, 13 MPa (1950 psi); tire condition, new; surface condition, damp.

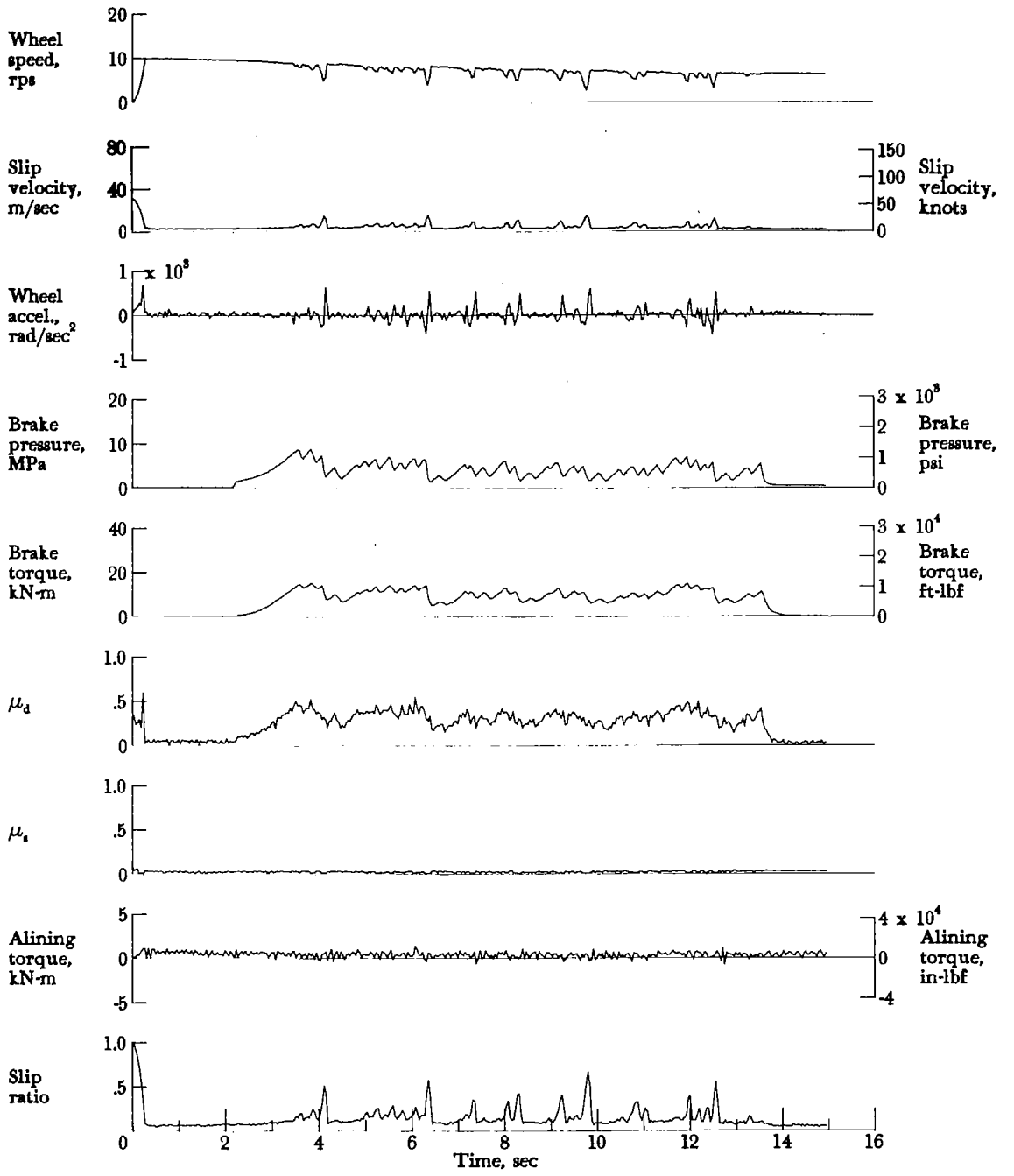

Figure A12.- Time histories for run 12. Nominal carriage speed, 44 knots; vertical load, 69.8 kN (15 700 lbf); yaw angle, 0°; brake pressure, 13 MPa (1850 psi); tire condition, new; surface condition, damp.

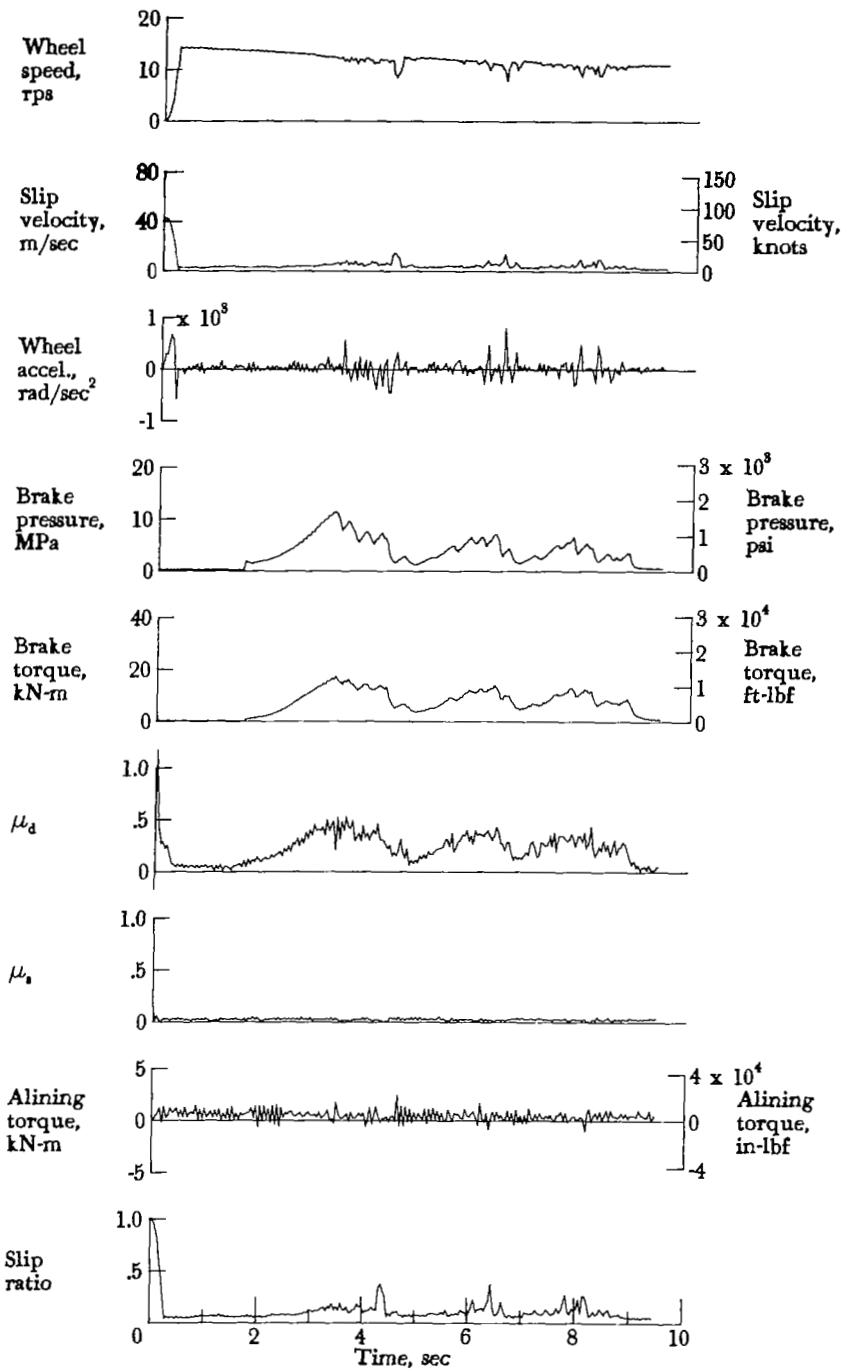

Figure A13.- Time histories for run 13. Nominal carriage speed, 71 knots; vertical load, 70.3 kN (15 800 lbf); yaw angle, 0°; brake pressure, 14 MPa (2000 psi); tire condition, new; surface condition, damp.

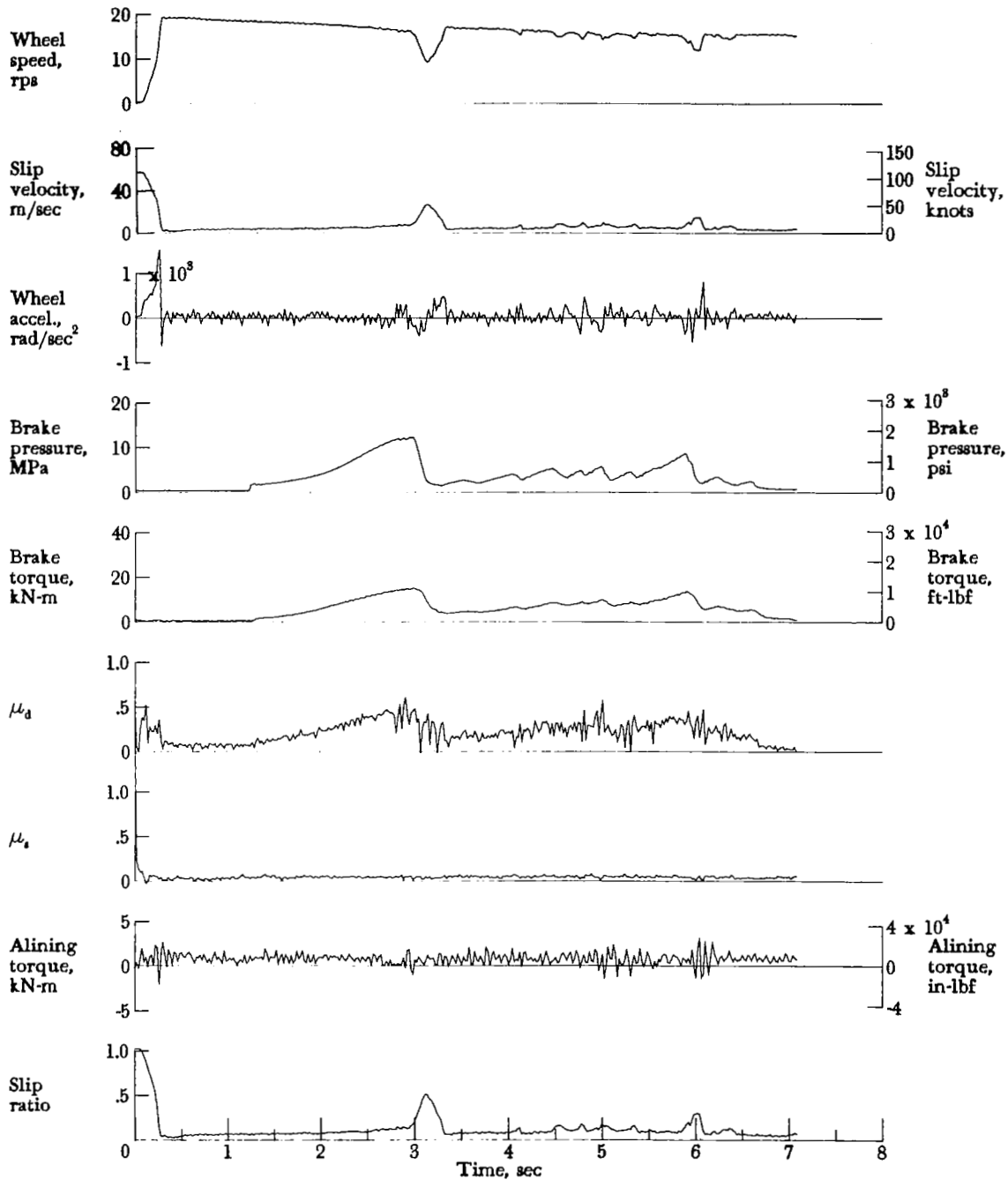

Figure A14.- Time histories for run 14. Nominal carriage speed, 98 knots; vertical load, 69.8 kN (15 700 lbf); yaw angle, 0°; brake pressure, 13 MPa (1950 psi); tire condition, new; surface condition, damp.

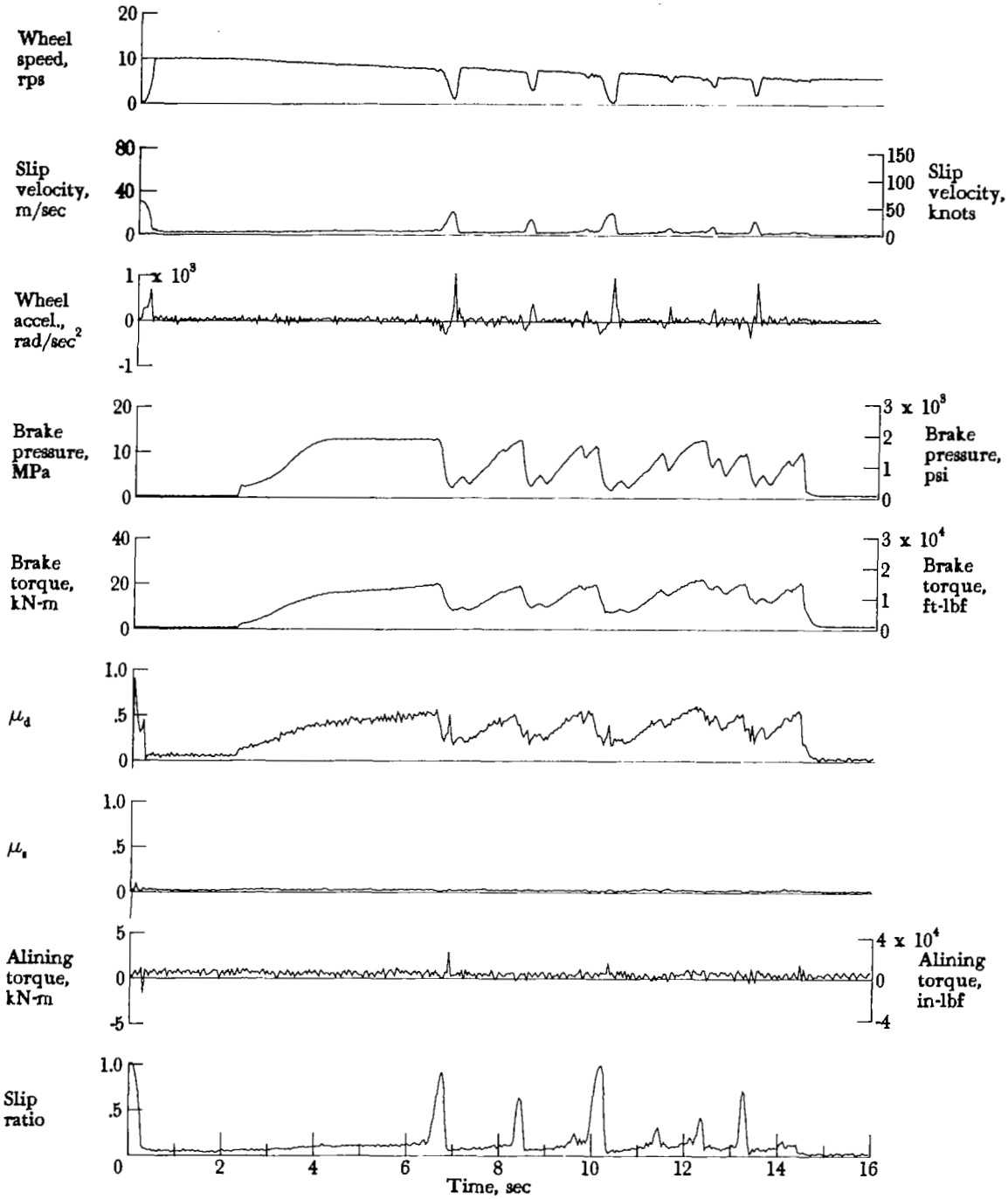

Figure A15.- Time histories for run 15. Nominal carriage speed, 41 knots; vertical load, 86.7 kN (19 500 lbf); yaw angle, 0°; brake pressure, 13 MPa (1850 psi); tire condition, new; surface condition, damp.

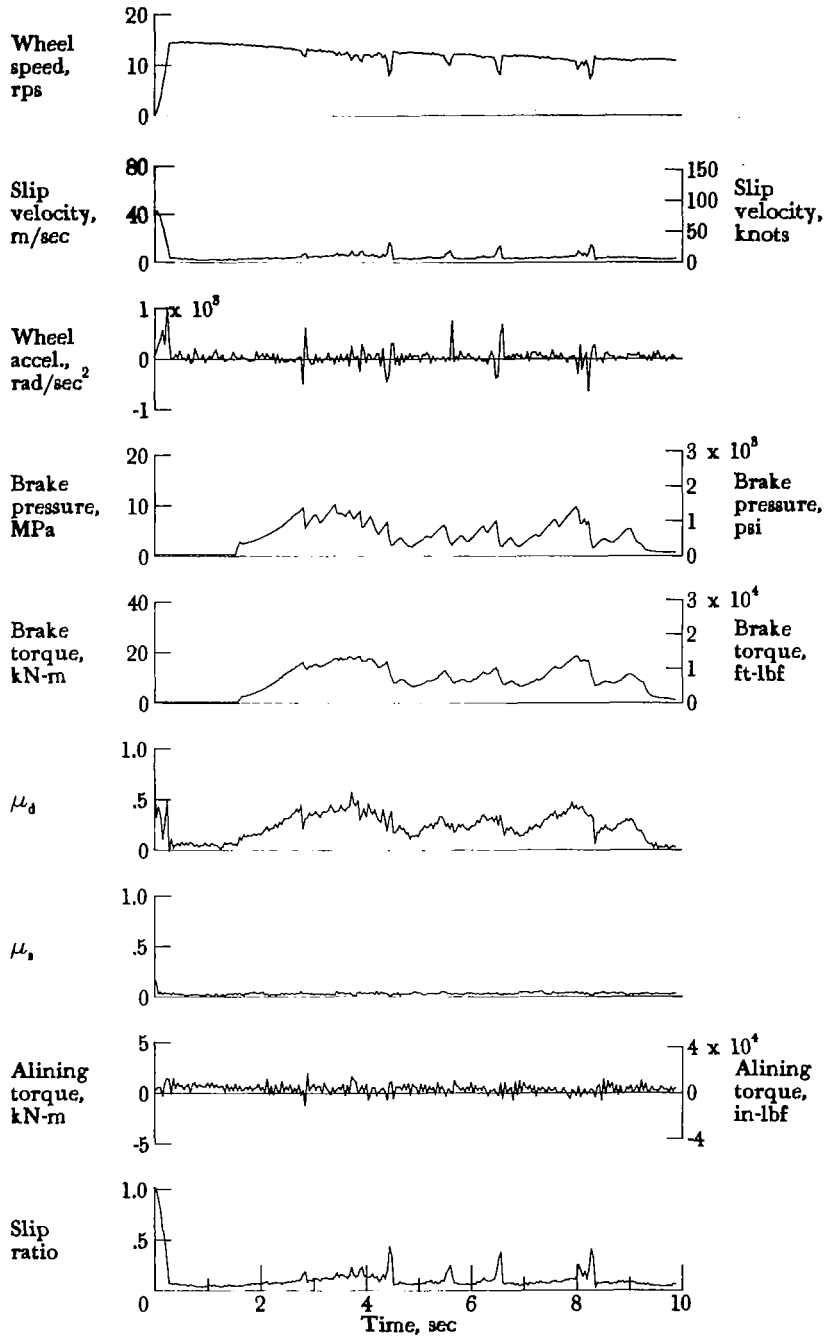

Figure A16.- Time histories for run 16. Nominal carriage speed, 70 knots; vertical load, 89.8 kN (20 200 lbf); yaw angle, 0°; brake pressure, 13 MPa (1900 psi); tire condition, new; surface condition, damp.

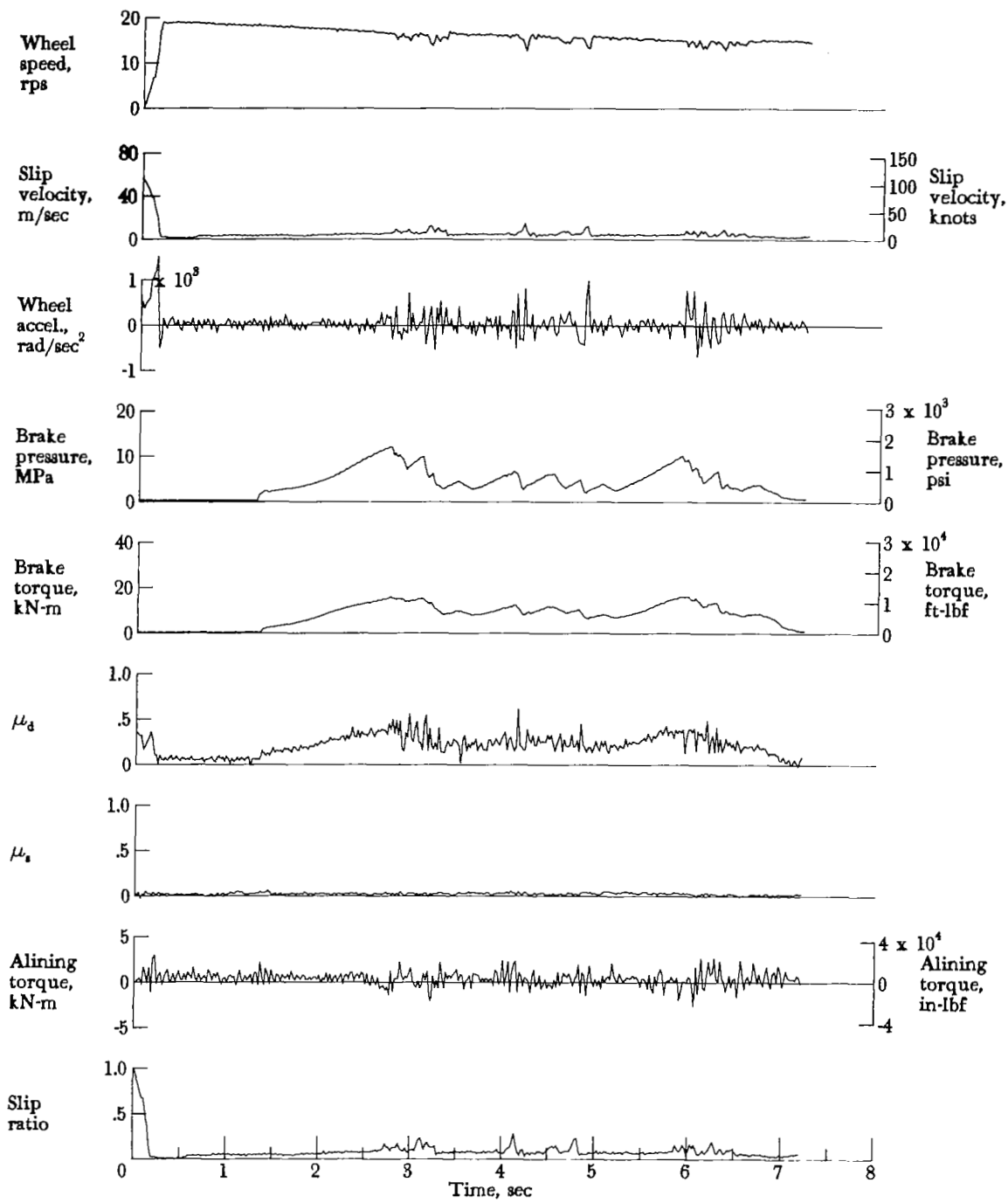

Figure A17.- Time histories for run 17. Nominal carriage speed, 96 knots; vertical load, 90.3 kN (20 300 lbf); yaw angle, 0°; brake pressure, 13 MPa (1950 psi); tire condition, new; surface condition, damp.

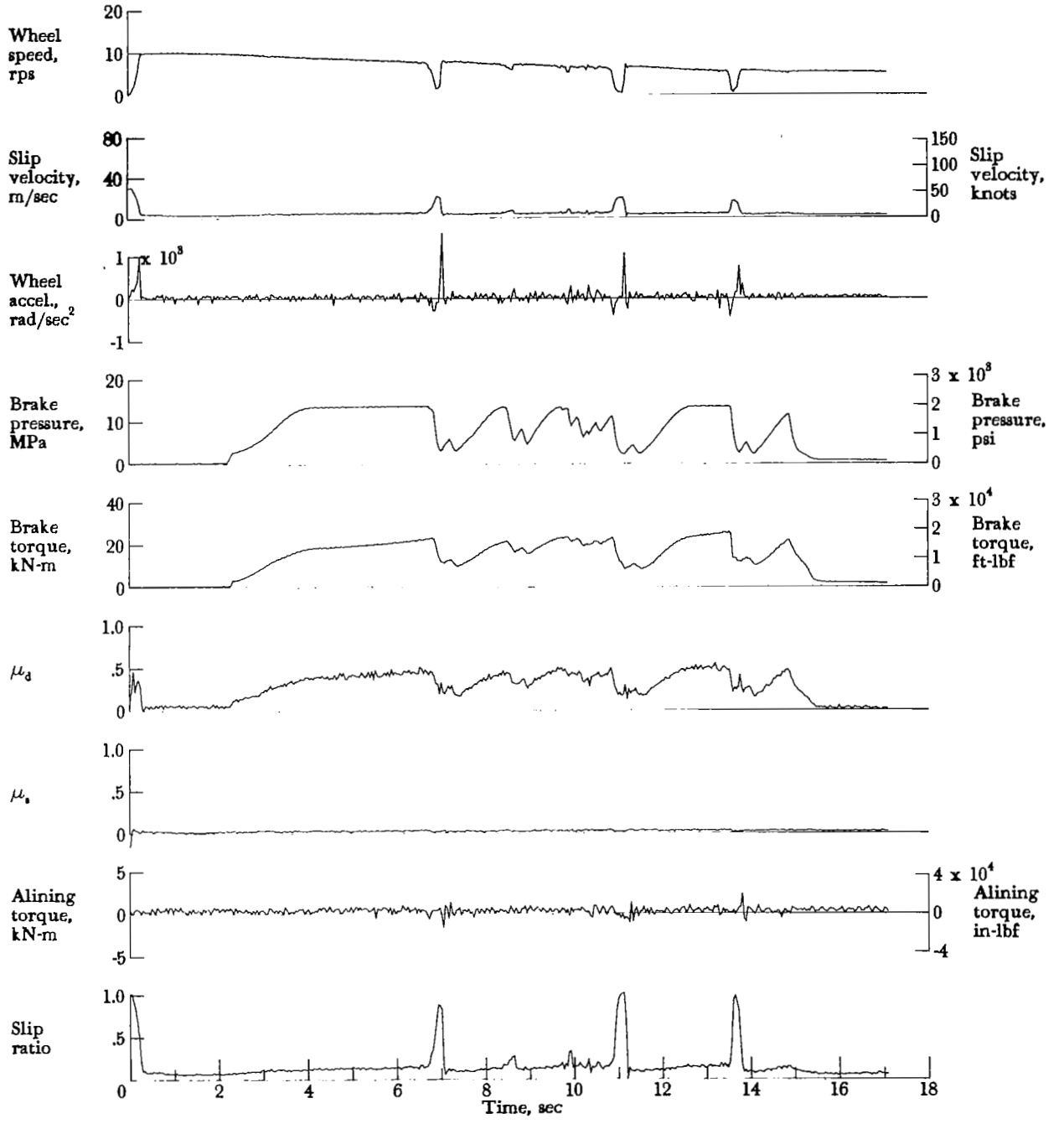

Figure A18.- Time histories for run 18. Nominal carriage speed, 39 knots; vertical load, 111.2 kN (25 000 lbf); yaw angle, 0°; brake pressure, 13 MPa (1950 psi); tire condition, new; surface condition, damp.

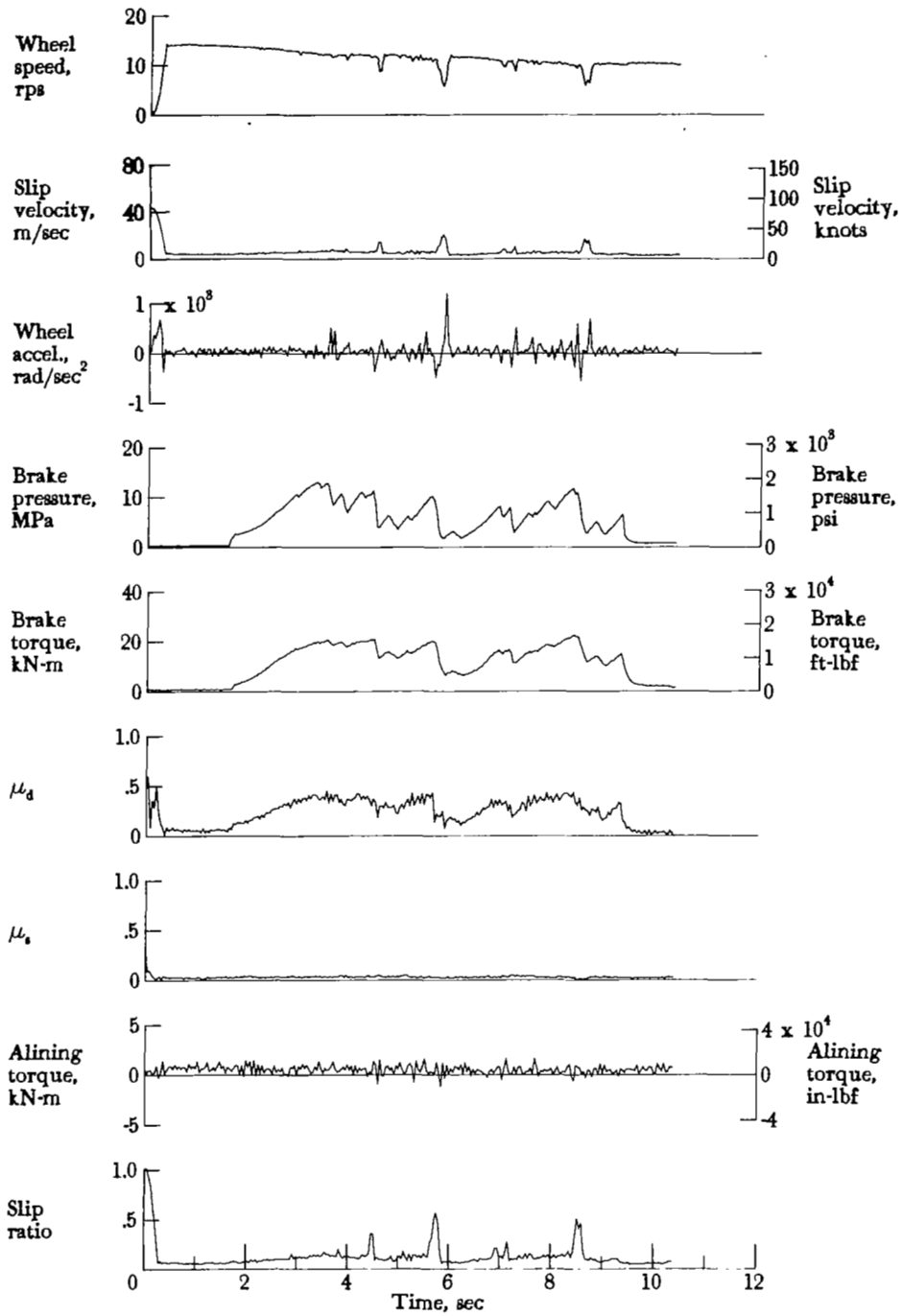

Figure A19.- Time histories for run 19. Nominal carriage speed, 66 knots; vertical load, 115.6 kN (26 000 lbf); yaw angle, 0°; brake pressure, 13 MPa (1950 psi); tire condition, new; surface condition, damp.

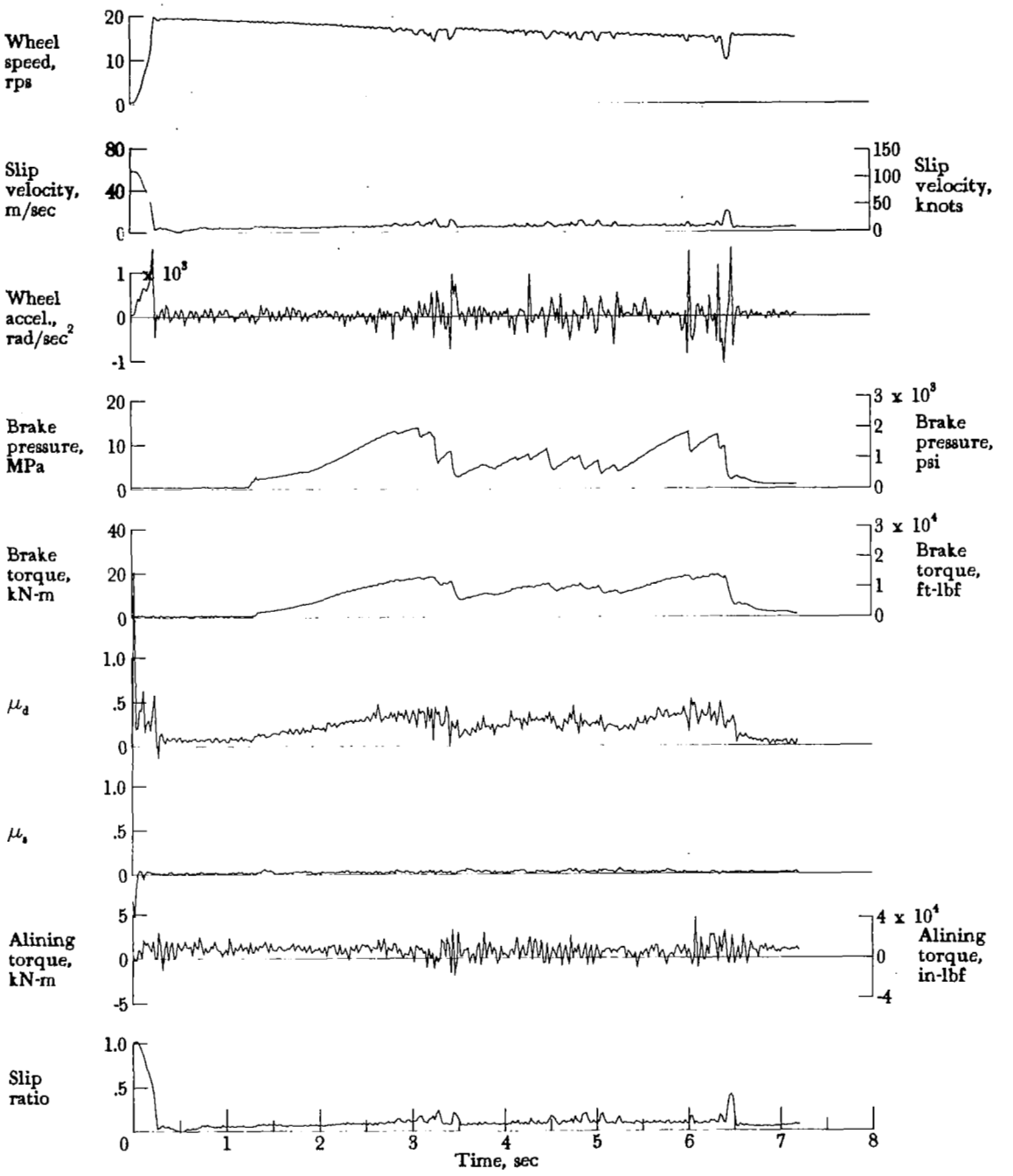

Figure A20.- Time histories for run 20. Nominal carriage speed, 96 knots; vertical load, 115.2 kN (25 900 lbf); yaw angle, 0°; brake pressure, 14 MPa (2000 psi); tire condition, new; surface condition, damp.

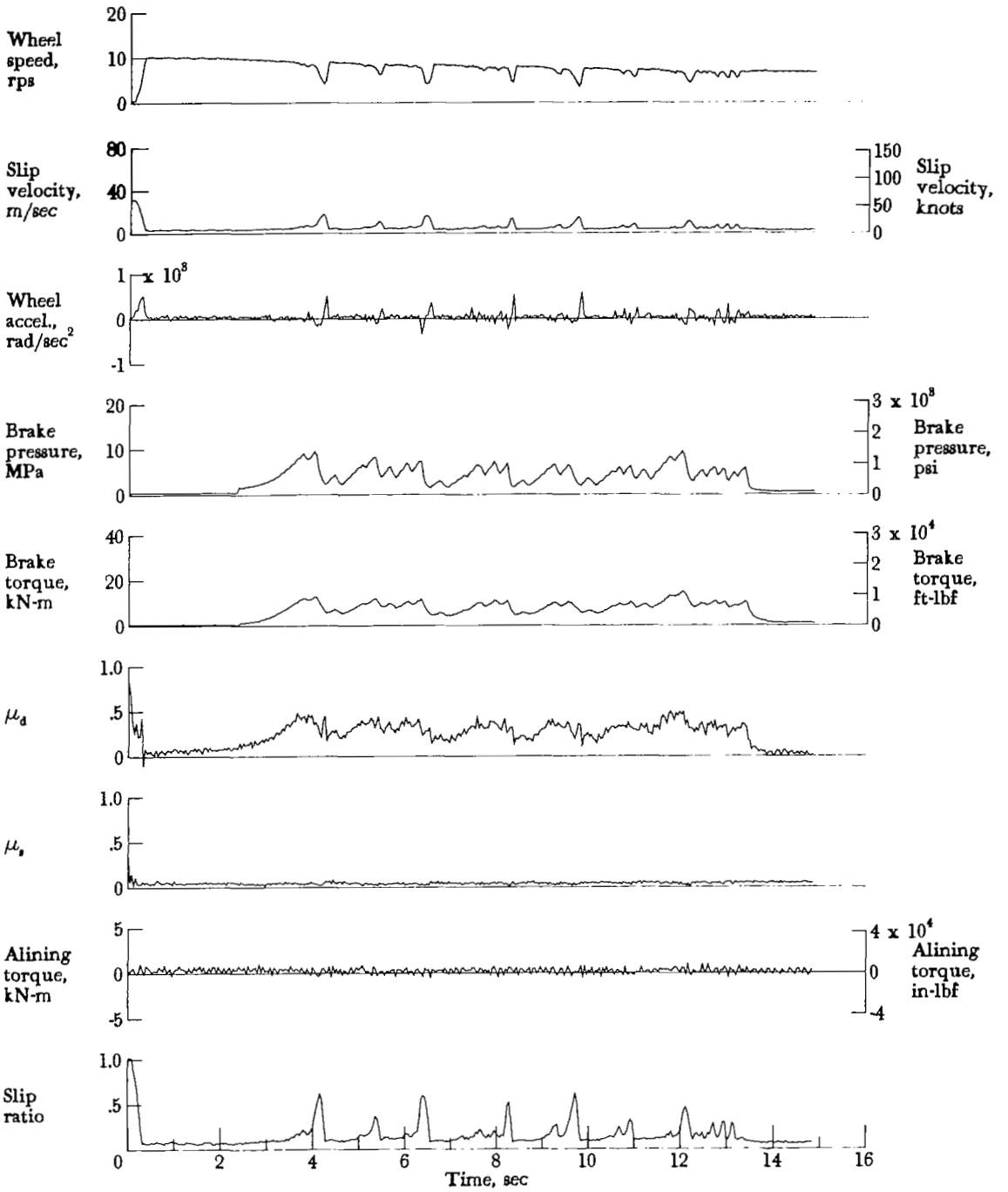

Figure A21.- Time histories for run 21. Nominal carriage speed, 46 knots; vertical load, 56.5 kN (12 700 lbf); yaw angle, 0°; brake pressure, 13 MPa (1900 psi); tire condition, new; surface condition, flooded.

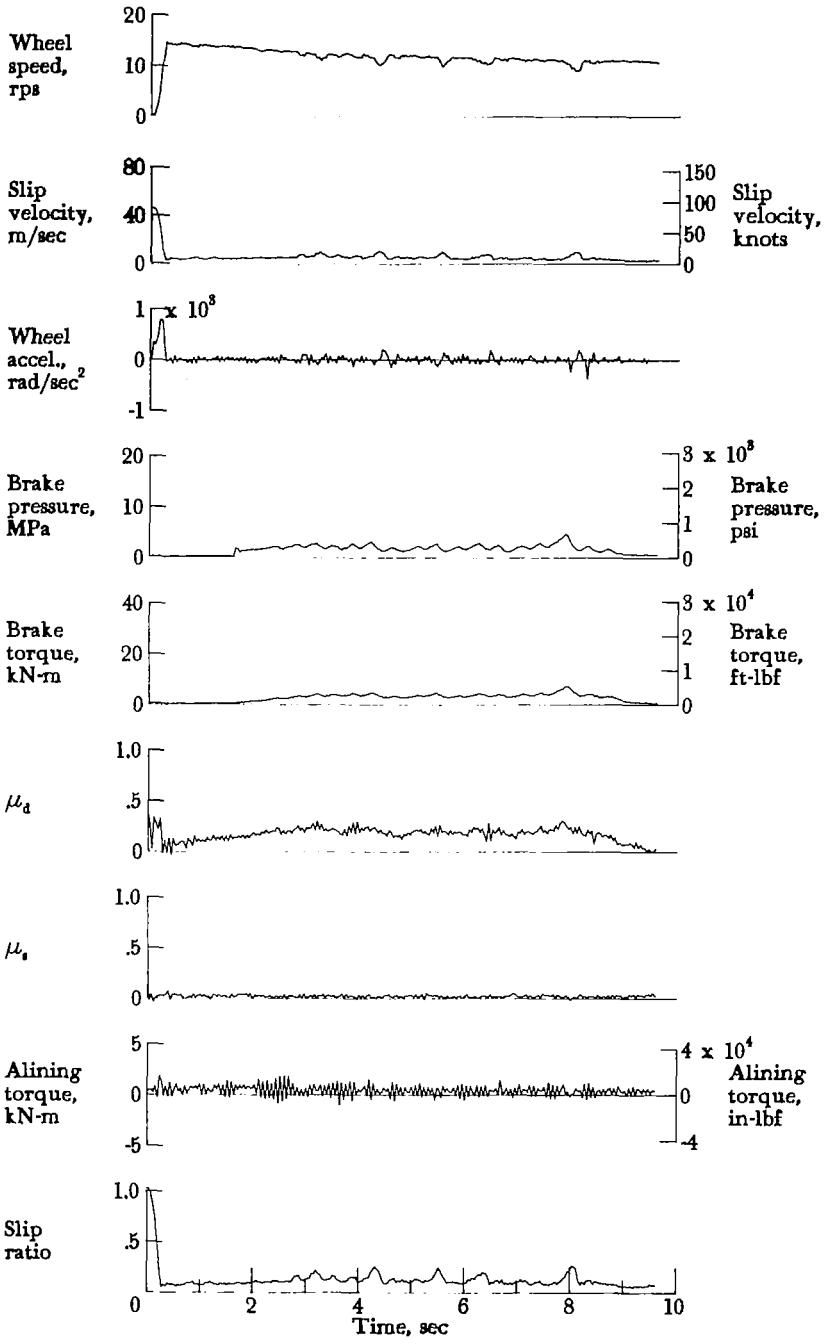

Figure A22.- Time histories for run 22. Nominal carriage speed, 72 knots; vertical load, 56.5 kN (12 700 lbf); yaw angle, 0°; brake pressure, 13 MPa (1900 psi); tire condition, new; surface condition, flooded.

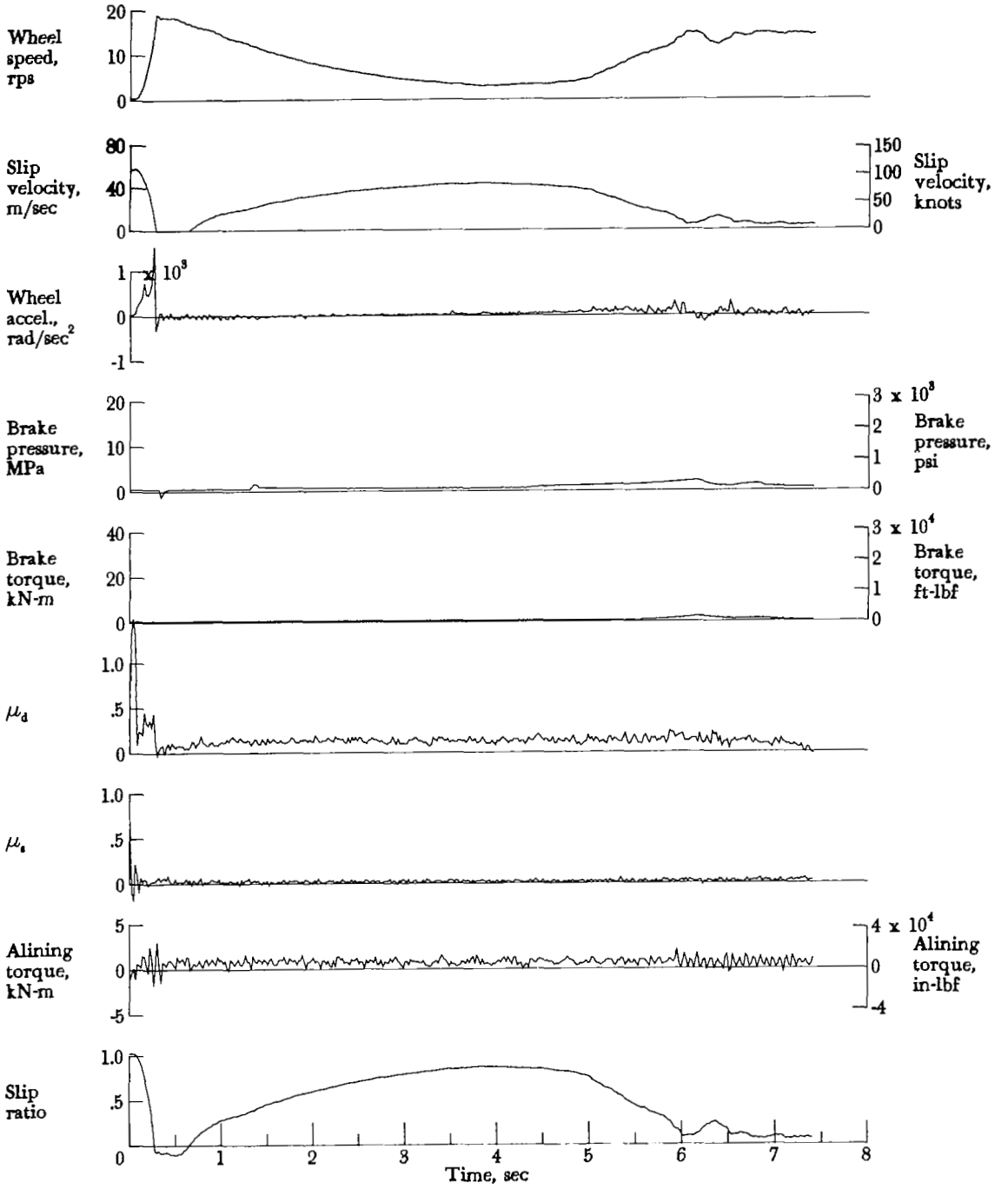

Figure A23.- Time histories for run 23. Nominal carriage speed, 94 knots; vertical load, 56.9 kN (12 800 lbf); yaw angle, 0°; brake pressure, 14 MPa (2000 psi); tire condition, new; surface condition, flooded.

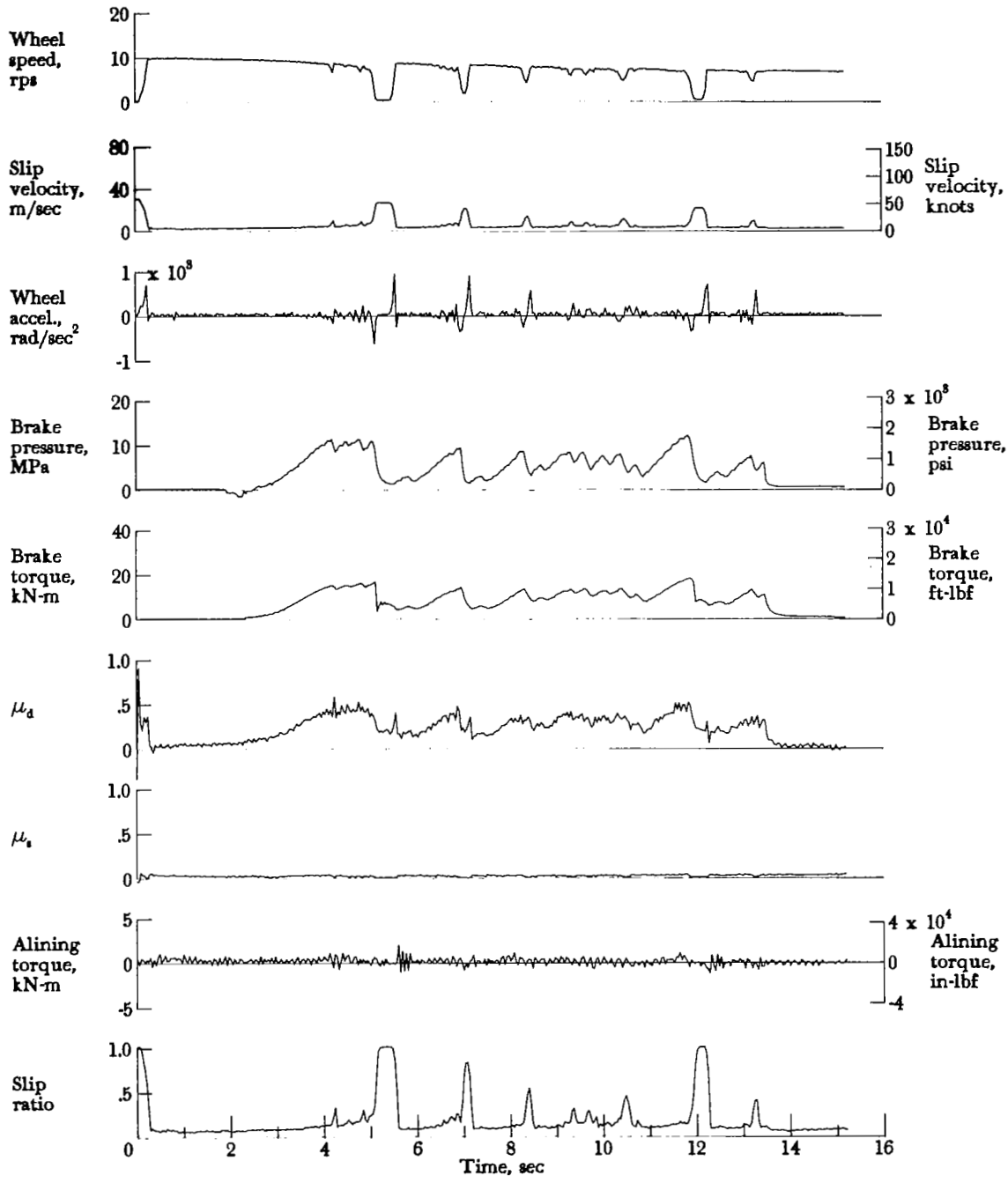

Figure A24.- Time histories for run 24. Nominal carriage speed, 45 knots; vertical load, 73.8 kN (16 600 lbf); yaw angle, 0°; brake pressure, 13 MPa (1850 psi); tire condition, new; surface condition, flooded.

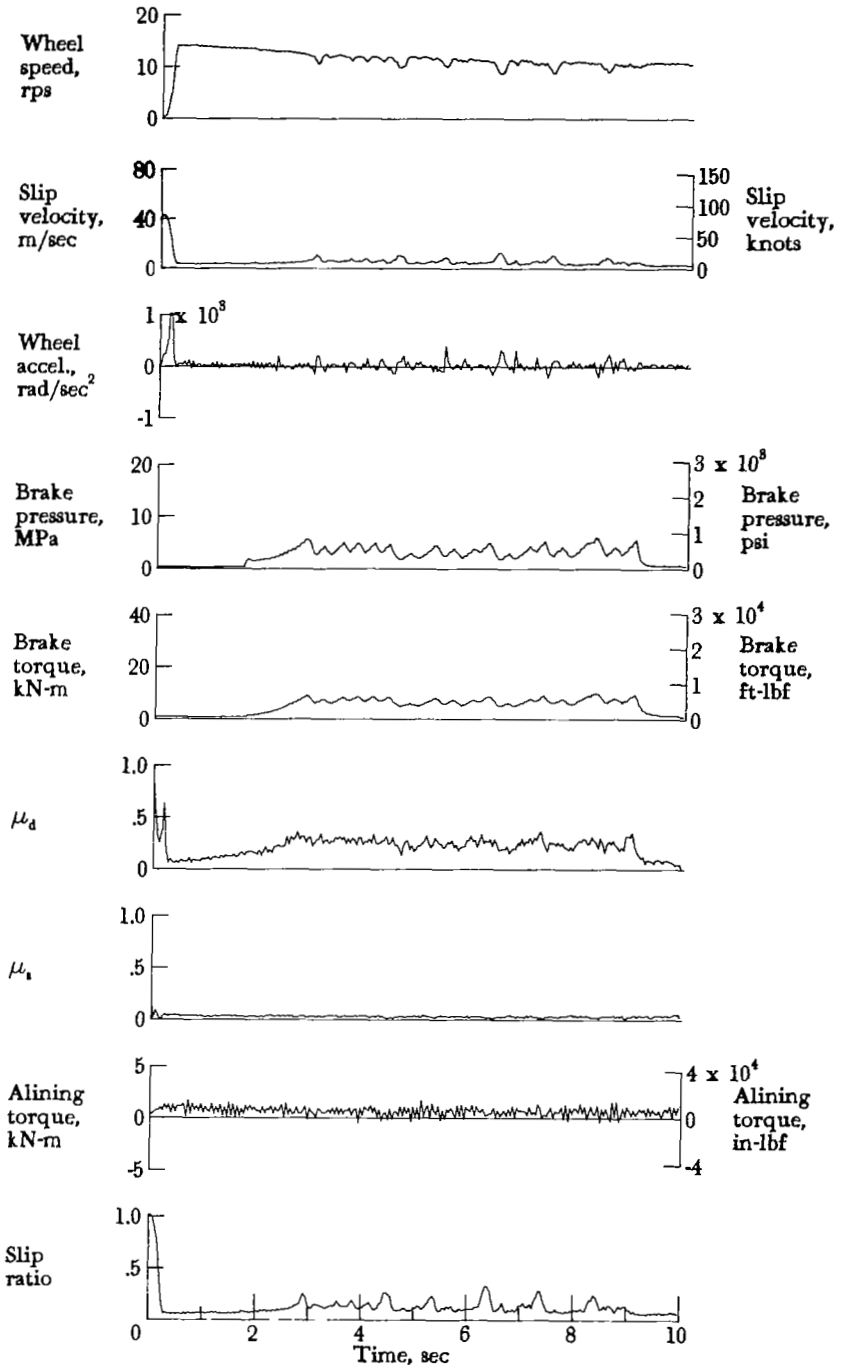

Figure A25.- Time histories for run 25. Nominal carriage speed, 69 knots; vertical load, 71.6 kN (16 100 lbf); yaw angle, 0°; brake pressure, 13 MPa (1900 psi); tire condition, new; surface condition, flooded.

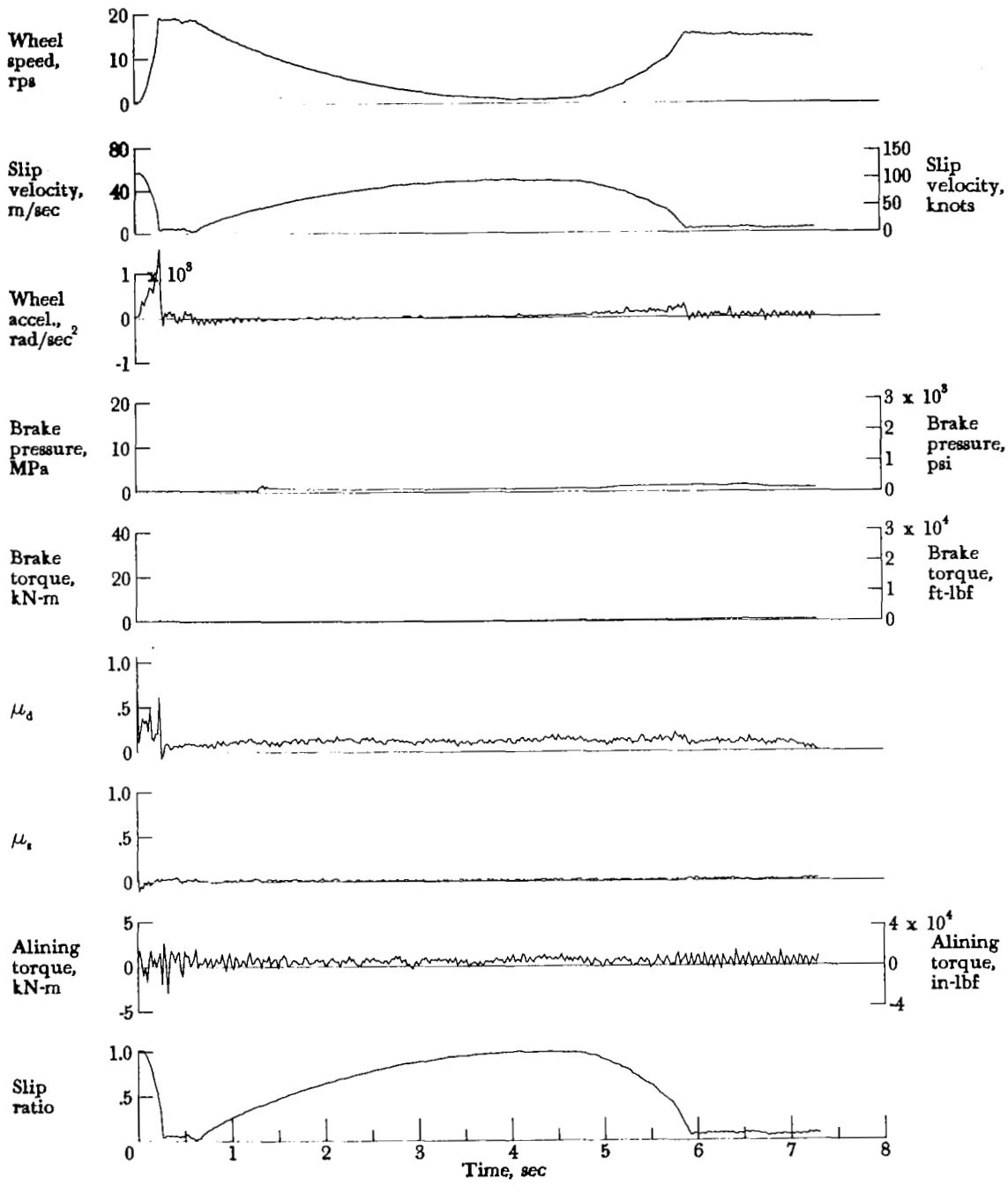

Figure A26.- Time histories for run 26. Nominal carriage speed, 96 knots; vertical load, 70.7 kN (15 900 lbf); yaw angle, 0°; brake pressure, 13 MPa (1900 psi); tire condition, new; surface condition, flooded.

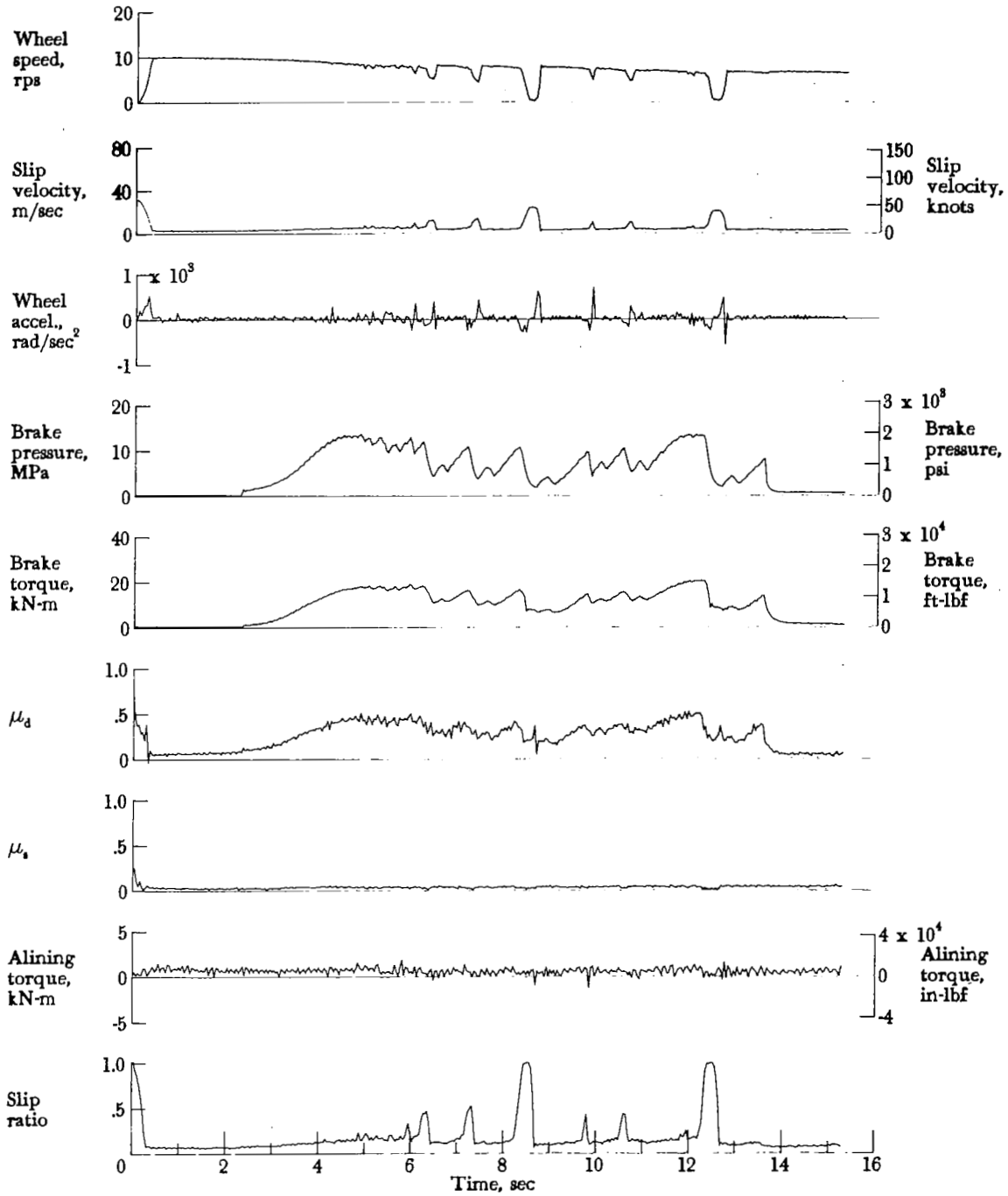

Figure A27.- Time histories for run 27. Nominal carriage speed, 45 knots; vertical load, 89.4 kN (20 100 lbf); yaw angle, 0°; brake pressure, 13 MPa (1900 psi); tire condition, new; surface condition, flooded.

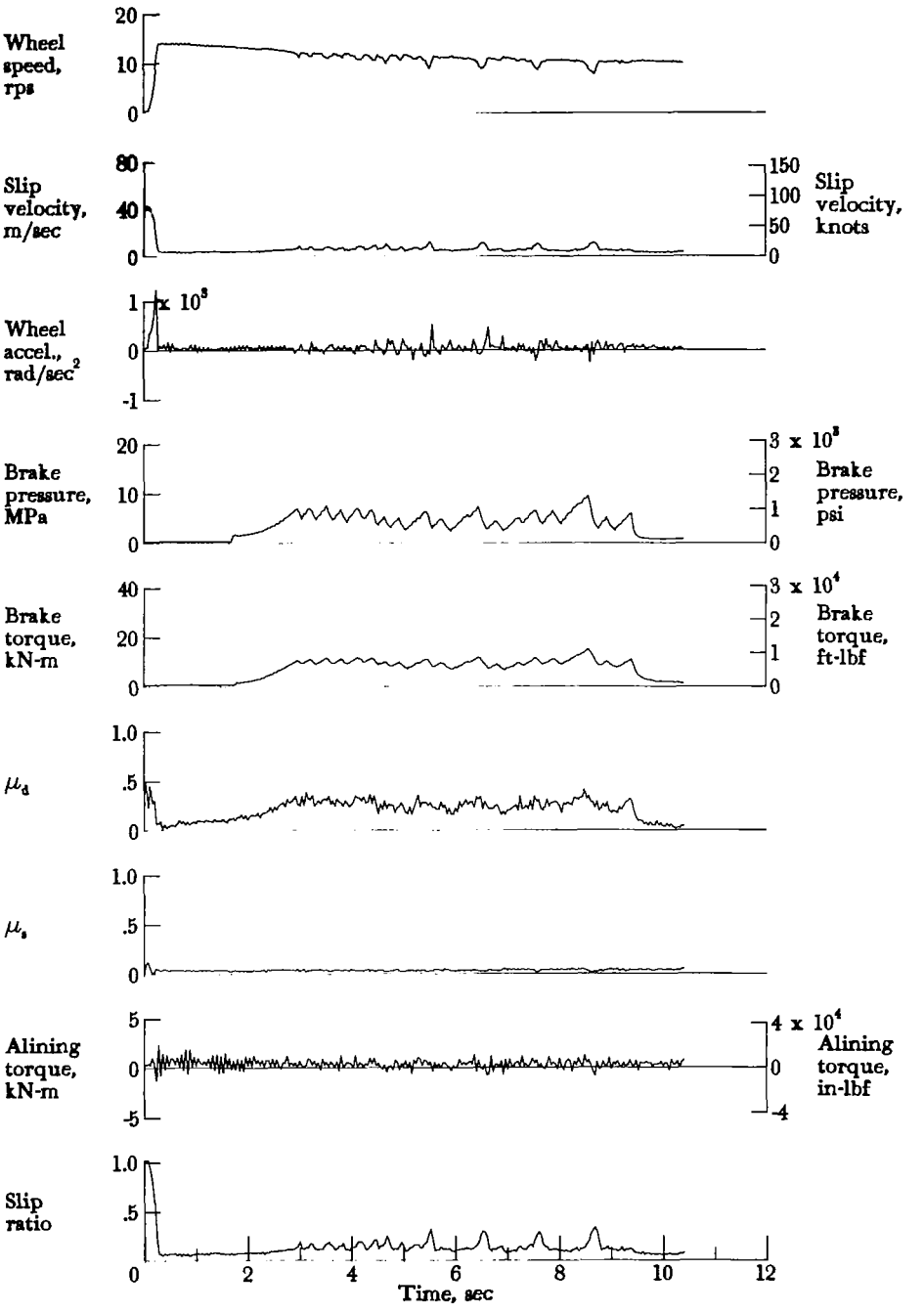

Figure A28.- Time histories for run 28. Nominal carriage speed, 66 knots; vertical load, 84.5 kN (19 000 lbf); yaw angle, 0°; brake pressure, 13 MPa (1900 psi); tire condition, new; surface condition, flooded.

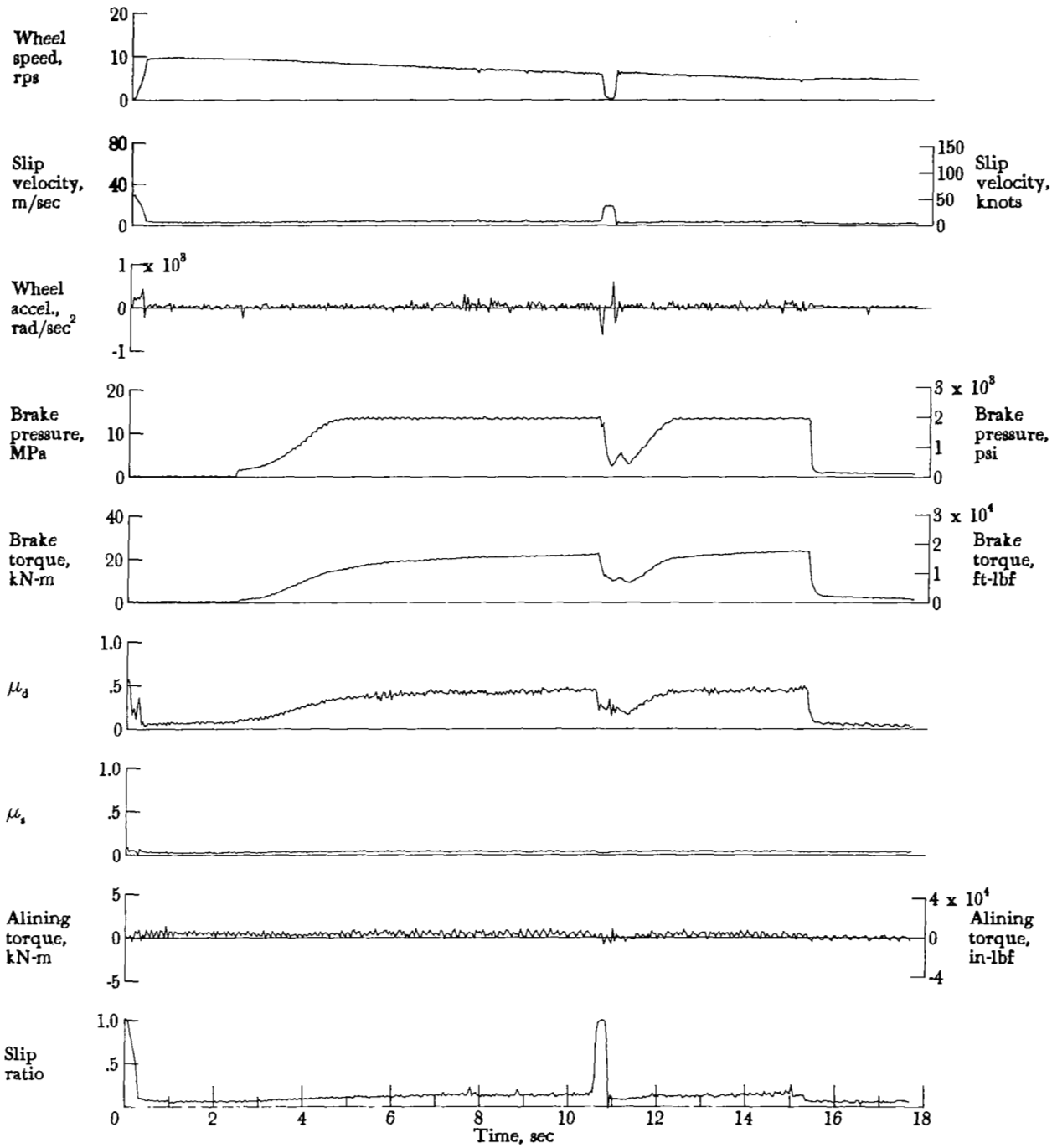

Figure A29.- Time histories for run 29. Nominal carriage speed, 37 knots; vertical load, 112.5 kN (25 300 lbf); yaw angle, 0°; brake pressure, 14 MPa (2000 psi); tire condition, new; surface condition, flooded.

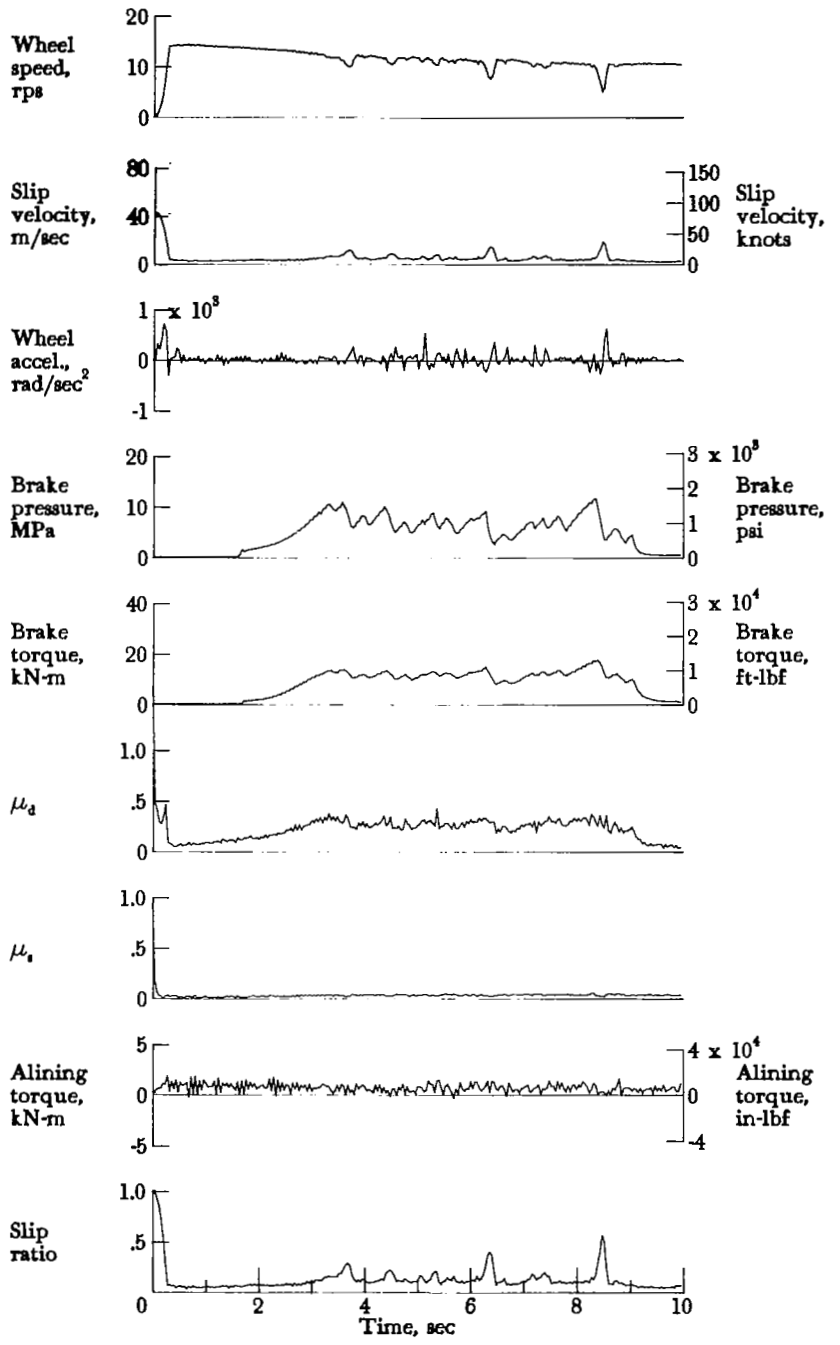

Figure A30.- Time histories for run 30. Nominal carriage speed, 69 knots; vertical load, 114.3 kN (25 700 lbf); yaw angle, 0°; brake pressure, 14 MPa (2000 psi); tire condition, new; surface condition, flooded.

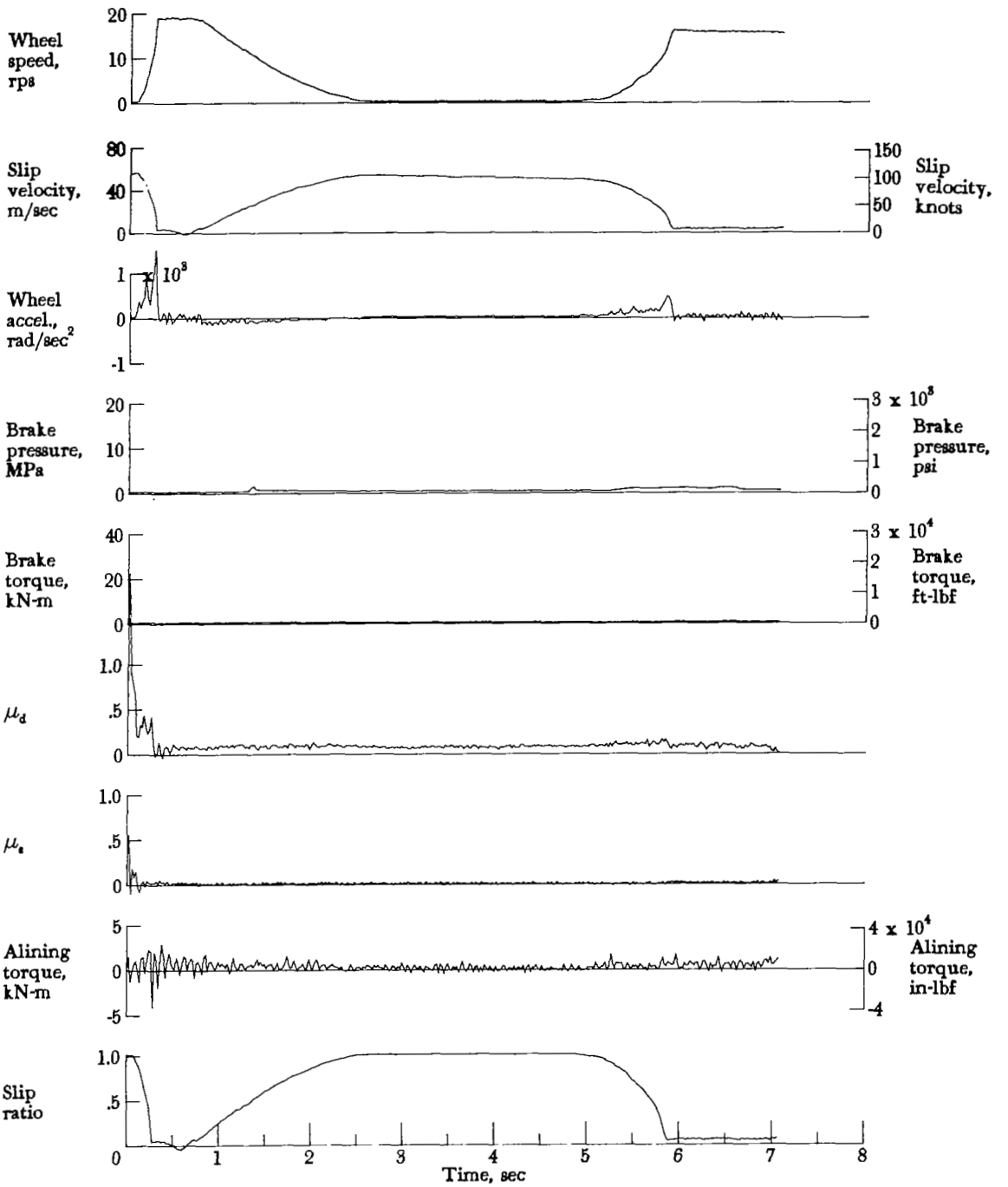

Figure A31.- Time histories for run 31. Nominal carriage speed, 98 knots; vertical load, 112.1 kN (25 200 lbf); yaw angle, 0°; brake pressure, 14 MPa (2000 psi); tire condition, new; surface condition, flooded.

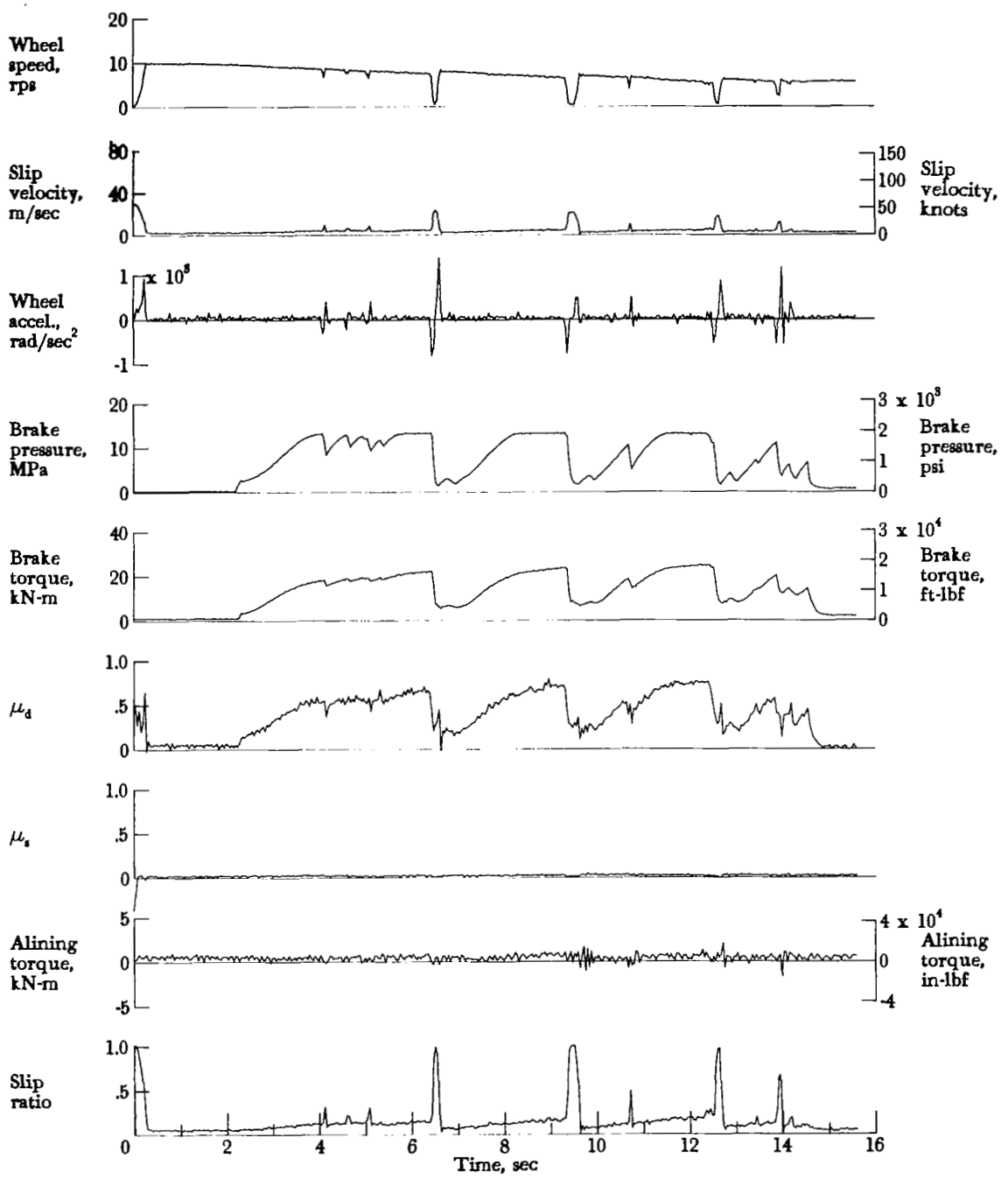

Figure A32.- Time histories for run 32. Nominal carriage speed, 41 knots; vertical load, 68.1 kN (15 300 lbf); yaw angle, 0°; brake pressure, 13 MPa (1900 psi); tire condition, new; surface condition, alternating dry and damp at 30.5-m (100-ft) intervals.

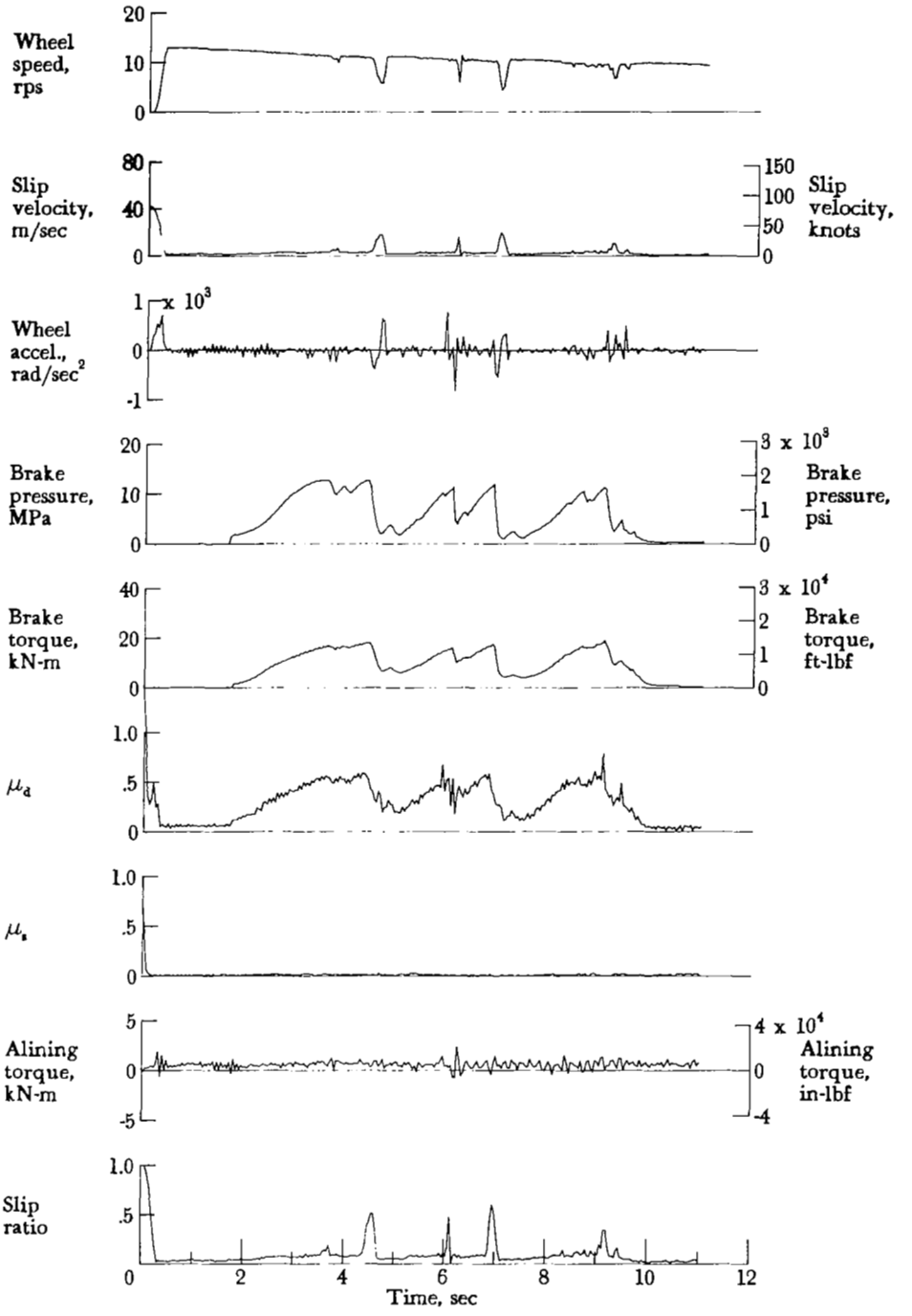

Figure A33.- Time histories for run 33. Nominal carriage speed, 65 knots; vertical load, 67.6 kN (15 200 lbf); yaw angle, 0°; brake pressure, 13 MPa (1950 psi); tire condition, new; surface condition, alternating dry and damp at 30.5-m (100-ft) intervals.

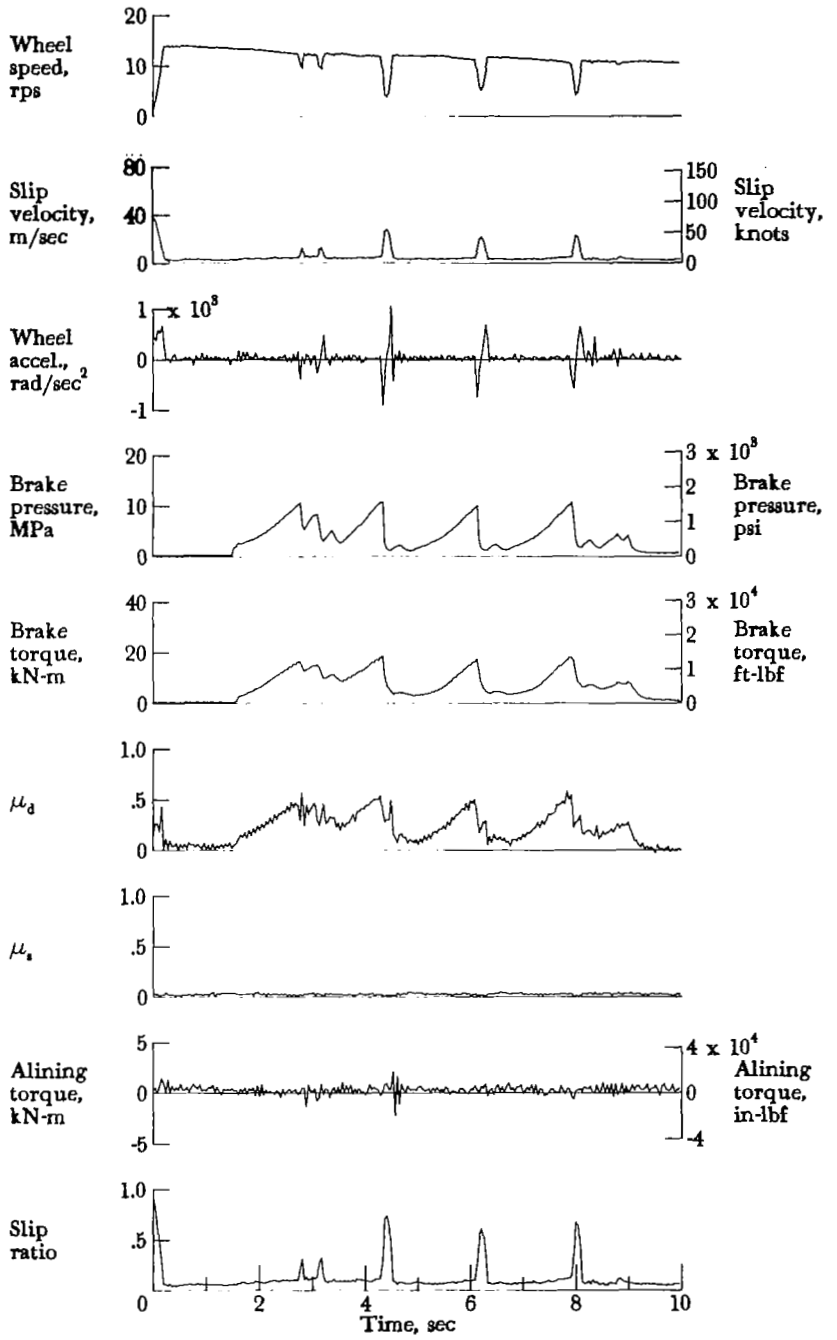

Figure A34.- Time histories for run 34. Nominal carriage speed, 68 knots; vertical load, 68.9 kN (15 500 lbf); yaw angle, 0°; brake pressure, 13 MPa (1950 psi); tire condition, new; surface condition, alternating dry and damp at 30.5-m (100-ft) intervals.

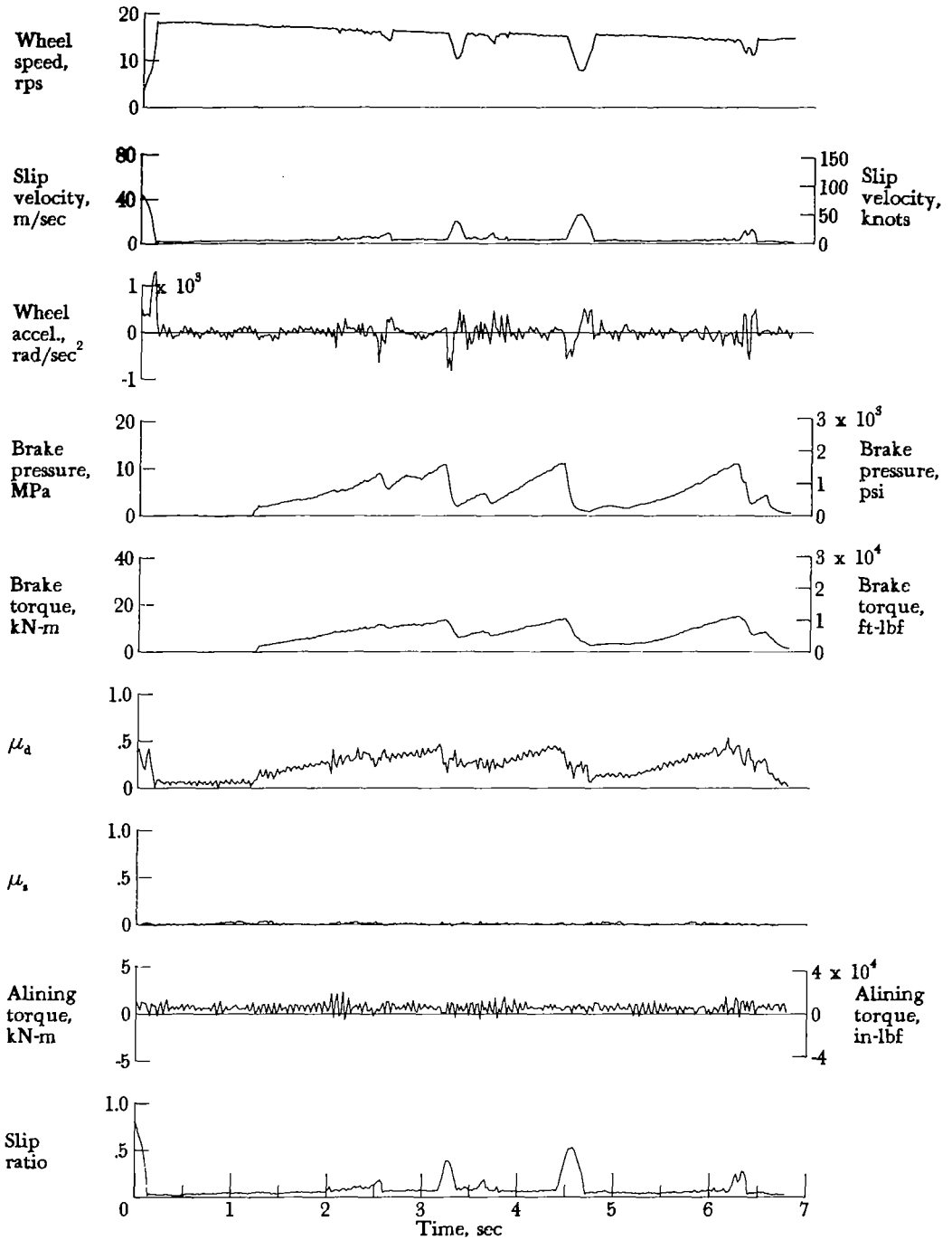

Figure A35.- Time histories for run 35. Nominal carriage speed, 97 knots; vertical load, 69.8 kN (15 700 lbf); yaw angle, 0°; brake pressure, 13 MPa (1950 psi); tire condition, new; surface condition, alternating dry and damp at 30.5-m (100-ft) intervals.

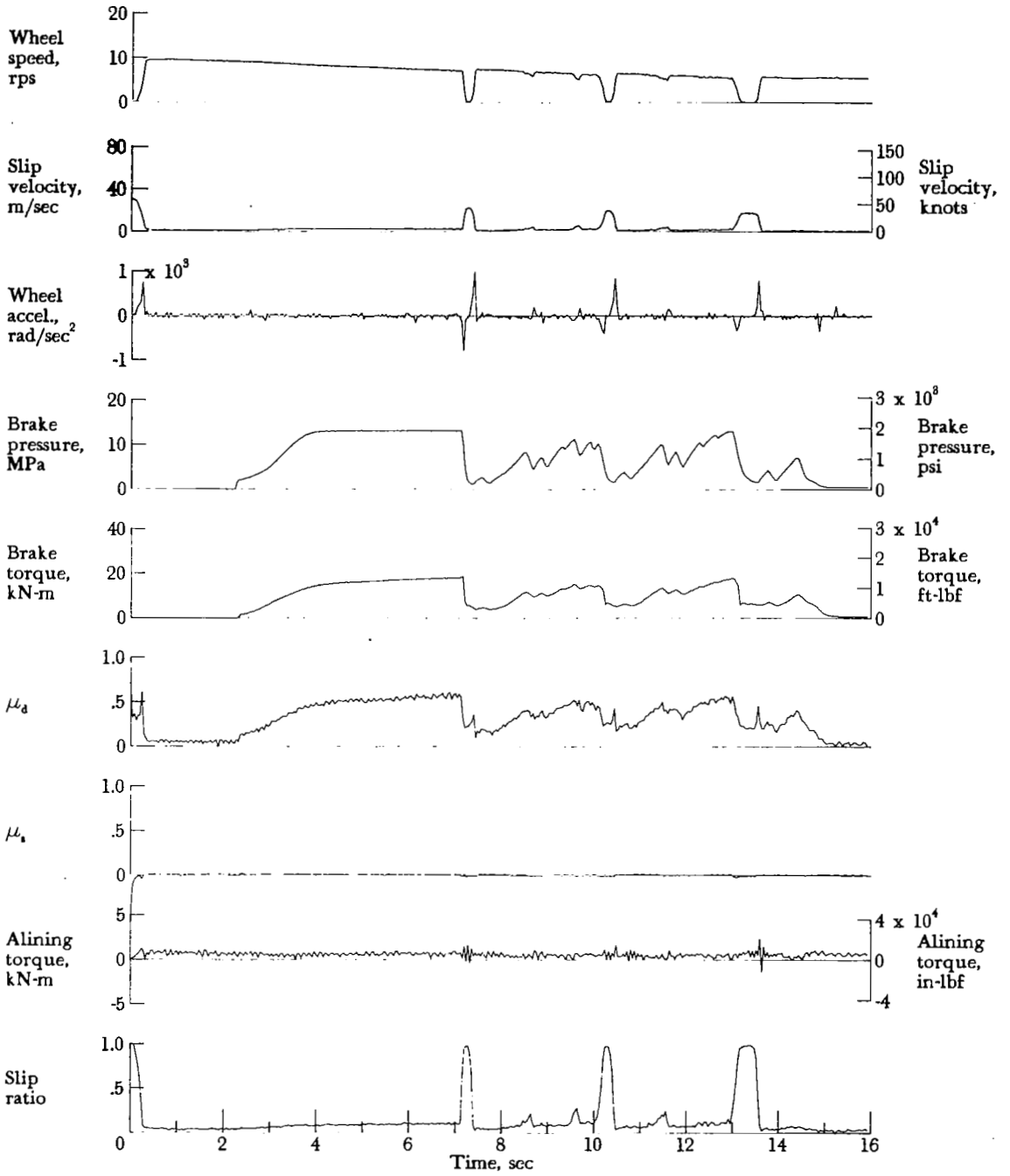

Figure A36.- Time histories for run 36. Nominal carriage speed, 41 knots; vertical load, 69.3 kN (15 600 lbf); yaw angle, 0°; brake pressure, 13 MPa (1950 psi); tire condition, new; surface condition, dry/flooded.

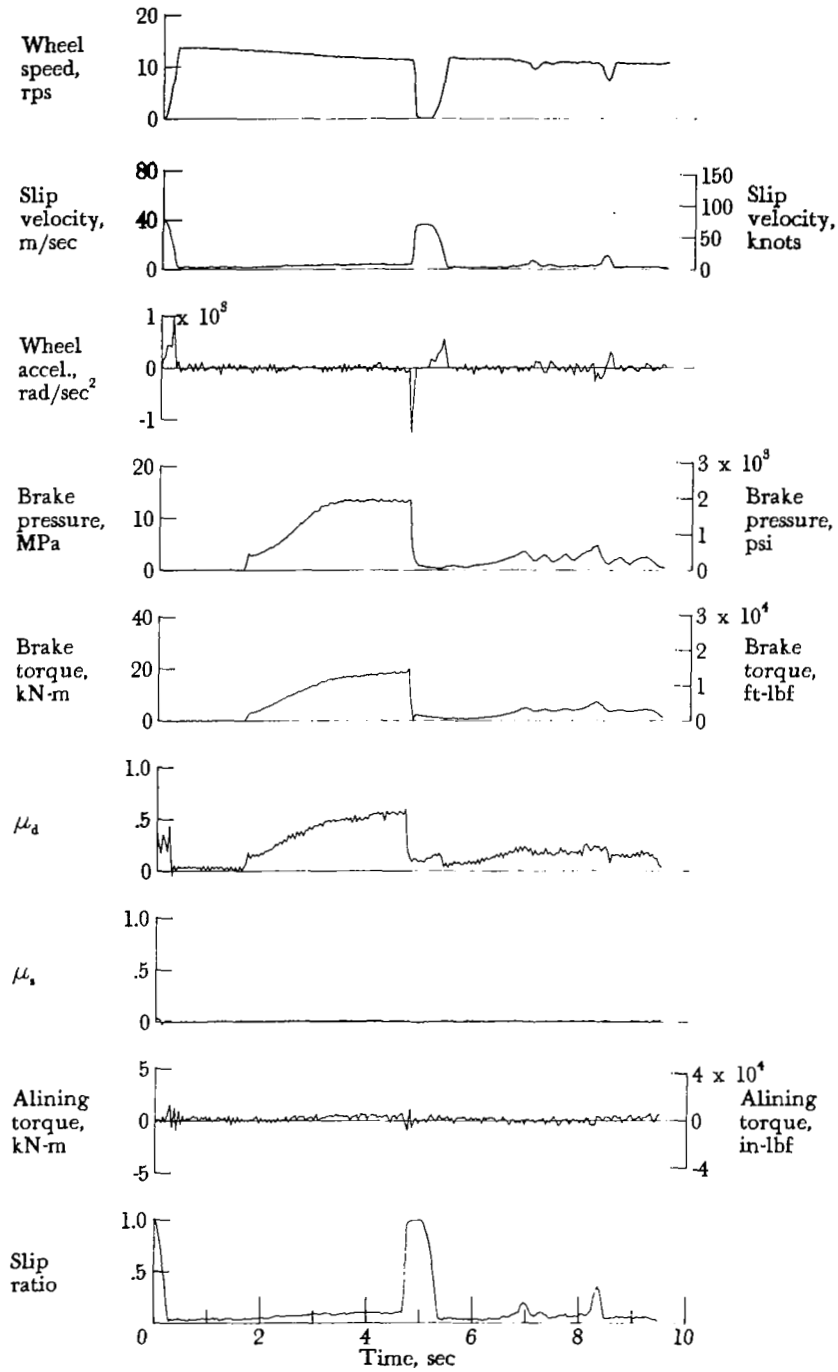

Figure A37.- Time histories for run 37. Nominal carriage speed, 70 knots; vertical load, 69.3 kN (15 600 lbf); yaw angle, 0°; brake pressure, 14 MPa (2000 psi); tire condition, new; surface condition, dry/damp.

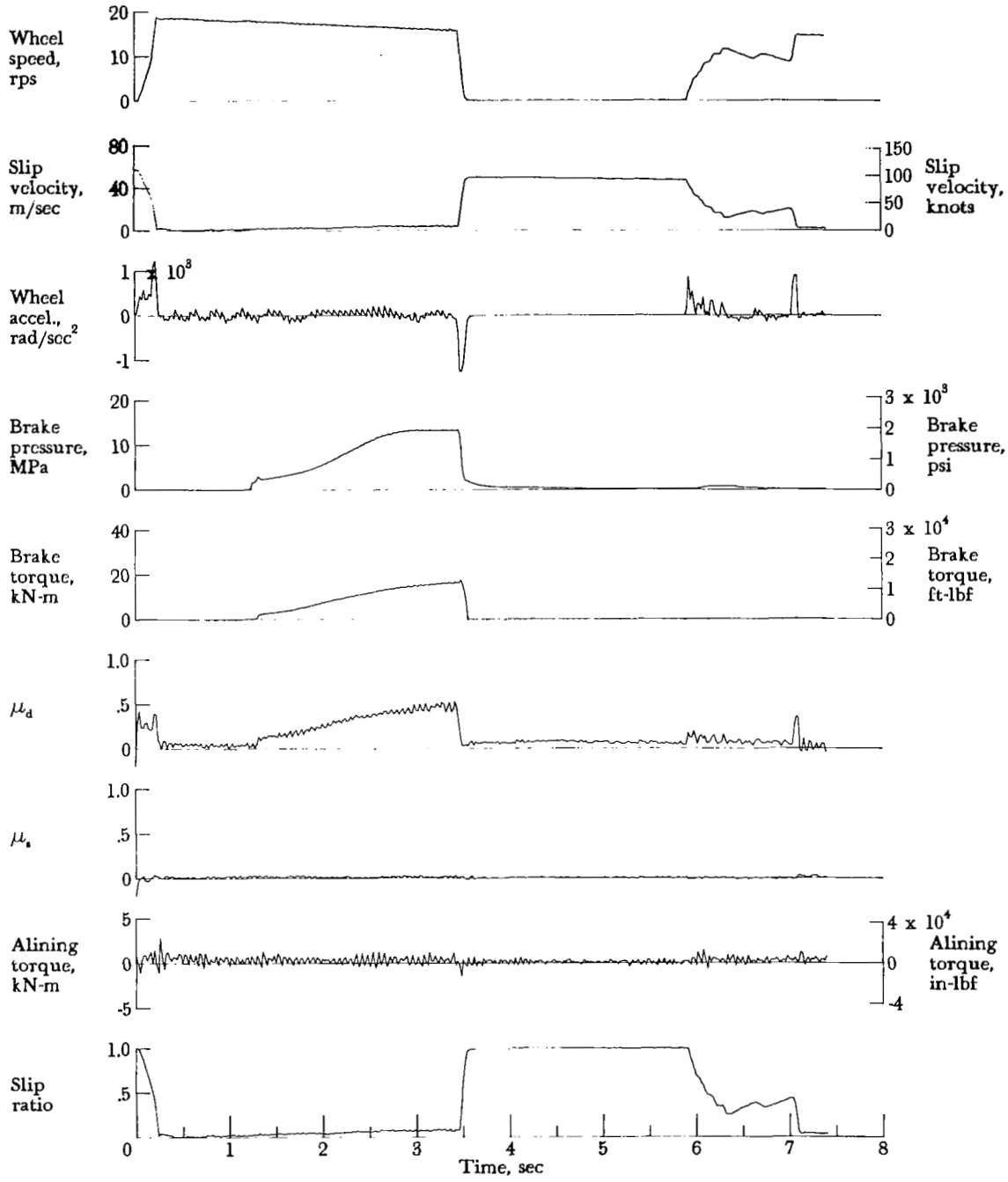

Figure A38.- Time histories for run 38. Nominal carriage speed, 97 knots; vertical load, 68.5 kN (15 400 lbf); yaw angle, 0°; brake pressure, 13 MPa (1950 psi); tire condition, new; surface condition, dry/flooded.

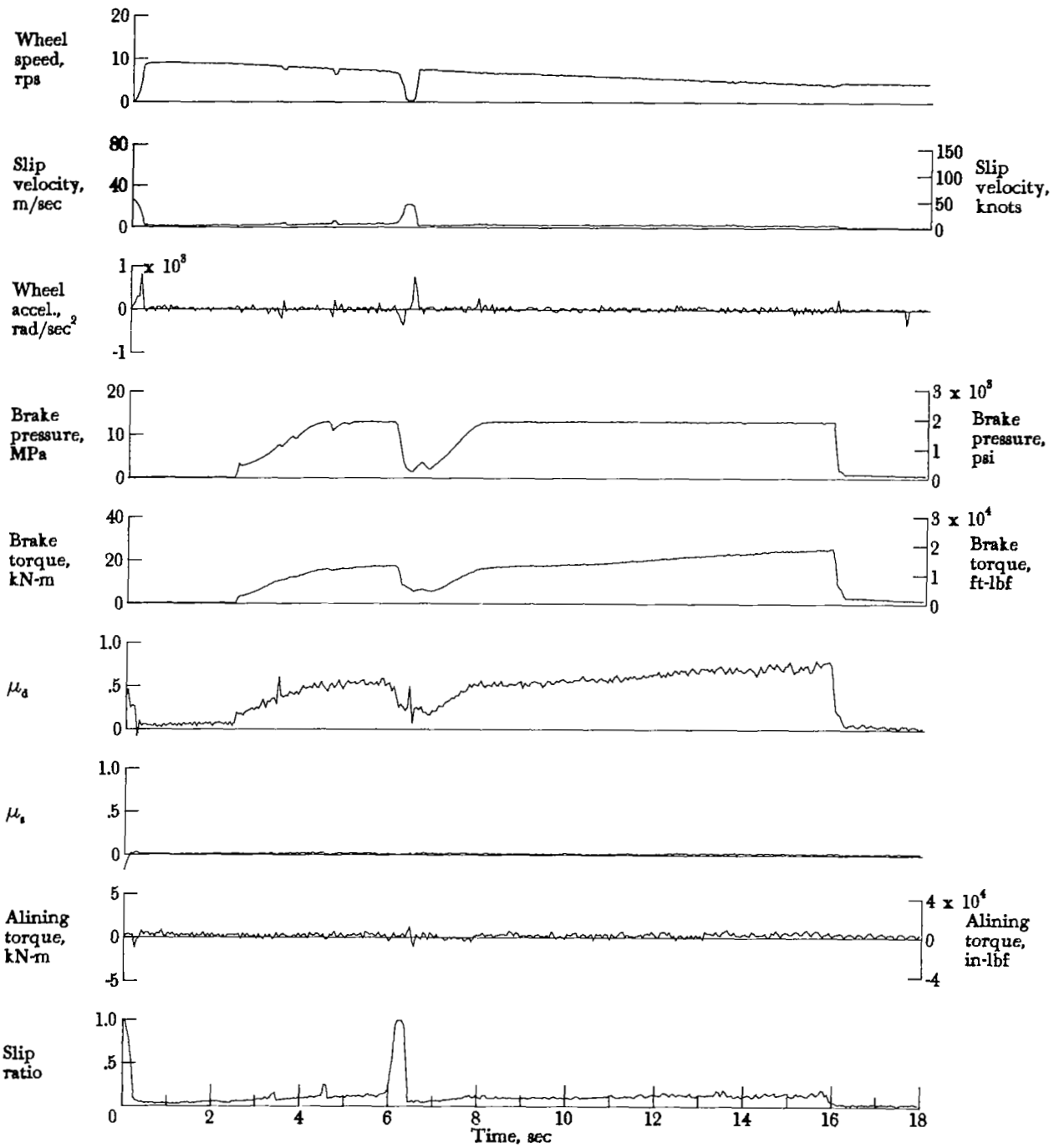

Figure A39.- Time histories for run 39. Nominal carriage speed, 36 knots; vertical load, 68.5 kN (15 400 lbf); yaw angle, 0°; brake pressure, 13 MPa (1950 psi); tire condition, new; surface condition, flooded/dry.

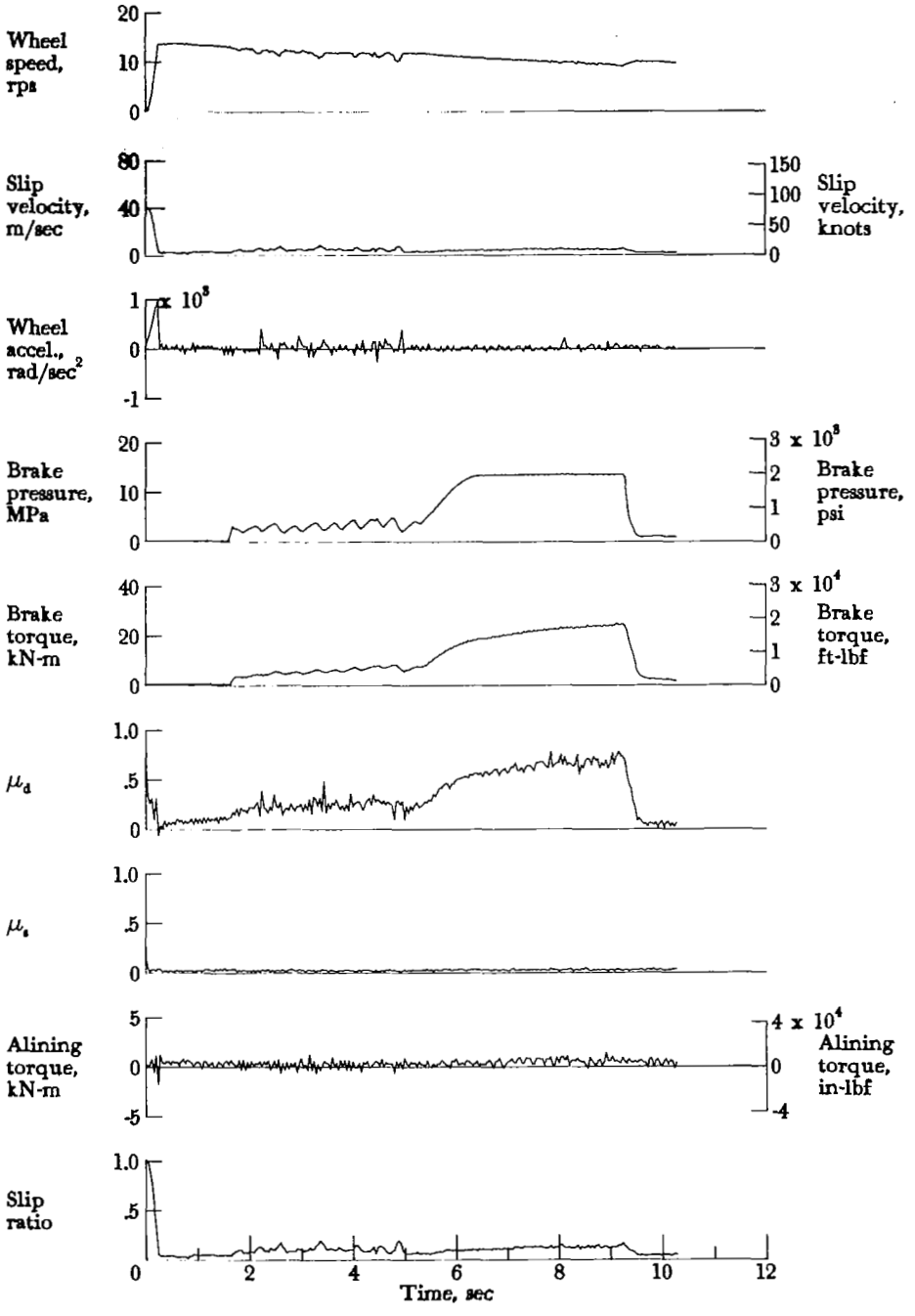

Figure A40.- Time histories for run 40. Nominal carriage speed, 67 knots; vertical load, 68.1 kN (15 300 lbf); yaw angle, 0°; brake pressure, 13 MPa (1950 psi); tire condition, new; surface condition, flooded/dry.

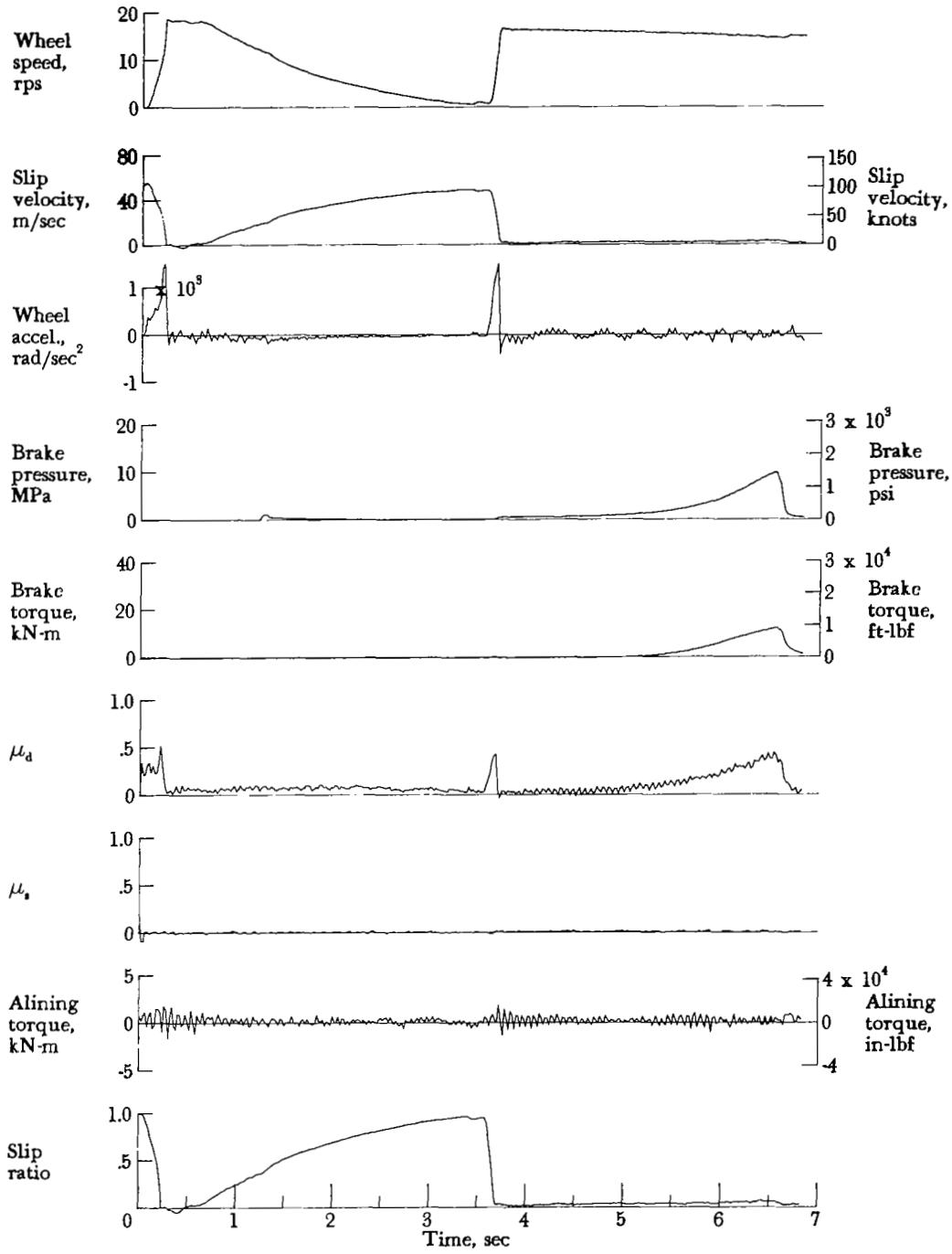

Figure A41.- Time histories for run 41. Nominal carriage speed, 98 knots; vertical load, 68.1 kN (15 300 lbf); yaw angle, 0°; brake pressure, 13 MPa (1850 psi); tire condition, new; surface condition, flooded/dry.

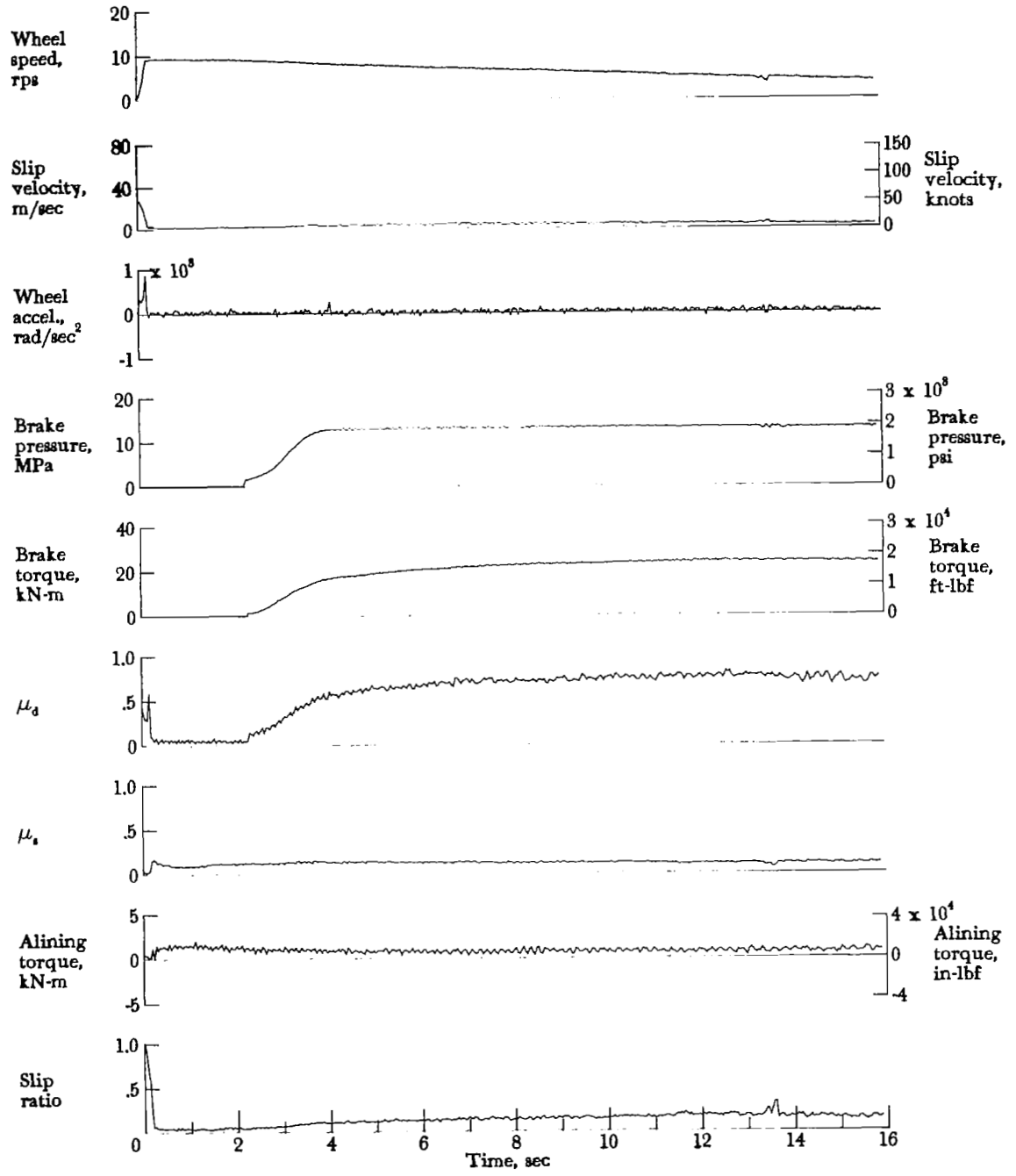

Figure A42.- Time histories for run 42. Nominal carriage speed, 36 knots; vertical load, 68.1 kN (15 300 lbf); yaw angle, 1°; brake pressure, 13 MPa (1900 psi); tire condition, new; surface condition, dry.

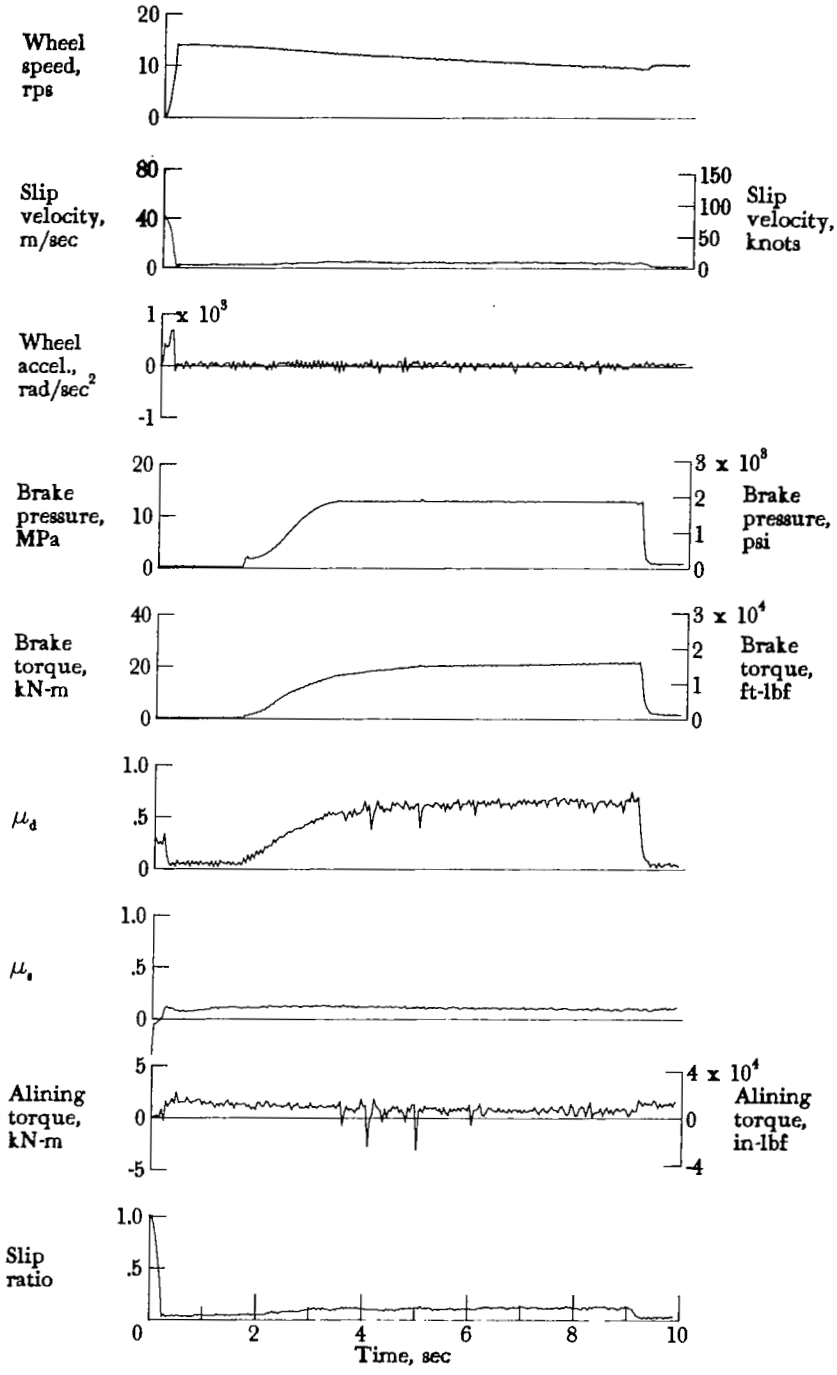

Figure A43.- Time histories for run 43. Nominal carriage speed, 68 knots; vertical load, 69.3 kN (15 600 lbf); yaw angle, 1°; brake pressure, 13 MPa (1900 psi); tire condition, new; surface condition, dry.

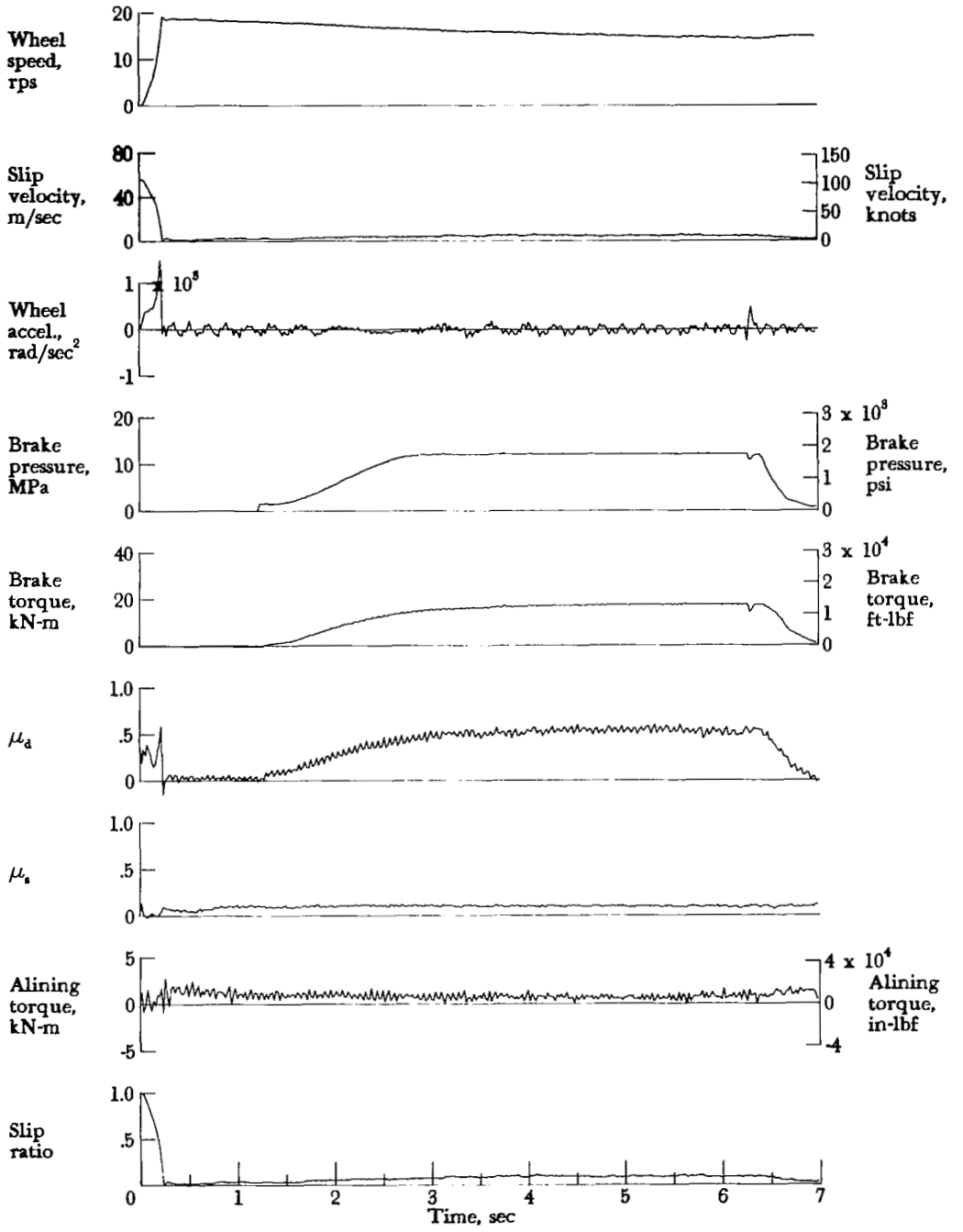

Figure A44.- Time histories for run 44. Nominal carriage speed, 99 knots; vertical load, 70.3 kN (15 800 lbf); yaw angle, 1°; brake pressure, 12 MPa (1800 psi); tire condition, new; surface condition, dry.

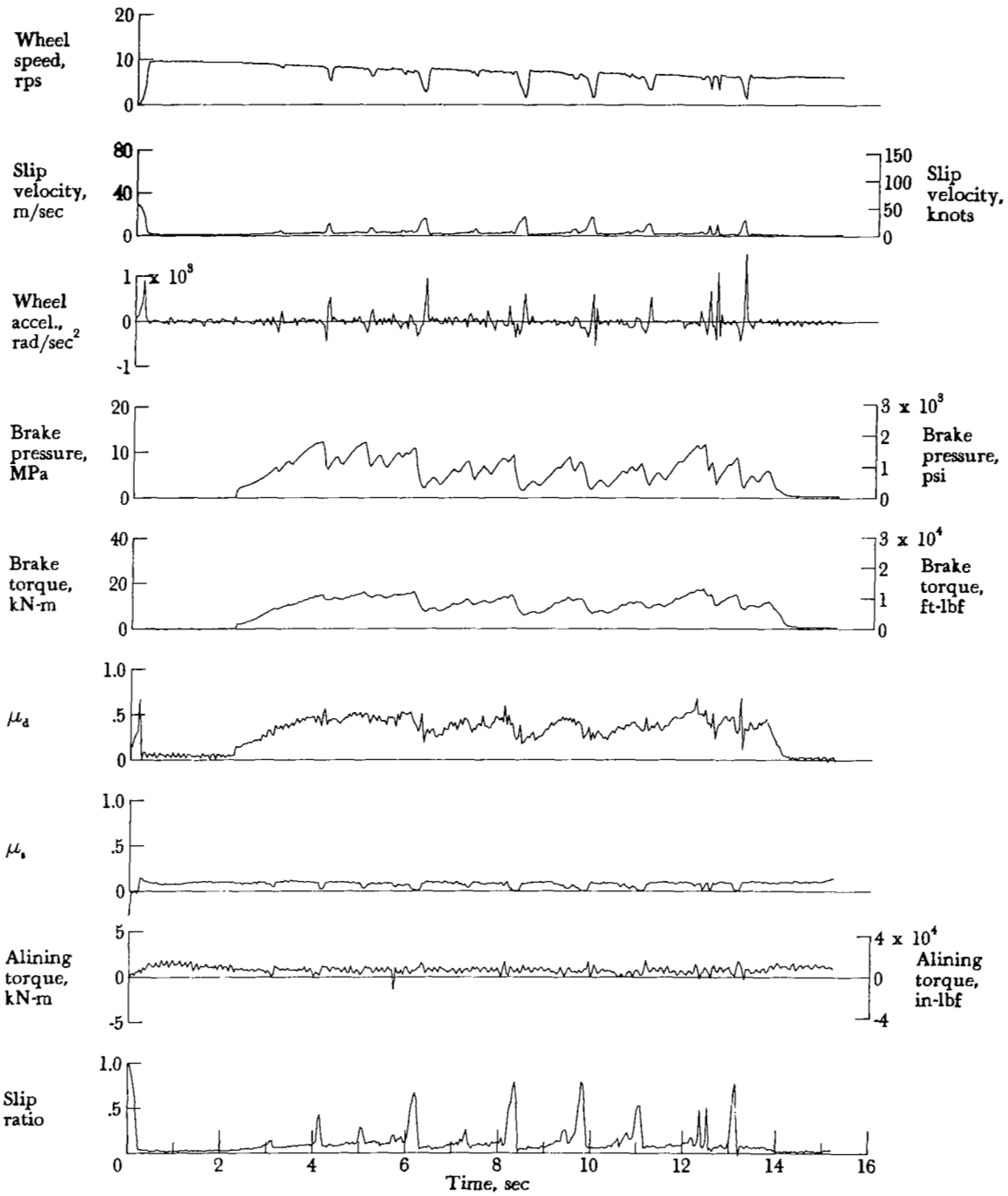

Figure A45.- Time histories for run 45. Nominal carriage speed, 44 knots; vertical load, 68.5 kN (15 400 lbf); yaw angle, 1°; brake pressure, 13 MPa (1900 psi); tire condition, new; surface condition, damp.

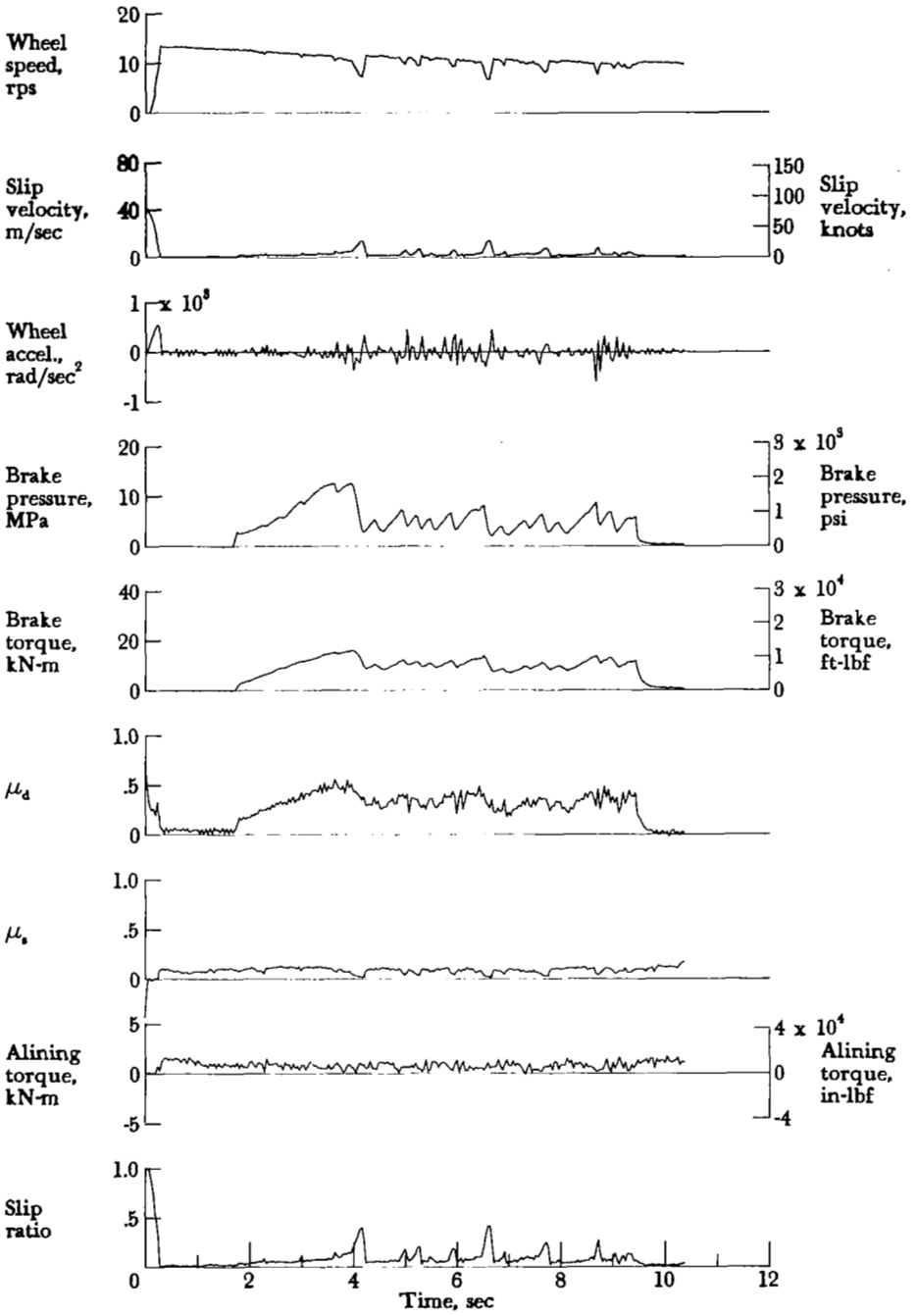

Figure A46.- Time histories for run 46. Nominal carriage speed, 66 knots; vertical load, 69.3 kN (15 600 lbf); yaw angle, 1°; brake pressure, 13 MPa (1950 psi); tire condition, new; surface condition, damp.

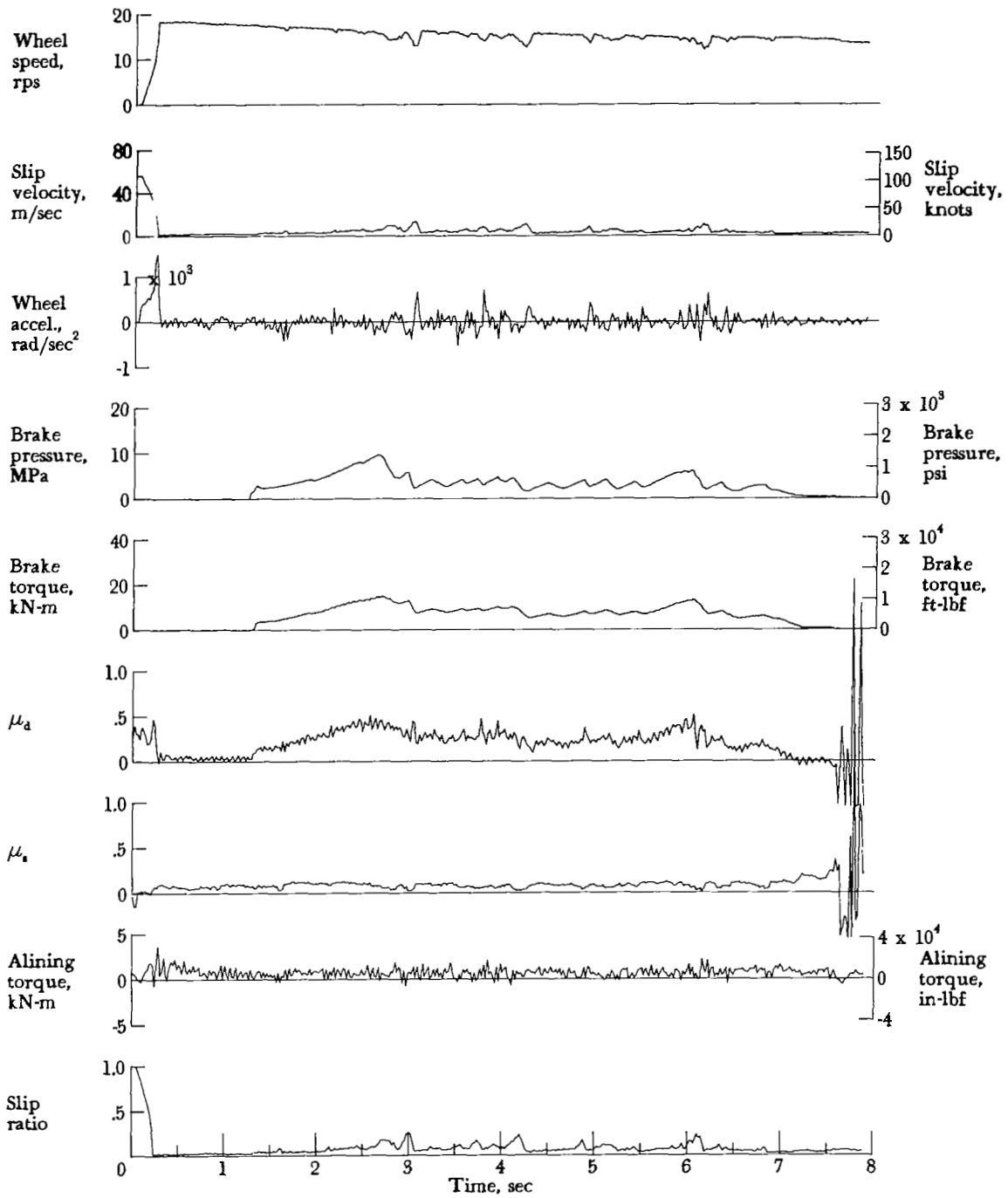

Figure A47.- Time histories for run 47. Nominal carriage speed, 95 knots; vertical load, 69.8 kN (15 700 lbf); yaw angle, 1°; brake pressure, 13 MPa (1850 psi); tire condition, new; surface condition, damp.

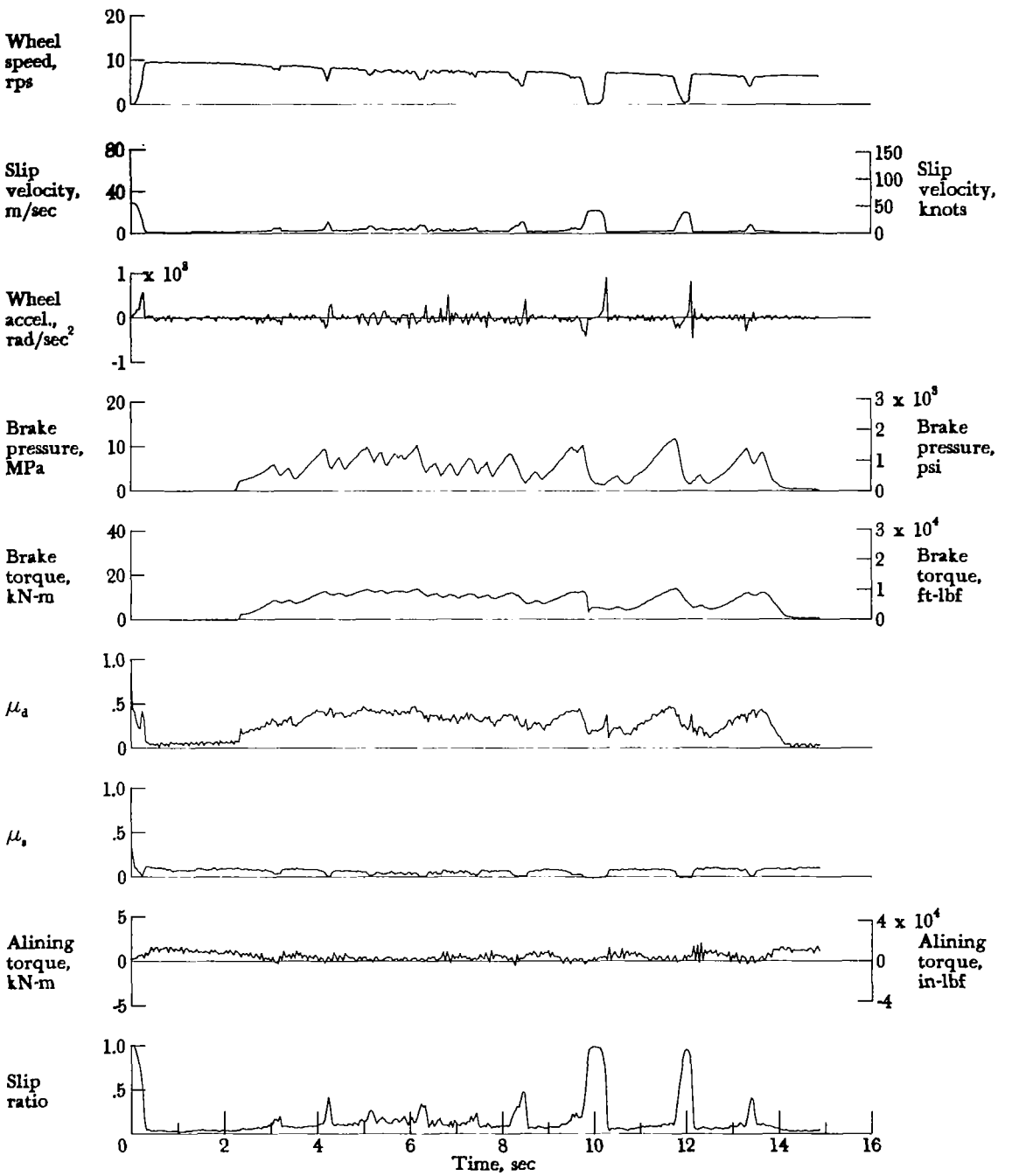

Figure A48.- Time histories for run 48. Nominal carriage speed, 45 knots; vertical load, 68.9 kN (15 500 lbf); yaw angle, 1°; brake pressure, 13 MPa (1900 psi); tire condition, new; surface condition, flooded.

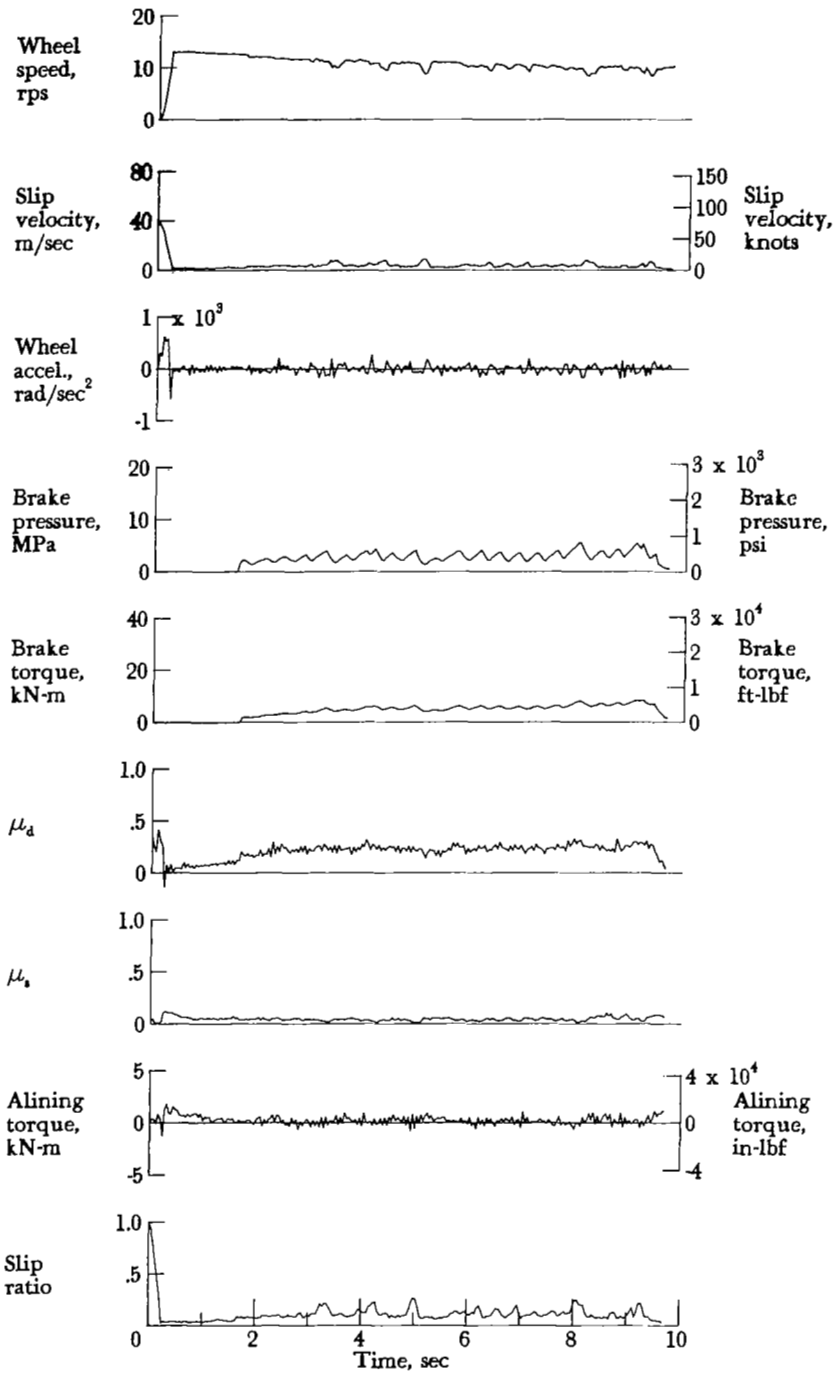

Figure A49.- Time histories for run 49. Nominal carriage speed, 67 knots; vertical load, 68.1 kN (15 300 lbf); yaw angle, 1°; brake pressure, 13 MPa (1950 psi); tire condition, new; surface condition, flooded.

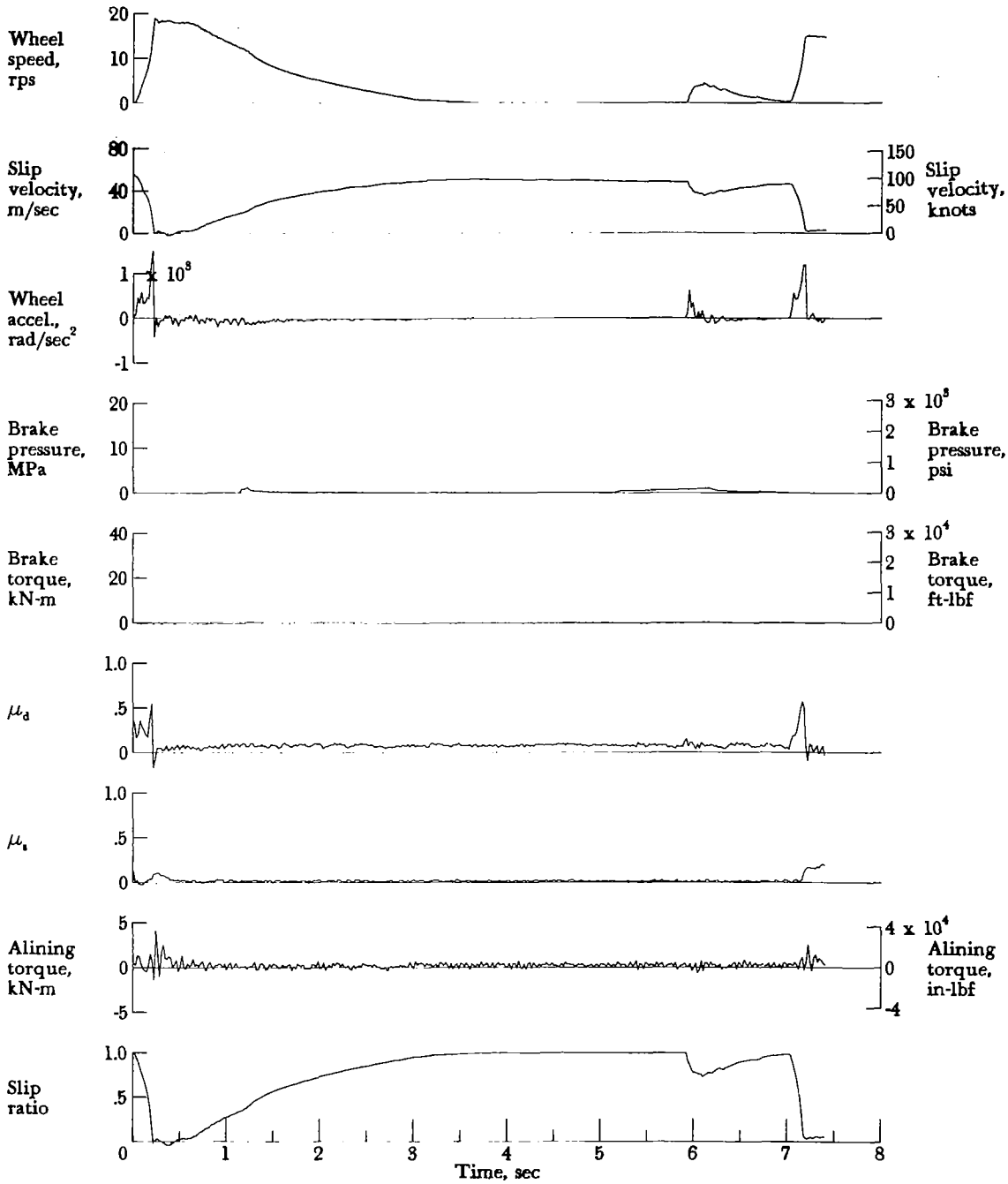

Figure A50.- Time histories for run 50. Nominal carriage speed, 97 knots; vertical load, 66.2 kN (15 100 lbf); yaw angle, 1°; brake pressure, 13 MPa (1950 psi); tire condition, new; surface condition, flooded.

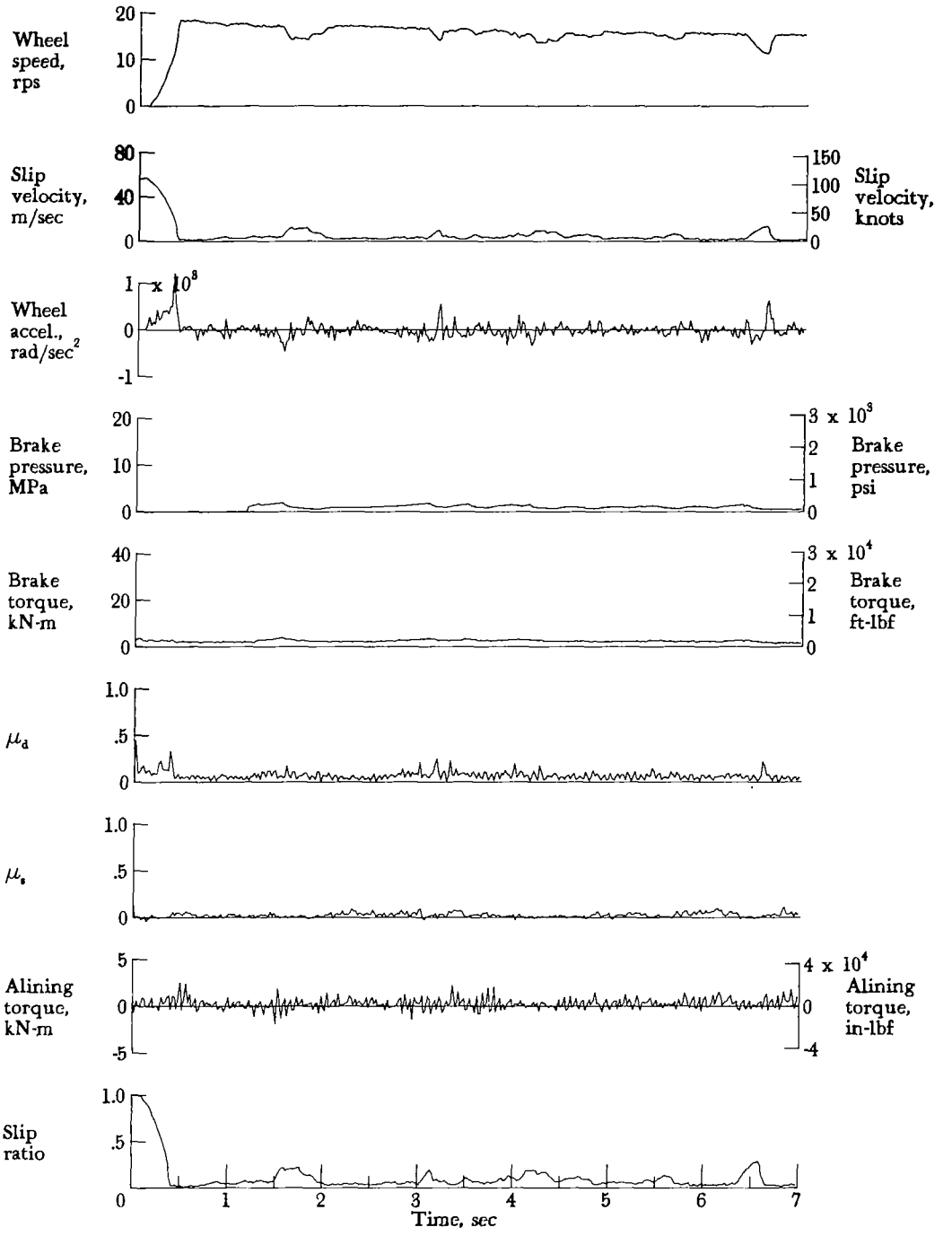

Figure A51.- Time histories for run 51. Nominal carriage speed, 99 knots; vertical load, 68.9 kN (15 500 lbf); yaw angle, 1°; brake pressure, 13 MPa (1850 psi); tire condition, new; surface condition, rain.

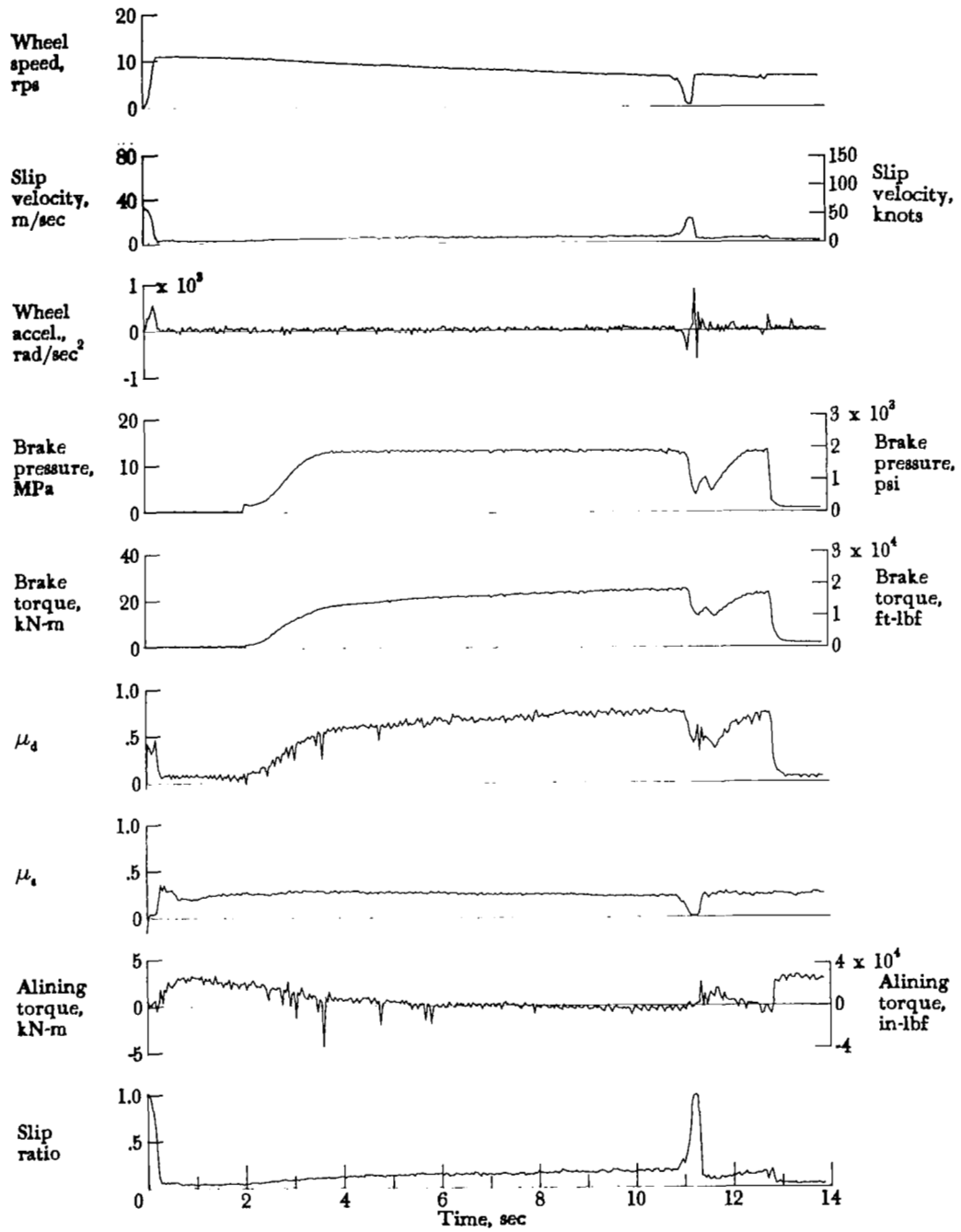

Figure A52.- Time histories for run 52. Nominal carriage speed, 47 knots; vertical load, 69.8 kN (15 700 lbf); yaw angle, 3°; brake pressure, 13 MPa (1950 psi); tire condition, new; surface condition, dry.

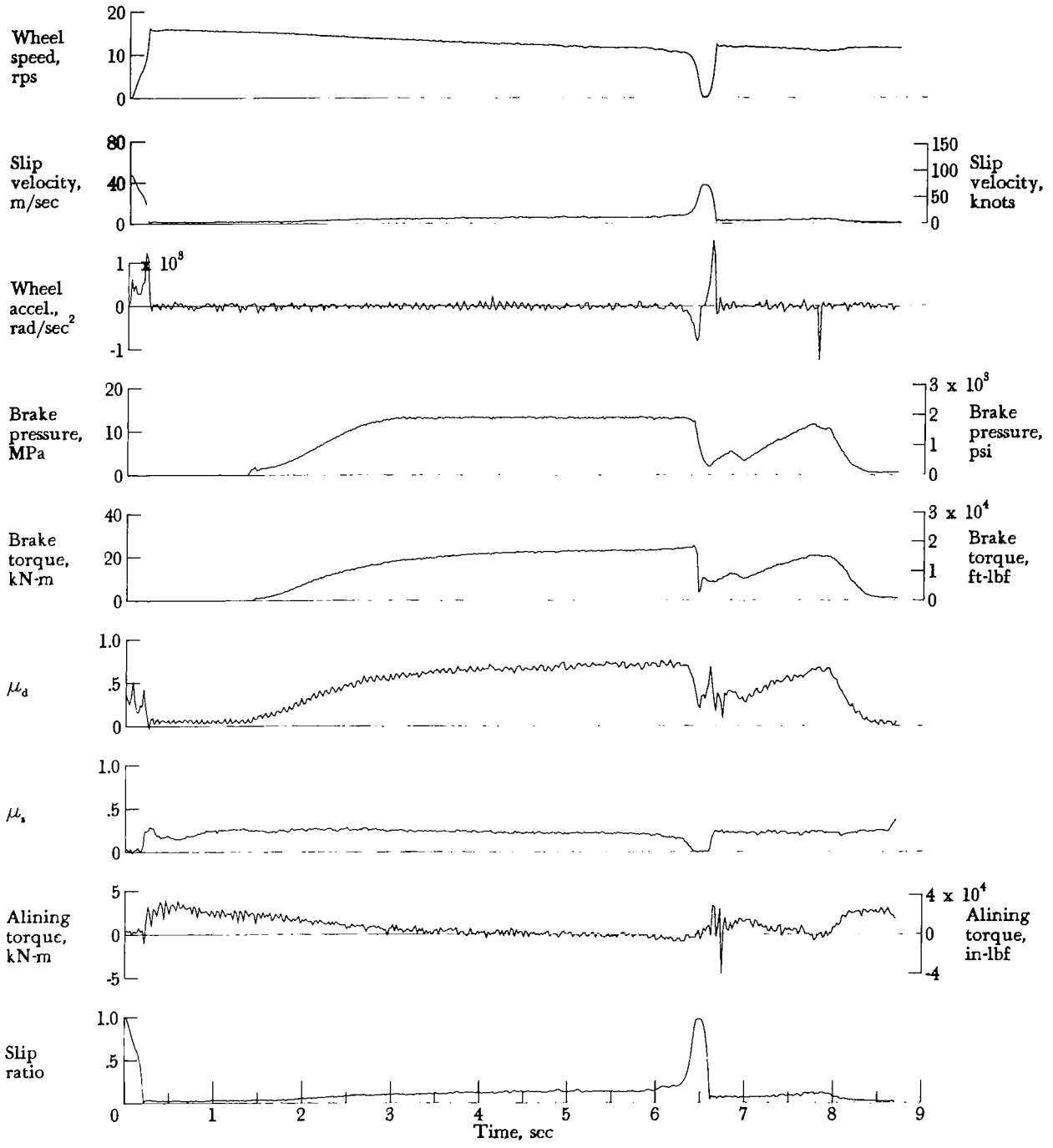

Figure A53.- Time histories for run 53. Nominal carriage speed, 79 knots; vertical load, 68.9 kN (15 500 lbf); yaw angle, 3°; brake pressure, 14 MPa (2000 psi); tire condition, new; surface condition, dry.

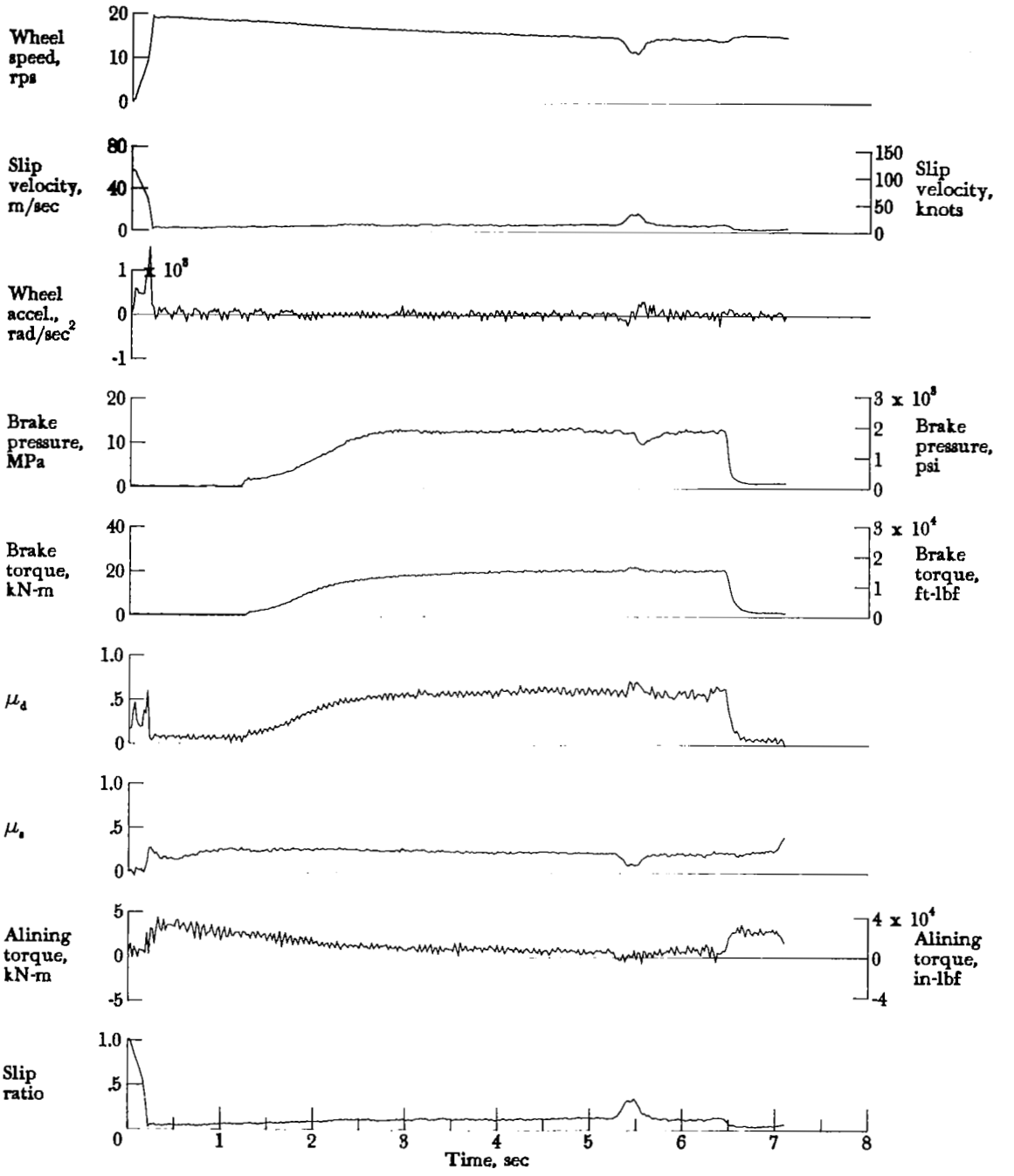

Figure A54.- Time histories for run 54. Nominal carriage speed, 98 knots; vertical load, 70.7 kN (15 900 lbf); yaw angle, 3°; brake pressure, 14 MPa (2000 psi); tire condition, new; surface condition, dry.

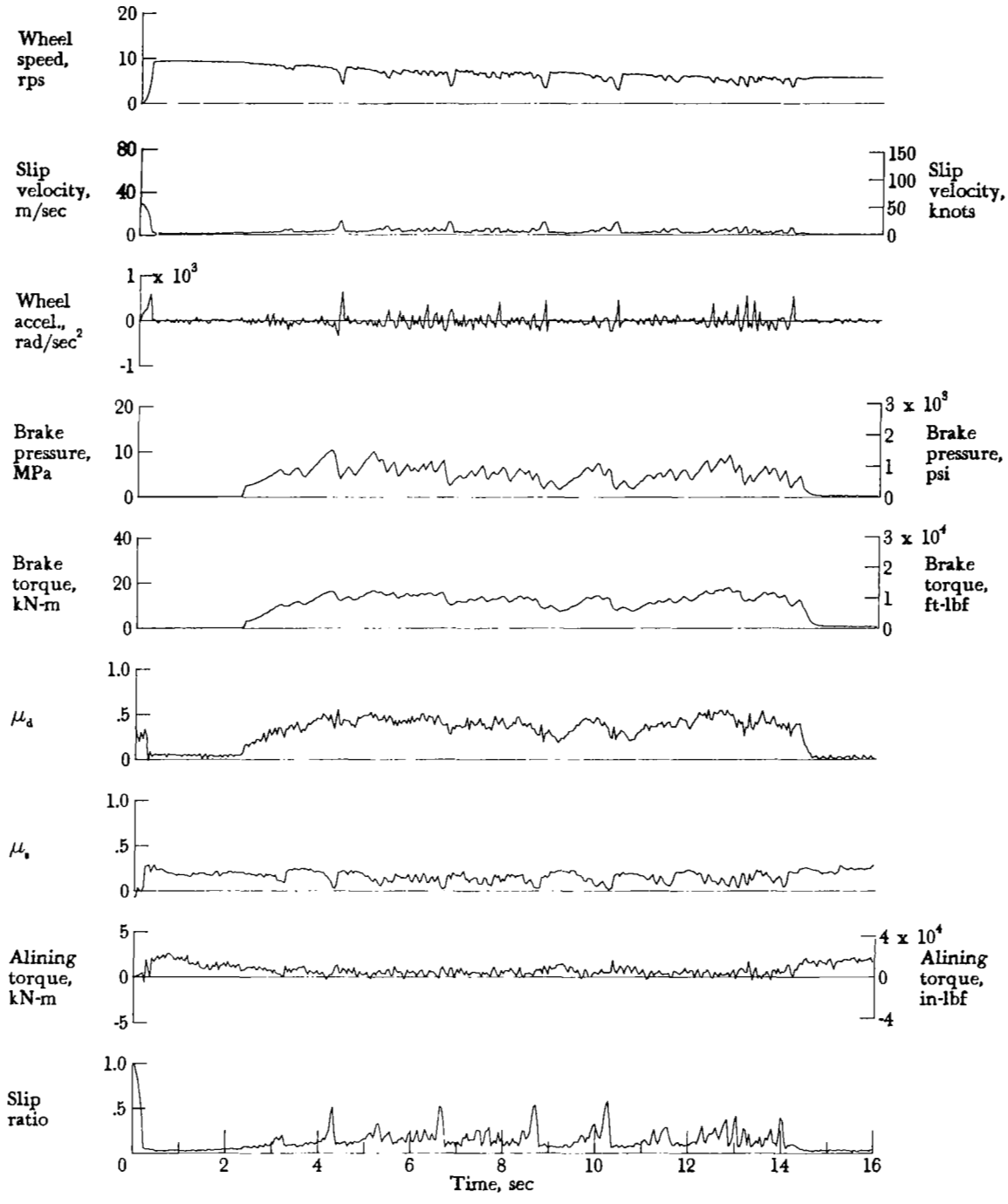

Figure A55.- Time histories for run 55. Nominal carriage speed, 42 knots; vertical load, 69.3 kN (15 600 lbf); yaw angle, 3°; brake pressure, 13 MPa (1850 psi); tire condition, new; surface condition, damp.

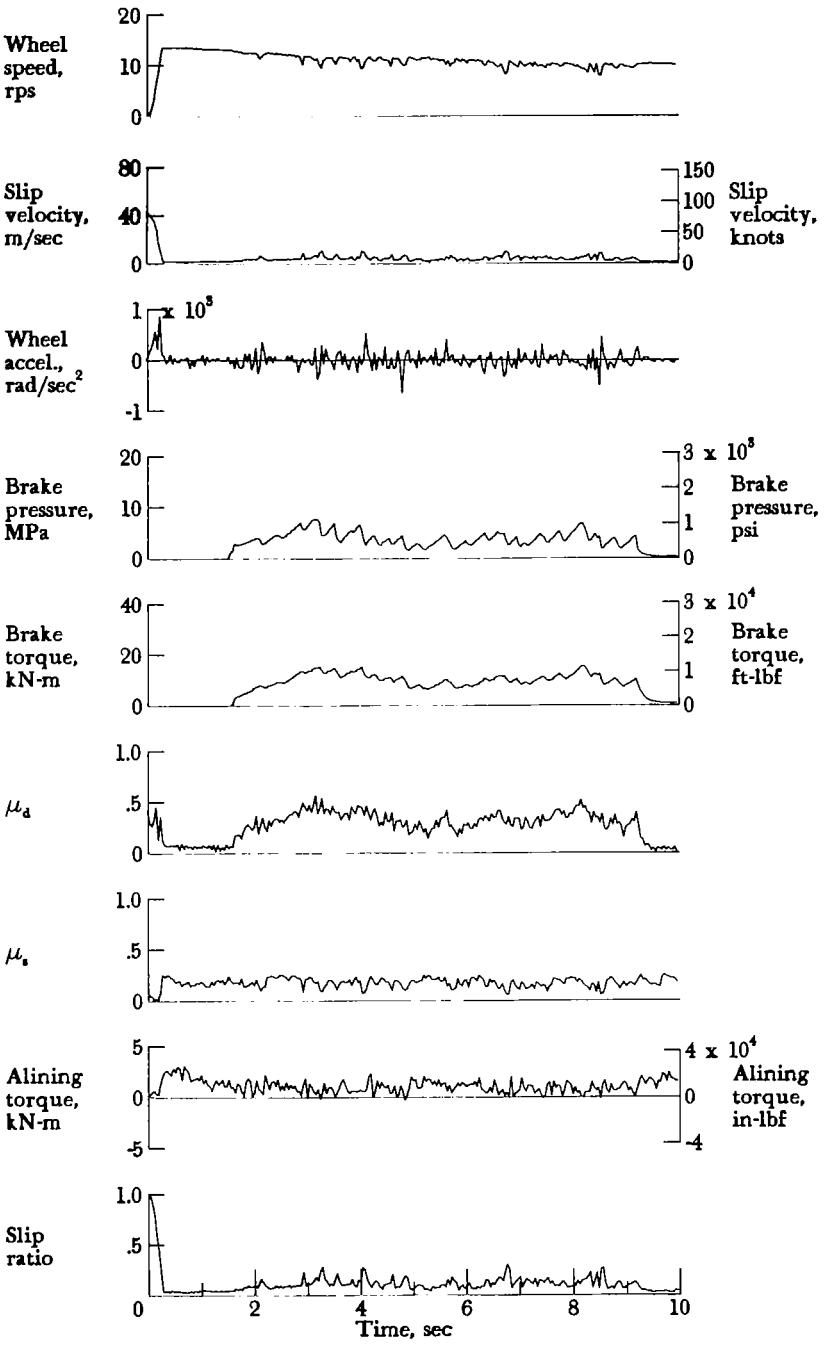

Figure A56.- Time histories for run 56. Nominal carriage speed, 67 knots; vertical load, 70.3 kN (15 800 lbf); yaw angle, 3°; brake pressure, 13 MPa (1850 psi); tire condition, new; surface condition, damp.

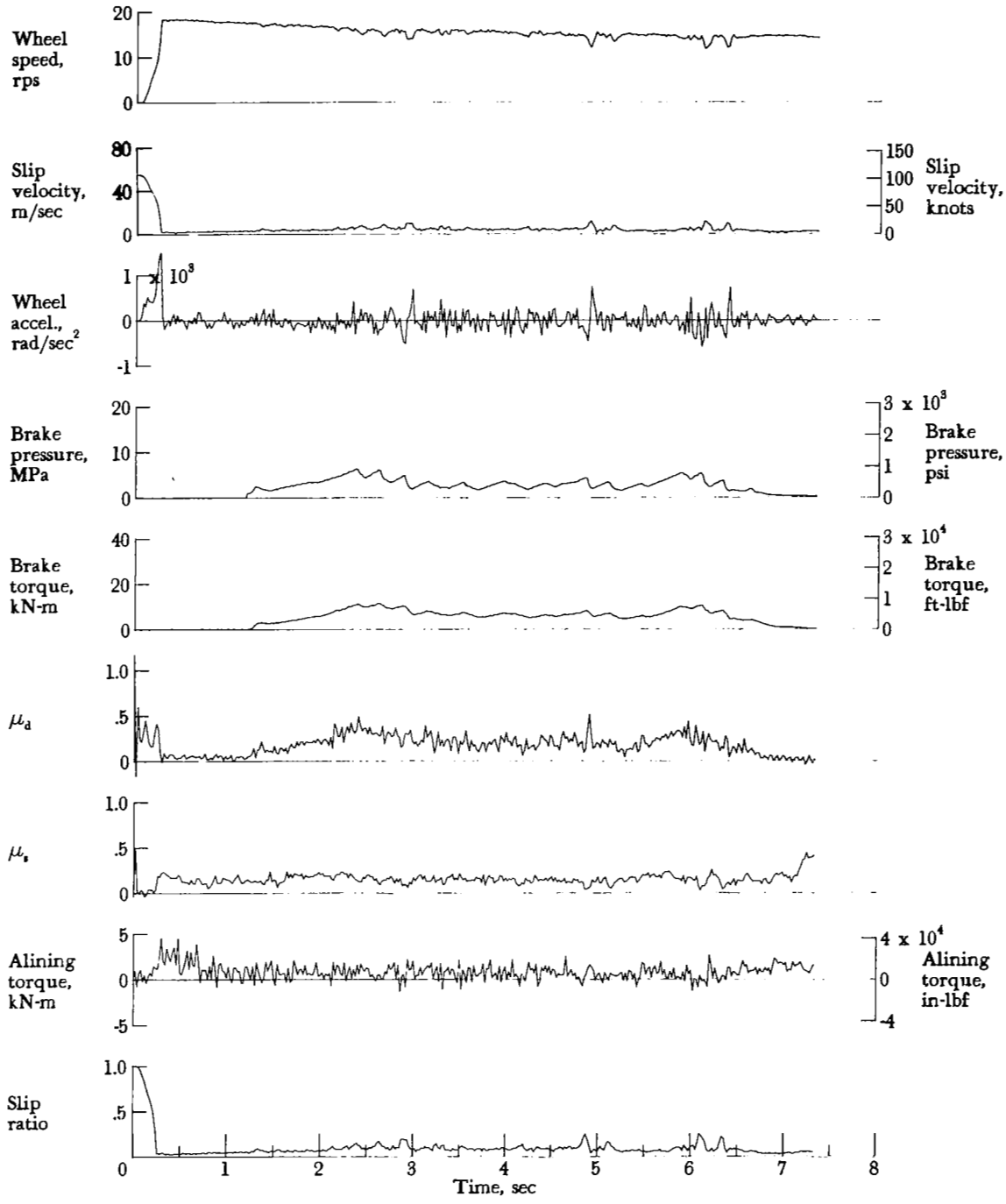

Figure A57.- Time histories for run 57. Nominal carriage speed, 96 knots; vertical load, 69.8 kN (15 700 lbf); yaw angle, 3°; brake pressure, 13 MPa (1850 psi); tire condition, new; surface condition, damp.

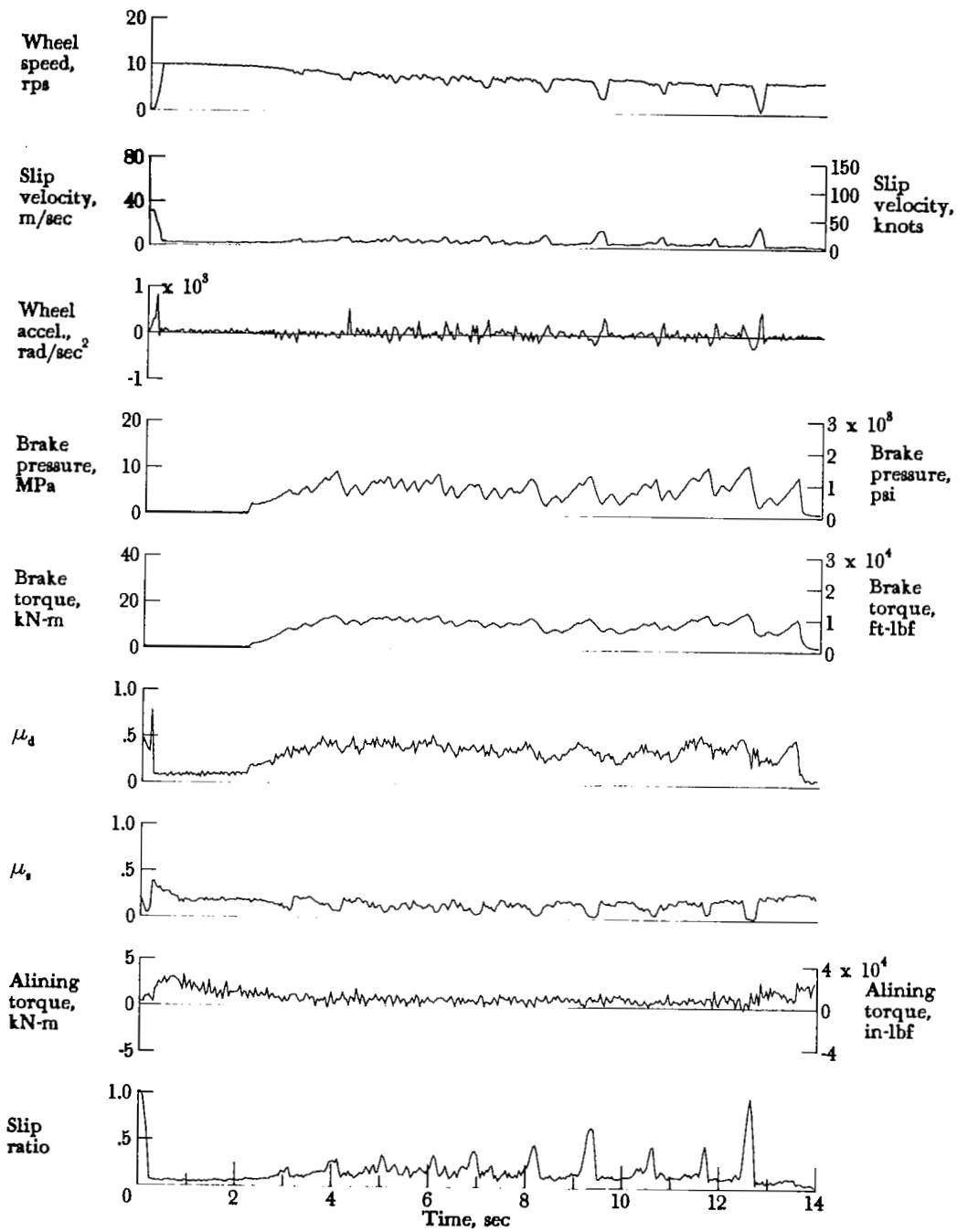

Figure A58.- Time histories for run 58. Nominal carriage speed, 45 knots; vertical load, 69.3 kN (15 600 lbf); yaw angle, 3°; brake pressure, 13 MPa (1950 psi); tire condition, new; surface condition, flooded.

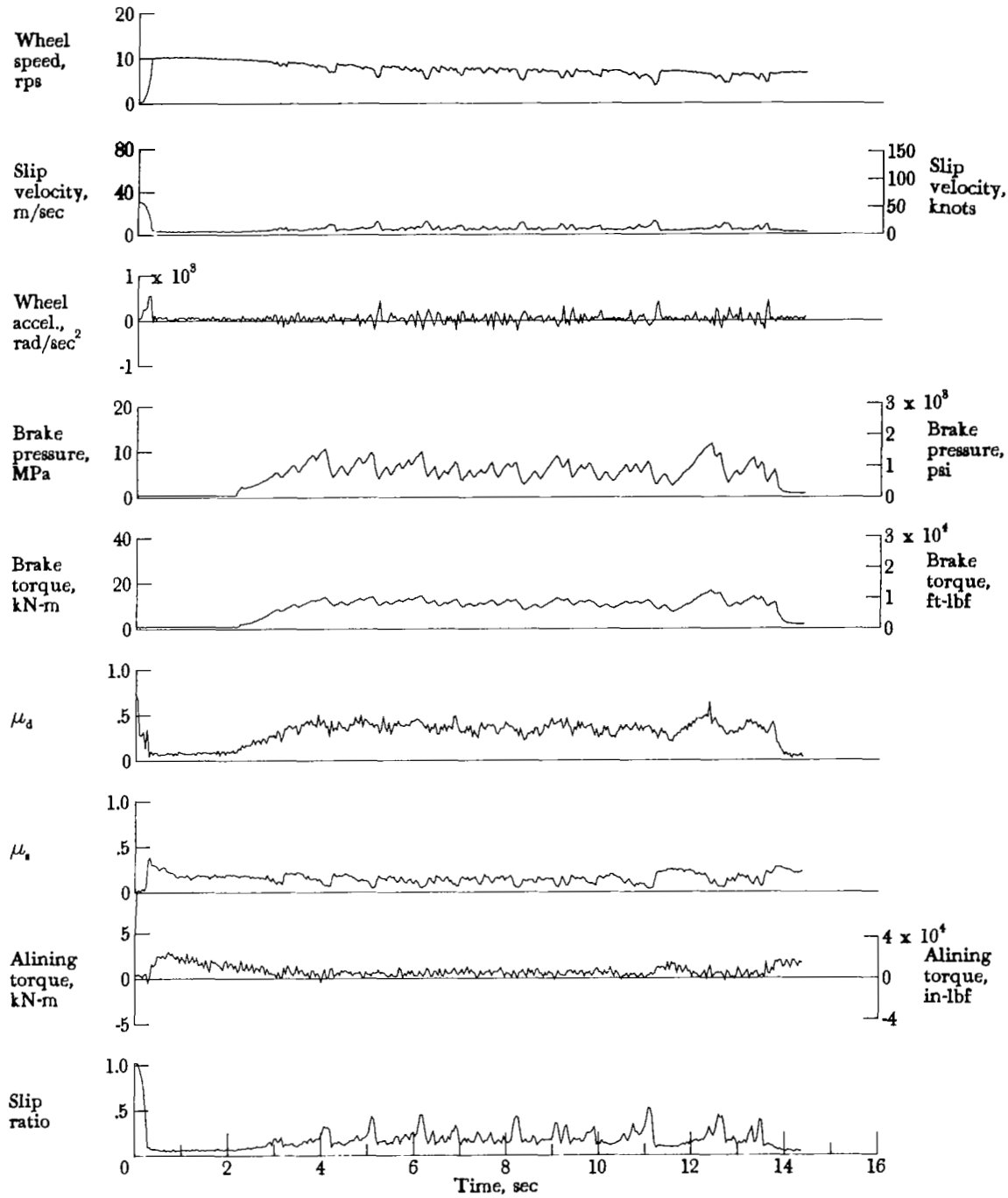

Figure A59.- Time histories for run 59. Nominal carriage speed, 45 knots; vertical load, 69.8 kN (15 700 lbf); yaw angle, 3°; brake pressure, 13 MPa (1950 psi); tire condition, new; surface condition, flooded.

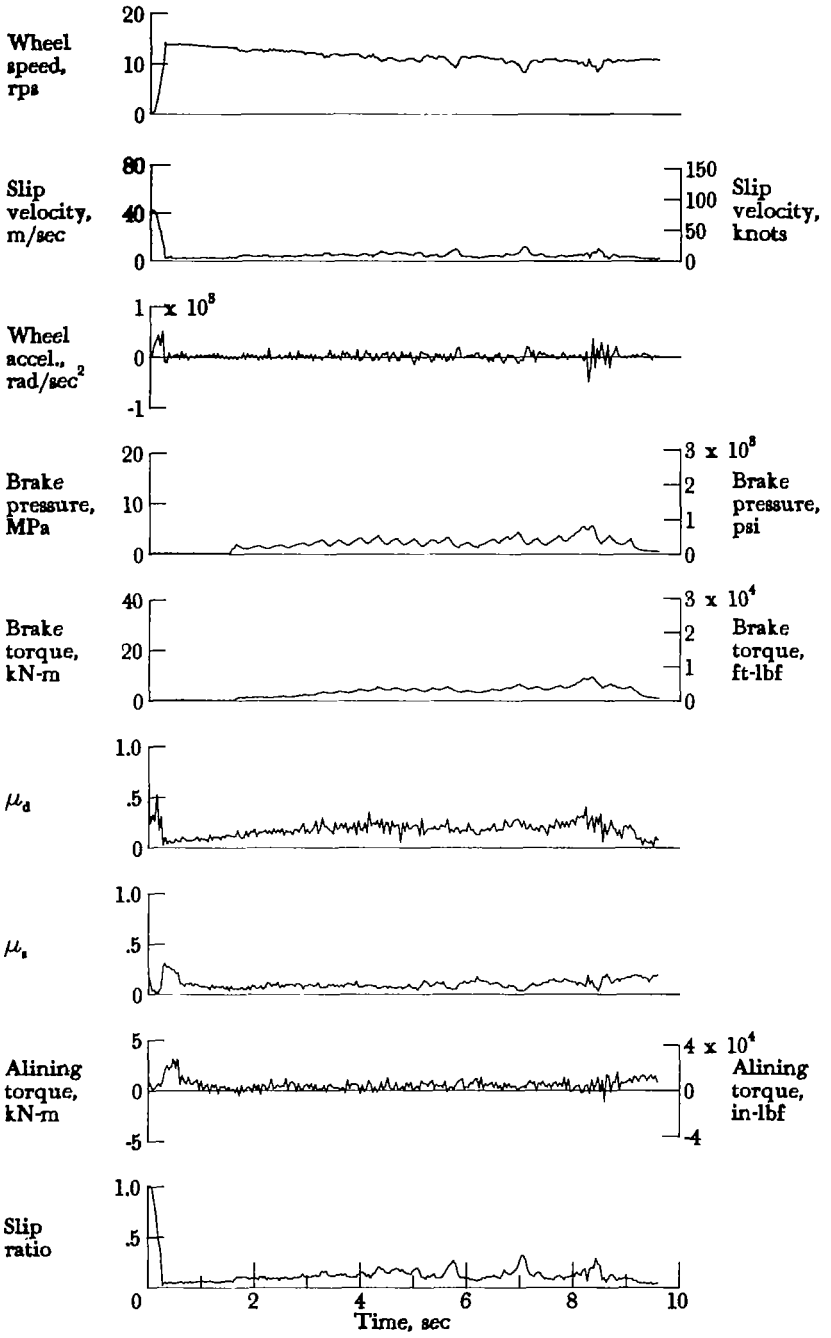

Figure A60.- Time histories for run 60. Nominal carriage speed, 69 knots; vertical load, 68.9 kN (15 500 lbf); yaw angle, 3°; brake pressure, 13 MPa (1900 psi); tire condition, new; surface condition, flooded.

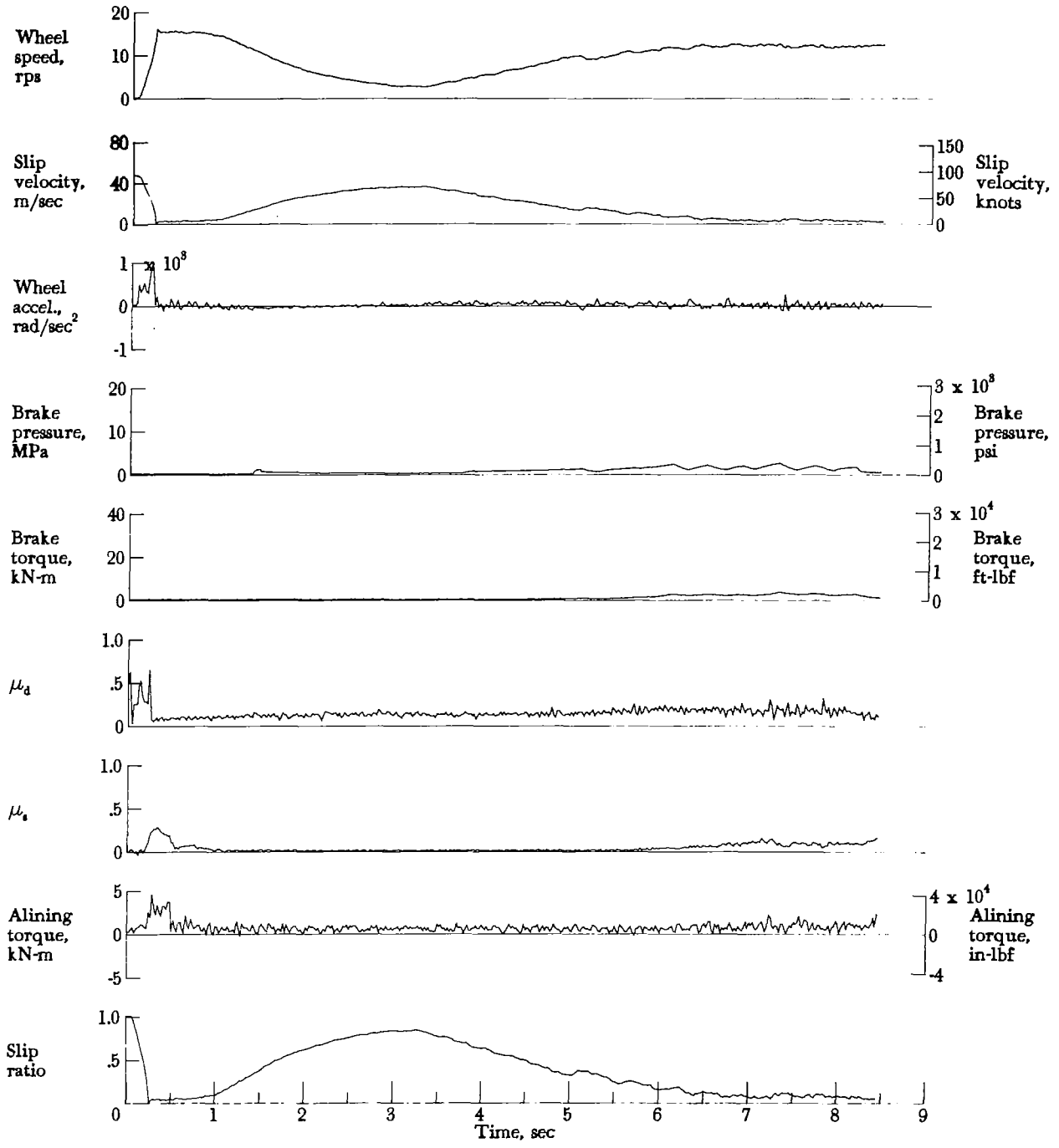

Figure A61.- Time histories for run 61. Nominal carriage speed, 79 knots; vertical load, 68.1 kN (15 300 lbf); yaw angle, 3°; brake pressure, 13 MPa (1850 psi); tire condition, new; surface condition, flooded.

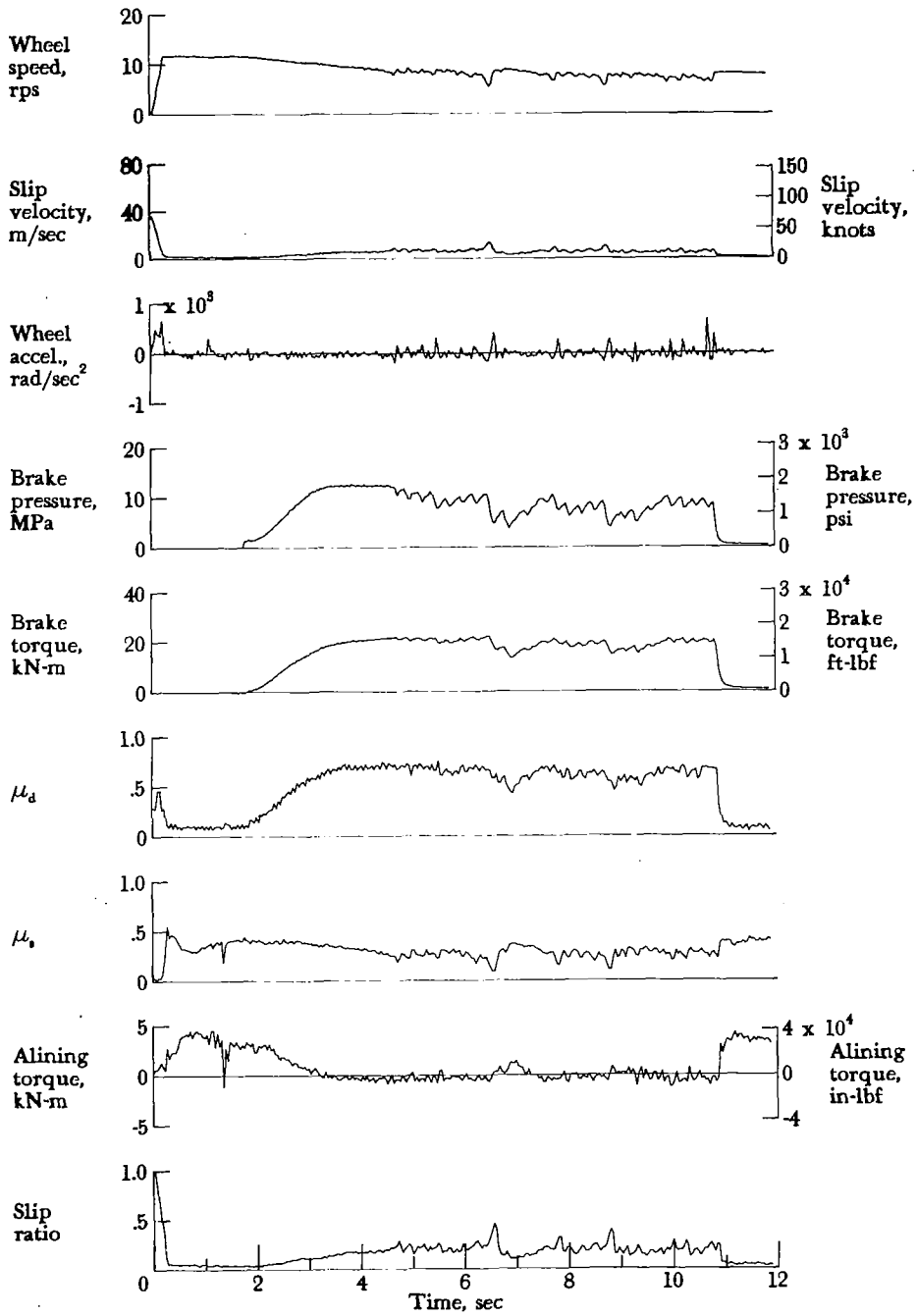

Figure A62.- Time histories for run 62. Nominal carriage speed, 56 knots; vertical load, 70.7 kN (15 900 lbf); yaw angle, 6°; brake pressure, 13 MPa (1900 psi); tire condition, new; surface condition, dry.

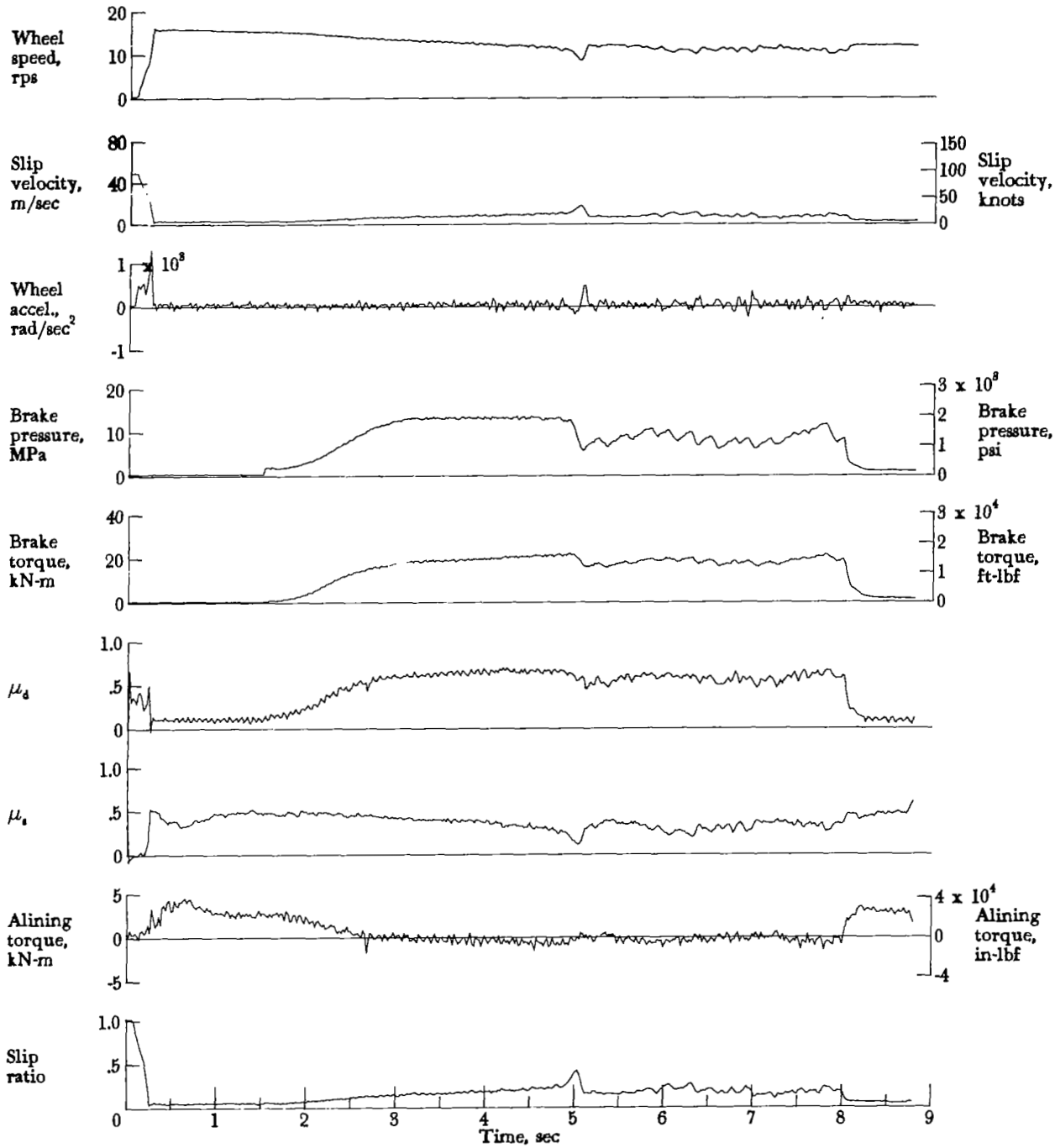

Figure A63.- Time histories for run 63. Nominal carriage speed, 78 knots; vertical load, 70.7 kN (15 900 lbf); yaw angle, 6°; brake pressure, 13 MPa (1950 psi); tire condition, new; surface condition, dry.

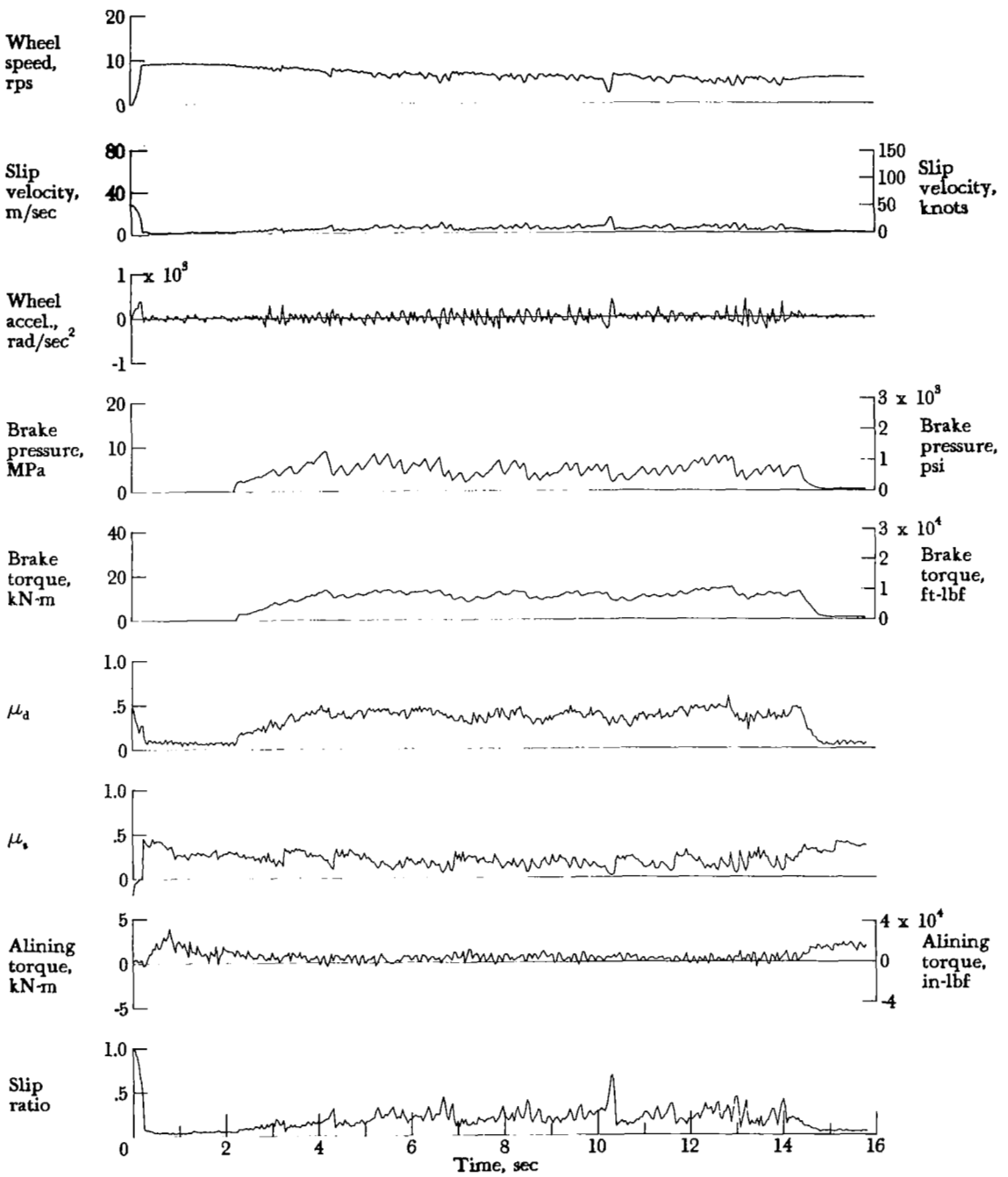

Figure A64.- Time histories for run 64. Nominal carriage speed, 42 knots; vertical load, 68.9 kN (15 500 lbf); yaw angle, 6°; brake pressure, 13 MPa (1850 psi); tire condition, new; surface condition, damp.

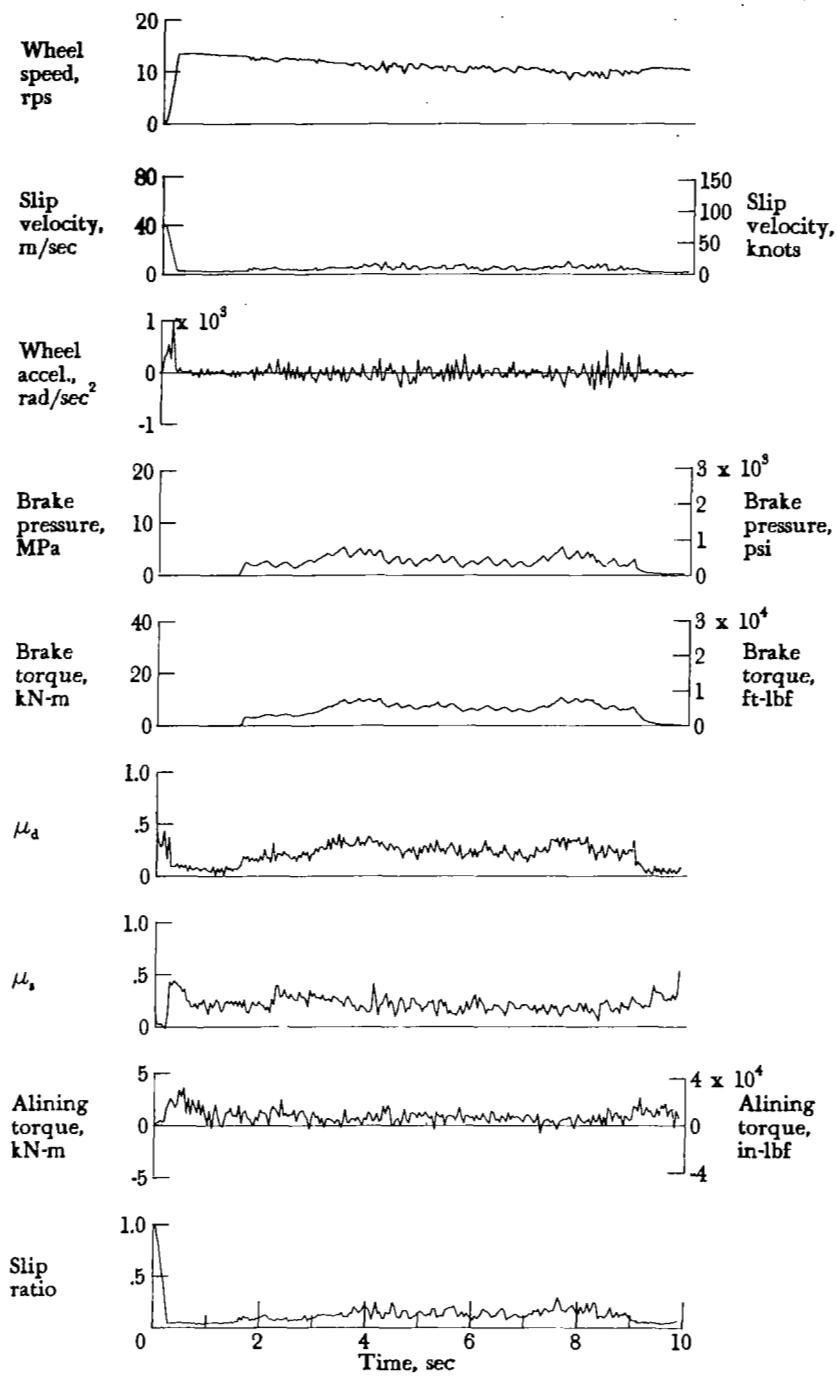

Figure A65.- Time histories for run 65. Nominal carriage speed, 70 knots; vertical load, 69.3 kN (15 600 lbf); yaw angle, 6°; brake pressure, 13 MPa (1850 psi); tire condition, new; surface condition, damp.

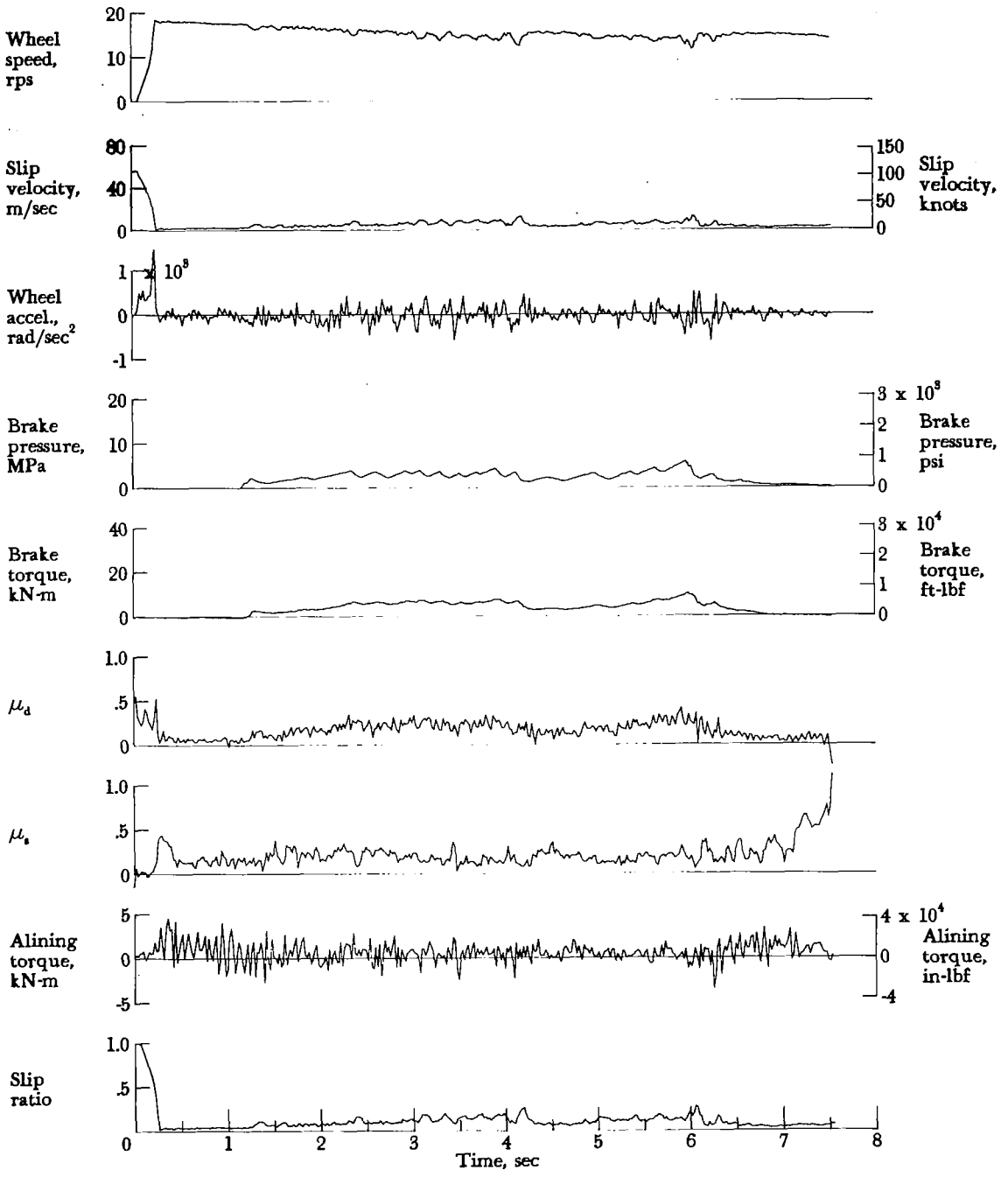

Figure A66.- Time histories for run 66. Nominal carriage speed, 96 knots; vertical load, 68.9 kN (15 500 lbf); yaw angle, 6°; brake pressure, 13 MPa (1950 psi); tire condition, new; surface condition, damp.

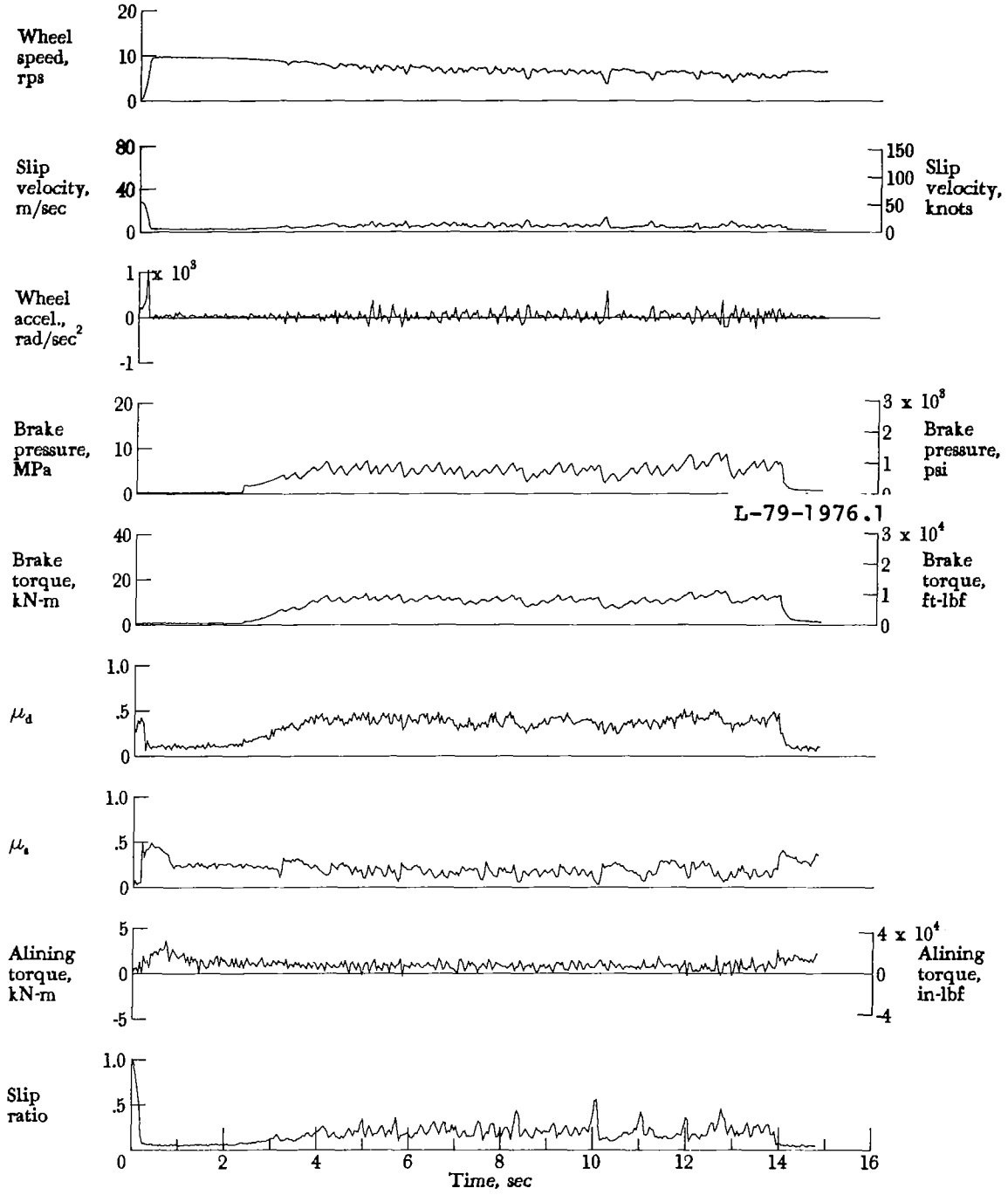

Figure A67.- Time histories for run 67. Nominal carriage speed, 44 knots; vertical load, 69.8 kN (15 700 lbf); yaw angle, 6°; brake pressure, 13 MPa (1950 psi); tire condition, new; surface condition, flooded.

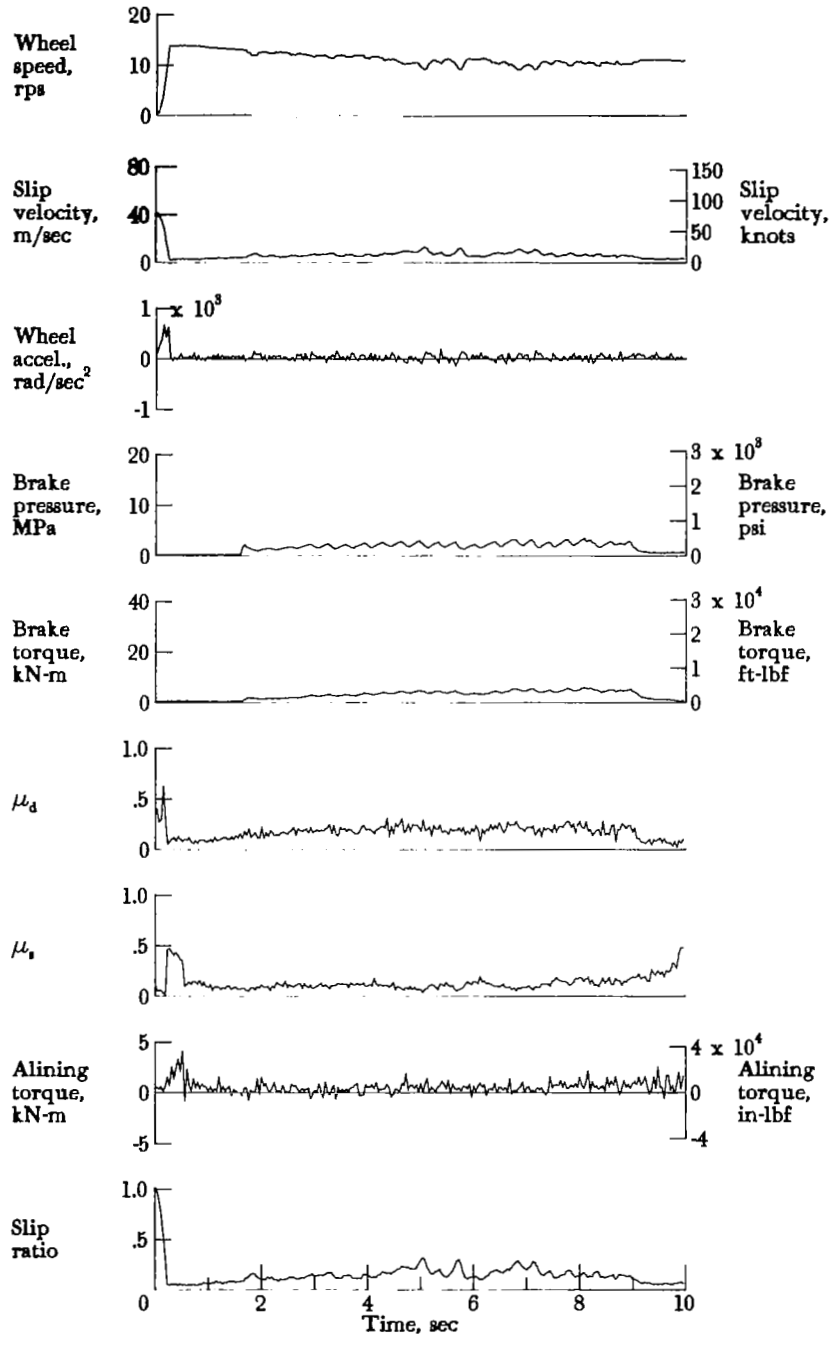

Figure A68.- Time histories for run 68. Nominal carriage speed, 70 knots; vertical load, 68.9 kN (15 500 lbf); yaw angle, 6°; brake pressure, 13 MPa (1950 psi); tire condition, new; surface condition, flooded.

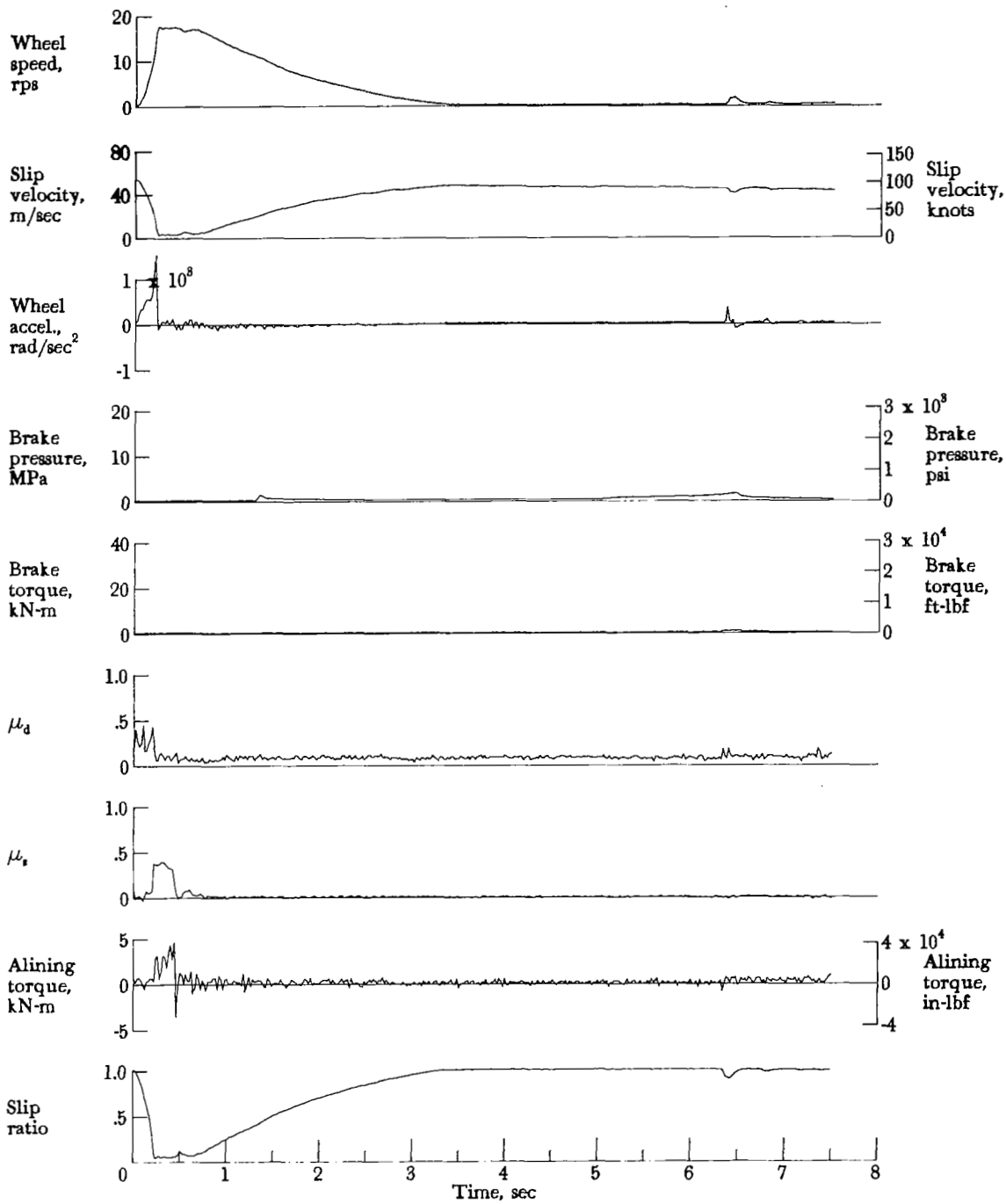

Figure A69.- Time histories for run 69. Nominal carriage speed, 91 knots; vertical load, 68.5 kN (15 400 lbf); yaw angle, 6°; brake pressure, 13 MPa (1950 psi); tire condition, new; surface condition, flooded.

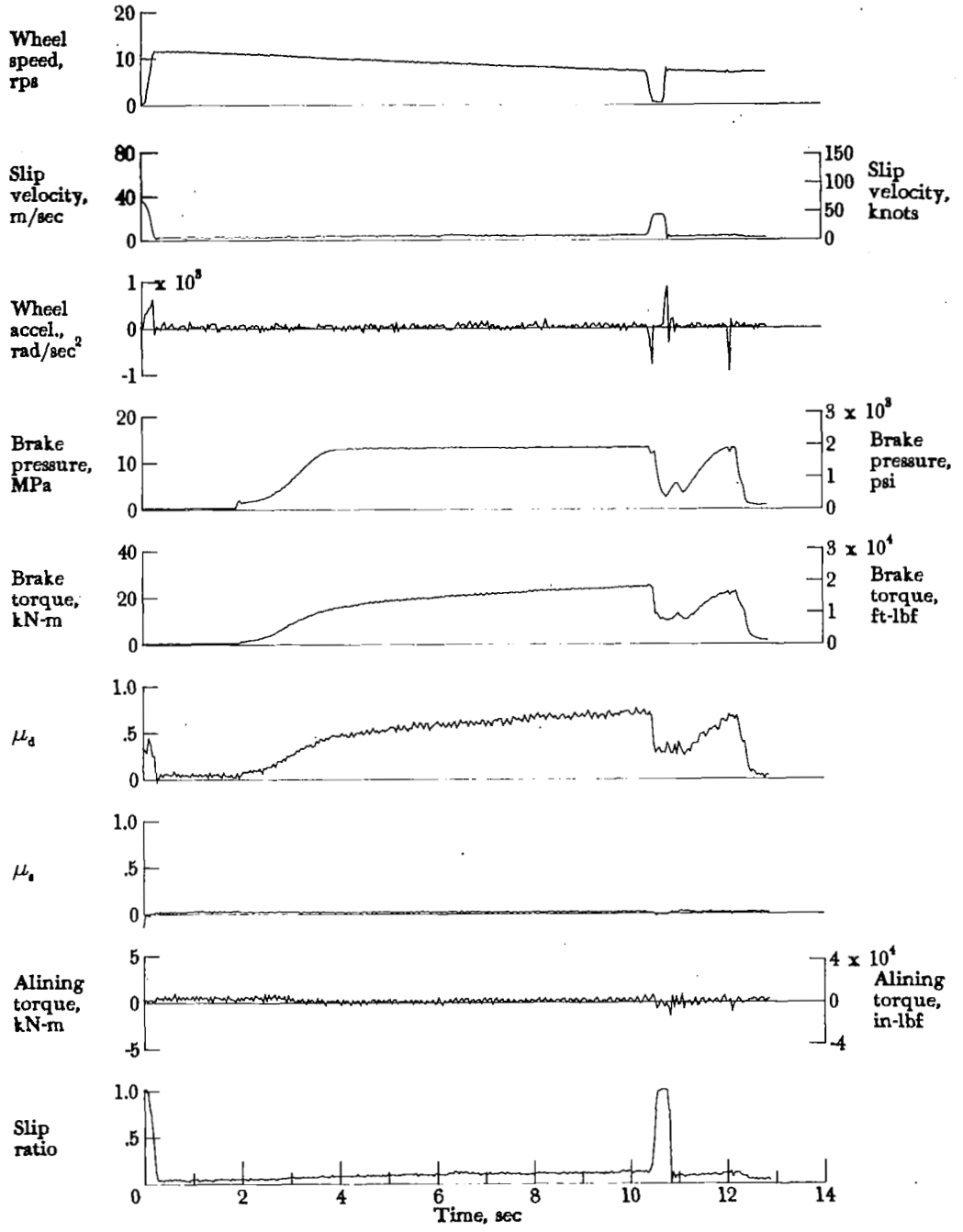

Figure A70.- Time histories for run 70. Nominal carriage speed, 50 knots; vertical load, 69.3 kN (15 600 lbf); yaw angle, 0°; brake pressure, 13 MPa (1950 psi); tire condition, worn; surface condition, dry.

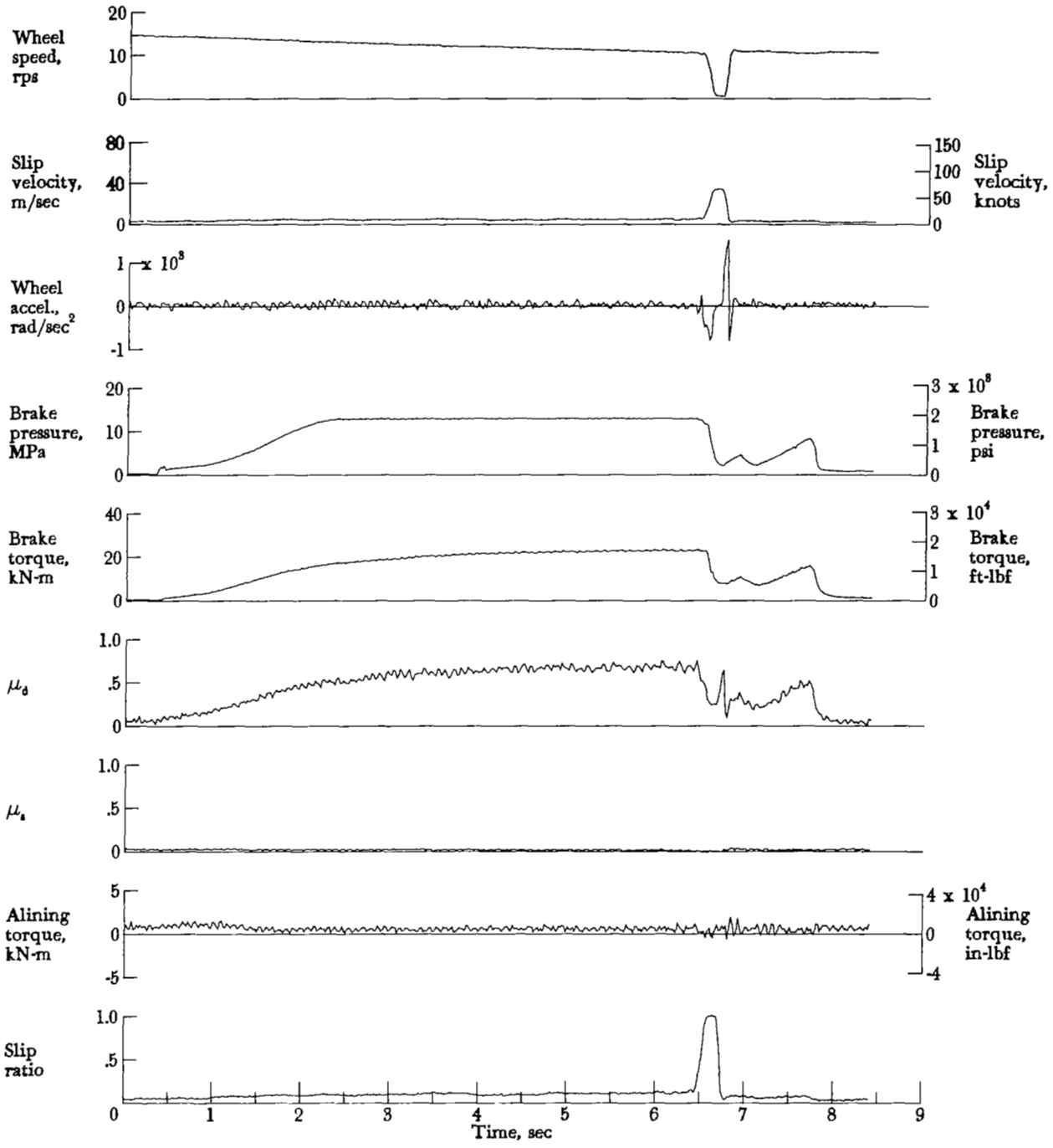

Figure A71.- Time histories for run 71. Nominal carriage speed, 72 knots; vertical load, 68.9 kN (15 500 lbf); yaw angle, 0°; brake pressure, 13 MPa (1950 psi); tire condition, worn; surface condition, dry.

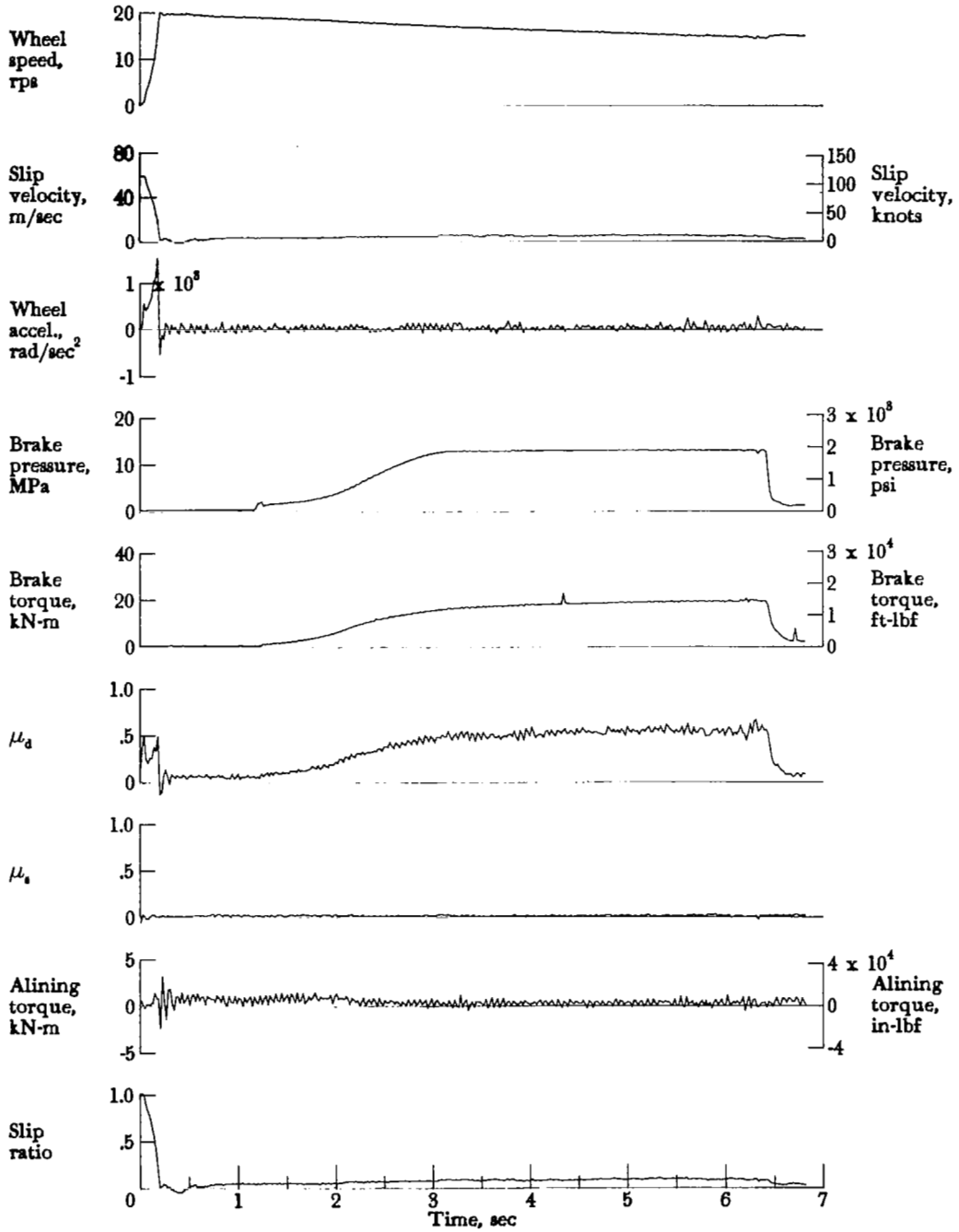

Figure A72.- Time histories for run 72. Nominal carriage speed, 98 knots; vertical load, 69.8 kN (15 700 lbf); yaw angle, 0°; brake pressure, 13 MPa (1900 psi); tire condition, worn; surface condition, dry.

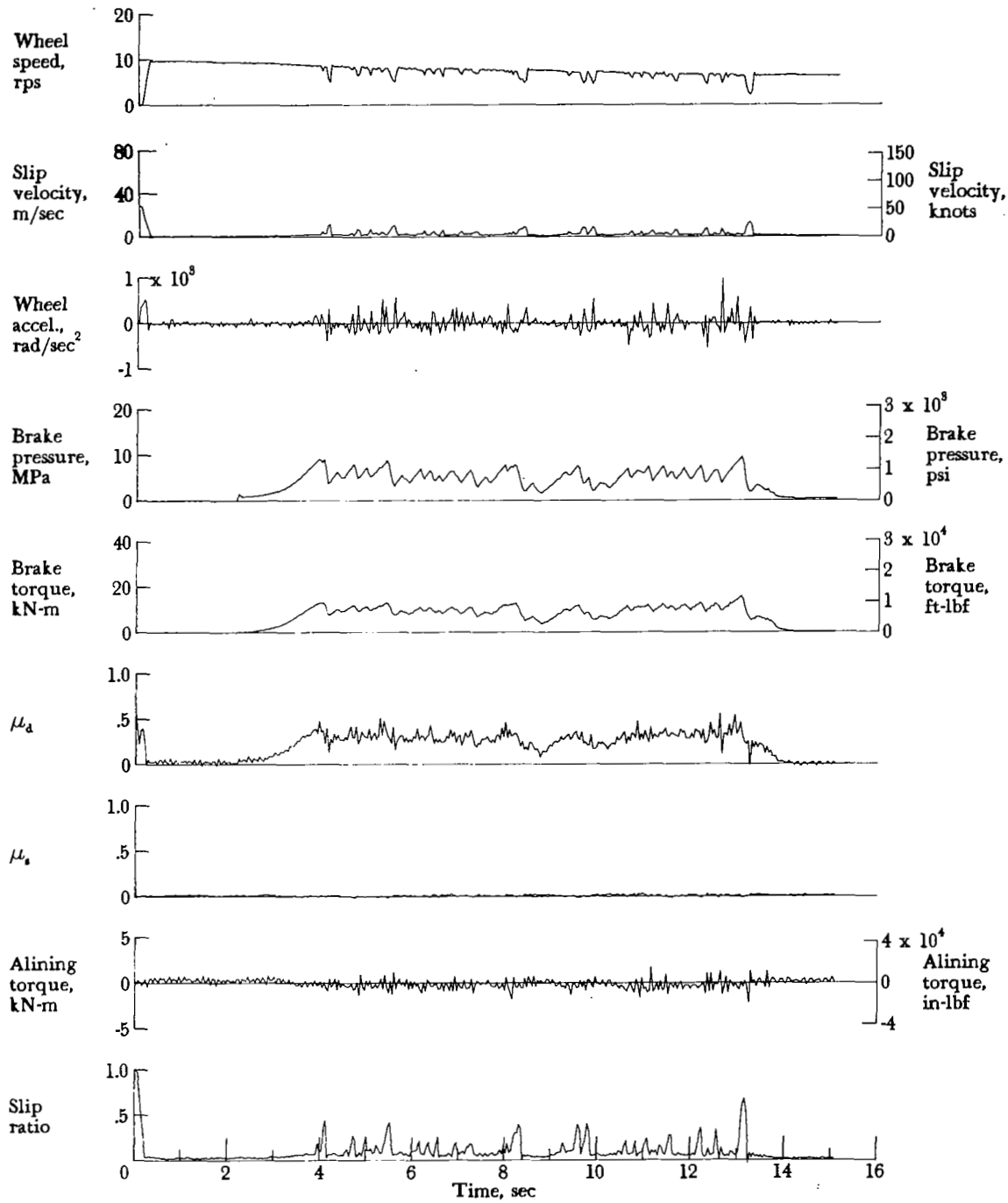

Figure A73.- Time histories for run 73. Nominal carriage speed, 44 knots; vertical load, 69.6 kN (15 600 lbf); yaw angle, 0°; brake pressure, 13 MPa (1900 psi); tire condition, worn; surface condition, damp.

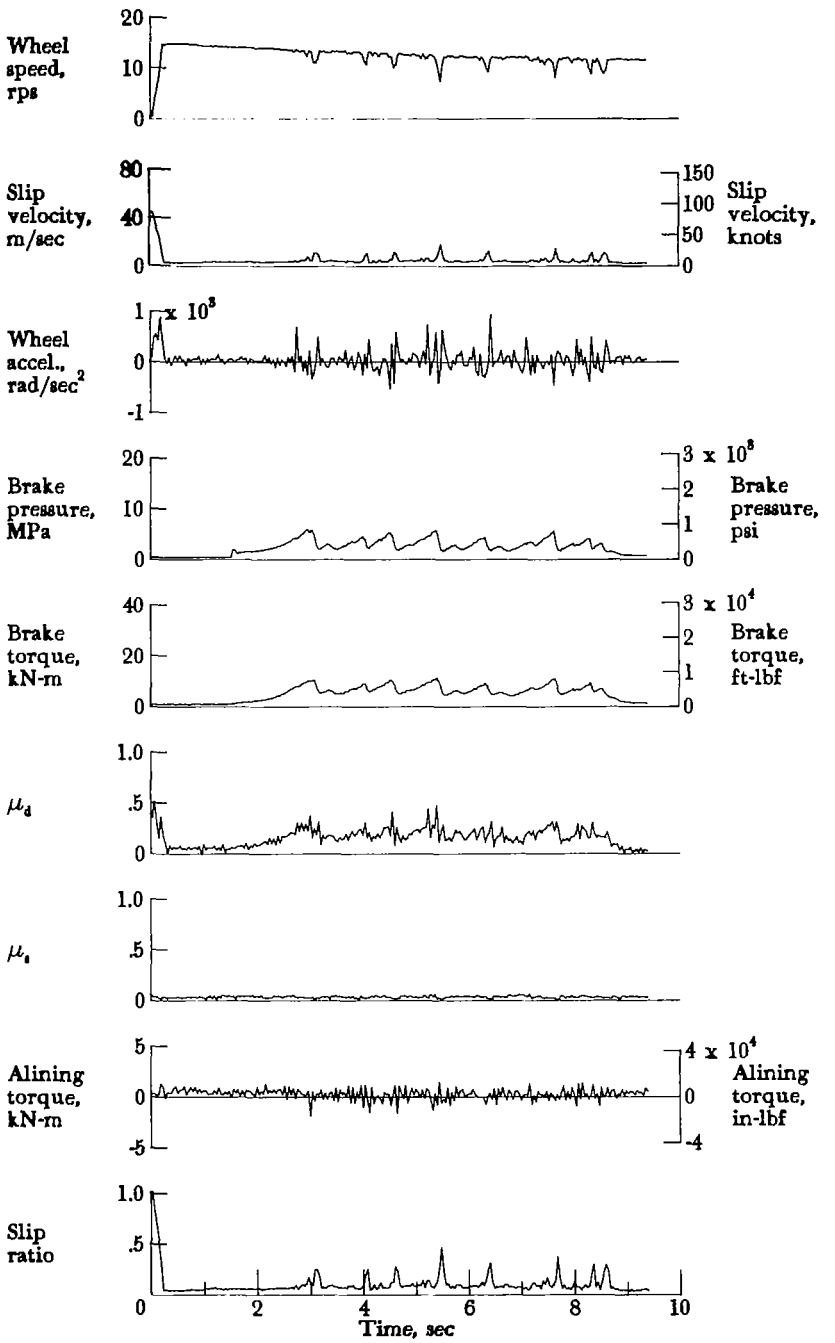

Figure A74.- Time histories for run 74. Nominal carriage speed, 72 knots; vertical load, 69.8 kN (15 700 lbf); yaw angle, 0°; brake pressure, 13 MPa (1900 psi); tire condition, worn; surface condition, damp.

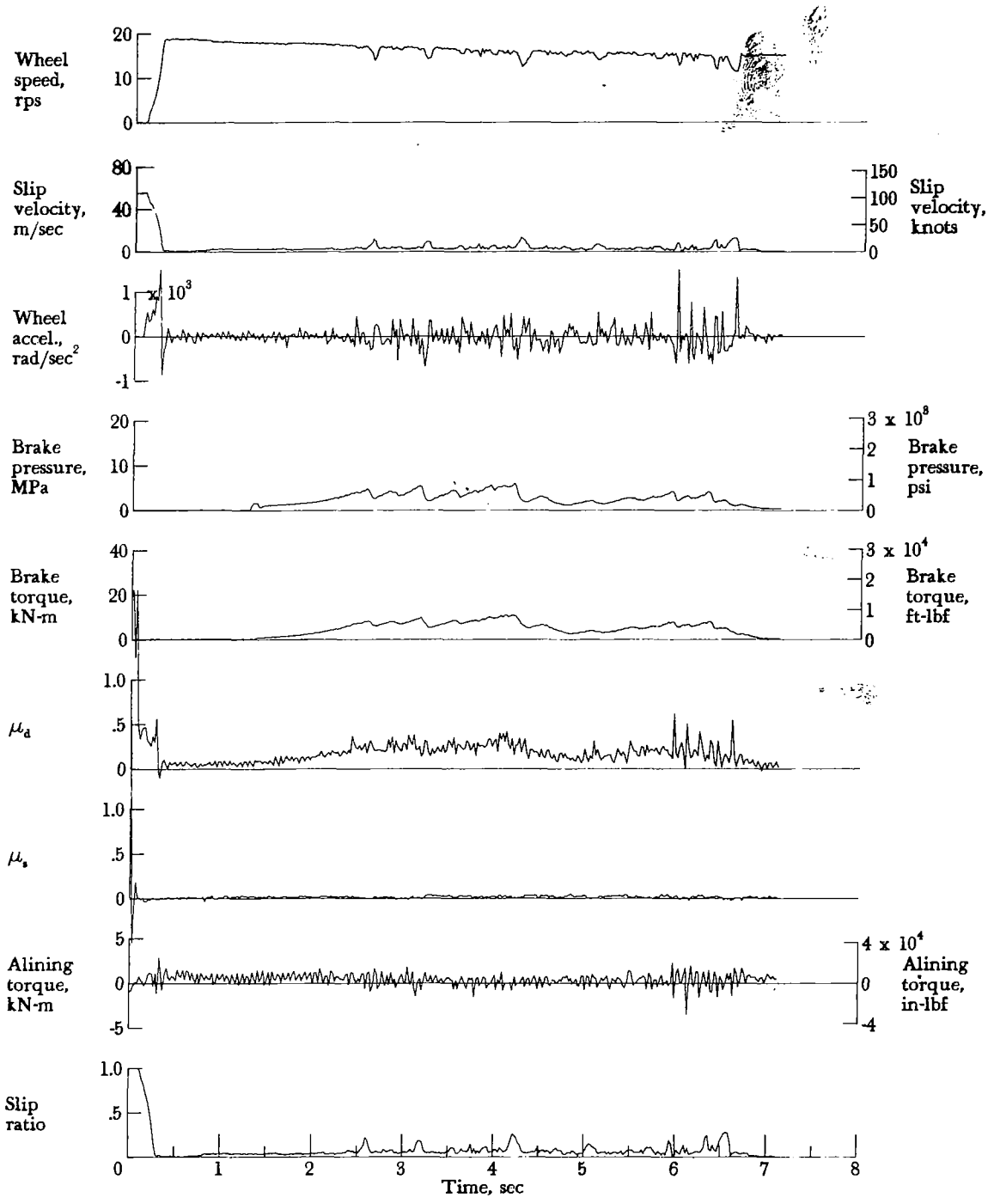

Figure A75.- Time histories for run 75. Nominal carriage speed, 98 knots; vertical load, 69.8 kN (15 700 lbf); yaw angle, 0°; brake pressure, 13 MPa (1950 psi); tire condition, worn; surface condition, damp.

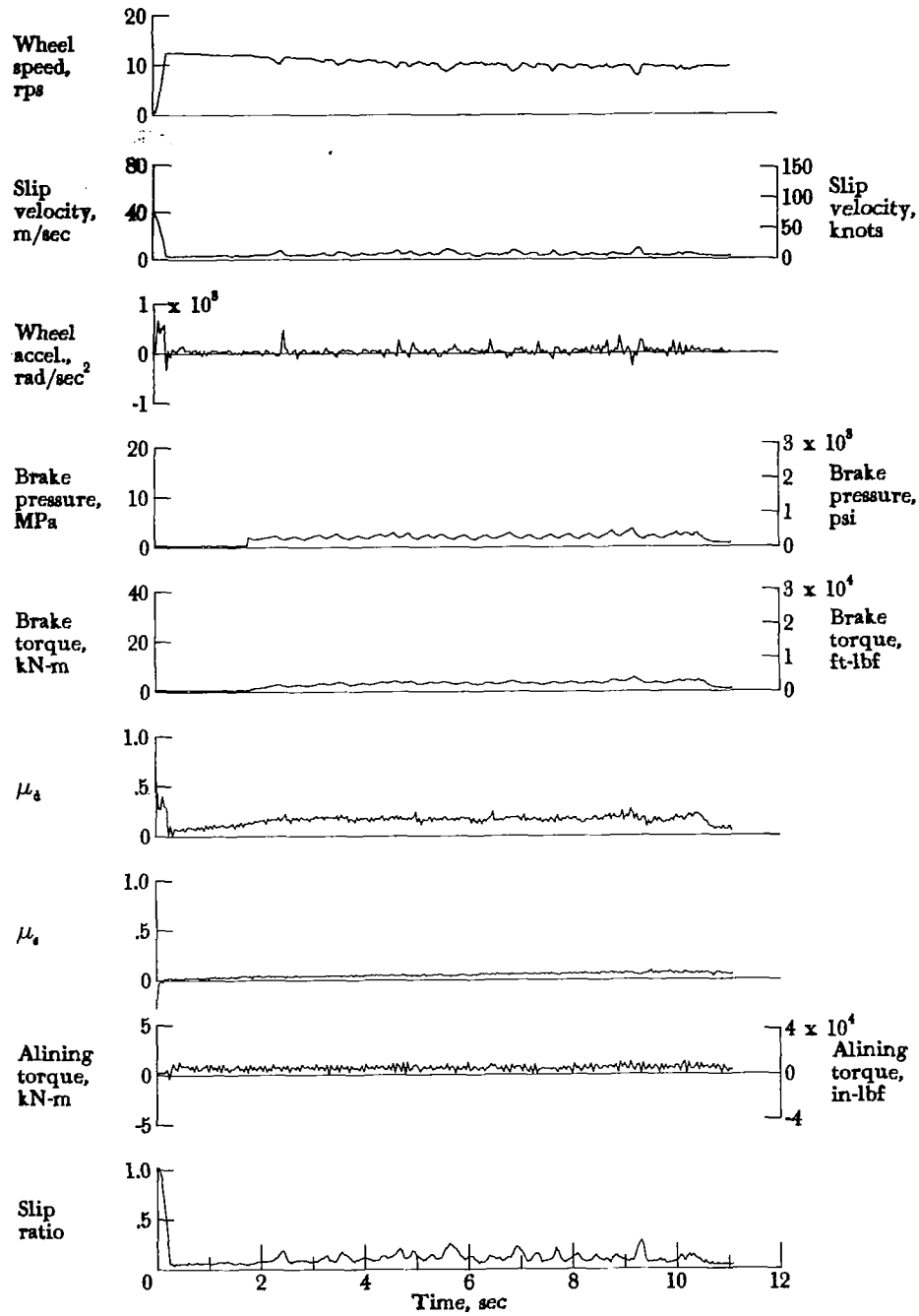

Figure A76.- Time histories for run 76. Nominal carriage speed, 60 knots; vertical load, 66.7 kN (15 000 lbf); yaw angle, 0°; brake pressure, 13 MPa (1900 psi); tire condition, worn; surface condition, flooded.

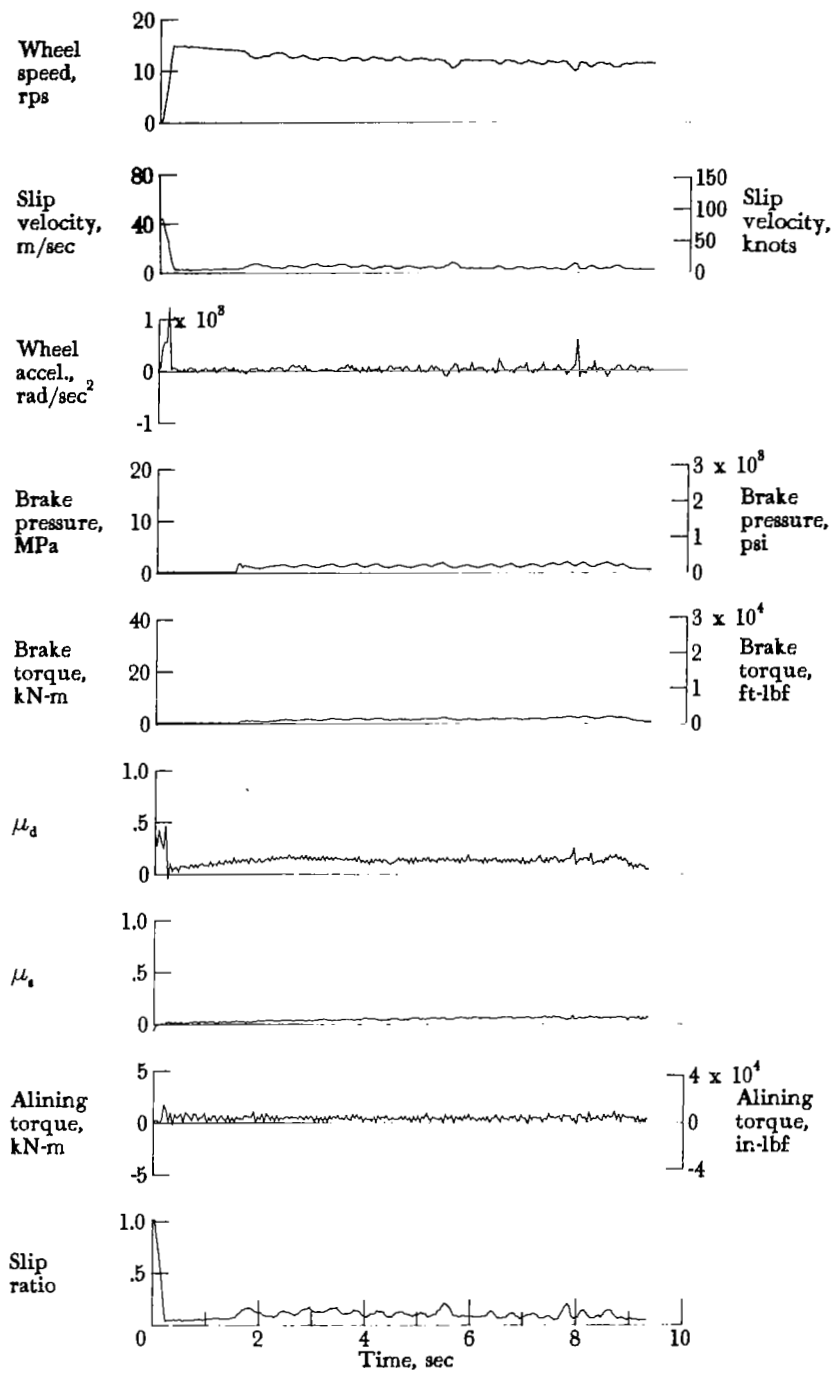

Figure A77.- Time histories for run 77. Nominal carriage speed, 72 knots; vertical load, 67.6 kN (15 200 lbf); yaw angle, 0°; brake pressure, 13 MPa (1850 psi); tire condition, worn; surface condition, flooded.

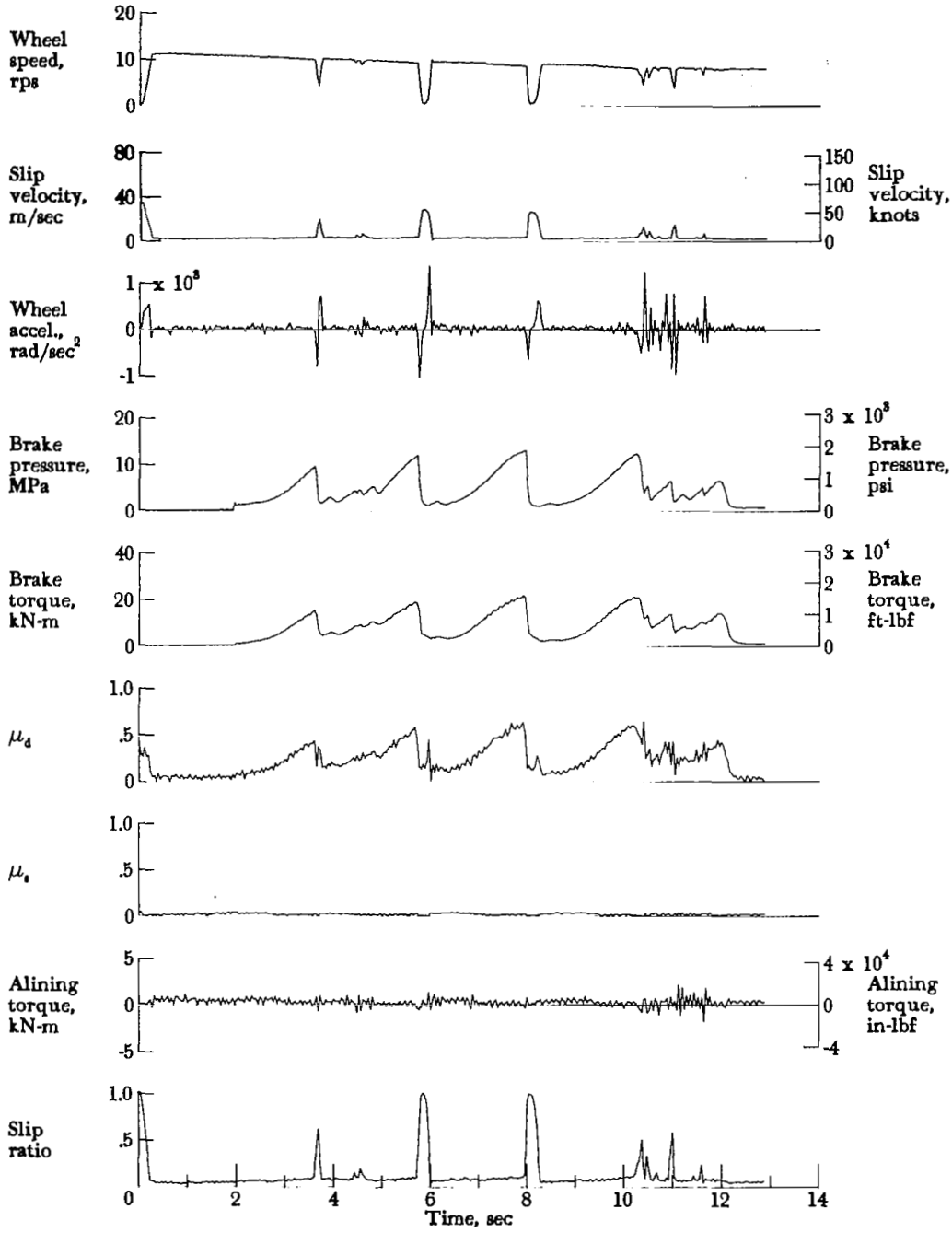

Figure A78.- Time histories for run 78. Nominal carriage speed, 52 knots; vertical load, 69.6 kN (15 600 lbf); yaw angle, 0°; brake pressure, 13 MPa (1950 psi); tire condition, worn; surface condition, alternating dry and damp at 30.5-m (100-ft) intervals.

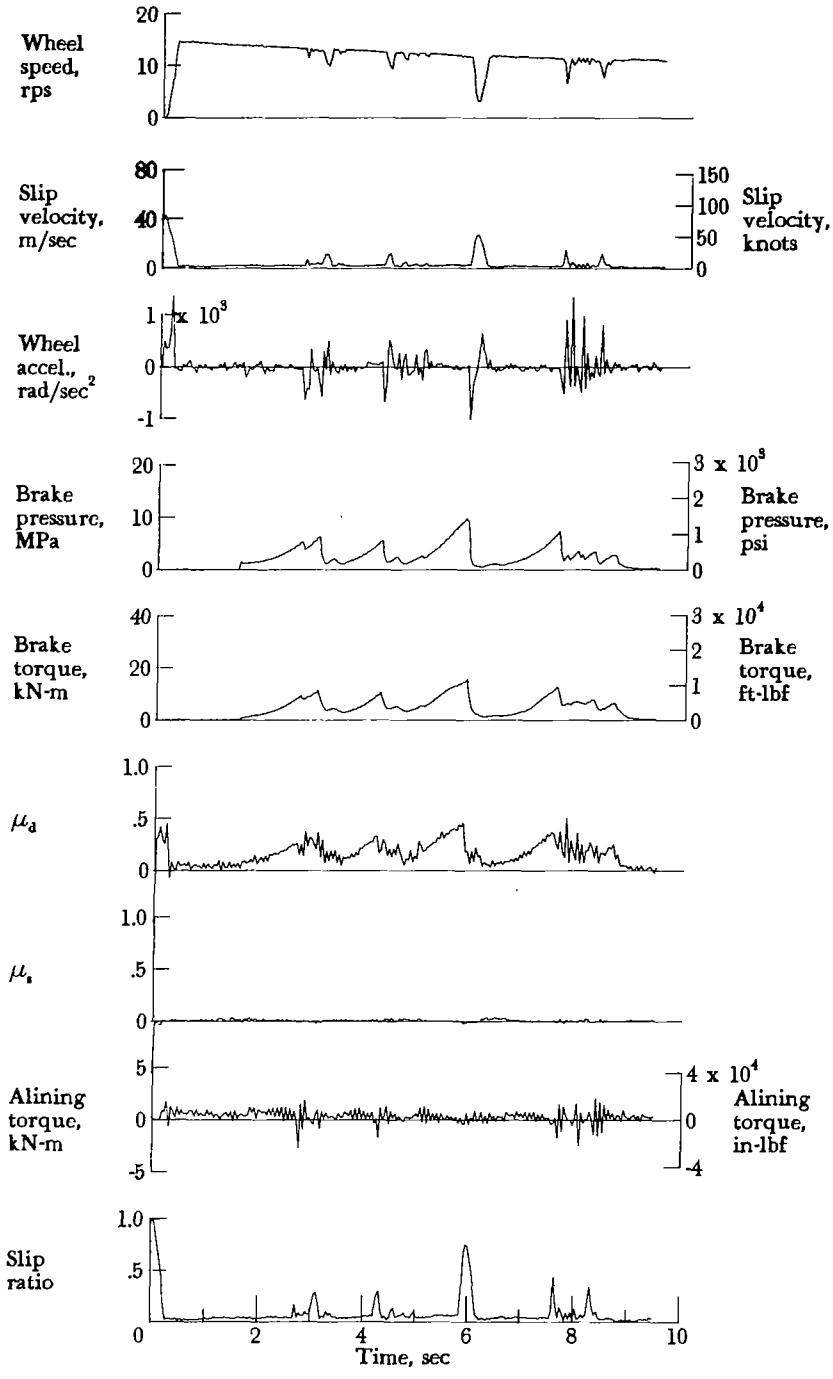

Figure A79.- Time histories for run 79. Nominal carriage speed, 73 knots; vertical load, 70.3 kN (15 800 lbf); yaw angle, 0°; brake pressure, 13 MPa (1950 psi); tire condition, worn; surface condition, alternating dry and damp at 30.5-m (100-ft) intervals.

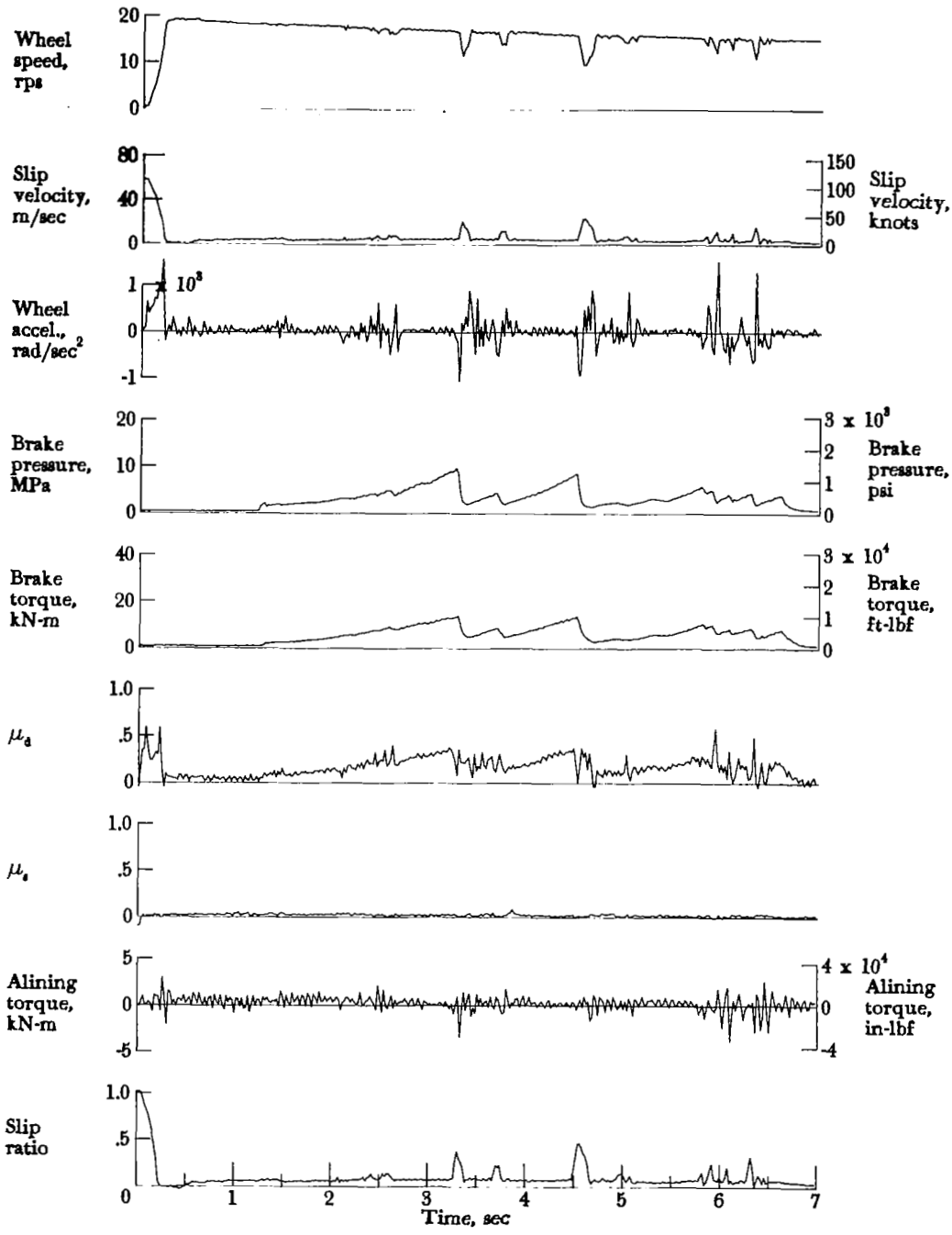

Figure A80.- Time histories for run 80. Nominal carriage speed, 96 knots; vertical load, 71.2 kN (16 000 lbf); yaw angle, 0°; brake pressure, 13 MPa (1900 psi); tire condition, worn; surface condition, alternating dry and damp at 30.5-m (100-ft) intervals.

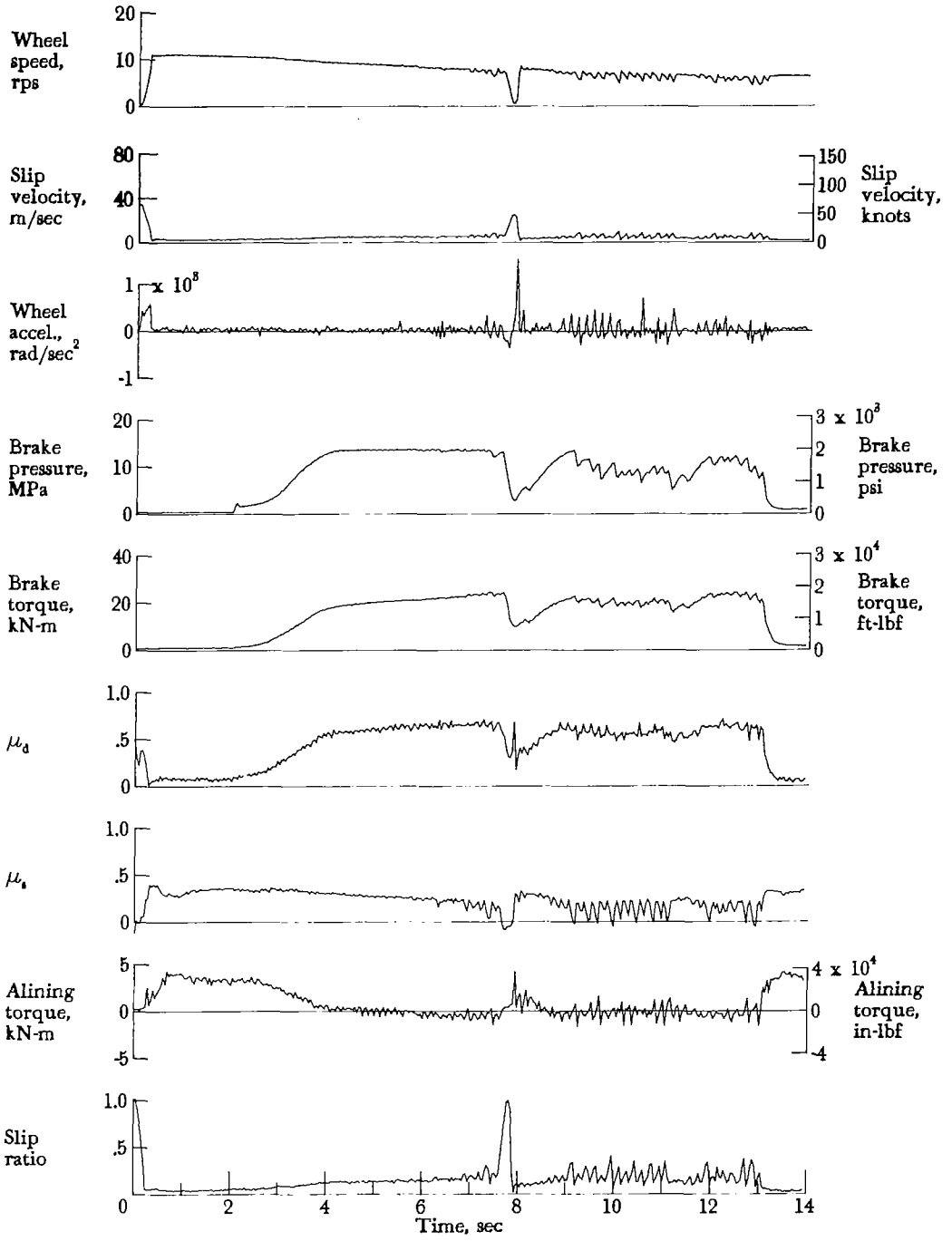

Figure A81.- Time histories for run 81. Nominal carriage speed, 46 knots; vertical load, 72.5 kN (16 300 lbf); yaw angle, 6°; brake pressure, 14 MPa (2000 psi); tire condition, worn; surface condition, dry.

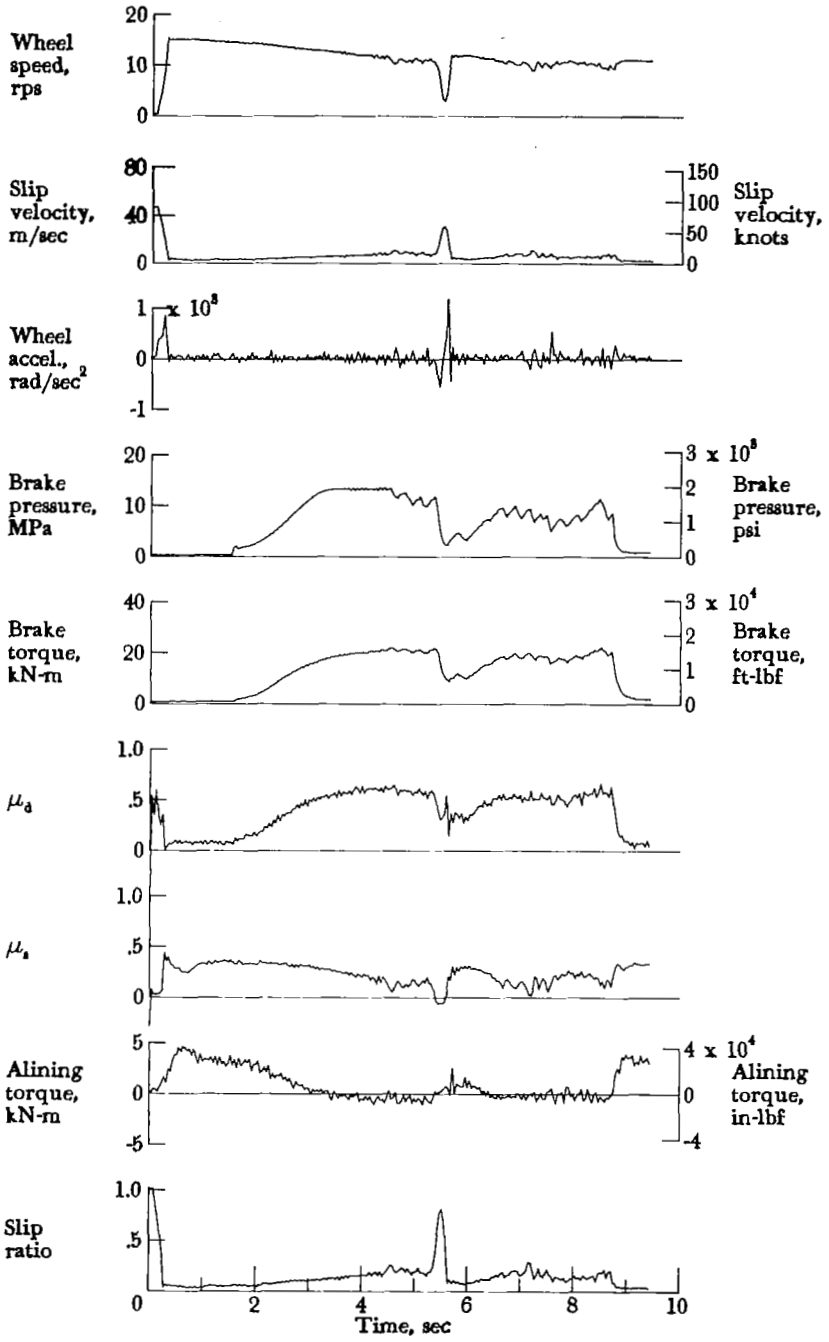

Figure A82.- Time histories for run 82. Nominal carriage speed, 72 knots; vertical load, 72.1 kN (16 200 lbf); yaw angle, 6°; brake pressure, 13 MPa (1950 psi); tire condition, worn; surface condition, dry.

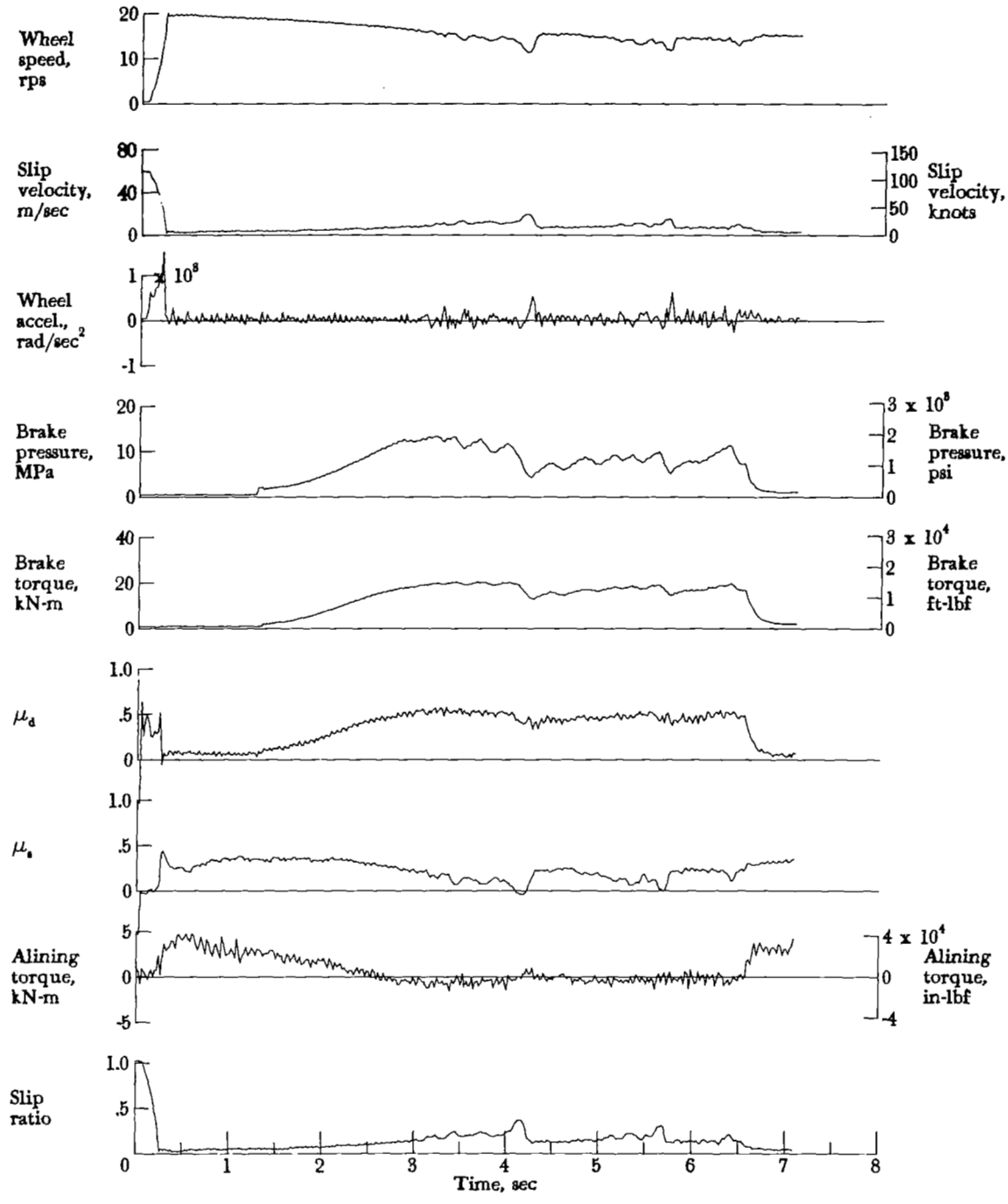

Figure A83.- Time histories for run 83. Nominal carriage speed, 97 knots; vertical load, 72.9 kN (16 400 lbf); yaw angle, 6°; brake pressure, 13 MPa (1950 psi); tire condition, worn; surface condition, dry.

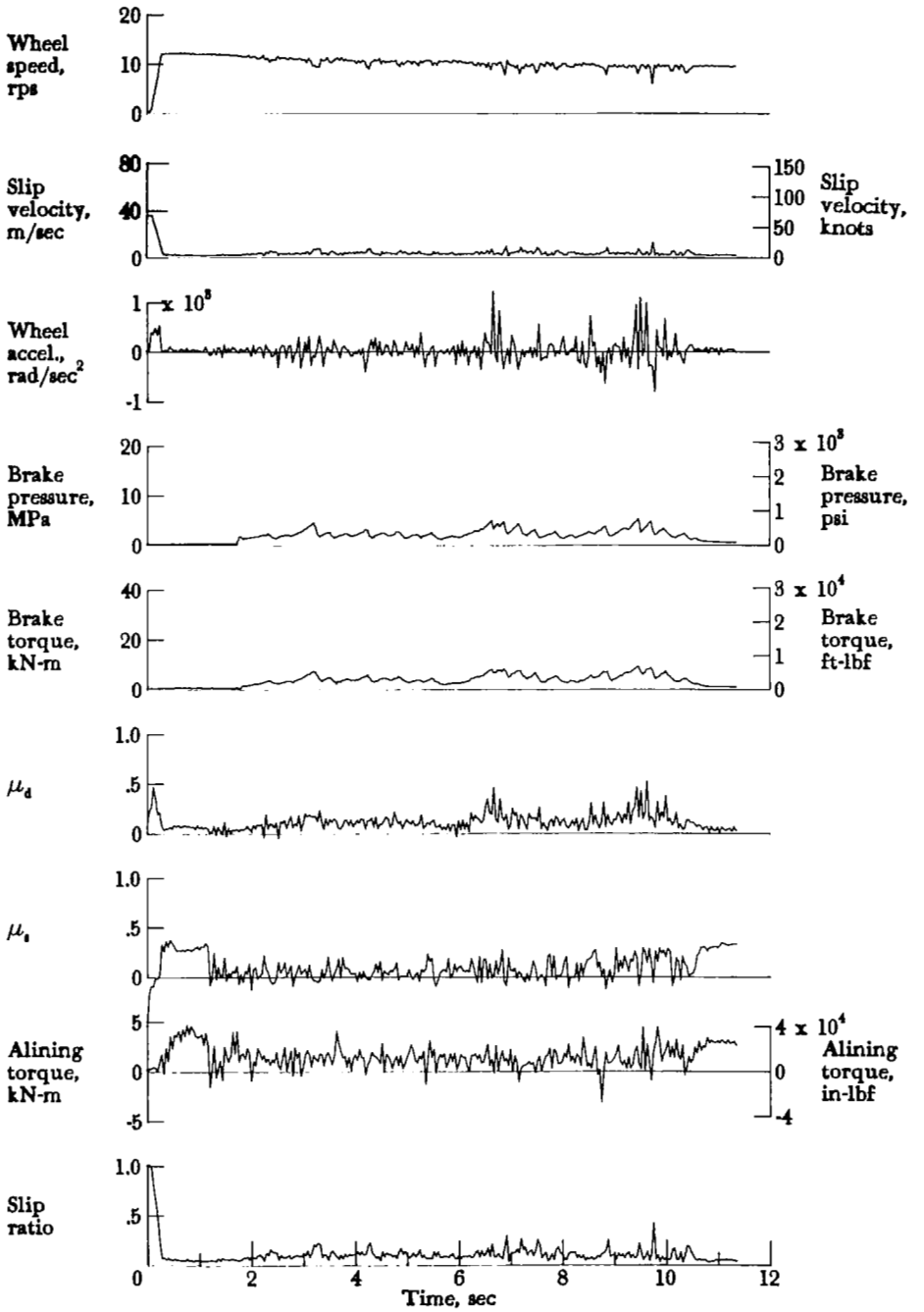

Figure A84.- Time histories for run 84. Nominal carriage speed, 59 knots; vertical load, 72.1 kN (16 200 lbf); yaw angle, 6°; brake pressure, 13 MPa (1900 psi); tire condition, worn; surface condition, damp.

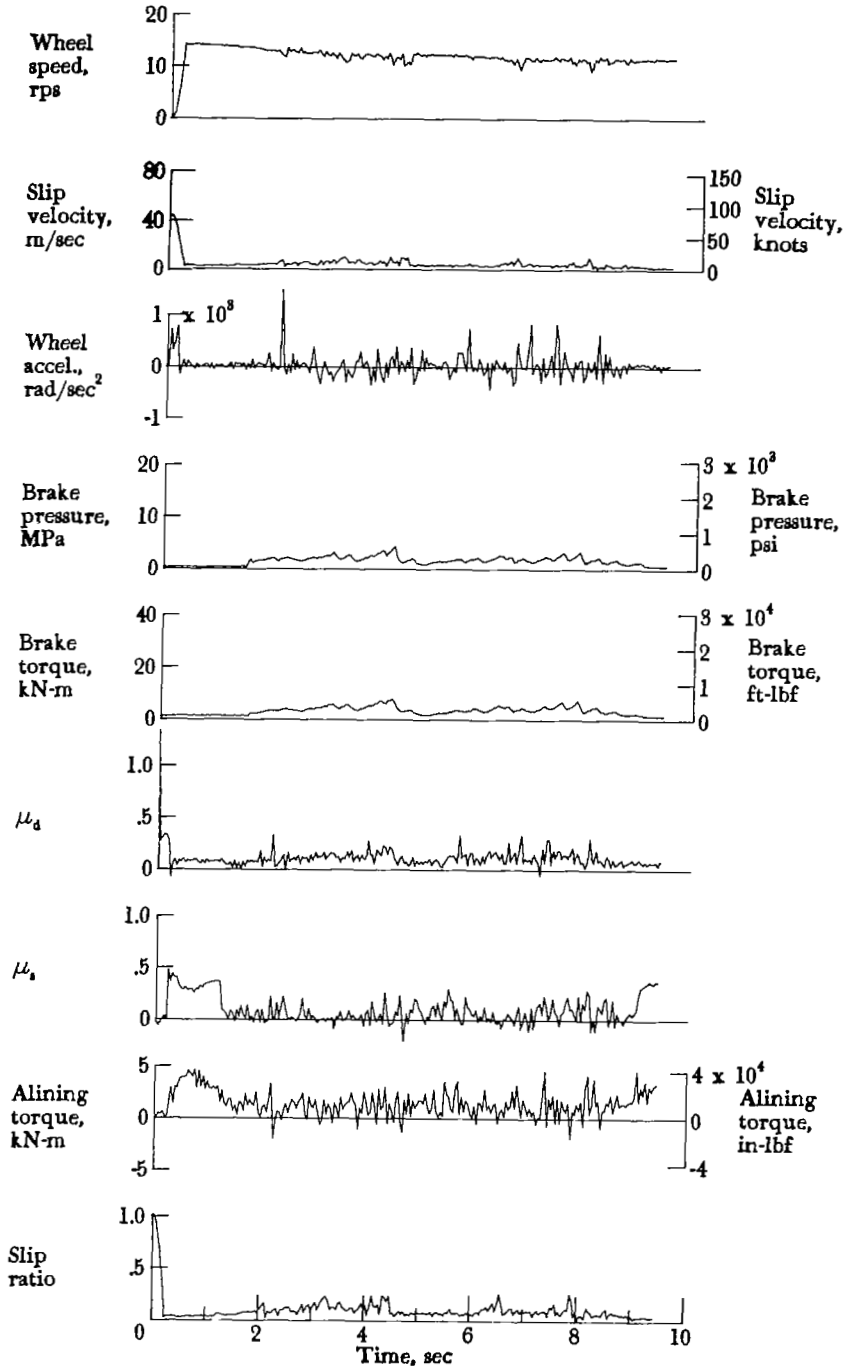

Figure A85.- Time histories for run 85. Nominal carriage speed, 71 knots; vertical load, 71.2 kN (16 000 lbf); yaw angle, 6°; brake pressure, 13 MPa (1950 psi); tire condition, worn; surface condition, damp.

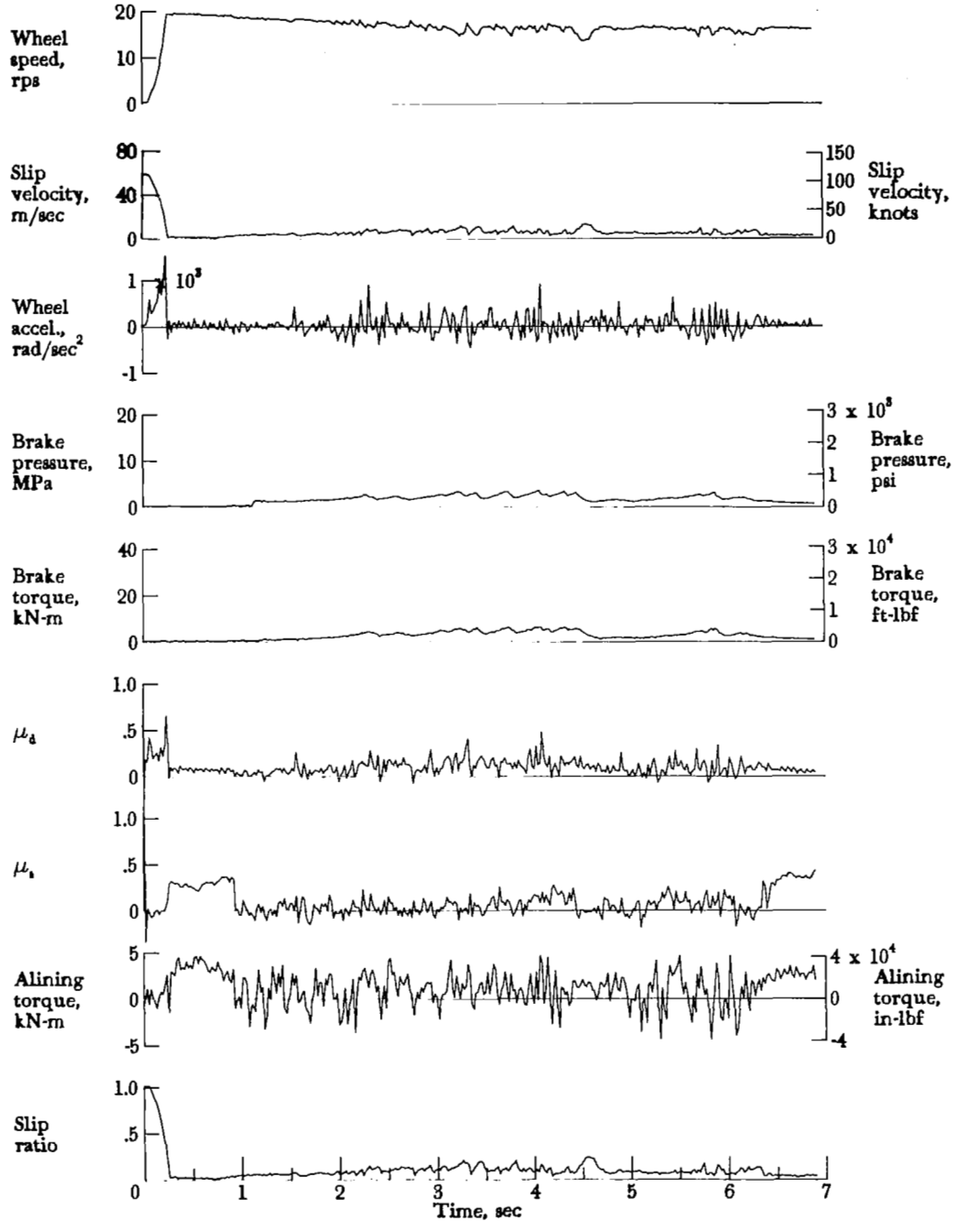

Figure A86.- Time histories for run 86. Nominal carriage speed, 100 knots; vertical load, 70.3 kN (15 800 lbf); yaw angle, 6°; brake pressure, 13 MPa (1950 psi); tire condition, worn; surface condition, damp.

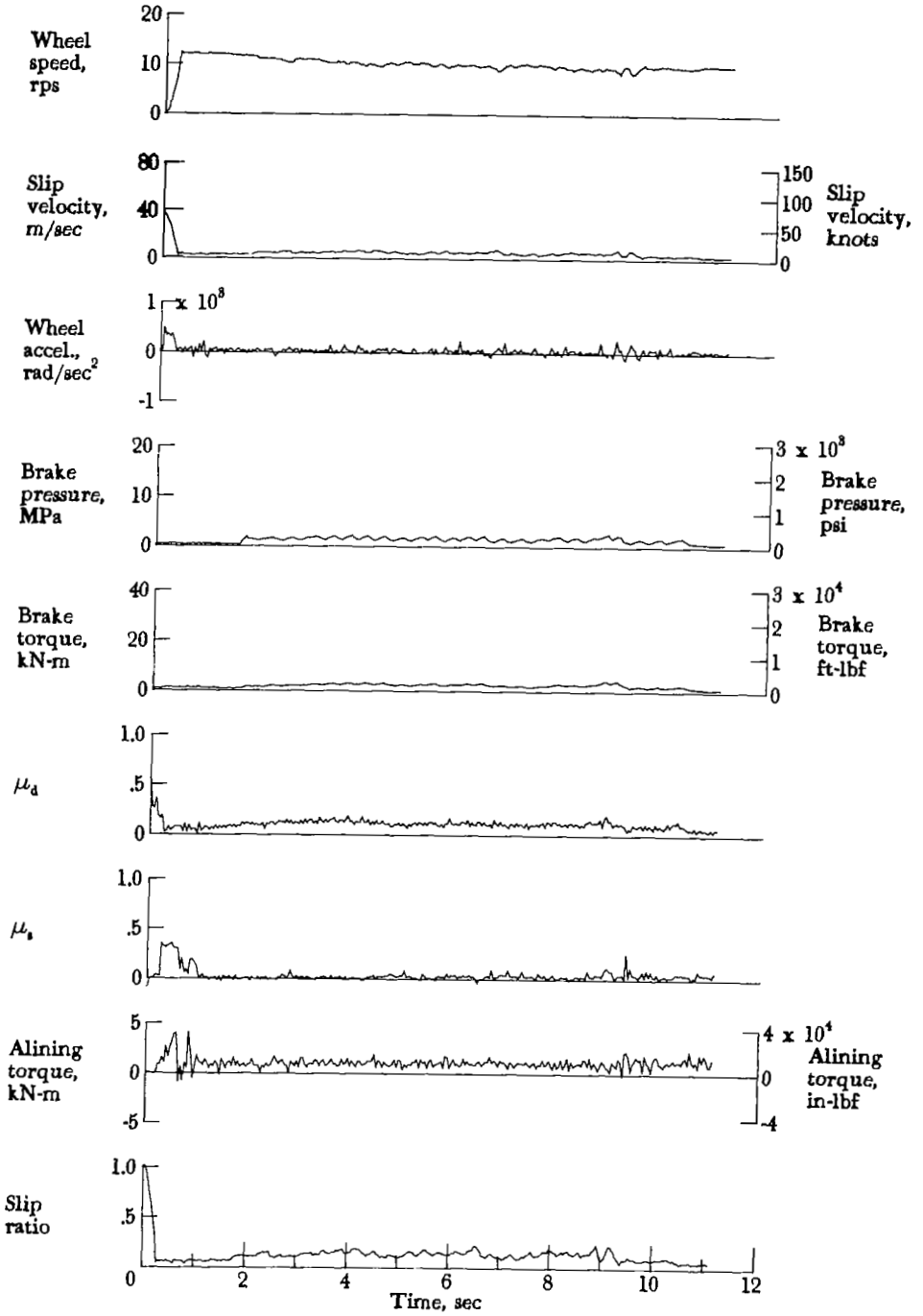

Figure A87.- Time histories for run 87. Nominal carriage speed, 61 knots; vertical load, 68.9 kN (15 500 lbf); yaw angle, 6°; brake pressure, 13 MPa (1950 psi); tire condition, worn; surface condition, flooded.

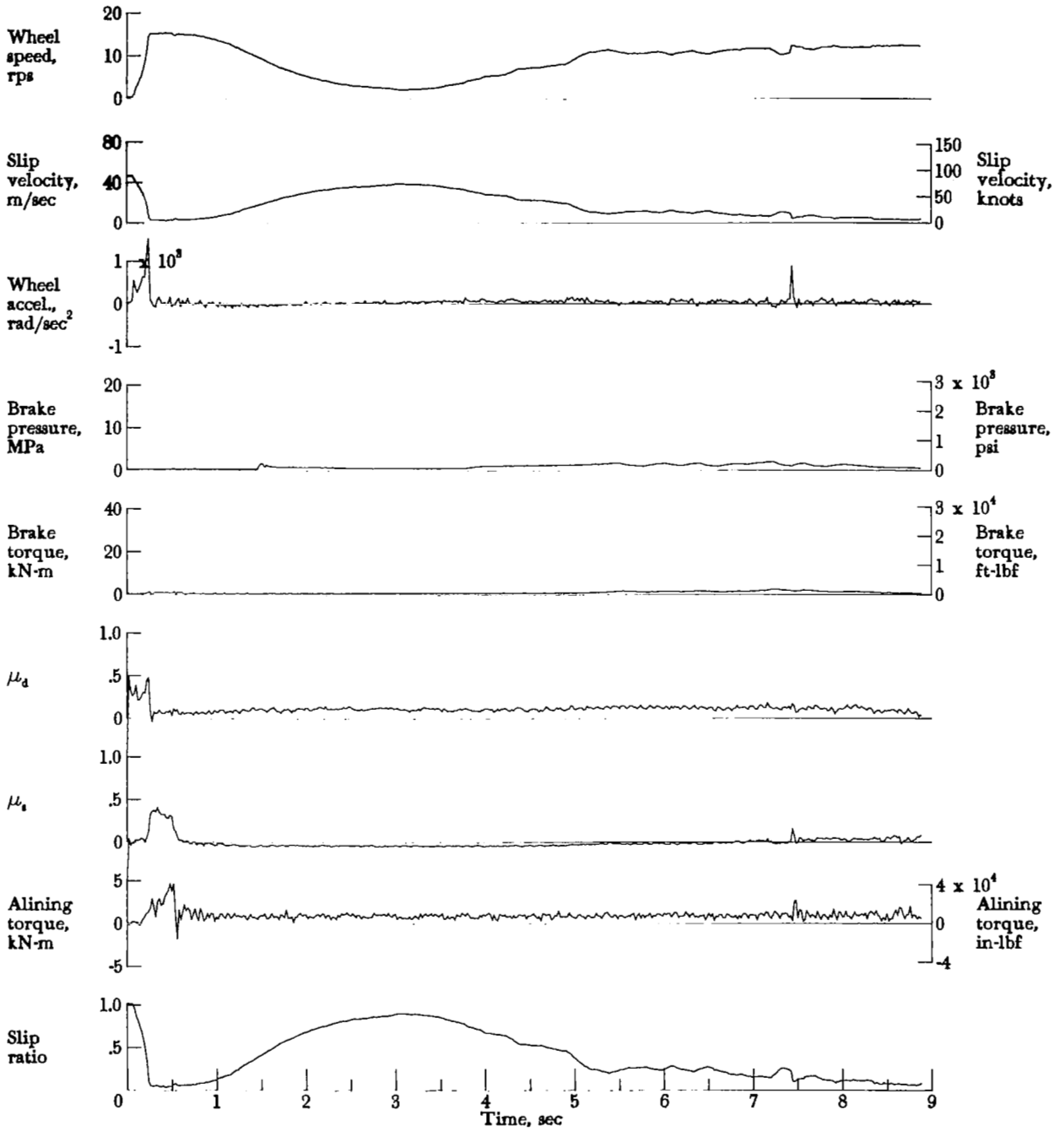

Figure A88.- Time histories for run 88. Nominal carriage speed, 77 knots; vertical load, 69.3 kN (15 600 lbf); yaw angle, 6°; brake pressure, 13 MPa (1950 psi); tire condition, worn; surface condition, flooded.

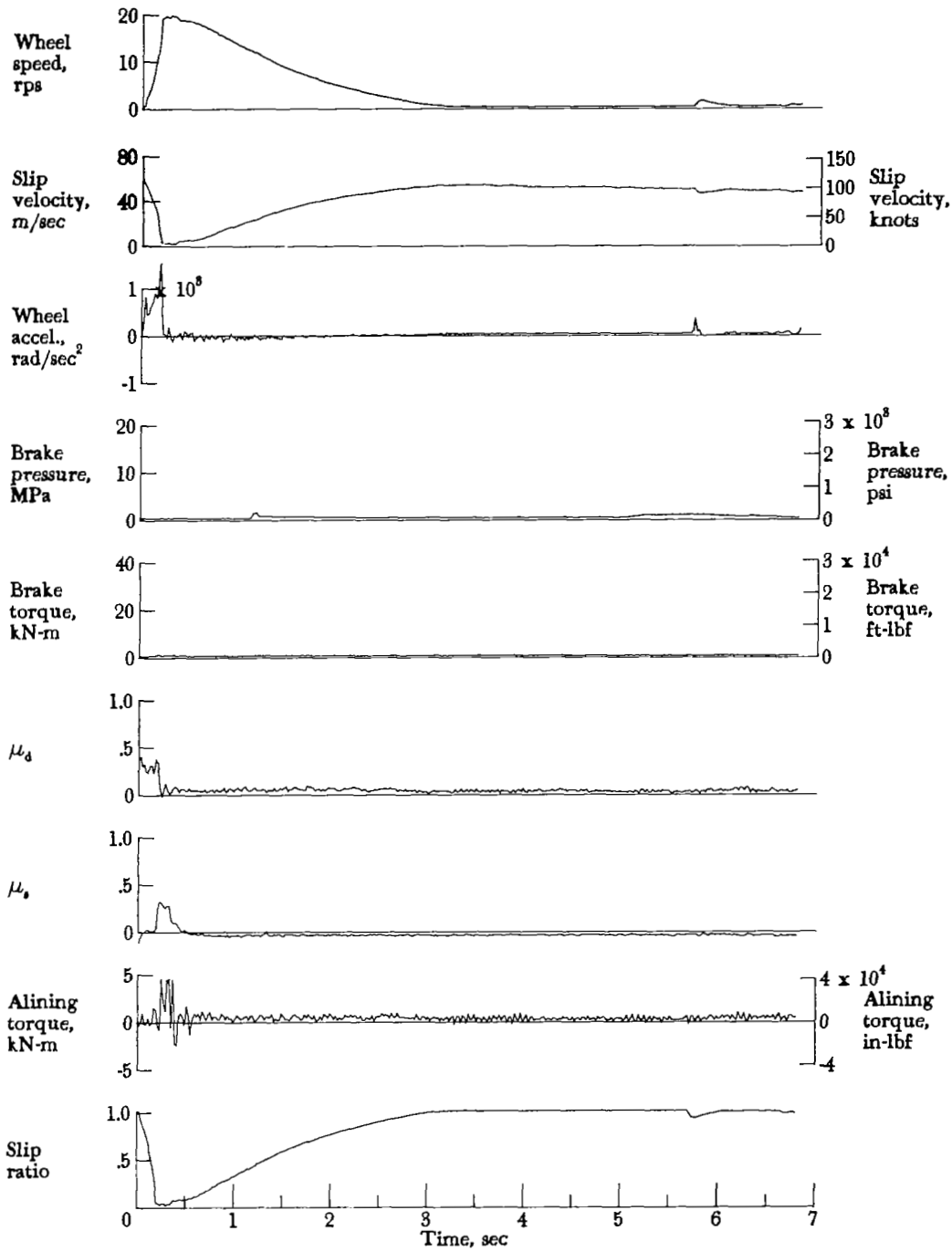

Figure A89.- Time histories for run 89. Nominal carriage speed, 101 knots; vertical load, 70.3 kN (15 800 lbf); yaw angle, 6°; brake pressure, 13 MPa (1950 psi); tire condition, worn; surface condition, flooded.

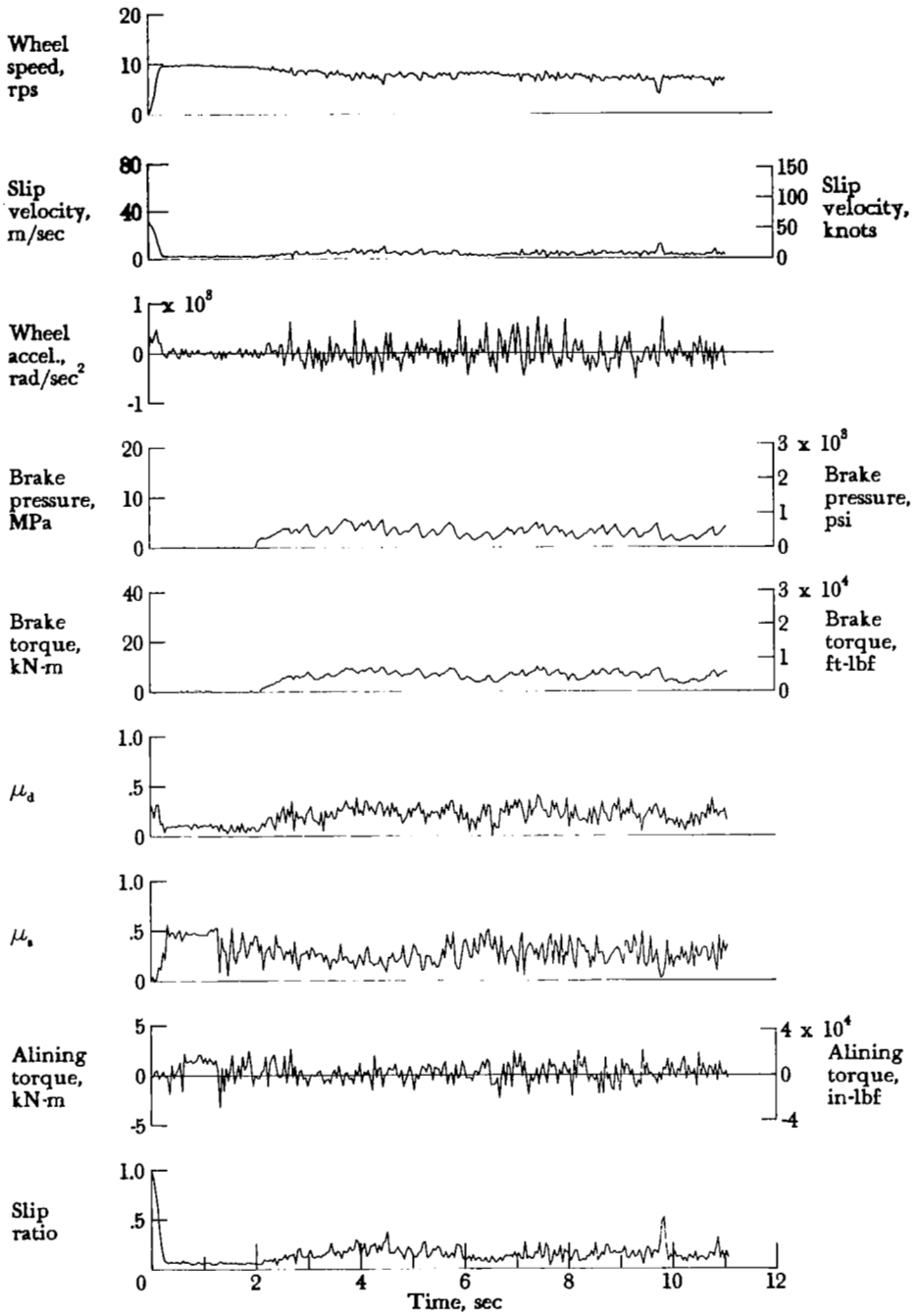

Figure A90.- Time histories for run 90. Nominal carriage speed, 50 knots; vertical load, 69.3 kN (15 600 lbf); yaw angle, 9°; brake pressure, 13 MPa (1950 psi); tire condition, worn; surface condition, damp.

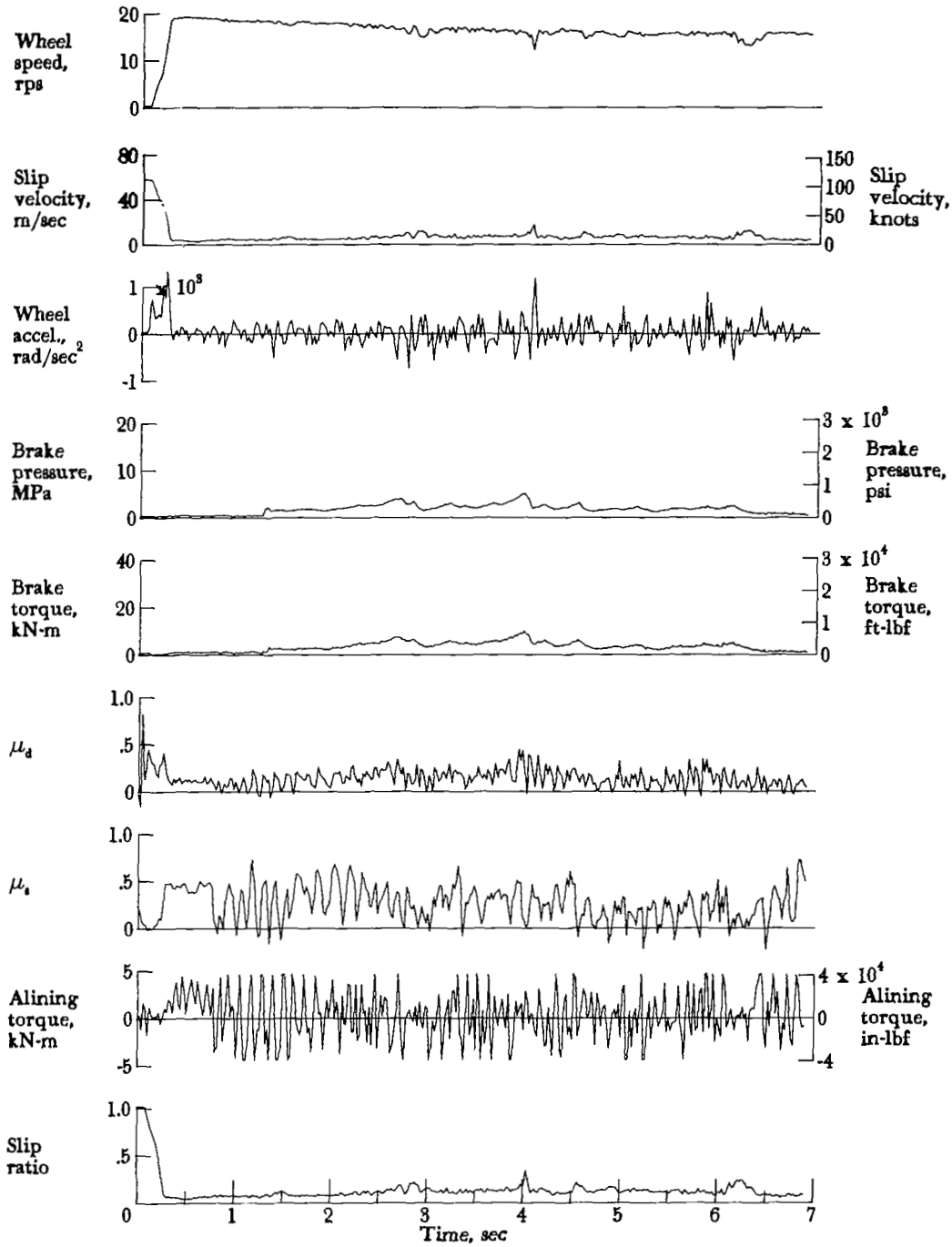

Figure A91.- Time histories for run 91. Nominal carriage speed, 102 knots; vertical load, 71.6 kN (16 100 lbf); yaw angle, 9°; brake pressure, 13 MPa (1950 psi); tire condition, worn; surface condition, damp.

1. Report No.	2. Government Accession No.	3. Recipient's Catalog No.
NASA TP-1877		

4. Title and Subtitle	5. Report Date
BEHAVIOR OF AIRCRAFT ANTISKID BRAKING SYSTEMS ON DRY AND WET RUNWAY SURFACES - HYDROMECHANICALLY CONTROLLED SYSTEM	August 1981
	6. Performing Organization Code 505-44-33-01
7. Author(s)	8. Performing Organization Report No.
John A. Tanner, Sandy M. Stubbs, and Eunice G. Smith	L-14549
	10. Work Unit No.
9. Performing Organization Name and Address	
NASA Langley Research Center Hampton, VA 23665	11. Contract or Grant No.
	13. Type of Report and Period Covered
12. Sponsoring Agency Name and Address	Technical Paper
National Aeronautics and Space Administration Washington, DC 20546	14. Sponsoring Agency Code

15. Supplementary Notes

16. Abstract

An experimental investigation was conducted at the Langley Aircraft Landing Loads and Traction Facility to study the braking and cornering response of a hydromechanically controlled aircraft antiskid braking system. The investigation, conducted on dry and wet runway surfaces, utilized one main gear wheel, brake, and tire assembly of a McDonnell Douglas DC-9 series 10 airplane. The landing-gear strut was replaced by a dynamometer. During maximum braking, average braking behavior indexes based upon brake pressure, brake torque, and drag-force friction coefficient developed by the antiskid system were generally higher on dry surfaces than on wet surfaces. The three braking behavior indexes gave similar results but should not be used interchangeably as a measure of the braking behavior of this antiskid system. During the transition from a dry to a flooded surface under heavy braking, the wheel entered into a deep skid but the antiskid system reacted quickly by reducing brake pressure and performed normally during the remainder of the run on the flooded surface. The brake-pressure recovery following transition from a flooded to a dry surface was shown to be a function of the antiskid modulating orifice.

17. Key Words (Suggested by Author(s))	18. Distribution Statement
Antiskid braking system Aircraft tires Cornering	Unclassified - Unlimited Subject Category 05

19. Security Classif. (of this report)	20. Security Classif. (of this page)	21. No. of Pages	22. Price
Unclassified	Unclassified	175	A08

For sale by the National Technical Information Service, Springfield, Virginia 22161

NASA-Langley, 1981